



SCMS SCHOOL OF ENGINEERING AND TECHNOLOGY, KARUKUTTY

3.3.1 Number of research papers published per teacher in the Journals notified on UGC CARE list during 2019-2020

SL NO:	Title of paper	Name of the author/s	Department of the teacher	Name of journal	Calendar Year of publication	ISSN number	Link to the recognition in UGC enlistment of the Journal /Digital Object Identifier (doi) number		
							Link to website of the Journal	Link to article / paper / abstract of the article	Is it listed in UGC Care list
1	Artificial Muscle Intelligence System with Deep Learning for Post-Stroke Assistance and Rehabilitation	Dr.Sunil Jacob	ECE	IEEE Access	September 2019	ISSN: 2169-3536	https://ieeexplore.ieee.org/Xplore/home.jsp	https://ieeexplore.ieee.org/document/8839118	SCI
2	Brain-controlled adaptive lower limb exoskeleton for rehabilitation of post-stroke paralyzed	VINOJ P G	ECE	IEEE Access	June 2019	ISSN: 2169-3536	https://ieeexplore.ieee.org/Xplore/home.jsp	https://ieeexplore.ieee.org/abstract/document/8732331	SCI
3	Towards reducing computational effort in Vortex Induced Vibration Predictions of a cylindrical riser	Dr. SheejaJanardhanan	MECH	Periodico Tche Quimica	November 2019	ISSN: 1806-0374	https://www.periodico.tchequimica.com/	https://www.tchequimica.com/arquivos/jornal/2019/33/856_Periodico33.pdf	SCOPUS
4	Review of IS 1893-1 (2002): Effect of Unreinforced Masonry Infill Walls on Seismic Response of Framed Structures	MG Airin	CE	Lecture Notes in Civil Engineering	December 2019	ISSN:2366-2557	https://www.springer.com/series/15087	https://link.springer.com/chapter/10.1007/978-3-030-26365-2_60	SCOPUS
5	Preventing hijacked research papers in fake (rogue) journals through social media and databases	Dr Varun G Menon	CSE	Library Hi Tech News	August 2019	ISSN: 0741-9058	https://www.emerald.com/insight/publication/issn/0741-9058	https://www.emerald.com/insight/content/doi/10.1108/LHTN-11-2018-0070/full.html	SCI
6	A Study on Women Educate and Empower	Divya M S	Basic Science and Humanities	INTERNATIONAL JOURNAL OF ENGLISH LANGUAGE, LITERATURE AND TRANSLATION STUDIES (IJELR)	March 2020	ISSN:2349-9451	http://ijelr.in/Abstract-Indexing.htm	http://ijelr.in/7.1.2020/179-183%20DIVYA%20MS.pdf	SCOPUS
7	Optimum range of angle tracking radars: a theoretical computing	Dr Varun G Menon	CSE	International Journal of Electrical and Computer Engineering (IJECE)	June 2019	ISSN:2088-8708	https://ijece.iascsare.com/index.php/IJECE/index	https://ijece.iascsare.com/index.php/IJECE/article/view/12191	SCOPUS

8	A secure and energy-efficient opportunistic routing protocol with void avoidance for underwater acoustic sensor networks	Dr Varun G Menon	CSE	Turkish Journal of Electrical Engineering & Computer Sciences	May 2020	ISSN: 1300-0632	https://journals.tubitak.gov.tr/elektrik/	https://journals.tubitak.gov.tr/elektrik/vol28/iss4/34/	SCI
9	SysDroid: a dynamic ML-based android"	Dr Vinod P	CSE	Cluster Computing	January 2020	ISSN: 1386-7857	https://www.springer.com/journal/10586	https://link.springer.com/article/10.1007/s10586-019-03045-6	SCI
10	Automated detection of retinal hemorrhage based on supervised classifiers	Sreeja K A	ECE	Indonesian Journal of Electrical Engineering and Informatics	March 2020	ISSN 2089-3272	http://section.iainonline.com/index.php/IJEEI	http://section.iainonline.com/index.php/IJEEI/article/view/1353	SCOPUS
11	Blockchain For Intelligent Transport System	Dr Varun G Menon	CSE	IETE Technical Review	May 2020	ISSN: 0256-4602	https://www.tandfonline.com/journals/titr20	https://www.tandfonline.com/doi/abs/10.1080/02564602.2020.1766385	SCI
12	Interfaced circuit using a non destructive method for moisture measurement	Dr Divyanath K	EEE	Microprocessors and Microsystems journal	March 2020	ISSN: 0141-9331	https://www.sciencedirect.com/journal/microprocessors-and-microsystems	https://www.sciencedirect.com/science/article/pii/S0141933119304806	SCI
13	Development of novel groundwater iron removal system using adsorptive Fe(II) process	Rathish Menon	CE	Groundwater for Sustainable Development	December 2019	ISSN: 2352-801X	https://www.journals.elsevier.com/groundwater-for-sustainable-development	https://www.sciencedirect.com/science/article/abs/pii/S2352801X19300785?via%3Dihub	SCI
14	Secure Brain to Brain Communication with Edge Computing for Assisting Post-Stroke Paralyzed Patients	Dr Varun G Menon	CSE	IEEE Internet of Things Journal	November 2019	ISSN 2327-4662	https://ieeexplore.ieee.org/document/8891712	https://ieeexplore.ieee.org/document/8891712	SCI
15	Depth information enhancement using block matching and image pyramiding stereo vision enabled RGB-D sensor	Dr.Sunil Jacob	ECE	IEEE Sensors Journal	January 2020	ISSN: 1530-437X	https://ieeexplore.ieee.org/xpl/RecentIssue.jsp?punumber=7361	https://ieeexplore.ieee.org/xpl/RecentIssue.jsp?punumber=7361	SCI
16	An Adaptive and Flexible Brain Energized Full Body Exoskeleton With IoT Edge for Assisting the Paralyzed Patients	Dr.Sunil Jacob	ECE	IEEE Access	May 2020	ISSN: 2169-3536	https://ieeexplore.ieee.org/xpl/RecentIssue.jsp?punumber=6287639	https://ieeexplore.ieee.org/document/9099875	SCI

17	A Study on Women Educate and Empower	Divya M S	Basic Science and Humanities	INTERNATIONAL JOURNAL OF ENGLISH LANGUAGE, LITERATURE AND TRANSLATION STUDIES (IJELR)	March 2020	ISSN:2349-9451	http://ijelr.in/Abstract-Indexing.htm	http://ijelr.in/7.1.2020/179-183%20DIVYA%20MS.pdf	SCOPUS
18	An Adaptive and Flexible Brain Energized Full Body Exoskeleton With IoT Edge for Assisting the Paralyzed Patients	Dr.Sunil Jacob	ECE	IEEE Access	May 2020	ISSN: 2169-3536	https://ieeexplore.ieee.org/xpl/RecentIssue.jsp?punumber=6287639	https://ieeexplore.ieee.org/document/9099875	SCI
19	Service learning in engineering education: A study of student participatory survey for urban canal rejuvenation in Kochi, India	Dr Rathish Menon	CE	Procedia Computer Science	2020	ISSN: 1877-0509	https://www.sciencedirect.com/journal/procedia-computer-science	http://dx.doi.org/10.1016/j.procs.2020.05.042	Scopus
20	Blockchain For Intelligent Transport System	Dr Varun G Menon	CSE	IETE Technical Review	May 2020	ISSN: 0256-4602	https://www.tandfonline.com/journals/itr20	https://www.tandfonline.com/doi/abs/10.1080/02564602.2020.1766385?journalCode=itr20	SCI
Total number of research papers published per teacher in the Journals notified on UGC CARE list during 2019-2020									20




 PRINCIPAL
 SCMS SCHOOL OF ENGINEERING & TECHNOLOGY
 VIDYANAGAR, PALLISSERY, KARUKUTTY
 ERNAKULAM, KERALA-683 576



SysDroid: a dynamic ML-based android malware analyzer using system call traces

Ananya A.¹ · Aswathy A.¹ · Amal T. R.¹ · Swathy P. G.¹ · Vinod P.¹ · Mohammad Shojafar^{2,3}

Received: 10 August 2019 / Revised: 29 November 2019 / Accepted: 31 December 2019 / Published online: 13 January 2020
© Springer Science+Business Media, LLC, part of Springer Nature 2020

Abstract

Android is a popular open-source operating system highly susceptible to malware attacks. Researchers have developed machine learning models, learned from attributes extracted using static/dynamic approaches to identify malicious applications. However, such models suffer from low detection accuracy, due to the presence of noisy attributes, extracted from conventional feature selection algorithms. Hence, in this paper, a new feature selection mechanism known as *selection of relevant attributes for improving locally extracted features using classical feature selectors* (SAILS), is proposed. SAILS, targets on discovering prominent system calls from applications, and is built on the top of conventional feature selection methods, such as mutual information, distinguishing feature selector and Galavotti–Sebastiani–Simi. These classical attribute selection methods are used as local feature selectors. Besides, a novel global feature selection method known as, weighted feature selection is proposed. Comprehensive analysis of the proposed feature selectors, is conducted with the traditional methods. SAILS results in improved values for evaluation metrics, compared to the conventional feature selection algorithms for distinct machine learning models, developed using Logistic Regression, CART, Random Forest, XGBoost and Deep Neural Networks. Our evaluations observe accuracies ranging between 95 and 99% for dropout rate and learning rate in the range 0.1–0.8 and 0.001–0.2, respectively. Finally, the security evaluation of malware classifiers on adversarial examples are thoroughly investigated. A decline in accuracy with adversarial examples is observed. Also, SAILS recall rate of classifier subjected to such examples estimate in the range of 24.79–92.2%. However, prior to the attack, the true positive rate obtained by the classifier is reported between 95.2 and 99.79%. The results suggest that the hackers can bypass detection, by discovering the classifier blind spots, on augmenting a small number of legitimate attributes.

Keywords Android malware · Machine learning (ML) · Deep learning (DL) · Feature selection · Adversarial machine learning (AML) · Attacks

✉ Mohammad Shojafar
mohammad.shojafar@unipd.it; m.shojafar@surrey.ac.uk

Ananya A.
ananya@scmsgroup.org

Aswathy A.
aswathy@scmsgroup.org

Amal T. R.
amal@scmsgroup.org

Swathy P. G.
swathy@scmsgroup.org

Vinod P.
vinodp@scmsgroup.org

¹ Department of Computer Science & Engineering, SCMS School of Engineering and Technology, Ernakulam, Kerala, India

² ICS/5GIC, University of Surrey, Guildford GU27XH, UK

³ University of Padua, 35131 Padua, Italy

1 Introduction

The number of Android users has exponentially increased over the past decade, and this has opened the doors for the attackers to innovate methods, to compromise devices through vulnerable Android applications. The rise in the number of malware variants, constraint the anti-virus vendors in the signature update process, thereby adversely affecting the security of smartphones and tablets. According to Symantec's Internet Security Threat Report 2018, there was an increase of 54% Android malware variants with the figures reported in 2017 [9]. Symantec's report also mentions that third-party app stores hosted 99.9% of malicious apps. Kaspersky Lab products detected 5,321,142 malicious installation packages, 151,359 new mobile banking Trojans and 60,176 new mobile ransomware Trojans for the year 2018 [22].

Conventional mechanisms of Android malware analysis are based on three approaches which are static, dynamic and hybrid analysis. The static analysis incorporates signature-based, permission-based, and component-based investigation. Dynamic analysis involves the execution of the application in real-time and observing the behaviour of the application. The hybrid analysis consists of combining static and dynamic features [24]. In literature, several researchers have developed machine learning (ML) techniques [17–19] to resolve the problems of Android malware attacks. Previous works have focused on evasion attacks, which results in misclassification of the sample [6]. Zhou and Jiang [37] have worked on detecting Android malware by AV vendors. DroidAPIMiner [1] performs extraction of API call frequency from android applications and performs malware detection using supervised learning algorithms.

Contributions Static analysis alone cannot be used to identify malware applications as malware hide payload in the encrypted form, installed on execution. To cope with this problem, it is essential to develop methods based on dynamic analysis. Hence, some questions arises: Is it possible to adopt strategies employing dynamics analysis to detect Android malware using different features? How can the proposed dynamic method be guaranteed, to swiftly update itself to dynamically changing real-time Android samples (applications)? The main aim of the paper is to respond to these queries by devising a new feature selection method, and evaluate the robustness of the classifier against adversarial attacks. Hence, a novel system call analysis is proposed to detect Android malware at run time. In this way, a new feature selection method called *SAILS* is proposed, which improves the performance of classifiers over the conventional feature selection methods. The classical identified by us in this paper are mutual

information (MI), Galavotti–Sebastiani–Simi (GSS) and Distinguishing Feature Selector (DFS), to extract relevant attributes representative of the target class. Experiments are conducted on benchmark dataset consisting of 2474 Drebin malware and 2475 benign apps. In summary, the main contributions of our work are listed as follows:

- A new feature selection mechanism known as Selection of relevant Atttributes for Improving Locally extracted features using classical feature Selectors (SAILS) is proposed.
- An extensive analysis of ML and deep learning (DL) algorithms under diverse classifier parameters is conducted.
- One of the key observation is that XGBoost has a higher prediction capability in comparison to other classification algorithms.
- The performance of the classification algorithms when subjected to adversarial examples is performed. It is experimentally verified that classifiers are misled even to small modification in attributes introduced by augmenting malware samples with few prominent benign features.

The rest of the paper is organised as follows. In Sect. 2, the related works proposed in the field of Android malware detection. Section 3 presents the methodology. The attack model is presented in Sect. 4. The experiments, results, and its analysis has been discussed in Sect. 5. Finally Sect. 6 discusses about the conclusion and future work.

2 Related work

Several anti-malware techniques have been introduced to detect malware on Android devices. These techniques can be broadly classified as static and dynamic analysis. In static analysis, malicious behaviour is analyzed by scanning the source code of the application, instead of executing an application/program. The source code of the program is investigated to identify the trigger of malicious event. On disassembling the apps, different features such as permissions, hardware components, intents, broadcast receivers, data flow, APIs, control flow, etc. can be derived. Dynamic analysis is performed during run time. Here, the malware scanners monitor the response generated by the operating system, on the execution of the program. Commonly used features include network connections, system calls, etc. To bridge the gap between static and dynamic analysis, hybrid anti-malware techniques were also developed to improve the performance of malware detector. In the following subsections, the background is categorized into static methods presented in Sect. 2.1, solutions based

on dynamic malware analysis approach presented in Sect. 2.2, and hybrid techniques presented in Sect. 2.3.

2.1 Static feature based approaches

The authors in [11] propose a method to evaluate the security of machine learning-based android malware detector. Classifiers were trained using API calls extracted from the smali files. To explore the security of the classifier, the authors considered evasion attacks on diverse threat models. They propose a robust secure-learning paradigm that can be applied to other security tasks like fraud detection. The goal of the research work was to improve the robustness of online malware scanners against adversarial examples created at test time.

Another group of authors in [14] designed a method that worked in discrete and binary input domains. For malware detection, they train the neural network on the Drebin dataset and achieve classification performance against similar works in literature. They use an AML algorithm to mislead the ML model to about 63% of all malware samples in the Drebin dataset.

2.2 Dynamic feature selection methods

Bhandari et al. [5] proposed a malware detection tool capable of handling code injection during runtime. This approach binds semantics of the program and a classification engine. A sequence of system calls demonstrates the semantics of the app. To capture the actual behaviour of the apps, the order of the system calls were conserved. They apply Markov property on the acquired system call traces and construct a sequential system call graph (SSG). The authors compute all the acyclic paths by considering the first, and the last system calls as the start and end node in SSG. They develop feature vectors from the typical sets by applying asymptotic equipartition property on each path. After that, they perform statistical analysis by finding the average logarithmic branching factor of each path to train the model. Further, they use the histogram binning technique to form the feature vector table and train them using supervised learning algorithms. They conduct experiments on dataset containing 2000 applications (1000 Benign and 1000 malware apps). Benign apps were collected from the Google play store, and malware apps belonged to 119 different families. The proposed system obtains a detection accuracy of 94.2%.

The authors in [12] have designed a two-step learning strategy named *KuafuDet*, that used adversarial detection to learn malware patterns. It is composed of an offline training step that could select and extract features from the samples and further use this model to compromise the online tool. An automated camouflage detector is used to

filter the false negatives and feed them back into the training phase. *KuafuDet* reduces false negatives and improves detection accuracy by 15%. This method was tested on more than 250,000 mobile applications to demonstrate the scalability of *KuafuDet*.

Additionally, in another work, the authors [35] propose a method that transforms the packed malware variant detection problem, to a system calls classification problem. They generated a sequence of sensitive system calls and further applied principal component analysis to extract relevant attributes. Then, multi-layer neural networks were utilized to classify benign and malicious applications. The proposed system was reported to achieve a detection accuracy of 95.6%.

The authors in [8] used strace tool to extract the system calls. Each invocation of system calls was mapped to a frequency-based feature vector. Experiments were performed on self-made 60 apps, and the proposed work reported accuracy between 85 and 100%. Later authors, in [2] proposed an ML-based dynamic malware detection method. They extracted API calls and system call traces. In particular, 74 API functions and 90 system calls were considered as features. For classification, Random Forest classifier was utilized. Experiments were conducted on the dataset comprising of 7520 apps, of 3780 samples were used for training and remaining (3740 application) were considered in the testing phase. The study demonstrated an accuracy of 96.66%.

The authors in [10] introduced an ML approach that helped in increasing the user effectiveness in handling system data to improve security and privacy. The proposed approach was evaluated on different ML algorithms deployed on real-world systems, and it showed better efficiency. Suci et al. [29] developed a Fail Attacker Model. The model effectiveness was evaluated on adversaries having limited capabilities. A poisoning attack was subjected on different ML algorithms. Consequently, the fail model exhibited better resilience on generalized transferability.

2.3 Hybrid feature selection methods

The authors in [25] propose a novel malware detection method called *HADM*—hybrid analysis for detection of malware. The set of features were represented as vectors fed to Deep Neural Network (DNN) with different kernels. To apply graph kernels onto the graph sets, they converted dynamic information into graph-based representations. Further, output from various vector were combined with graph feature sets using hierarchical multiple kernel learning (MKL), to build a final hybrid classifier. The authors in [4] propose a three-level hybrid model called *SAMADroid* for Android malware detection. By

combining the benefits of three levels, SAMADroid provides more detection accuracy on static and dynamic analysis, deployed on local and remote host. For static analysis, attributes from the manifest files and the dex code files were considered. For dynamic analysis, they generate system call logs based on the local inputs and send it to the remote server. Remote servers analyze the extracted static features and the logs. Finally, ML algorithms are used to classify malware and benign apps. They present that the SAMADroid can provide detection accuracy of 82.76% with Random Forest (RF). Also, the authors in [30] designed a novel hybrid approach and utilized the NetLink technology to generate patterns of system calls related to file and network access. They compare the pattern of malware and benign apps, to build a malicious pattern set. They aim to collect system calls and in offline compares both the malicious and normal pattern sets to identify the unknown app.

Besides, the paper [15] explains a hybrid method called *MalDAE* that combines the dynamic and static API sequences into one hybrid sequence based on semantics mapping. *MalDAE* experiments show that the system achieved accuracy in the range of 94.39% and 97.89%. Also, *MalDAE* provides an overall idea about the common types of malware and predictive support for understanding and resisting malware. Another novel hybrid method is [32] which consists of deep Autoencoder (DAE) and convolutional neural network (CNN). They reconstruct high-dimensional features of Android applications and use multiple CNN to detect Android malware. To increase sparseness, nonlinear activation function *Relu* was utilized to prevent overfitting in the serial CNN architecture *CNN-S*. To increase the capability of feature extraction, they bound the convolutional layer and pooling layer with the full-connection layer. Later, deep Autoencoder as a pre-training method of CNN was employed to reduce the training time. They tested their hybrid approach on 10,000 legitimate and 13,000 malicious apps. This resulted in 5% increase in the accuracy compared with SVM. Further, training time using the DAE-CNN model reduces by 83% compared with the CNN-S model. A hybrid scheme designed by Zhenlong Yuan et al. [34] aims to introduce an online deep-learning-based malware detection method called *DroidDetector*. *DroidDetector* performs prediction on thousands of Android apps and also thoroughly perform an in-depth study of the features and declares an accuracy of 96.76%.

3 Methodology

In this section, our proposed system is presented. Figure 1 describes the architecture and the working of our system. A clear description of the steps involved in the identification and evaluation of malware samples, is discussed in the subsequent sections.

3.1 Data collection

The data collection phase involves the collection of two types of Android applications, malware applications as well as trusted applications. A total of 4949 samples comprising of 2475 benign and 2474 Drebin applications [3, 23] were downloaded. In particular, legitimate application were considered from diverse app categories. Categories comprised of lifestyle, education, medical, comics, etc. from 9Apps site [38]. All these apps were scanned using VirusTotal [31], which is a web service that examines files or URLs to check whether they are malicious or not. Finally, samples labelled as benign were included for carrying out experiments.

3.2 Feature extraction

A system call sequence presents how an application requests a service from the kernel of the operating system. System calls generated during the execution of an application, are used as features to identify samples as malware or benign. The intention of using system calls is to deduce the behaviour of the application and to understand its interaction with the Android operating system. System calls have been logged using strace utility. Further, to mimic human interactions, Android Monkey Runner [20], a utility in sdk is periodically accessed. Specifically, Android Monkey was configured to direct 200 random UI events in a minute. Some events generated are: (i) reception of SMS (ii) answer and make call, (iii) change geolocation, (iv) swipes and (v) update the battery charge status These set of events were selected as it generalizes the operations performed on the smartphones. To collect the call traces, the following procedures were adopted:

1. Install the app (using ADB install command)
2. Extract the package name and class of the application
3. Gets the process id (PID) corresponding to each application
4. Invoke strace command, and at each timestamp log system calls
5. Start Monkey command with application package name as the parameter
6. Suspend the application for ten seconds
7. Kill the app

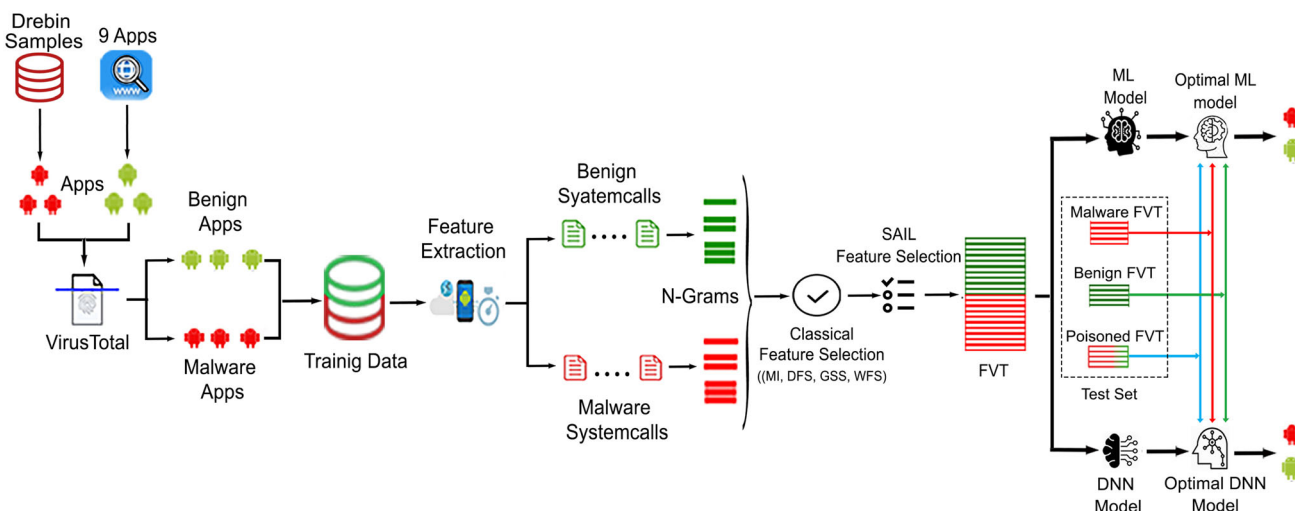


Fig. 1 The proposed architecture

8. Uninstall the app (using ADB uninstall command)
9. Delete app from device, finally reset the emulator clean state

Alternatively, in-order to extract system calls a human expert well versed in Android programming also interacted with the installed applications. In the feature extraction phase, initially, an emulator or an Android virtual device is created by specifying the basic configuration details such as device name, memory size, OS version, storage area, skins, screen resolution etc. Subsequently the .apk file, is installed into the emulator using the command: adb -s emulator-id install sample_app.apk.

Likewise, all other applications on the emulator are installed, and the system calls (strace -p process_id -o output_path) are recorded. Simultaneously, the Android monkey continuously interacts with the app during (adb shell monkey -p pkg_name -v 200). Once the specified events are completed, the process stops, and finally, the emulator is restored back into its clean state.

3.3 N-gram generation

In this part of the paper, the process of generation of *N-grams* is discussed. *N-gram* is a sequence of *n* items from a given sample. In *N-gram* model, the occurrence of an item is predicted based on the occurrence of its previous *n - 1* items. They are used to store the context of the words and can be used to make the next word predictions. *N-gram* for any range usually perform the best, and is shown to be applied in the domain of malware detection [27]. Since *N-grams* overlap, they not only capture the statistics about substrings of length but also implicitly capture frequencies of longer substrings as well.

Experiments on unigrams, bigrams, and trigrams are performed. Consider for an example a set of extracted features and the corresponding unigrams, bigrams, and trigrams generated:

- (i) **Features:** read prctl openat epoll_ct socketpair recvform
- (ii) **Unigram:** read, prctl, openat, epoll_ct, socketpair, recvform
- (iii) **Bigram:** read:prctl, prctl:openat, openat:epoll_ct, epoll_ct:socketpair, socketpair:recvform
- (iv) **Trigram:** read:prctl:openat, prctl:openat:epoll_ct, openat:epoll_ct:socketpair, epoll_ct:socketpair:recvform

Once the features are obtained, the corresponding bigrams and trigrams are generated, and analysis is performed on all *N-grams* to investigate the effect of *N-gram* size on classification accuracy.

3.4 Feature selection

Feature selection is one of the most crucial phase of ML, which has a huge impact on the classification model generated. Irrelevant and redundant features must be removed or else they may negatively impact the classification. Irrelevant are variables/attributes which have less correlation with a class, and redundant features have correlation with one or more attributes in the feature space. Thus, feature selection allows us to filter out attributes so that only the important features which help in classification is left out. Some of the conventional feature selection methods previously applied in the domain of malware detection are MI [21], GSS [36] and DFS [33]. Mutual information (MI) is a measure between two random variables quantifying the amount of information obtained from one random variable compared to the other random variable. DFS method exploits the hypothesis that certain term

appearing in more number of documents are highly relevant for categorization. GSS coefficient is a simplified variant of the Chi-square statistics proposed by Galavotti et al. In this approach, Chi-square is used to measure the correlation between the attribute and class. Thus, if a variable carries more information about a target class, such attributes are known as a characteristic feature, also have a high value. Thus, in summary, the benefits of performing feature selection improve accuracy reduce overfitting, and reduces training time. The following subsection highlights the feature selection methods employed in our experiment.

3.4.1 SAILS: selection of relevant attributes for improving locally extracted features using classical feature selectors

We propose *SAILS* as a novel feature selection method. The following steps outline the proposed feature selection methods through a simple example.

Step 1 Set of malware and benign system calls are listed. Let S_i denote a system call.

	S_1	S_2	S_3	S_4
M	bind	munmap	capget	ioctl
B	fcntl	lseek	writew	prctl

Step 2 Feature selection algorithms such as MI, GSS and DFS are used to give score for the samples.

Let $FS = \{f_1, f_2, \dots, f_n\}$
 $f_i(a_j) = \text{Malware/Benign score}$

Step 3 System calls are sorted based on the malware and benign scores.

	S_1	S_2	S_3	S_4
M	bind	munmap	capget	ioctl
B	fcntl	lseek	writew	prctl

Sorted list containing system calls is arranged in descending order of prominence.

M	S_2	S_4	S_3	S_1
B	S_1	S_4	S_2	S_3

Step 4 System calls are added to the new list

To do so, first, system calls from both malware and benign list are taken. Then, a check is performed to identify whether the system call already exists in the final list, if it is not present, it is augmented to the final result.

M	S_2	S_4	S_3	S_1
B	S_1	S_4	S_2	S_3
	S_2	S_1		

Next, the second system call from both malware and benign list is picked and their presence in the final list is

checked. Here S_4 appears in both malware and benign list, hence it is added once in the final list.

M	S_2	S_4	S_3	S_1
B	S_1	S_4	S_2	S_3
	S_2	S_1	S_4	

Similarly, the third system call is chosen, i.e., S_3 and S_2 . Here, S_2 is already present in the final list, hence only S_3 is added in the final list.

M	S_2	S_4	S_3	S_1
B	S_1	S_4	S_2	S_3
	S_2	S_1	S_4	S_3

Here, both S_1 and S_3 are already present in the final list, hence no need to add these two system calls again.

M	S_2	S_4	S_3	S_1
B	S_1	S_4	S_2	S_3
	S_2	S_1	S_4	S_3

This method is built over the conventional feature selection methods such as MI, GSS, and DFS. Initially, the malware and benign score of the union of malware and benign system calls are computed using the conventional feature selection methods. Then the features are ranked in the descending order of scores for the target classes. Once two separate lists of system calls are obtained, the new list of attributes based on SAILS are derived. For this purpose, the alternate system calls are selected, one each from the malware score ranked list and the other from the benign score ranked list and these system calls, are added into the new list provided, they are not the same and are not already present in the list. If the two calls are similar, only one instance of the feature is added to the list.

Algorithm 1 gives a brief description of the steps involved in SAILS. The input to the algorithm is the list of system calls, $S = \{s_1, s_2, \dots, s_N\}$; where m is the set of malware system calls and b is the set of benign system calls (line 1). In lines 2–3, call present in the applications are sorted. Lists, u and v consist of system calls arranged in the descending order of precedence of malware and benign score, respectively. X is the set of system calls that forms the final output. In the following steps, it is first checked whether the current sorted malware system call from u is present in X , if not, then, the presence of the benign system call from v is checked in X . If absent, both malware and benign system calls are added to X at positions j and $j + 1$ respectively (lines 7-8). Similarly, if the benign system call is already found in X then only the malware system call is added (line 10). Alternatively, if the malware system call is already present in X , then the presence of benign system call is checked, if not present, only the benign call is added

into X . Finally, if the benign system call from v is already present in X then there is no need to add either the malware (u) or the benign (v) system call into X . Finally, the list X is returned as output, as shown in line number 20.

The implementation of SAILS was performed using binary Max-Heap tree. Thus, two heap trees one for malware and another for benign system calls is obtained. Since this tree is populated using identical (union) system calls from both the dataset, hence it contains the same number of system calls, but arranged in different fashion due to the difference in local scores, corresponding to each system call. In this way, the space complexity in worst case is $O(N)$, to be precise as the number of system calls are less (approximately 393 in Linux Kernel 3.7), the space complexity is also less. The time complexity to create Max-Heap tree is $O(\log N)$. Generally, both the trees contain system call with maximum score at the root node. A system call with maximum score is picked and appended to the list X . During this course of action the system call with the highest score is deleted from the tree and a heapify operation is performed. Thus, the time required to undertake heapify operation in the worst case requires $O(N \log N)$. Therefore, in the worst case the total time to arrange the system calls will need $O(N \log N)$.

Algorithm 1 System calls extracted using SAILS

```

1: Procedure SAILS( $S, m, b$ )
2:  $u \leftarrow \text{sort}(m)$ 
3:  $v \leftarrow \text{sort}(b)$ 
4: while  $i \neq |S|$  do
5:   if  $u[i] \notin X$  then
6:     if  $v[i] \notin X$  then
7:        $X[j] \leftarrow u[i]$ 
8:        $X[j + 1] \leftarrow v[i]$ 
9:     else
10:       $X[j] \leftarrow u[i]$ 
11:    end if
12:  else
13:    if  $v[i] \notin X$  then
14:       $X[j] \leftarrow v[i]$ 
15:    else
16:      //do nothing
17:    end if
18:  end if
19: end while
20: return  $X$ 
    
```

3.4.2 Weighted feature selection (WFS)

Another method used in our experiment for feature selection is WFS. Here the weight of system calls are first computed, and then ordered in descending order of the corresponding malware and benign scores separately. The prominent system calls are used to create the feature vector matrix, which is further used to train the model and to evaluate the performance of the generated model.

Algorithm 2 discusses the steps involved in feature selection using WFS. The input to the algorithm is the set of system calls, S , as shown in line number 1. From line number 3 to 6, we compute the weight of system calls in the malware set. In particular, the weight of system call is computed as the product of the ratio of occurrences of system calls in malwares to the total occurrence of system calls in both training samples and the frequency of the calls in malware files, to the total number of malware samples in the training set. The time complexity for computing the weight is $O(1)$. Similarly, line number 8 to 10 depicts the calculation of the weight of system calls for benign examples. Finally, the average weight of system calls is determined (refer to line 12). The steps 3–12 steps are repeated until the weight corresponding to each call in set S is ascertained.

Algorithm 2 System calls extracted using WFS

```

1: Procedure WFS( $S$ )
2:  $S = \{s_1, s_2, \dots, s_N\}$ ; set of system calls.
3: while  $i \neq |S|$  do
4:   //Determine weight of system call in malware set
5:    $T(S_i, M) \leftarrow \frac{\text{occ}(S_i, M)}{\text{occ}(S_i, M) + \text{occ}(S_i, B)}$ 
6:    $U(S_i, M) \leftarrow \frac{\text{freq}(S_i, M)}{|M|}$ 
7:    $wt(S_i, M) \leftarrow T(S_i, M) * U(S_i, M)$ 
8:   //Determine weight of system call in Benign set
9:    $T(S_i, B) \leftarrow \frac{\text{occ}(S_i, B)}{\text{occ}(S_i, M) + \text{occ}(S_i, B)}$ 
10:   $U(S_i, B) \leftarrow \frac{\text{freq}(S_i, B)}{|B|}$ 
11:   $wt(S_i, B) \leftarrow T(S_i, B) * U(S_i, B)$ 
12:   $\text{avg}(S_i) \leftarrow \frac{wt(S_i, M) + wt(S_i, B)}{2}$ 
13: end while
14: return  $\text{avg}(S_i)$ 
    
```

3.5 Feature vector table

The feature vector table is the collection of vectors consisting of n rows and $m + 1$ columns. Here, n represents the number of applications in the dataset, and m is the number of unique system calls invoked by both malware and

	V_1		V_k		V_m	Y
X_1	a_{11}	...	a_{1k}	...	a_{1m}	0
X_2	a_{21}	...	a_{2k}	...	a_{2m}	0

X_j	a_{j1}	...	a_{jk}	...	a_{jm}	1

X_n	a_{n1}	...	a_{n2}	...	a_{nm}	1

Fig. 2 Feature vector table

benign APKs. An example of a feature vector table is depicted in Fig. 2. The columns 1 to m denote the attributes obtained after the feature selection phase. The last column denotes the class label associated with each sample. Here, the class label '1' identifies malware samples, and '0' denotes benign apps. Each row denotes a vector X with dimension m that correspond to samples in the dataset. Lastly, a_{ij} denotes the number of times j th system call was invoked by i th sample.

3.6 Training and testing phases

Once the feature selection phase is concluded, the next step is to train the model and predict new samples. Training phase largely include construction of a feature occurrence matrix, a data structure that record the frequency of attributes obtained after the feature selection process. Eventually, the classification algorithm learns patterns discriminant to the target classes. Later, the test samples are supplied to a trained ML model. The learned model assigns class labels to each apk in the test set. The performance of the classifiers is evaluated using performance metrics, such as accuracy, precision, recall, and F1-score. Models are developed using Logistic Regression (LR), Classification and Regression Tree, RF, XGBoost, and DNNs.

Train-test split method is used in this work. Specifically, 60% samples are assigned to train set and the remaining 40% of the apks are included in the test set. The train-test split method may sometimes result in the overfitted model.

3.7 Classifiers

Classification or predictive modelling is a method of approximating a hypothesis function (f) which maps to discrete output variables (y) for input observations (X). In particular, classification is a supervised approach where a program learns patterns from input examples and predict the class for a new sample. Multiple ML classification algorithms such as RF [7], Classification and Regression Tree (CART) [26], LR [16] and XGBoost [13] were used in our work. DNNs were also used to analyze the performance and to compare the performance obtained with machine learning algorithms.

3.7.1 Classification and regression tree (CART)

A decision tree is a non-parametric ML technique for regression and classification problems. Given the input observation, decision tree forms a hierarchical structure. Each internal node corresponds to attribute and leaf node corresponds to class labels. CART is a Gini index-based

method. Initially, all training samples are put in the root node. Subsequently, the best partition is explored to minimize the Gini impurity. Noisy or impure attributes classify a randomly selected sample into the wrong subset. Besides, gini impurity equals zero if samples belong to one class. The best discovered partition is further divided into parts, each of which is subsequently seen as a new node. This process is repeated until leaf nodes are obtained.

3.7.2 Random forest (RF)

Random Forest (RF) consists of a large number of decision trees which can function as an ensemble. Each tree is created from the set of a randomly selected subset of training examples. The individual tree generates a class prediction, further, the class that receives maximum votes is the outcome of the entire classification process.

RF hyper-parameters are used to improve the model's predictive ability. Commonly used hyper-parameters include a number of trees that the algorithm builds before taking the maximum vote or considers the average prediction. A higher number of trees generally increases performance and makes predictions more stable, however, suffers from speed. Alternatively, Random Forest can be configured with another hyperparameter like split criterion, min/max number of leaf nodes, the height of the tree etc.

3.7.3 Logistic regression (LR)

Logistic Regression is used when the target variable (i.e., dependent variable) is a categorical/binary response. A sigmoid function is used as a logistic function which outputs real value for the corresponding input feature vector. The obtained output value is subsequently converted to binary based on the threshold, in particular, the output is the estimated probability. Additionally, the coefficients also help in predicting the importance of each input variable.

3.7.4 XGBoost

XGBoost is a scalable and precise implementation of gradient boosting, developed solely for improving model performance and speed. Gradient Boosting is an ensemble learner, it creates a final model based on a prediction obtained from the collection of individual models. As the predictive power of individual models is weak and susceptible to overfitting, hence ensembles of weak models improve the overall result. Newly generated models can predict error of prior models. XGBoost utilizes gradient descent approach to reduce the error while combining the models

3.7.5 Deep neural network (DNN)

A DNN is a network contain multiple layers in between the input and output layer. In DNN, nodes in each layer are trained on a set of features of the previous output layer. As the number of layers increases, the complexity of the network increases, and it learns complex attributes. At higher dimensions, traditional ML algorithms such as LR, KNN, etc. exhibit poor performance, whereas in the case of neural networks, as the size of the data increases, the performance of the model increases. Additionally, hyperparameters like drop out, and the learning rate may be altered to improve the model performance.

Drop out is a regularization technique for neural networks, to avoid overfitting. It is an approach in which randomly selected neurons are ignored during training. Thus, in the forward pass, the contribution to the activation of the neurons in subsequent layers are ignored, and any updates in weights are also not applicable in the backward phase. Dropout enables a model to learn more robust features. Learning rate indicates the amount of change made to the model during each step of the search process.

3.8 Evaluation of the classifiers

In this paper, evaluation metrics considered are accuracy (see Eq. (1)), precision (see Eq. (2)), recall (or true positive rate) (see Eq. (3)) and F1-score (see Eq. (4)) to identify the classifier performance. *True negative* (α), is the number of truly classified benign samples. *True positive* (β) is the number of correctly classified malware files. The number of mis-classified legitimate applications are referred as *false positive* (γ). Malicious applications wrongly classified as benign are called as *False negative* (θ). Using TP (β), TN (α), FP (γ) and FN (θ), accuracy, recall, precision and F1-score is computed.

$$\text{Accuracy}(\mathcal{A}) = \frac{\alpha + \beta}{\alpha + \beta + \gamma + \theta} \quad (1)$$

$$\text{Precision}(\mathcal{PRC}) = \frac{\beta}{\beta + \gamma} \quad (2)$$

$$\text{Recall}(\mathcal{REC}) = \frac{\beta}{\beta + \theta} \quad (3)$$

$$\text{F1 - Score}(\mathcal{F}_1) = 2 * \left(\frac{\mathcal{PRC} * \mathcal{REC}}{\mathcal{PRC} + \mathcal{REC}} \right) \quad (4)$$

4 Attack model

Adversarial machine learning involves techniques, where the malicious samples injected with attributes of legitimate applications, forces machine learning system to misclassify such perturbed malware apps. The modified(perturbed) examples are also known as adversarial examples.

Adversarial examples can be broadly classified as (a) poisoning attack-performed during the training phase and (b) evasion attack-perturbed samples created in the prediction phase to mislead detection. Additionally, an adversary may use one/more, threat models. These threat model are related to the knowledge an attacker possesses, with reference to a machine learning system. In a white-box threat model, an adversary has complete knowledge of training samples and classifier parameters. Such attack models are used to evaluate the performance of a machine learning system in the worst case. Moreover, in a black-box attack model, the adversary does not have access to classifier and the training set. She can make a limited number of attempts to fool the classification system.

4.1 Evasion attack

In evasion attack, an attackers feed adversarial input to the classifier to increase misclassification. To accomplish this task and adversary create synthetic malware samples, imitating the properties of the benign applications. To start with, 10% (247 apps) of the total malware samples (2474 samples) are chosen. Then, prominent system calls invoked by benign samples absent in malware applications are appended to it at a varied concentration (1%, 2%, 3%, etc.). Such modified malware samples form the test set, which are later used to predict the performance of the models.

Algorithm 3 Evasion attack

```

1: Procedure Poisoning ( $M, S, j$ )
2:  $V \leftarrow j(M)$  //extract  $j$  percentage of samples from
   malware set
3:  $X \leftarrow S(M)$  //percentage of Unique system calls present
   only in benign set are extracted
4: for each file in  $V$  do
5:   append  $X$  at the end of file
6: end for
7: return file

```

Algorithm 3 gives a brief description of the evasion attack. The input to the algorithm includes M , which is the set of malware files and $S = \{s_1, s_2, \dots, s_N\}$, a set of prominent benign system calls which are absent in malware files, to be injected into the malware samples, at the specified concentration for creating adversarial examples. In particular, system calls in benign Max-Heap tree, are referred to as prominent calls which are absent in the first half of the malware Max-Heap tree. Thus, in the worst-case half the number of nodes in malware Max-Heap tree (half the height of tree) is searched. Hence, in worst case the time complexity to search legitimate system call in malware Max-Heap require $O(\log N)$, where N is the total number of system calls. In line 2, $j\%$ of the malware samples from original malware set are extracted. To be

precise, j is the percentage of malware files that needs to be poisoned (line 1). Next, prominent system calls invoked by benign APKs at the required concentration, i.e. (1%, 2%, ...) are selected (line 3). In lines 4 to 7, for each in file V , the system calls from X are added to samples in V depending on the supplied concentration rate. Finally, the output is a set of perturbed malware instances, injected with a sequence of the calls from benign apps (line 7).

5 Performance analysis

In this section, the experiments along with results are detailed. The experiments are conducted on Ubuntu 18.04 platform with the support of Intel Core i5-8250U CPU @ 1.80 GHz with 8GB RAM. The dataset consisted of 2475 benign and 2474 malware applications. Benign applications are downloaded from 9Apps site and verified for benignness by scanning samples using VirusTotal. The apps from Drebin dataset constituted malware set. This dataset contain malware samples belonging to 179 families. An automated tool, i.e., Android Monkey which is a part of the Android SDK, along with `strace` utility are used to record the system calls. On the completion of system calls extraction, the emulator process is killed and clean snapshot of the emulator is loaded for the analysis of subsequent samples. Comprehensive experiments were performed for evaluating the following:

- Performance of machine learning classifiers using proposed feature selection methods.
- Investigation of optimal feature category and feature length.
- Performance comparison of machine learning and deep learning algorithms.
- Investigation of the effect of drop out and learning rate in the performance of deep learning neural network.

5.1 Experiment-I: feature selection method

A novel feature selection method (SAILS) was developed on the top of classical feature selection approaches. Traditional feature selection methods like MI, GSS and DFS were employed as local feature selectors to estimate the score of each system call. These calls were further ranked using our proposed attribute ranking approach, yielding an enhanced outcome, both in terms of evaluation metrics and feature-length.

Table 1 depicts the comparison of accuracies obtained with proposed feature selectors and the conventional approaches. In this experiment, classification models were developed using RF, CART, LR and XGBoost. On observing the results, it is noted that the accuracy obtained

for our proposed system is higher in most of the cases, and for remaining experiments, the performance was at least equal to the conventional approach. It was observed that the highest accuracy was recorded for RF with unigrams, and for bigrams, the best outcome was achieved using XGBoost. In the case of trigrams, LR exhibited the highest accuracy. It is worth mentioning that the results obtained with the proposed methods exceed with fewer feature-length.

5.2 Experiment II: robustness of N-grams

Figure 3 illustrates the malware and benign scores of 20 system calls which were predominant in benign samples. From Fig. 3a, for unigrams, it can be seen that scores are identical or marginally differ. This suggests statistical similarity in the feature vectors for both malware and benign examples. Considering Fig. 3b and c it seen that the benign system call score is lesser when compared to the malware call score. Similar trend is observed in case of GSS^* , WFS^* and MI^* as shown in Appendix Figs. 11, 12 and 13 respectively.

5.3 Experiments-III: comparison of classification algorithms

In this experiment, the effectiveness of different ML algorithms in identifying malware applications is evaluated. In particular LR, Classification and Regression Tree (CART), Random Forest (RF), eXtreme Gradient Boost (XGBoost) and DNN are chosen. Additionally, a comprehensive analysis on the performance of DNN is performed by determining optimal values of dropout and learning rate.

From Fig. 4 it is clear that for GSS feature selection, the accuracy and F1-Score obtained with SAILS is better compared to the conventional approach.

Further, the average score of each system call was computed, the system calls were then arranged in the descending order of the average scores. Finally, sorted calls using the aforesaid approach was utilized in the training phase. For unigram, it was observed that Random Forest achieved the highest accuracy of 95.85% with F1-score of 95.87%. In the case of bigram, XGBoost showed better results with an accuracy of 99.4% and F1-score of 99.4%. Figure 4c depicts that for trigram, LR shows the highest accuracy of 99.34% and F1-score of 99.34%, which was higher than other classifiers.

A similar pattern of results was obtained with Random Forest and XGBoost employing DFS and MI feature selectors as depicted in Figs. 5 and 6. In the case of DFS feature selector, with Random Forest, the highest accuracy and F1-score obtained for unigram was 96.31% and

Table 1 Performance of classification algorithms with proposed feature selection approach and classical feature selectors

Classifier	Feature selectors	Unigram		Bigram		Trigram	
		FL	\mathcal{A}	FL	\mathcal{A}	FL	\mathcal{A}
LR	MI*	100(98)	97.66	100(2212)	97.16	90(18318)	99.44
	AVG-MI	100(98)	91.05	100(2212)	96.41	90(18318)	96.75
	GSS*	50(47)	88.58	80(1769)	99.13	80(16283)	99.34
	AVG-GSS	90(88)	88.43	100(2212)	99.08	100(20354)	99.34
	DFS*	100(98)	91.96	90(1990)	97.61	100(20354)	99.34
	AVG-GSS	90(88)	88.43	100(2212)	99.08	100(20354)	99.34
	WFS*	40(37)	89.3	100(2212)	98.0	100(20354)	99.4
CART	MI*	100(98)	96.5	100(2212)	96.65	100(20354)	98.83
	AVG-MI	100(98)	92.26	100(2212)	94.94	100(20354)	94.78
	GSS*	90(88)	92.67	80(1769)	97.77	80(16283)	98.58
	AVG-GSS	90(88)	92.57	80(1769)	95.08	100(20354)	98.17
	DFS*	90(88)	92.32	70(1548)	96.7	90(18318)	98.22
	AVG-DFS	90(88)	92.02	90(1990)	95.39	90(18318)	97.89
	WFS*	40(37)	93.1	100(2212)	96.7	100(20354)	98.7
RF	MI*	100(98)	96.75	80(1769)	97.21	100(20354)	98.23
	AVG-MI	100(98)	96.1	80(1769)	97.21	100(20354)	96.8
	GSS*	90(88)	95.85	90(1990)	98.78	80(16283)	98.17
	AVG-GSS	100(98)	95.5	100(2212)	98.53	100(20354)	97.77
	DFS*	100(98)	96.31	100(2212)	97.66	100(20354)	97.82
	AVG-DFS	100(98)	96.11	100(2212)	97.21	100(20354)	97.97
	WFS*	90(88)	97.2	20(442)	97.6	100(20354)	97.5
XGBoost	MI*	100(98)	95.6	90(1990)	99.3	100(20354)	99.2
	AVG-MI	100(98)	95.5	90(1990)	99.3	100(20354)	99.2
	GSS*	80(78)	95.75	70(1548)	99.44	80(16283)	98.32
	AVG-GSS	80(78)	92.65	70(1548)	97.67	80(16283)	97.72
	DFS*	90(88)	95.7	100(2212)	99.4	80(16283)	98.2
	AVG-DFS	90(88)	95.4	100(2212)	97.3	80(16283)	98.2
	WFS*	70(68)	96.6	40(884)	97.9	20(4070)	97.7

FL denotes feature length at which best outcomes were obtained. FL is represented in the form of $P(Q)$, where P denote the percentage of features extracted from the feature space and Q denote the number of attributes used to create model

Asterisks indicate a revised feature set after the application of SAILS

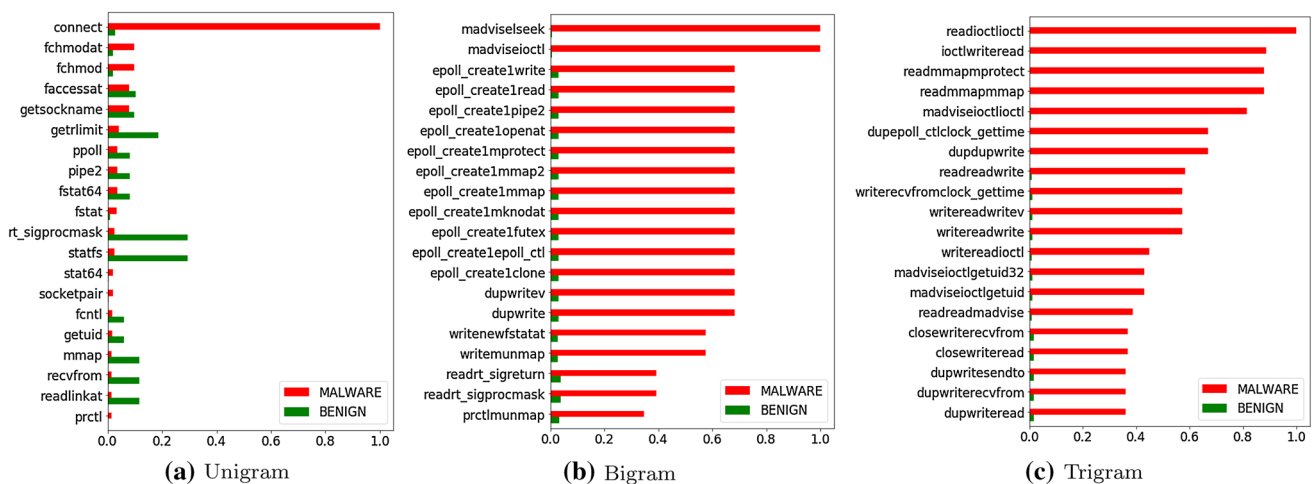


Fig. 3 Score difference of N-grams for DFS*

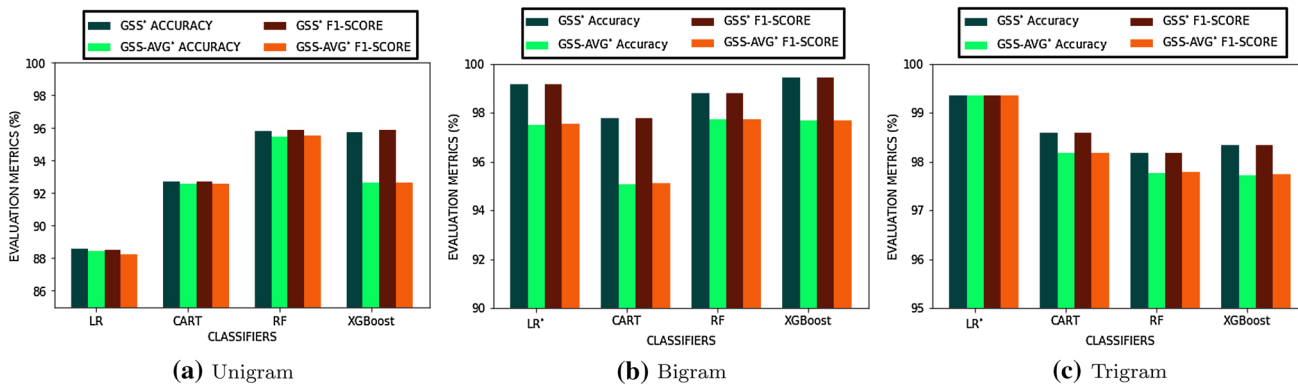


Fig. 4 Performance of GSS* feature selection on unigram, bigram, trigram

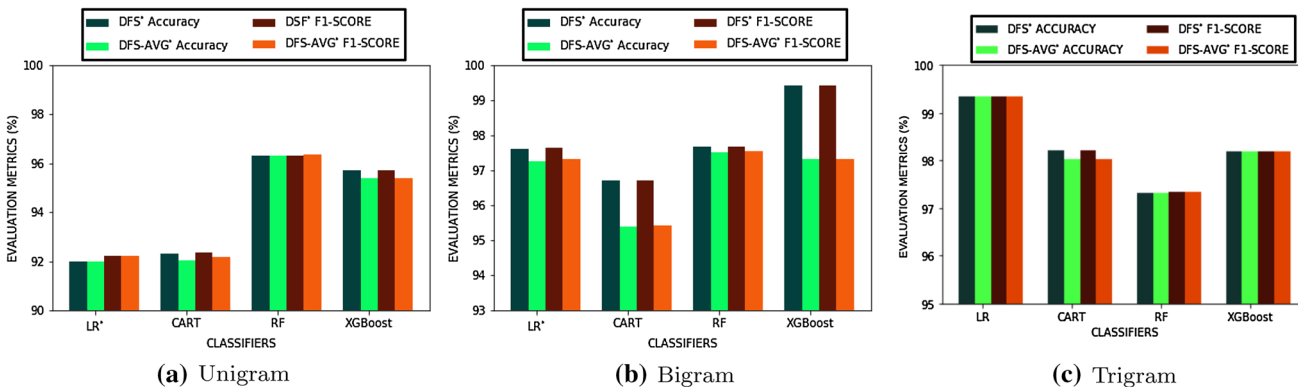


Fig. 5 Performance of DFS* feature selection on unigram, bigram, and trigram

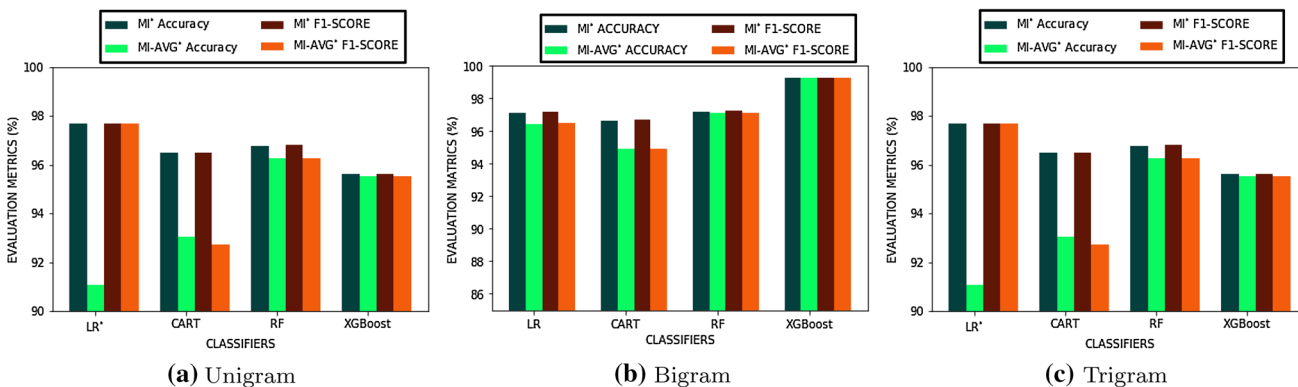


Fig. 6 Performance of MI* feature selection on unigram, bigram, and trigram

96.32%. In the case of bigram with XGBoost, accuracy and F1-score were 99.4% and 99.4% respectively.

Further, considering system call trigram with LR, the best accuracy achieved was 99.34% along with F1-score of 99.34%. Considering MI feature selector for unigram with Random Forest, the best accuracy attained was 96.75% and obtained F1-score of 96.79%. In the case of bigram, the best accuracy and F1-score obtained with XGBoost was 98% and 97.9% respectively. Whereas with LR, trigram

achieved accuracy and F1-score of 99.4% and 99.5% respectively.

Summary The results lead to the conclusion that the proposed feature selection method could derive attributes that had a higher correlation with the target class. Thus, resulting in improved outcome. In the case of unigram, Random Forest achieved higher accuracy and F1-score comparing other classifiers. Further for bigram, among all four classifiers, XGBoost exhibited better accuracy and F1-score. Comparing the results of trigram, LR achieved better

accuracy and F1-score compared to other classifiers. This is because, LR exhibited improved results as the feature vectors become linear in higher dimensional attribute space. The trend was clearly evident for the three Logistic regression model (i.e., unigram, bigram and trigram). Intuitively, in all cases of classification algorithms trained using bigrams and trigrams reported better performance compared to unigram.

5.4 Experiment IV: performance with DL classifier

In this experiment, DL was used to distinguish malware and legitimate applications. This experiment was conducted to analyze the performance of DNN compared to conventional ML approaches. A DNN model named DNN-2L with two hidden layers was designed. The first hidden layer consisted of 50% of attributes of the input feature space, as the number of neurons. Subsequently, the second layer contained 50% of the neurons, that were present in the previous layer. For example, if the feature set contained 1000 attributes, then the first layer will be created with 500 neurons and the second layer will be formed using 250 neurons. In DNN-2L, all layers contained Rectified Linear Unit (ReLU) activation function. Sigmoid activation function was used in the output layer, as malware identification is a binary classification problem. For faster convergence and to avoid overfitting, Adam optimization algorithm and cross entropy loss function was utilized respectively. Employing DNN-2L comprehensive analysis was conducted under following experimental settings and we investigated: (i) effect of dropout rate in the performance of model (Sect. 5.4.1) and (ii) effect of learning rate in the performance of model (Sect. 5.4.2).

5.4.1 Effect of dropout rate in the performance of model

To avoid overfitting on training data, dropout was proposed by Srivastava et al. [28]. Dropout is a regularization technique in which randomly selected neurons are removed during the training phase. This indicates that, the contribution of such neurons will be temporarily removed, during the forward pass and weight update will be ignored, in the backward pass. During the learning phase, a neuron specific to a particular layer relies on the neighbouring neurons. In a fully connected topology, a neuron tuned to specific feature was passed on to the upstream neurons. Thus, the network becomes more specific to the training data. On the contrary, if certain neurons were randomly eliminated, then the predictions are performed with the existing neurons. This suggests that many new patterns/representations, will be created and subsequently learned by the network. Thus, the network would be less sensitive

to the weights of neurons and less likely to overfit the training data.

To study the impact of dropout rate, a diverse classification model learned with attributes derived by our proposed feature selection method was created. In particular, the well known feature selectors were improved by deriving the call/sequence of calls having the ability to identify target classes. The outcome of the results are shown in Fig. 7. The results in Fig. 7a indicates that dropout rates of 0.2, 0.5 and 0.6 gave the best results for all three categories of features (i.e., unigram, bigram and trigram). An identical trend can be observed in Fig. 7b and c, i.e., better results are obtained at dropout rate of 0.3, 0.5 and 0.6. Finally, it was observed that DNN-2L learned with unigram, bigram and trigram at dropout rate of 0.2, 0.5 and 0.7 respectively, attained the best results as depicted in Fig. 7d. A similar observation has been observed when considering the F1-score as the evaluation metric, to evaluate the performance of the DL classifiers as show in Fig. 8.

5.4.2 Effect of learning rate in the performance of model

Further the importance of learning rate on the results of classification was explored. Learning rate is a hyper-parameter which denotes how much a model needs to be modified each time, by adjusting the weight. Lower value of learning rate indicates more time spent on training or in particular more steps needed to reach local minima. Conversely, large gradient descent learning rate would overshoot, besides missing local minima. Specifically, the model would fail to converge. In this study, the learning rate was varied such that it began with a small value (i.e. 0.001) and progressively increased by 0.01 until the maximum value of learning rate (i.e., 0.3) was reached (refer to Table 2).

5.5 Experiment V: evaluation against adversarial examples

The performance of any ML based system might degrade over time, eventually fortifying the system. In order to evaluate the detection capability of the classifier in the presence of adversarial samples, synthetic malware's mimicking statistical properties of legitimate set were created. In this context, adversarial malware samples were developed, by injecting varied proportion of prominent system calls, frequently invoked by the benign applications. The point of argument here is that, the classification algorithms fail to detect adversarial malware samples. The results show that as the proportion of system calls injected into each of the samples was increased, the recall declined dramatically, indicating that the classification algorithms fail to detect the malware samples (refer Table 3).

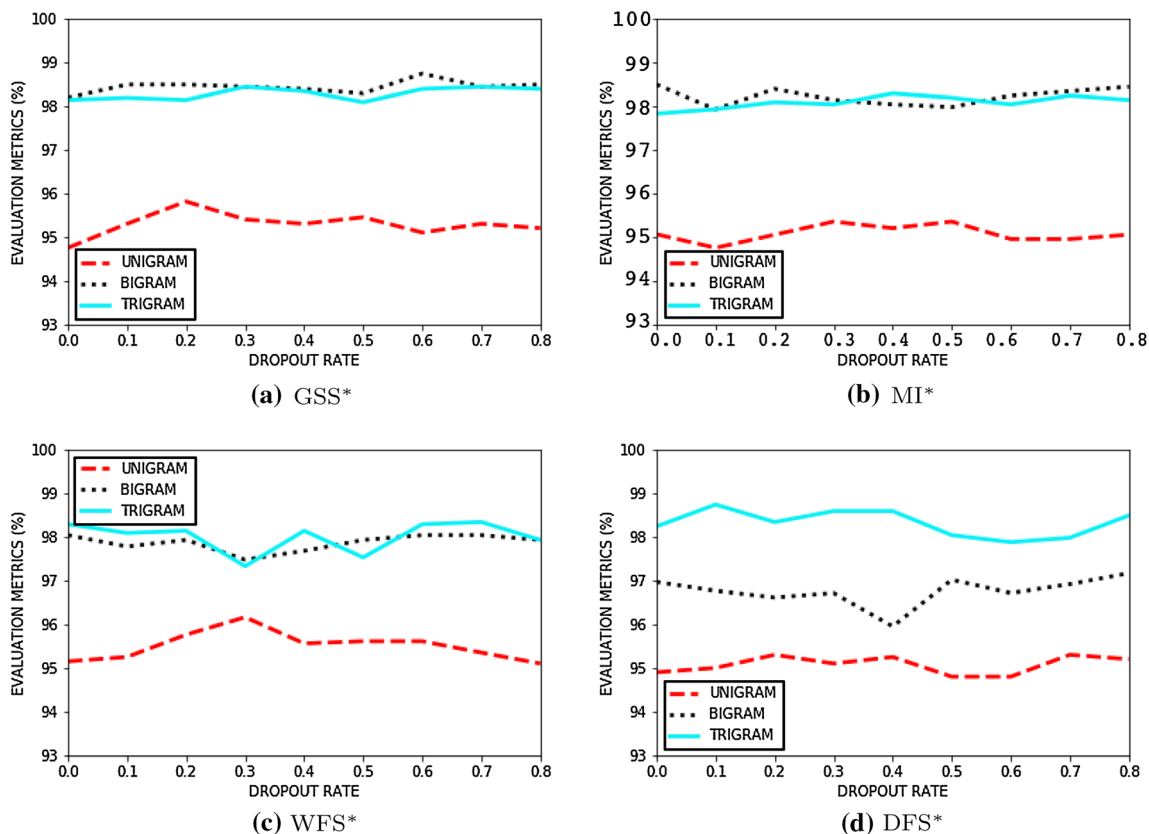


Fig. 7 Accuracy comparisons for different DL classifiers of proposed feature selection approach using dropout rate

In this experiment, adversarial samples for five detection models were generated. For each model, the recall rate was evaluated for 1%, 2% and 3% of prominent Benign system calls that were used to poison the malware samples. Figure 9a shows that the recall rate for Unigram in CART prior to the attack was 96.55% and after the attack, it got reduced to 33.73%. This was the case of 1% of prominent benign system calls that were appended to the malware samples for poisoning and the trend continued for both 2% and 3% of prominent benign system calls. Considering 2% of benign system calls, after poisoning the recall rate was minimized to 58.94% and for 3% of benign system calls it dropped to 30.89%. In case of a bigram, the recall rate reduced from 97.26 to 29.26% for 1% of benign system calls and for 2% benign system calls, the recall rate diminished to 30.0%. Likewise, for 3% of benign system calls, recall was minimized to 24.79%. Further for trigram, the recall rate for 1% of benign system calls reduced from 98.88 to 45.93%. Whereas for 2% of benign system calls, the rate minimized to 57.48% and for 3% of benign system calls, the rate reduced to 39.67 %.

Figure 9b depicts that for 1% benign system calls of unigram, LR shows a recall rate of 98.68% prior to poisoning, and after poisoning it was reduced to 50.4%. In case of 2% and 3% of system calls, the true positive rate

was reduced to 68.29% and 66.66% respectively. For bigram after poisoning, the recall rate was reduced from 98.78 to 77.64%, 81.3% and 69.1% for 1%, 2% and 3% of benign system calls. Considering trigram, from 99.79% of recall rate, it diminished to 86.17%, 86.6% and 85.02% for 1% 2% and 3% of prominent benign system calls respectively.

Figure 9c shows that in case of Random Forest, for unigram the true positive rate declined from 97.89 to 61.38%, 74.79% and 35.77% for 1%, 2% and 3% of benign system calls respectively. Considering 1%, 2% and 3% of benign system calls of bigram, the recall rate reduced from 98.38 to 79.26%, 83.33%, and 74.39% respectively. Further, for poisoned trigram, the recall rate diminished from 98.58 to 82.11%, 84.61% and 84.61% for 1%, 2% and 3% of benign system calls.

From Fig. 9d it is clear that with XGBoost, the recall rate of unigram reduced from 95.8 to 80.01% for 1%, 2% and 3% of benign system calls after poisoning. Considering 1%, 2% and 3% of benign system calls in Bigram after poisoning, the recall rate reduced from 98.7 to 92.22%. In case of Trigram, for 1%, 2% and 3% of benign system calls, the recall rate of 99% diminished to 91.9%.

Figure 10 depicts that for unigram, the recall rate diminished from 95.2 to 44.53% in case of 1% of

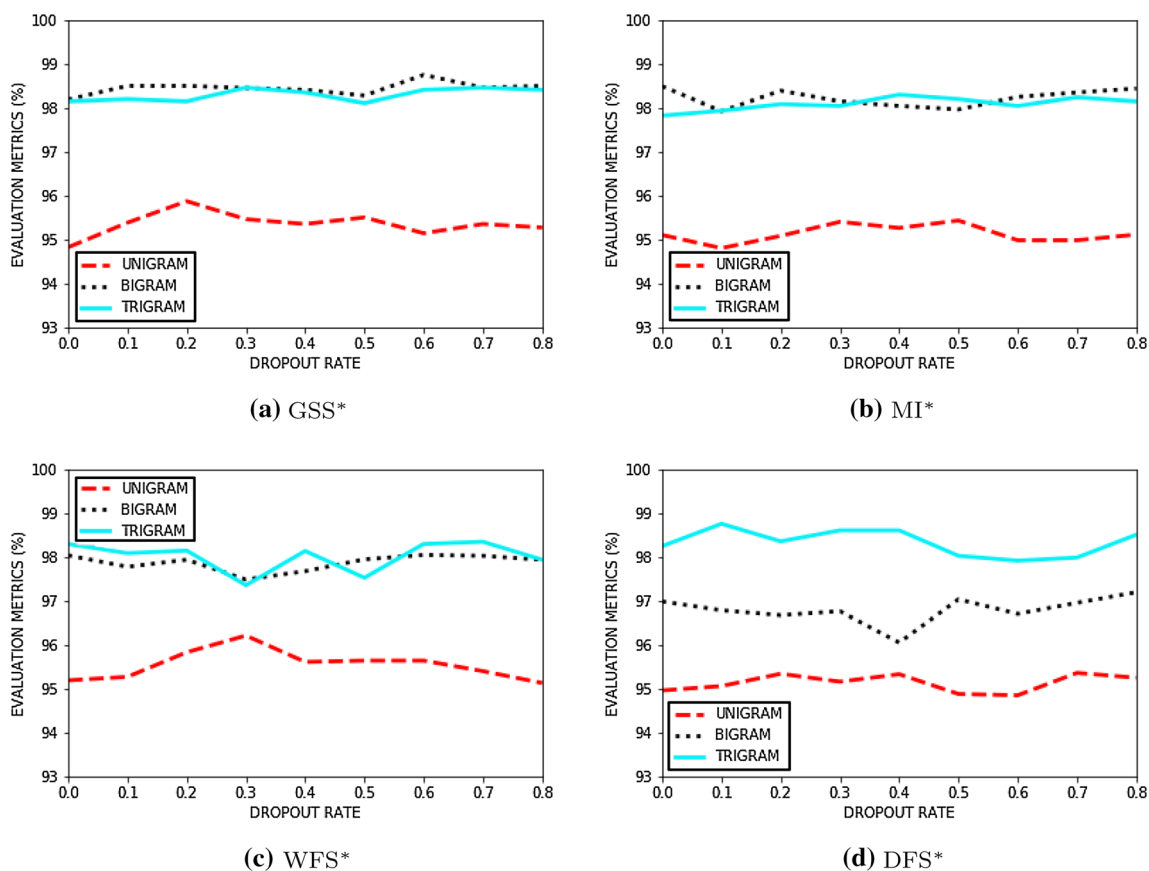


Fig. 8 F1-Score comparisons for different DL classifiers of proposed feature selection approach using dropout rate

Table 2 Performance of DL classifier with proposed feature selection approaches using dropout rate and learning rate

Feature selectors	Category	Drop out	LR	\mathcal{A}	\mathcal{F}_1	\mathcal{PRC}	\mathcal{REC}
GSS*	UNIGRAM	0.2	0.1	0.952	0.952	0.950	0.956
	BIGRAM	0.6	0.2	0.990	0.990	0.990	0.994
	TRIGRAM	0.8	0.1	0.980	0.980	0.980	0.990
DFS*	UNIGRAM	0.7	0.001	0.950	0.950	0.953	0.943
	BIGRAM	0.8	0.1	0.990	0.990	0.984	0.992
	TRIGRAM	0.1	0.1	0.980	0.981	0.970	0.991
MI*	UNIGRAM	0.5	0.001	0.952	0.952	0.952	0.952
	BIGRAM	0.8	0.1	0.980	0.980	0.980	0.982
	TRIGRAM	0.4	0.001	0.987	0.987	0.986	0.989

Asterisks indicate a revised feature set after the application of SAILS

prominent benign system calls and for 2% and 3% of benign system calls, the recall rate reduced to 43.3% and 42.1%. Considering 1% of injected bigram, the recall rate minimized from 98.2 to 40.48%, the recall at 2% and 3% injection rate reduced to 34.81% and 32.39% respectively. Further for trigram, in case of 1% injected calls, the recall declined from 98.58 to 48.18%, moreover, for 2% to 3%, the recall dropped from 42.51 and 37.65% respectively.

6 Conclusion and future directions

In this paper, a new feature selection method, SAILS, is designed, which can provide better results compared to conventional feature selection approaches. Also, the classifier performance of different N -grams is studied. We performed parallel analysis of the Android malware detector using deep learning network and machine learning algorithms. Further, the performance of the model was evaluated by analysing the change in dropout and learning rate.

Table 3 Performance comparison of WFS feature selection method with other approaches

Classifier	Feature selectors	Unigram		Bigram		Trigram	
		FL	\mathcal{A}	FL	\mathcal{A}	FL	\mathcal{A}
LR	WFS*	40(37)	89.3	100(2212)	98.0	100(20354)	99.4
	MI-AVG	100(98)	91.05	100(2212)	96.41	90(18318)	96.75
	GSS-AVG	90(88)	88.43	100(2212)	99.08	100(20354)	99.34
	DFS-AVG	100(98)	91.96	90(1990)	97.16	100(20354)	99.34
CART	WFS*	40(37)	93.1	100(2212)	96.7	100(20354)	98.7
	MI-AVG	100(98)	92.26	100(2212)	94.94	100(20354)	94.78
	GSS-AVG	90(88)	92.57	80(1769)	95.08	100(20354)	98.17
	DFS-AVG	90(88)	92.02	90(1990)	95.39	90(18318)	97.89
RF	WFS*	90(88)	97.2	20(442)	97.6	100(20354)	97.5
	MI-AVG	100(98)	96.1	80(1769)	97.21	100(20354)	96.8
	GSS-AVG	100(98)	95.5	100(2212)	98.53	100(20354)	97.77
	DFS-AVG	100(98)	96.11	100(2212)	97.21	100(20354)	97.97
XGBoost	WFS*	70(68)	96.6	40(884)	97.9	20(4070)	97.7
	MI-AVG	100(98)	95.5	90(1990)	99.3	100(20354)	99.2
	GSS-AVG	80(78)	92.65	70(1548)	97.67	80(16283)	97.72
	DFS-AVG	90(88)	95.4	100(2212)	97.3	80(16283)	98.2

FL denotes feature length at which the best outcomes were obtained. FL is expressed in the form of $P(Q)$, where P denotes the percentage of features extracted from the feature space and Q denote the number of attributes used to create the model

Asterisks indicate a revised feature set after the application of SAILS

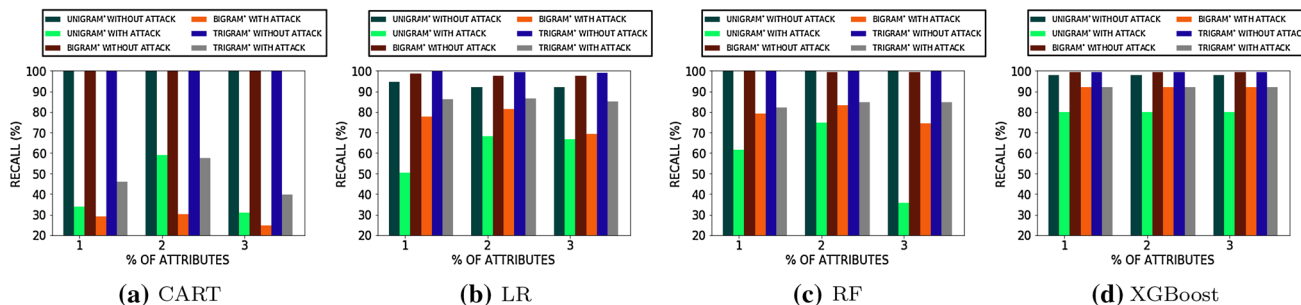


Fig. 9 Performance evaluation of unigram, bigram and trigram after poisoning using ML

Adversarial attacks are also performed on the ML models. It is observed that the adversary could deceive the current ML based malware detectors. A drop in performance is observed when the trained models were given evasive examples as input. Thus, it is important to develop robust ML models trained with adversarial patterns, such that Android malware detectors are capable of recognizing tainted samples.

Our current work focuses on dynamic analysis of Android malware. In future work, we envisage the use hybrid analysis on a larger dataset. It is also planned to

include features relating to network packets (packet size, packet payload size, packet inter-arrival time, TCP flag status, the total number of bytes in packets, packet direction, protocols, etc.), to train ML algorithms. The collection of these features along-with systems calls would undoubtedly reveal promising patterns for identifying malware. We also plan to model new feature selection techniques having high correlation with class, but loosely correlated with other features. Finally, we plan to carry out attacks on classifier ensembles, and develop

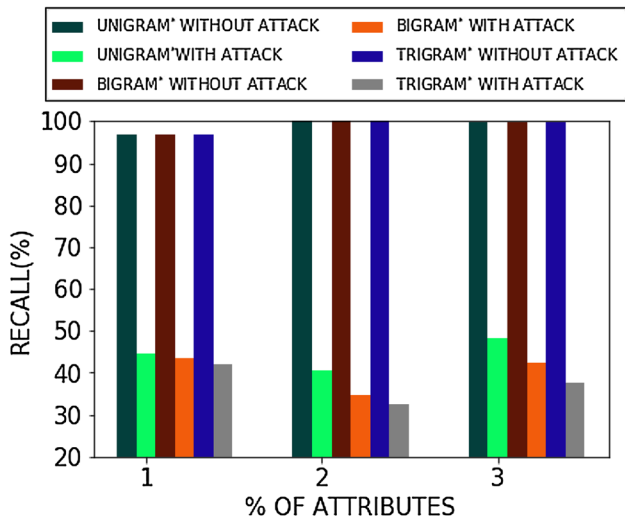


Fig. 10 Performance evaluation of unigram, bigram and trigram after poisoning using DL

countermeasures to harden classifier for minimizing misclassification rate.

Compliance with ethical standards

Conflicts of interest There is no conflict of interest for the paper.

Appendix

In this section, different scores of N-gram for GSS, WFS, and MI are presented to illustrate the malware and benign samples for various features (see the Figs. 11, 12 and 13).

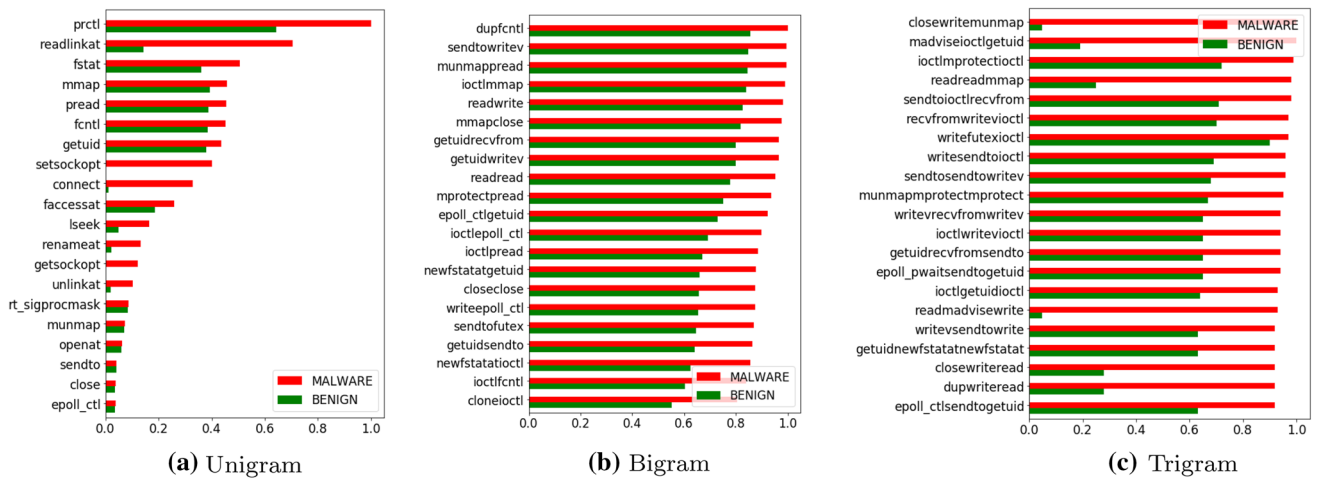


Fig. 11 Score difference of N-grams for GSS*

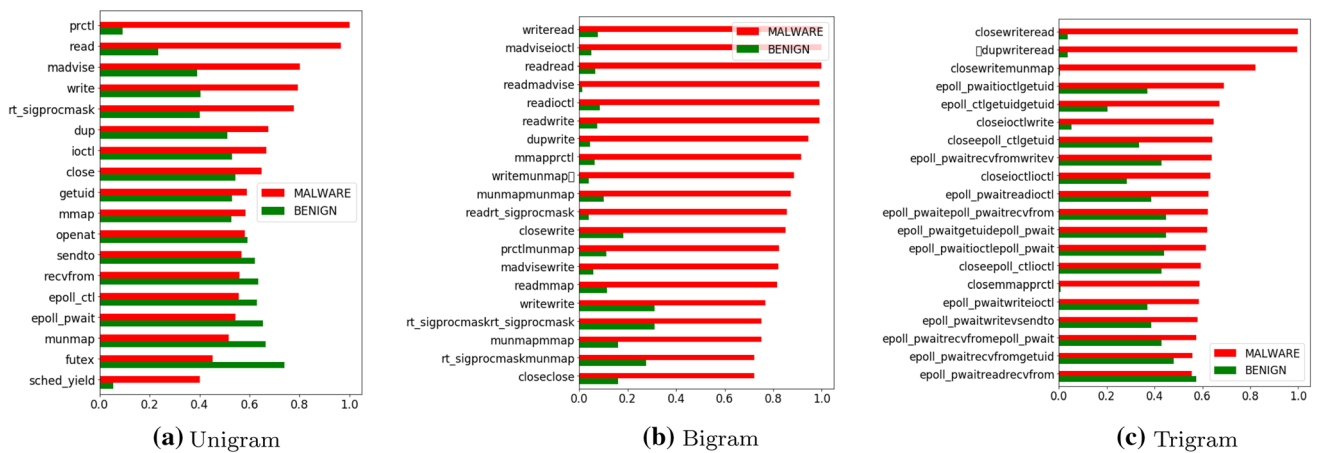


Fig. 12 Score difference of N-grams for WFS*

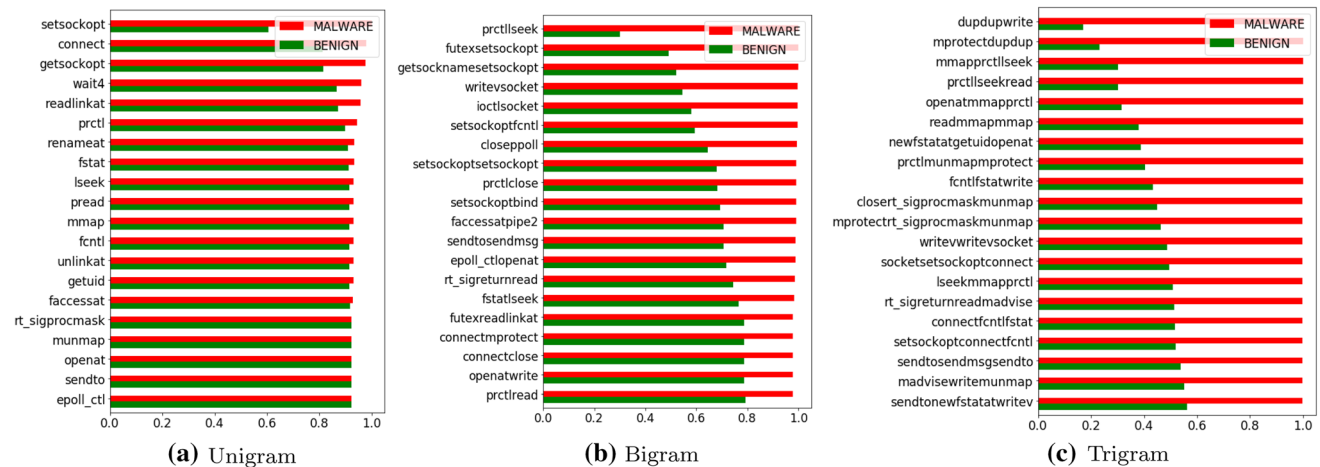


Fig. 13 Score difference of N-grams for MI*

References

1. Aafer, Y., Du, W., Yin, H.: Droidapiminer: mining api-level features for robust malware detection in android. In: International Conference on Security and Privacy in Communication Systems, pp. 86–103. Springer, Berlin (2013)
2. Afonso, V.M., de Amorim, M.F., Grégio, A.R.A., Junquera, G.B., de Geus, P.L.: Identifying android malware using dynamically obtained features. *J. Comput. Virol. Hacking Tech.* **11**(1), 9–17 (2015)
3. Arp, D., Spreitzenbarth, M., Hubner, M., Gascon, H., Rieck, K., Siemens, C.: Drebin: effective and explainable detection of android malware in your pocket. *Ndss* **14**, 23–26 (2014)
4. Arshad, S., Shah, M.A., Wahid, A., Mehmood, A., Song, H., Yu, H.: Samadroid: a novel 3-level hybrid malware detection model for android operating system. *IEEE Access* **6**, 4321–4339 (2018)
5. Bhandari, S., Panihar, R., Naval, S., Laxmi, V., Zemmari, A., Gaur, M.S.: Sword: semantic aware android malware detector. *J. Inf. Secur. Appl.* **42**, 46–56 (2018)
6. Biggio, B., Corona, I., Maiorca, D., Nelson, B., Šmrdić, N., Laskov, P., Giacinto, G., Roli, F.: Evasion attacks against machine learning at test time. In: Joint European Conference on Machine Learning and Knowledge Discovery in Databases, pp. 387–402. Springer, Berlin (2013)
7. Breiman, L.: Random forests. *Mach. Learn.* **45**(1), 5–32 (2001)
8. Burguera, I., Zurutuza, U., Nadjm-Tehrani, S.: Crowddroid: behavior-based malware detection system for android. In: Proceedings of the 1st ACM Workshop on Security and Privacy in Smartphones and Mobile Devices, pp. 15–26. ACM (2011)
9. Cyber security facts and statistics for 2019. <https://us.norton.com/internetsecurity-emerging-threats-10-facts-/about-todays-cybersecurity-landscape-that-you-should-know.html> (2019). Accessed 10 Aug 2019
10. Cao, Y., Yang, J.: Towards making systems forget with machine unlearning. In: 2015 IEEE Symposium on Security and Privacy, pp. 463–480. IEEE (2015)
11. Chen, L., Hou, S., Ye, Y., Chen, L.: An adversarial machine learning model against android malware evasion attacks. In: Asia-Pacific Web (APWeb) and Web-Age Information Management (WAIM) Joint Conference on Web and Big Data, pp. 43–55. Springer, Berlin (2017)
12. Chen, S., Xue, M., Fan, L., Hao, S., Xu, L., Zhu, H., Li, B.: Automated poisoning attacks and defenses in malware detection systems: an adversarial machine learning approach. *Comput. Secur.* **73**, 326–344 (2018)
13. Chen, T., Guestrin, C.: Xgboost: a scalable tree boosting system. In: Proceedings of the 22nd ACM SIGKDD International Conference on Knowledge Discovery and Data Mining, pp. 785–794. ACM (2016)
14. Grosse, K., Papernot, N., Manoharan, P., Backes, M., McDaniel, P.: Adversarial examples for malware detection. In: European Symposium on Research in Computer Security, pp. 62–79. Springer, Berlin (2017)
15. Han, W., Xue, J., Wang, Y., Huang, L., Kong, Z., Mao, L.: Maldae: detecting and explaining malware based on correlation and fusion of static and dynamic characteristics. *Comput. Secur.* **83**, 208–233 (2019)
16. Hosmer Jr., D.W., Lemeshow, S., Sturdivant, R.X.: Applied Logistic Regression, vol. 398. Wiley, New York (2013)
17. Hou, S., Saas, A., Chen, L., Ye, Y.: Deep4maldroid: a deep learning framework for android malware detection based on linux kernel system call graphs. In: 2016 IEEE/WIC/ACM International Conference on Web Intelligence Workshops (WIW), pp. 104–111. IEEE (2016)
18. Hou, S., Saas, A., Ye, Y., Chen, L.: Droiddelver: an android malware detection system using deep belief network based on API call blocks. In: International Conference on Web-Age Information Management, pp. 54–66. Springer, Berlin (2016)
19. Hou, S., Ye, Y., Song, Y., Abdulhayoglu, M.: Hindroid: an intelligent android malware detection system based on structured heterogeneous information network. In: Proceedings of the 23rd ACM SIGKDD International Conference on Knowledge Discovery and Data Mining, pp. 1507–1515. ACM (2017)
20. Ishibashi, H., Hihara, S., Iriki, A.: Acquisition and development of monkey tool-use: behavioral and kinematic analyses. *Can. J. Physiol. Pharmacol.* **78**(11), 958–966 (2000)
21. Largeton, C., Moulin, C., Géry, M.: Entropy based feature selection for text categorization. In: Proceedings of the 2011 ACM Symposium on Applied Computing, pp. 924–928. ACM (2011)
22. Mobile malware evolution 2019. <https://securelist.com/mobile-malware-evolution-2018/89689/> (2019). Accessed 10 Aug 2019
23. Michael, S., Florian, E., Thomas, S., Felix, C.F., Hoffmann, J.: Mobilesandbox: looking deeper into android applications. In: Proceedings of the 28th International ACM Symposium on Applied Computing (SAC) (2013)
24. Naway, A., Li, Y.: A review on the use of deep learning in android malware detection. arXiv preprint arXiv:1812.10360 (2018)

25. Roundy, K.A., Miller, B.P.: Hybrid analysis and control of malware. In: International Workshop on Recent Advances in Intrusion Detection, pp. 317–338. Springer, Berlin (2010)
26. Safavian, S.R., Landgrebe, D.: A survey of decision tree classifier methodology. *IEEE Trans. Syst. Man Cybern.* **21**(3), 660–674 (1991)
27. Santos, I., Peña, Y.K., Devesa, J., Bringas, P.G.: N-grams-based file signatures for malware detection. *ICEIS* **2**(9), 317–320 (2009)
28. Srivastava, N., Hinton, G., Krizhevsky, A., Sutskever, I., Salakhutdinov, R.: Dropout: a simple way to prevent neural networks from overfitting. *J. Mach. Learn. Res.* **15**(1), 1929–1958 (2014)
29. Suci, O., Marginean, R., Kaya, Y., Daume III, H., Dumitras, T.: When does machine learning FAIL? Generalized transferability for evasion and poisoning attacks. In: 27th USENIX Security Symposium (USENIX Security 18), pp. 1299–1316 (2018)
30. Tong, F., Yan, Z.: A hybrid approach of mobile malware detection in android. *J. Parallel Distrib. Comput.* **103**, 22–31 (2017)
31. VirusTotal. <http://virustotal.com/> (2019). Accessed 10 Aug 2019
32. Wang, W., Zhao, M., Wang, J.: Effective android malware detection with a hybrid model based on deep autoencoder and convolutional neural network. *J. Ambient Intell. Humaniz. Comput.* **10**(8), 3035–3043 (2019)
33. Yang, Y., Shen, H.T., Ma, Z., Huang, Z., Zhou, X.: L2, 1-norm regularized discriminative feature selection for unsupervised. In: Twenty-Second International Joint Conference on Artificial Intelligence (2011)
34. Yuan, Z., Lu, Y., Xue, Y.: Droiddetector: android malware characterization and detection using deep learning. *Tsinghua Sci. Technol.* **21**(1), 114–123 (2016)
35. Zhang, J., Zhang, K., Qin, Z., Yin, H., Wu, Q.: Sensitive system calls based packed malware variants detection using principal component initialized multilayers neural networks. *Cybersecurity* **1**(1), 10 (2018)
36. Zheng, Z., Wu, X., Srihari, R.: Feature selection for text categorization on imbalanced data. *ACM SIGKDD Explor. Newslett.* **6**(1), 80–89 (2004)
37. Zhou, Y., Jiang, X.: Dissecting android malware: characterization and evolution. In: 2012 IEEE Symposium on Security and Privacy, pp. 95–109. IEEE (2012)
38. 9apps: Android app website. <https://www.9apps.com/> (2019). Accessed 10 Aug 2019

Publisher's Note Springer Nature remains neutral with regard to jurisdictional claims in published maps and institutional affiliations.



Ananya Asok graduated from SCMS School of Engineering and Technology, Kochi, Kerala in May 2019 with a Bachelor's of Technology in Computer Science and Engineering. She has keen interests in the area of machine learning. Her main research interest is Android Mobile security and privacy and machine learning.



Aswathy A. graduated from SCMS School of Engineering & Technology in July 2019 with a bachelor's of technology in Computer Science and Engineering. She has a keen interest in the field of machine learning and her involvement in the developer community ecosystem had made a great impact on the lives of many aspiring women engineers. Her main research interest is Android Mobile security and privacy and machine learning.



Amal T.R. received his Bachelor of Science in Mathematics from Calicut University in 2016. Also, he received a Master's degree in Computer Applications from APJ Abdul Kalam Technical University in 2019. His main research interest is Android Mobile security and privacy and machine learning.



Swathy P.G. graduated from SCMS School of Engineering and Technology in July 2019 with a Master's in Computer Science and Information Systems. Her main research interest is Android Mobile security and privacy and machine learning.



Vinod P. is Professor in Department of Computer Science & Engineering at SCMS School of Engineering and Technology, Kerala, India. He was Post Doc at Department of Mathematics, University of Padua, Italy. During his Post Doctoral research he was actively involved in executing EU-H2020 project TagitSmart. He holds his Ph.D in Computer Engineering from Malaviya National Institute of Technology, Jaipur, India. He has more than numerous research articles published in peer reviewed Journals and International Conferences. He is reviewer of number of security journals, and has also served as programme committee member in the

International Conferences related to Computer and Information Security. His current research is involved in the development of malware scanner for mobile application using machine learning techniques. Vinod's area of interest is Adversarial machine learning, Malware analysis, context aware privacy persevering data mining, ethical hacking and natural language processing.



Mohammad Shojarf is an Intel Innovator, a Senior IEEE member, a Senior Researcher and a Marie Curie Fellow in the SPRITZ Security and Privacy Research group at the University of Padua, Italy. Also, he was CNIT Senior Researcher at the University of Rome Tor Vergata contributed to 5G PPP European H2020 “SUPERFLUIDITY” project. He is a PI on PRISE-NODE project, a 275,000 euro Horizon 2020 Marie Curie project in the areas of network

security and Fog computing and resource scheduling collaborating

between the University of Padua and University of Melbourne. He also was a PI on an Italian SDN security and privacy (60,000 euro) supported by the University of Padua in 2018. He also contributed to some Italian projects in telecommunications like GAUChO—A Green Adaptive Fog Computing and Networking Architecture (400,000 euro), and SAMM-Clouds- Secure and Adaptive Management of Multi-Clouds (30,000 euro) collaborating among Italian universities. He received a Ph.D. in ICT from Sapienza University of Rome, Italy, in 2016 with an “Excellent” degree. His main research interests are in the area of Computer Networks, Network Security, and Privacy. In this area, he published more than 100+ papers in topmost international peer-reviewed journals and conferences, e.g., IEEE TCC, IEEE TNSM, IEEE TGCN, IEEE TSUSC, IEEE Network, IEEE SMC, IEEE PIMRC, and IEEE ICC/GLOBECOM. He served as a PC member of several prestigious conferences, including IEEE INFOCOM Workshops in 2019, IEEE GLOBECOM, IEEE ICC, IEEE UCC, IEEE ScalCom, and IEEE SMC. He was GC in FMEC 2019, INCoS 2019, INCoS 2018, and a Technical Program Chair in IEEE FMEC 2020. He served as an Associate Editor in IEEE Transactions on Consumer Electronics, IET Communication, Springer Cluster Computing, and Ad Hoc & Sensor Wireless Networks Journals.

Numerical Study on the Undrained Response of Silty Sands Under Static Triaxial Loading



M. Akhila, K. Rangaswamy and N. Sankar

Abstract The silty soils are more susceptible to liquefaction, even under static loading, than the coarse sands. Pore pressure developed during dynamic events may not dissipate easily due to the presence of more number of small voids. Hence, the rate of pore pressure build-up under static/dynamic loading conditions is much faster in silty sands, which lead to a reduction in the soil strength. This phenomenon may be assessed in terms of either contraction or dilation behaviour under triaxial loading. Therefore, it is necessary to analyse the undrained response of silty sands under triaxial loading so that the damages occurring during future dynamic events may be predicted. The present study involves both the experimental and numerical simulations on various silty sands, which contain 0, 10, 20, 30 and 40% silt fines. Initially, experimental static triaxial testing was performed to determine the undrained response of silty sands moulded to cylindrical specimens at medium relative density. The saturated samples are isotropically consolidated at 100 kPa pressure before shearing. Further, numerical simulations were performed on silty sands by inputting the material parameters into the hypoplastic model. This model requires eight material constants as input including critical friction angle, hardness coefficients, limited void ratios, peak state and stiffness coefficients. These constants were determined for each silty sand combination after conducting basic laboratory tests according to the formulations build in the hypoplastic model program. The experimental trends were compared with numerical model simulations under triaxial testing. The effect of the initial state of soil and the amount of silt fines on the undrained response of fine sands is discussed in detail. The liquefaction susceptibility of silty sand is described based on steady state line concept. The results indicate that the silt sands behave as highly contractive, i.e. more liquefiable when compared with sands.

M. Akhila (✉)

Department of Civil Engineering, SCMS School of Engineering and Technology,
Ernakulam, Kerala, India
e-mail: akhila144@gmail.com

K. Rangaswamy · N. Sankar

Department of Civil Engineering, NIT Calicut, Calicut, India

© Springer Nature Singapore Pte Ltd. 2020

A. Prashant et al. (eds.), *Advances in Computer Methods and Geomechanics*, Lecture Notes in Civil Engineering 56,
https://doi.org/10.1007/978-981-15-0890-5_17

9th World Engineering Education Forum 2019, WEEF 2019

Service Learning in Engineering Education: A Study of Student-Participatory Survey for Urban Canal Rejuvenation in Kochi, India

Sunny George¹, Ratish Menon¹, Pramod Thevanoor¹ and John Tharakan^{2,*}

¹SCMS Water Institute, SSET Campus, Karukutty, Kerala, India

^{2,*}College of Engineering and Architecture, Howard University, Washington DC 20059, USA

Abstract

It is widely accepted that learning through doing, or service learning (SL) and engaging students in community centred project based learning (PBL) is transformative in terms of enhancing student learning and employability, effectively improving both technical and soft skills that are sought after by employers, while at the same time growing and developing an informed and educated citizenry. Participatory learning here is a pedagogical approach in which students involve themselves in a community-based project, which has proven to be more effective than direct lecture based transfer and absorption of knowledge. In this paper, we present a case study from Kochi city in Kerala, India, where undergraduate (UG) engineering students from the environmental engineering (EE) program at SCMS School of Engineering and Technology (SSET) participated voluntarily in the comprehensive survey of a 10.87 km canal running through busy, dense and heavily populated urban area of Kochi City. This Thevara-Perandoor (T-P) canal was a heavily used commercial artery for the city. Unfortunately, the T-P canal is now totally degraded, primarily due to unregulated solid waste dumping and untreated sewage inflows at numerous locations along its course throughout the urban space. The UG students of the CE program at SSET voluntarily came forward to do the study on behalf of Kochi Municipal Corporation (KMC). This partnership, between an academic program and a community based entity, such as a municipal corporation or any other community based entity, establishes a model for integrating meaningful service learning into engineering education. The partnership provided an immense opportunity for the students to implement whatever they had learned in the classroom and doing so by working for the benefit of the community in which they themselves were resident. This paper describes the practices that are being followed in this service learning exercise. The paper also focuses on the impediments as well as the opportunities that exist for both widening and deepening the knowledge domain of the students, while working on the mentioned urban canal survey. The value and impact of the model described through the examined case study is especially important, given that the notion of service learning as a pedagogical approach is gaining momentum in the Indian engineering education sector, and when programs such as *Unnat Bharath Abhiyan* which focuses on and mandates utilizing student voluntary work for rural development are being implemented.

© 2020 The Authors. Published by Elsevier B.V.

This is an open access article under the CC BY-NC-ND license (<http://creativecommons.org/licenses/by-nc-nd/4.0/>)

Peer-review under responsibility of the scientific committee of the 9th World Engineering Education Forum 2019.

Keywords: Service Learning; Urban Canal Rejuvenation; Engineering Education; Kochi; Thevara-Perandoor Canal;

Received May 10, 2020, accepted May 22, 2020, date of publication May 26, 2020, date of current version June 9, 2020.

Digital Object Identifier 10.1109/ACCESS.2020.2997727

An Adaptive and Flexible Brain Energized Full Body Exoskeleton With IoT Edge for Assisting the Paralyzed Patients

SUNIL JACOB^{1,2}, (Member, IEEE), MUKIL ALAGIRISAMY³,
VARUN G. MENON⁴, (Senior Member, IEEE), B. MANOJ KUMAR⁵, N. Z. JHANJHI⁶,
VASAKI PONNUSAMY⁷, P. G. SHYNU⁸, AND VENKI BALASUBRAMANIAN^{9,10}, (Member, IEEE)

¹Department of Electronics and Communication Engineering, Lincoln University College, Petaling Jaya 47301, Malaysia

²Department of Electronics and Communication Engineering, SCMS School of Engineering and Technology, Ernakulam 683576, India

³Department of Electrical and Electronics and Engineering, Lincoln University College, Petaling Jaya 47301, Malaysia

⁴Department of Computer Science and Engineering, SCMS School of Engineering and Technology, Ernakulam 683576, India

⁵Department of Automobile Engineering, SCMS School of Engineering and Technology, Ernakulam 683576, India

⁶School of Computer Science and Engineering, Taylor's University, Subang Jaya 47500, Malaysia

⁷Faculty of Information and Communication Technology, Universiti Tunku Abdul Rahman, Kampar 31900, Malaysia

⁸School of Information Technology and Engineering, Vellore Institute of Technology, Vellore 632014, India

⁹School of Science, Engineering and Information Technology, Federation University, Mount Helen, VIC 3350, Australia

¹⁰Anidra Tech Ventures Pvt Ltd., Wyndham Vale, VIC 3024, Australia

Corresponding authors: Sunil Jacob (sunil@scmsgroup.org) and Vasaki Ponnusamy (vasaki@utar.edu.my)

This work was supported in part by the Institute of Electrical and Electronics Engineers (IEEE) EPICS, USA, under Grant 2016-12.

ABSTRACT The paralyzed population is increasing worldwide due to stroke, spinal cord injury, post-polio, and other related diseases. Different assistive technologies are used to improve the physical and mental health of the affected patients. Exoskeletons have emerged as one of the most promising technology to provide movement and rehabilitation for the paralyzed. But exoskeletons are limited by the constraints of weight, flexibility, and adaptability. To resolve these issues, we propose an adaptive and flexible Brain Energized Full Body Exoskeleton (BFBE) for assisting the paralyzed people. This paper describes the design, control, and testing of BFBE with 15 degrees of freedom (DoF) for assisting the users in their daily activities. The flexibility is incorporated into the system by a modular design approach. The brain signals captured by the Electroencephalogram (EEG) sensors are used for controlling the movements of BFBE. The processing happens at the edge, reducing delay in decision making and the system is further integrated with an IoT module that helps to send an alert message to multiple caregivers in case of an emergency. The potential energy harvesting is used in the system to solve the power issues related to the exoskeleton. The stability in the gait cycle is ensured by using adaptive sensory feedback. The system validation is done by using six natural movements on ten different paralyzed persons. The system recognizes human intentions with an accuracy of 85%. The result shows that BFBE can be an efficient method for providing assistance and rehabilitation for paralyzed patients.

INDEX TERMS Artificial intelligence, assistive technologies, brain-computer interface, edge computing, Internet of Things (IoT), rehabilitation.

I. INTRODUCTION

A recent survey carried out by Toyota Foundations revealed that 30% of the paralyzed population is disappointed with the assistive devices in the market. The outdated design of assistive devices is causing constant pain and frustration. Survey participants also recommended that future assistive

The associate editor coordinating the review of this manuscript and approving it for publication was Zhenyu Zhou¹⁰.

devices should be easy to handle and help in daily activities. The respondents also indicated that the design should be natural, like an extension of their body, providing them freedom and independence [1], [2]. Currently, exoskeletons are the most popular solution used in rehabilitation and assistance of the paralyzed people [3]–[8]. Numerous types of exoskeletons are designed for purposes ranging from rehabilitation and assistance to transportation and handling heavy load in industries.

In rehabilitation, the exoskeletons are used to work in parallel with the human legs and carry out the desired actions with ease. These devices are specifically designed to treat disabilities of patients in a clinical setting. The rehabilitation exoskeleton helps paralyzed patients to engage with real-world things and to monitor the movement of body parts. Exoskeletons are also designed for healthy subjects, enabling them to interact with a virtual environment [9]. As healthy people use these haptic exoskeletons, ease of wearability is not a major issue, but portability and efficient finger tracking are highly required. In recent times, to assist children having cerebral palsy disorders, exoskeletons have been designed [10]. The architecture of the control unit, the mechanical system, and feature extraction is discussed in detail. In [11], a wearable hip assist robot is discussed, which is used to improve the gait function and reduce muscle effort and metabolic activities. The device can reduce knee and ankle muscle activity along with a decrease in hip movements. The robot can stabilize the trunk during walking in adults. But the system has not investigated the effectiveness of gait rehabilitation.

In [12], the translation of gait without using crutches gait in a biped robot is demonstrated. The mathematical hybrid model analysis is carried out to find different gait and walking speeds. The walking gaits are stabilized using a centralized controller. A knee exoskeleton that can be used for sit to stand assistance is discussed in [13]. Here, the torque control is improved using a unique transmission configuration, also with reduced output impedance. Design specifications of the current lower limb exoskeletons are reviewed, and the human biomechanical consideration in lower limb design is analyzed in [14]. The classification and design challenges in the field of Exoskeleton and Orthoses are discussed in [15]. In [16], the classification of exoskeletons into the palm, upper limb, and lower limb exoskeleton is discussed. Further, the paper discusses various exoskeletons proposed for rehabilitation and enhancement purposes. The paper also puts forward the concept of developing a full-body exoskeleton.

In [17], a wearable full-body exoskeleton is designed for a mobile cyber-physical system. Here, the design of a new technique for identifying the gate phase is also discussed. Energy harvesting using human's daily actions is proposed to charge the battery of exoskeleton in [18]. Conventional and alternative methods for providing power to exoskeletons are discussed. A systematic review of various types of exoskeletons for using with the lower limb in neurorehabilitation is presented in [19]. In [20], an exoskeleton to aid patient rehabilitation with postural equilibrium is designed. Multi-variable robust control with the patient's Electro Myographical (EMG) signals is utilized to achieve equilibrium. Berkeley Lower Limb Exoskeleton (BLEEX) [21] is designed to transfer load and body weight into the ground, which reduces the metabolic cost of the wearer. This parallel exoskeleton is able to enhance the endurance of the user. The exoskeleton, which augments the torque and power of the user during lifting and daily activities, is discussed.

Software-Defined Network (SDN) assisted solutions with exoskeletons for use in rehabilitation are also proposed recently [22]. The majority of the existing exoskeletons have weight, flexibility, and adaptability constraints. Easy wearability and portability are other significant limitations experienced by current assistive exoskeleton-based solutions for rehabilitation [23]–[25].

To overcome the current issues existing with exoskeletons, we propose an adaptive and flexible Brain Energized Full Body Exoskeleton (BFBE) for assisting the paralyzed people. In the BFBE system, the brain signals captured by the EEG sensors are used for controlling the movements of the exoskeleton. The flexibility is incorporated into the system by a modular design approach. The BFBE system has a BCI module, a Control Unit (CU), and a Body-Part Actuation Module (BAM). BCI module captures the brain signal and transforms it into a signal that can be used by the CU. The processing happens at the edge, thus reducing delay in decision making, and the system is further integrated with an IoT module that helps to send an alert message to multiple caregivers in case of an emergency. The system is non-invasive, and the fabricated EEG sensor is used to collect the signals from the scalp. An instrumentation amplifier is used to enhance the strength of the obtained signals. The output signal from the amplifier is subjected to filtering and pre-processing. The signals are generated for different basic human actions (sitting, standing, sleeping) and then after the pre-processing is stored in a database. When the paralyzed person has an intention to make a particular movement, the microcontroller in the CU uses this database and produces the signal for activating the particular body part. The generated EEG pattern of the person is mapped into the corresponding action. The BAM then uses the motor driver circuit to pass the activation signal to the corresponding part of the body. The potential energy harvesting is used in the system to solve the power issues related to the exoskeleton. The stability in the gait cycle is ensured by using adaptive sensory feed-back.

The paper is arranged into 4 sections. The proposed work is discussed in Section 2. The system architecture is discussed initially, and then the theoretical analysis is presented. Section 3 presents and discusses the system working and testing details and the results obtained. Finally, the paper concludes in section 4. The list of abbreviations is listed in table 1.

II. PROPOSED SYSTEM

A. SYSTEM ARCHITECTURE

The architecture of the Brain Energized Full Body Exoskeleton (BFBE) system is shown in Figure 1. The BFBE system has three major modules 1) BCI module, 2) Control Unit, and 3) Body-Part Actuation Module. The primary function of the BCI module is to collect the EEG signals from the scalp and then convert it into a form that can be used by the CU. We have fabricated a sixteen-electrode based EEG sensor, which is used in the proposed system for collecting the signals and also for analyzing the brain activity. For removing the

TABLE 1. List of abbreviations.

Abbreviation	Description
BFBE	Brain Energized Full Body Exoskeleton
DoF	Degrees of Freedom
EEG	Electroencephalogram
EMG	Electro Myographical
BLEEX	Berkeley Lower Limb Exoskeleton
SDN	Software-Defined Network
CU	Control Unit
BAM	Body-Part Actuation Module
IoT	Internet of Things
BCI	Brain Computer Interface
WHT	Walsh Hadamard Transform

TABLE 2. Body parts of BFBE and its corresponding joints.

Different modules of the exoskeleton	Joints used to control the movements
Lower limb (Left & Right)	Knee Joint Left, Foot Joint Left, Knee Joint Right, Foot Joint Right
Upper limb (Left & Right)	Elbow Joint Right, Elbow Joint Left, Hand Joint Left, Hand Joint Right
Head & Neck	Head Joint, Neck Joint
Shoulder (Left & Right)	Shoulder Joint Left, Shoulder Joint Right
Hip	Torso Joint, Hip Joint Left, Hip Joint Right
Lower limb (Left & Right)	Knee Joint Left, Foot Joint Left, Knee Joint Right, Foot Joint Right

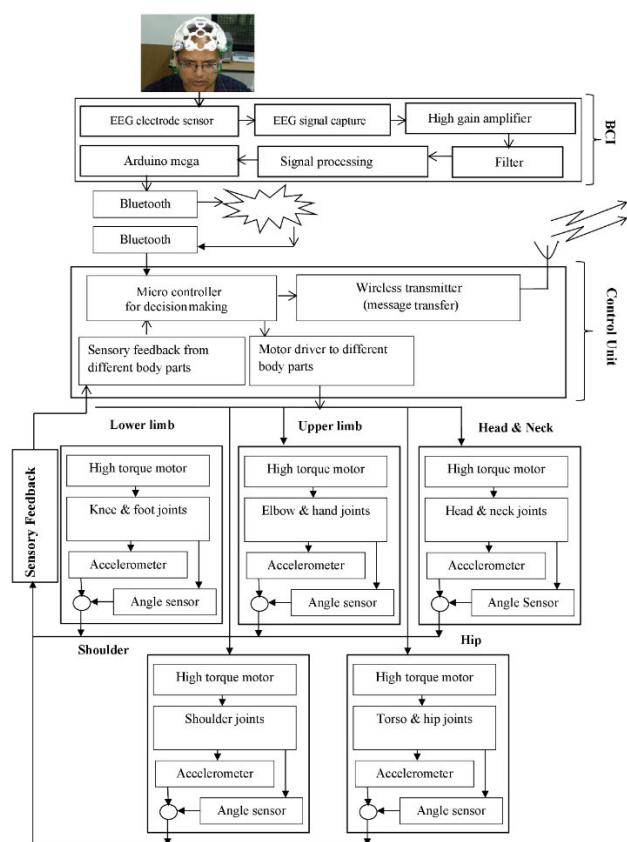


FIGURE 1. System architecture: Brain Energized Full Body Exoskeleton (BFBE).

high-frequency noise, we use a bandpass. Walsh Hadamard Transform (WHT) is then used to transform the signals into the frequency domain.

The signals are further transformed into a digital form and provided to the Arduino Mega, which transmits the signal via Bluetooth to the Control Unit. The signals are generated for different basic human actions (sitting, standing, sleeping) and then after the pre-processing is stored in a database. When the paralyzed person has an intention to make a particular movement, the microcontroller in the CU uses this

database and produces the signal for activating the particular part of the body. The generated EEG pattern of the person is mapped into the corresponding action. The BAM then uses the motor driver circuit to pass the activation signal to the corresponding part of the body. The potential energy harvesting is used in the system to solve the power issues related to the exoskeleton. The stability in the gait cycle is ensured by using adaptive sensory feed-back. The feedback to the CU is provided using a multi-level sensing technique so that corrections can be made in the process. Required corrections for producing the actuation signals are done by the microcontroller using this feedback and thus improving the decision-making accuracy. An accelerometer is used on the backside for detecting accidental falls. The processing happens at the edge, thus reducing delay in decision making, and the system is further integrated with an IoT module that helps to send an alert message to multiple caregivers in case of an emergency. If the measured tilt passes a particular threshold, a similar emergency message will be given to the caregiver via a wireless transmitter. The secure communication is ensured between paralyzed persons and caregivers using a double encrypted NTSA algorithm [26]. The material used for the development is carbon fiber, so that it can easily replicate various body movements with ease. The BFBE has a total of 15 degrees of freedom spread across different joints of the body, as indicated in Table 2.

Each of these joints is realized using high torque motors. Controlling the angle of rotation of the motors enables the system to make different movements. The exoskeleton is easy to wear due to its flexible and detachable components. The straps are used to tie the exoskeleton to different body parts. To further improve the stability of the person, support is provided on the backside and ankle region. In order to check if the applied force is sufficient to make the exoskeleton stable, angle sensors are placed on the joints.

B. SYSTEM DESIGN AND METHODOLOGY

The full-body structure of the exoskeleton mainly consists of five different body parts, which are lower limb, upper limb, head & neck, shoulder, and hip. The BFBE structured is designed by integrating these parts. The modular design provides BFBE with the highly required flexibility. The system can thus be used by people with different degrees of paralysis.

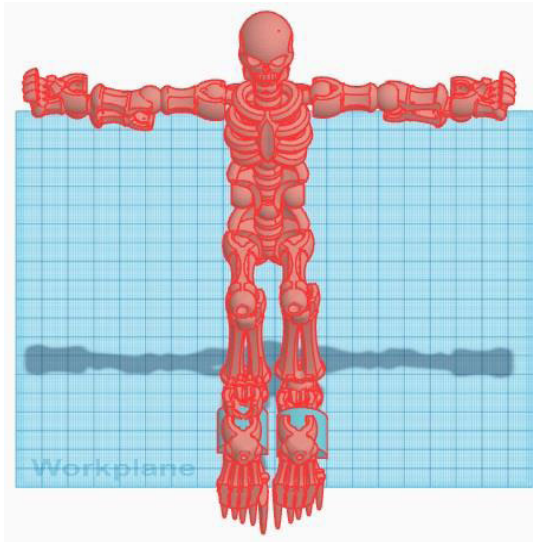


FIGURE 2. Sitting posture of BFBE (3D model).

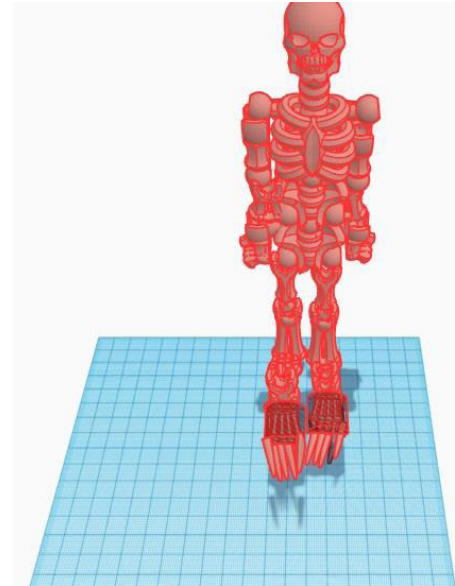


FIGURE 3. Standing posture of BFBE (3D model).

1) EXOSKELETON DESIGN FOR DIFFERENT POSTURES

In this section, we discuss the design generated for the exoskeleton in different body postures. BFBE exoskeleton is constructed to mirror the anatomy of the human body. Figure 2 illustrates the full-body exoskeleton designed using 3D software to emulate sitting posture. The major advantage of the exoskeleton system is that the various parts and the joints can be attached and detached easily. The system can thus be used by people with different degrees of paralysis. The full-body exoskeleton can be used by a completely paralyzed person. paralysis can be provided with a customized exoskeleton. People experience the ease of wearability and mobility because of the development of the exoskeleton with carbon fiber material. To further improve the stability of the person, on the backside and in the ankle region, a support is provided with the system. Actuating the motors placed at the corresponding joints helps to move from sleeping to the sitting posture.

Figure 3 shows the standing posture of the full-body exoskeleton. The system translates from sleeping to standing based on the acquired human intentions. The high torque motors placed at the different joints help in lifting the human weight. If the actuation signals produced are not sufficient, more accurate signals will be generated based on the feedback received. A customized execution pattern is used to maintain stability and reduce errors. The design also ensures that no direct transition from sleeping to standing or vice versa.

III. MATHEMATICAL ANALYSIS OF THE PROPOSED SYSTEM

The mathematical analysis is done on the full-body exoskeleton to identify the desired torque proportional to the mass. The joints used to provide 15 degrees of freedom are utilized to control the different bones of the human skeleton. Figure 4 presents the exoskeleton structure used for the analysis. Here, *A* is the head joint (HJ), *b* is the neck joint (NJ),

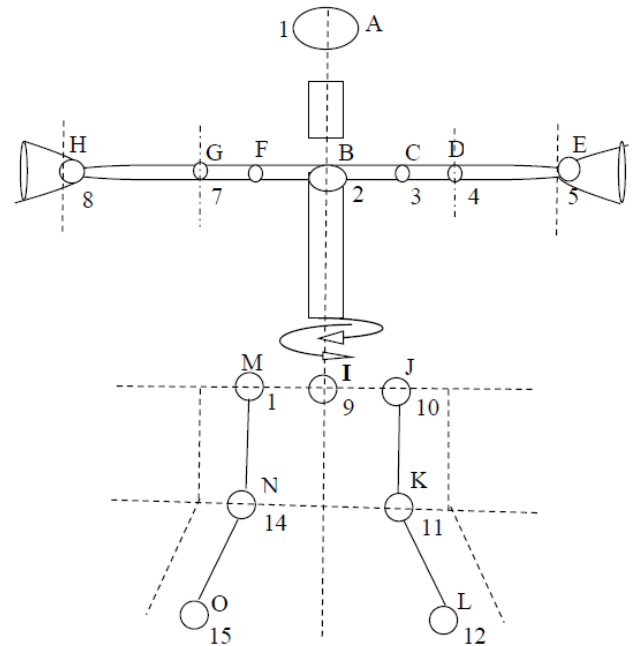


FIGURE 4. Exoskeleton structure used for analysis.

c is the left shoulder joint left (SJL), *d* is the elbow joint left (EJL), *e* is the hand joint left (HJL), *f* is the shoulder joint right (SJR), *g* is the elbow joint right (EJR), *h* is the hand joint right (HJR), *lr* and *lh* are the links for humanoid limbs.

Let the angle of the limb with respect to vertical and horizontal axis is denoted by ' θ ', the masses of the element by m_i , the length of the elements by l_i , and the center of gravity of the system by G_i . The spring of the element is represented by spring coefficient K_i . The angles are referenced with horizontal and vertical axis where *L* denotes the kinetic and *P* denotes

the potential energy, and \in is the force to be applied to the joint.

Let the different control signals to be applied at hip and knee joint of human and exoskeleton be defined as \hat{A} for the angular acceleration of knee, $\hat{\dot{A}}$ for the angular velocity of the knee, \hat{A} for the angular position of the knee, \hat{J} for the total torque applied on the knee and the ankle, \hat{I} for the inertia on the foot and the shank. Let the length of the shank is $\hat{L}m$, length of the foot is $\hat{L}m$, the mass of the shank is \hat{O} kg, mass of the foot is \hat{O} kg and let the torque be proportional to mass.

Consider the upper part of the body. The driving motor is located at the head joint driven by V_{HJ} , V_{NJ} is the neck joint motor driving voltage, V_{SJL} is the shoulder joint left motor driving voltage, V_{SJR} is the shoulder joint right motor driving voltage. Because of the DC voltage, we have currents I_{HJ} , I_{NJ} , I_{SJL} , I_{SJR} , entering the exoskeleton upper part. The current flowing from the neck joint to the head joint is denoted by I_{NH} . We have $I_{NJ} = I_{NH}$, $I_{SJL} = 0$, $I_{SJR} = 0$, $I_{HJ} = -I_{NH}$ and $I_{NH} = S_M(V_{NJ}, V_{SJR}, V_{SJL}, V_{HJ})$, where S_M is a function classified based on the portion at the exoskeleton. Also ' \in ' is the force to be applied to the joint to move from an initial position or angle ' θ ' to final position angle ' θ' '. The length of the exoskeleton part be l_i and the width is w_i and the initial position of the exoskeleton is ' x ' along the axis. The net force applied to the head joint movement will be,

$$\in_{HJ} = \int_0^{<\theta} \in_{HJ}^1 W_i dx \quad (1)$$

With \in^1 as the force applied per unit area, the width W_i becomes constant, thus we have,

$$\in_{HJ} = W_i \int_0^{<\theta} \in_{HJ}^1 dx \quad (2)$$

Similarly, we obtain other values of force applied on shoulder joint left and shoulder joint right as,

$$\in_{SJL} = W_i \int_0^{<\theta} \in_{SJL}^1 dx \quad (3)$$

$$\in_{SJR} = W_i \int_0^{<\theta} \in_{SJR}^1 dx \quad (4)$$

We can say that the net force applied to the head joint, shoulder joint left and shoulder joint right movement as a function of different voltages given by,

$$\in_{HJ} = f_{HJ}(V_{NJ}, V_{SJL}, V_{SJR}, V_{HJ}) \quad (5)$$

$$\in_{SJL} = f_{SJL}(V_{NJ}, V_{SJL}, V_{SJR}, V_{HJ}) \quad (6)$$

$$\in_{SJR} = f_{SJR}(V_{NJ}, V_{SJL}, V_{SJR}, V_{HJ}) \quad (7)$$

If we consider a time-varying voltage V_{NJ} , V_{SJL} , V_{SJR} , V_{HJ} to move the exoskeleton at any position at any time, the neck to head force, shoulder joint left and shoulder joint right, as a function of time t is given by,

$$\in_{NH}^{(t)} = f_{HJ}(V_{NJ}(t), V_{SJL}(t), V_{SJR}(t), V_{HJ}(t)) \quad (8)$$

$$\in_{SJL}^{(t)} = f_{SJL}(V_{NJ}(t), V_{SJL}(t), V_{SJR}(t), V_{HJ}(t)) \quad (9)$$

$$\in_{SJR}^{(t)} = f_{SJR}(V_{NJ}(t), V_{SJL}(t), V_{SJR}(t), V_{HJ}(t)) \quad (10)$$

Here 'f' is the function taking the time-varying force into consideration. Now we have current acting at shoulder joint left and shoulder joint right given by,

$$I_{SJL}(t) = \frac{d}{dt} \in_{SJL} \quad (11)$$

$$I_{SJR}(t) = \frac{d}{dt} \in_{SJR} \quad (12)$$

As the incoming current is equal to the outgoing current, we have, $I_{NJ}(t) + I_{HJ}(t) = \frac{d}{dt} \in_{NH}$. With $I_{NJD}(t)$ as the initial position, we have $I_{NJ}(t) = I_{\mu}(t) + I_{NJD}(t)$, $I_{HJ}(t) = -I_{\mu}(t) + I_{HJD}(t)$ and $I_{NJD}(t) + I_{HJD}(t) = \frac{d}{dt} \in_{NH}$.

Here, $I_{\mu}(t)$ is fully responsible for the exact movement at the exact time and I_{NJD} and I_{HJD} for the correct initial position. We can call them as the returned coordinates. If $I_{NJD}(t)$ is causing the change in the movement of exoskeleton by an angle θ' in the given time Δt , then $I_{NJD}(t) = \frac{d}{dt} \in'_{\theta}$, and if $I_{HJD}(t)$ is causing the change in the movement of exoskeleton by θ'' in the given time Δt , then $I_{HJD} = \frac{d}{dt} \in''_{\theta}$.

Change in the variation between the neck and the head joint is given by $\frac{d}{dt} \in'_{\theta} + \frac{d}{dt} \in''_{\theta} = \frac{d}{dt} \in_{NH}$ that is $\in'_{\theta} + \in''_{\theta} = \in_{NH}$. Assuming two different movement angle force at $<\in'_{\theta}$ and $<\in''_{\theta}$ we have the force, variations given by,

$$\in'_{\theta'} = W_i \int_0^{<\theta'} \frac{x}{l_i} \in'_{HJ} dx \quad (13)$$

$$\in''_{\theta''} = W_i \int_0^{<\theta''} \left(1 - \frac{x}{l_i}\right) \in'_{HJ} dx \quad (14)$$

The net force applied is written as a function of different voltages given by,

$$\in'_{\theta'} = f_{\theta'}(V_{NJ}, V_{SJL}, V_{SJR}, V_{HJ}) \quad (15)$$

$$\in''_{\theta''} = f_{\theta''}(V_{NJ}, V_{SJL}, V_{SJR}, V_{HJ}) \quad (16)$$

Considering the time-varying voltage V_{NJ} , V_{SJL} , V_{SJR} , V_{HJ} to move the exoskeleton at any position at any time, the neck to head force, shoulder joint left and shoulder joint right, as a function of time t is given by,

$$\in'_{\theta'}(t) = f_{\theta'}(V_{NJ}(t), V_{SJL}(t), V_{SJR}(t), V_{HJ}(t)) \quad (17)$$

$$\in''_{\theta''}(t) = f_{\theta''}(V_{NJ}(t), V_{SJL}(t), V_{SJR}(t), V_{HJ}(t)) \quad (18)$$

Considering the 'f' function takes time varying force into considerations, we have the current acting as,

$$I_{HJD}(t) = \frac{d}{dt} \in_{\theta'} \quad (19)$$

$$I_{HJD}(t) = \frac{d}{dt} \in_{\theta''} \quad (20)$$

$$I_{SJL}(t) = \frac{d}{dt} \in_{SJL} \quad (21)$$

$$I_{SJR}(t) = \frac{d}{dt} \in_{SJR} \quad (22)$$

The net current flowing through the exoskeleton is zero and given by,

$$I_{NJ}(t) + I_{HJ}(t) + I_{SJL}(t) + I_{SJR}(t) = 0 \quad (23)$$

$$I_{NJD}(t) + I_{HJD}(t) + I_{SJL}(t) + I_{SJR}(t) = 0 \quad (24)$$

Using the chain value of differentiation on the current values we obtain,

$$I_{NJD}(t) = \frac{\partial \epsilon_{\theta'}}{\partial V_{NJ}} \frac{d}{dt} V_{NJ} + \frac{\partial \epsilon_{\theta'}}{\partial V_{SJL}} \frac{d}{dt} V_{SJL} + \frac{\partial \epsilon_{\theta'}}{\partial V_{SJR}} \frac{d}{dt} V_{SJR} + \frac{\partial \epsilon_{\theta'}}{\partial V_{HJ}} \frac{d}{dt} V_{HJ} \quad (25)$$

$$I_{HJD}(t) = \frac{\partial \epsilon_{\theta''}}{\partial V_{NJ}} \frac{d}{dt} V_{NJ} + \frac{\partial \epsilon_{\theta''}}{\partial V_{SJL}} \frac{d}{dt} V_{SJL} + \frac{\partial \epsilon_{\theta''}}{\partial V_{SJR}} \frac{d}{dt} V_{SJR} + \frac{\partial \epsilon_{\theta''}}{\partial V_{HJ}} \frac{d}{dt} V_{HJ} \quad (26)$$

$$I_{SJL}(t) = \frac{\partial \epsilon_{SJL}}{\partial V_{NJ}} \frac{d}{dt} V_{NJ} + \frac{\partial \epsilon_{SJL}}{\partial V_{SJL}} \frac{d}{dt} V_{SJL} + \frac{\partial \epsilon_{SJL}}{\partial V_{SJR}} \frac{d}{dt} V_{SJR} + \frac{\partial \epsilon_{SJL}}{\partial V_{HJ}} \frac{d}{dt} V_{HJ} \quad (27)$$

$$I_{SJR}(t) = \frac{\partial \epsilon_{SJR}}{\partial V_{NJ}} \frac{d}{dt} V_{NJ} + \frac{\partial \epsilon_{SJR}}{\partial V_{SJL}} \frac{d}{dt} V_{SJL} + \frac{\partial \epsilon_{SJR}}{\partial V_{SJR}} \frac{d}{dt} V_{SJR} + \frac{\partial \epsilon_{SJR}}{\partial V_{HJ}} \frac{d}{dt} V_{HJ} \quad (28)$$

With dx as a small incremental moment for an incremental time $d\tau$ we obtain,

$$dx = \frac{-K_i W_i}{\tilde{A}} \epsilon'_{HJ} d\tau \quad (29)$$

Substituting the above value of dx in (2) and (3) we obtain,

$$\epsilon_{SJL} = W_i \int_{\theta'}^{\theta''} \epsilon'_{SJL} \left(\frac{-K_i W_i}{\tilde{A}} \epsilon'_{HJ} d\tau \right) \quad (30)$$

$$\epsilon_{SJL} = \frac{-K_i W_i^2}{\tilde{A}} \int_{\theta'}^{\theta''} \epsilon'_{SJL} \epsilon'_{HJ} d\tau \quad (31)$$

$$\epsilon_{SJR} = \frac{-K_i W_i^2}{\tilde{A}} \int_{\theta'}^{\theta''} \epsilon'_{SJR} \epsilon'_{HJ} d\tau \quad (32)$$

$$\epsilon_{HJ} = \frac{-K_i W_i^2}{\tilde{A}} \int_{\theta'}^{\theta''} (\epsilon'_{HJ})^2 d\tau \quad (33)$$

Substituting the above value of dx in (12) and (13) we obtain,

$$\epsilon'_{\theta'} = \frac{-K_i W_i^2}{\tilde{A}} \int_{\theta'}^{\theta''} \frac{x}{l_i} (\epsilon'_{HJ})^2 d\tau \quad (34)$$

$$\epsilon''_{\theta''} = \frac{-K_i W_i^2}{\tilde{A}} \int_{\theta'}^{\theta''} \left(1 - \frac{x}{l_i} \right) (\epsilon'_{HJ})^2 d\tau \quad (35)$$

Calculating 'x' in terms of torque we integrate 'x' from initial angle θ' to final angle θ'' .

$$x = \frac{-K_i W_i}{\tilde{A}} \int_{\theta'}^{\theta''} \epsilon'_{HJ} d\tau \quad (36)$$

The V_{NJ} value for which we reach the maximum limit is V_{max} . If the value of V_{NJ} is raised above V_{max} , the exoskeleton movements will remain unaltered and practically constant. The human body parts will act as the dielectric of the capacitor with the exoskeleton acting as the plate of the capacitor. Here V_{OI} is the voltage applied between outer and inner exoskeleton, P_{limb} is the potential drop across the thickness of the limb, P_{IX} is the potential drop across the inner

surface of the exoskeleton, and P_{CM} is the potential at all the contact point across the exoskeleton and human limb. We now have,

$$VOJ = P_{limb} + PIX + PCM \quad (37)$$

The variation in the voltage is given by, $\Delta V_{OJ} = \Delta P_{limb} + \Delta PIX + P_{CM}$ where, P_{CM} is constant.

Now there are three potential charges across the exoskeleton and the limb, φ_{OE} is the charge on the outer exoskeleton, φ_{limb} is the charge on the limb, φ_{IE} is the charge on the inner exoskeleton, and we have $\varphi_{OE} + \varphi_{limb} + \varphi_{IE} = 0$ and $\tilde{\varphi}_{OE} + \tilde{\varphi}_{limb} + \tilde{\varphi}_{IE} = 0$. The charges per unit area are given by $\Delta \tilde{\varphi}_{OE} + \Delta \tilde{\varphi}_{IE} = 0$ with $\tilde{\varphi}_{limb}$ as constant.

To analyze the effect of external voltage on the exoskeleton, and the human limb, we are defining a threshold voltage depending on the EEG signal V_{th} . The minimum voltage required to trigger the movement is, if $VOI < V_{th}$ then $\tilde{\varphi}_{IE} > 0$ and $PIX < 0$, if $VOI \geq V_{th}$ then $\tilde{\varphi}_{IE} < 0$ and $PIX > 0$, if $VOI = V_{th}$ then $\tilde{\varphi}_{IE} = 0$ and $PIX = 0$. The signal from EEG headset to limb is defined as $R_{surface-limb}$, ST is the potential depending on the thickness of limb, and LT is the length of the limb. The ratio of the potential drop across the inner surface of the exoskeleton to the length of the limb is given by P_{IX}/L_T . The signal transferred from EEG headset to the limb is given by,

$$R_{surface-limb} = S_T e^{P_{IX}/L_T} \quad (38)$$

The potential depending on the thickness of the limb is calculated as,

$$S_T = S_L e^{-P_{RX}/L_T} \quad (39)$$

Substituting the value of ST in (39), we obtain,

$$R_{surface-limb} = S_L e^{(P_{IX} - P_{RX})/L_T} \quad (40)$$

The capacitance coefficient variation in the direction of x and capacitance coefficient variation in the opposite direction of x given by,

$$K(x) = K_0 e^{P(x)/L_T} \quad (41)$$

$$K(y) = L_0 e^{-P(x)/L_T} \quad (42)$$

Potential is at its local maximum, which indicates that the system in the equilibrium state is unstable. We apply a small displacement to the exoskeleton and move it to a random small distance from its equilibrium state, and the total force of the exoskeleton makes it to move even farther. Mobility displacement along the x direction is given by,

$$\mu(x) = \vartheta (K(y) - K(x) - P_A) \quad (43)$$

$$\frac{d^2 P}{dy^2} = \frac{-\vartheta}{\mu_s} \left[L_0 e^{-P(x)/L_T} - K_0 e^{P(x)/L_T} - P_A \right] \quad (44)$$

The charge on the inner skeleton is given by,

$$\tilde{\varphi}_{IE} = \frac{\mp \sqrt{2\vartheta \mu_s P_A} \sqrt{L_T e^{-P(x)/L_T} + P_{IX}}}{\sqrt{-L_T + e^{-P_{RX}/L_T} (L_T e^{P/L_T} - P_{IX} - L_T)}} \quad (45)$$

$$\tilde{\varphi}_{IE} = \tilde{C}_{limb} P_{limb} \quad (46)$$

$$\tilde{\varphi}_{IE} = -\sqrt{2\vartheta \mu_s P_A} \sqrt{P_{IX} + L_T e^{(P_{IX} - P_{RX})/L_T}} \quad (47)$$

$$\tilde{\varphi}_{IE} = \tilde{\varphi}_{RL} + \tilde{\varphi}_{SL} \quad (48)$$

The charge on the right-side outer skeleton to the limb is calculated as,

$$\tilde{\varphi}_{RL} = \int_{initial\theta}^{final} (\vartheta) K(x) (Adx) \quad (49)$$

The charge on the left-side outer skeleton to the limb is calculated as,

$$\tilde{\varphi}_{SL} = -\vartheta \int_{initial}^{final} K(x) dx \quad (50)$$

The body parameter constant with static exoskeleton movement is given by,

$$T_B = \sqrt{\frac{2\mu_s}{\vartheta P_A}} \sqrt{P_{IX}} \quad (51)$$

The small variation in the charge on the inner skeleton is given by, $\Delta\tilde{\varphi}_{IE} = \Delta\tilde{\varphi}_{RL} + \Delta\tilde{\varphi}_{SL}$ where $\tilde{\varphi}_{RL} = \tilde{\varphi}_{RL}(P_{IX})$ and $\tilde{\varphi}_{SL} = \tilde{\varphi}_{SL}(P_{IX})$. The voltage applied between the outer and inner exoskeleton is given by,

$$V_{OI} = V_{th} + P_{IX} - \frac{\tilde{\varphi}_{SL}(P_{IX}) + \tilde{\varphi}_{RL}(P_{IX})}{\tilde{limb}} \quad (52)$$

IV. RESULTS AND DISCUSSION

The designed system is tested on six different subjects, three healthy and three paralyzed persons. The collection of data is done in the offline and online phases. The experiments are carried out for three different human intentions like sleeping, standing, and sitting. To maintain stability, the movements are executed based on the designed pattern. In the offline training phase, the brain patterns corresponding to each of these intended movements are acquired using the 64 channel EEG sensor. Figure 5 presents the EEG Sensor manufactured with 16 Electrodes for collecting the signals.

Signal analysis is carried out using WHT, and the unique features required for the classification are extracted. Large amount of EEG signals is compressed using WHT, and a faster computation is also provided. The database is designed using the extracted information corresponding to each human thought obtained during the training phase. In the online phase, the WHT coefficients, along with extracted information, are transmitted from the brain to the full-body exoskeleton for the reconstruction of the original signal.

The EEG signals corresponding to human intentions of sitting and standing are depicted in figure 6. Here, the original signal and the reconstructed signal for both the postures are presented. Figure 7 shows the area matching of EEG patterns obtained for the sitting and standing postures. The original and reconstructed signal is correlated at the receiver side to identify the movement to be executed. Based on the classification results, the required joints are actuated to produce the desired movement by the exoskeleton system.

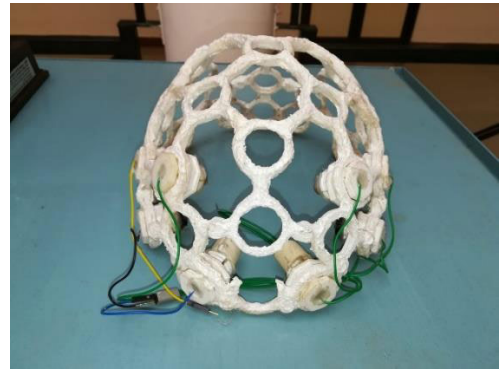


FIGURE 5. EEG sensor manufactured with 16 electrodes.

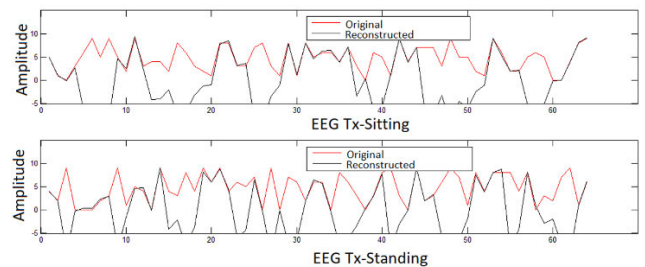


FIGURE 6. Original and reconstructed EEG signal in sitting and standing positions with BFBE.

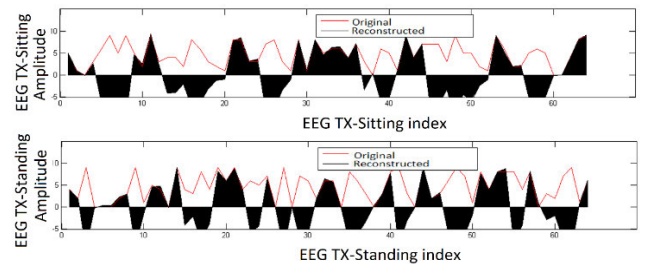


FIGURE 7. Area matching of EEG patterns obtained for sitting and standing posture.

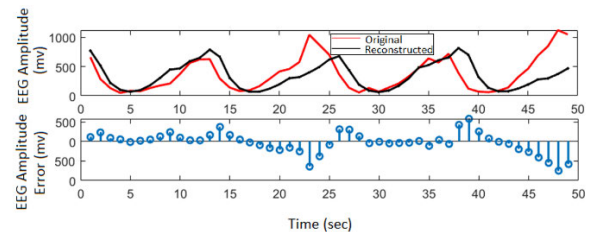


FIGURE 8. EEG amplitude and EEG amplitude error for original and reconstructed signals.

Figure 8 shows the varying of the EEG signal captured by the brain headset with time. The error in EEG amplitude for the signal is also shown in the figure. Figure 9 presents the brain pattern variations at different frequencies using the proposed system. The voltage spectral density variations at frequencies 6 Hz, 10 Hz and 22 Hz are presented and highlighted in the figure.

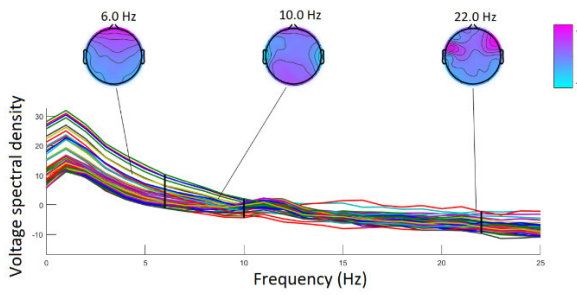


FIGURE 9. Brain pattern variations at different frequencies.

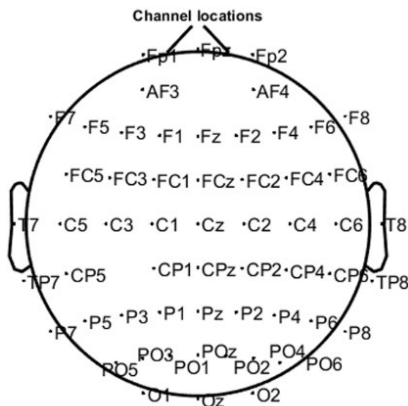


FIGURE 10. Electrode placement locations in the EEG headset.

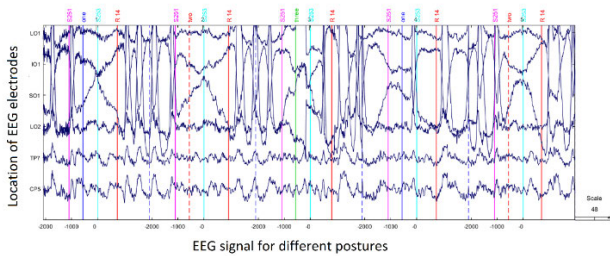


FIGURE 11. EEG for different postures with placement of electrodes from CP5 to LO1.

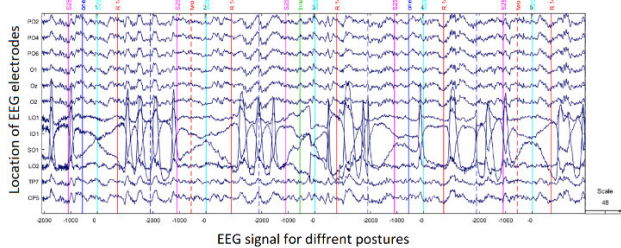


FIGURE 12. EEG for different postures with the placement of electrodes from CP5 to PO2.

In the proposed system, EEG analysis is carried out using realistic head models to identify the unique EEG signal features and to validate the brain network connectivity. Here, a 64-electrode placement scheme is used in the proposed system. The electrodes are placed in the frontal and parietal

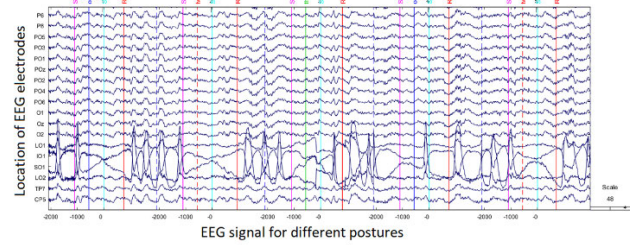


FIGURE 13. EEG for different postures with the placement of electrodes from CP5 to P6.

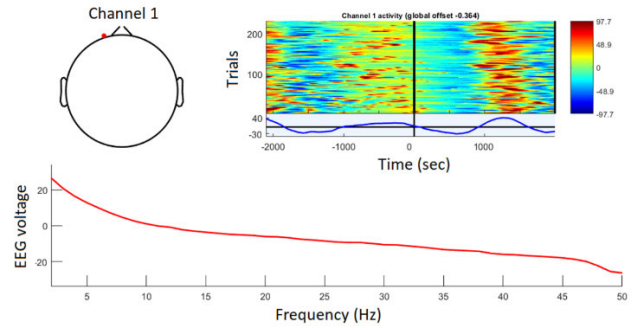


FIGURE 14. EEG voltage for different frequency and number of trials per second.

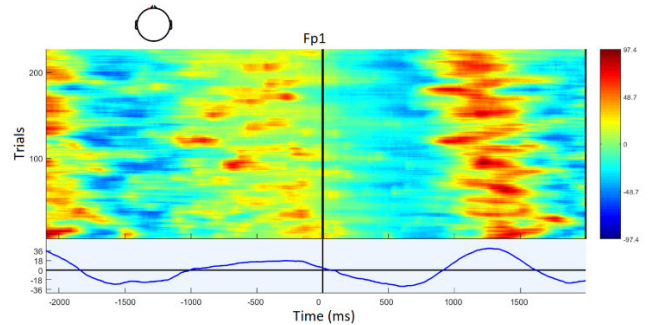


FIGURE 15. Number of trials with time.

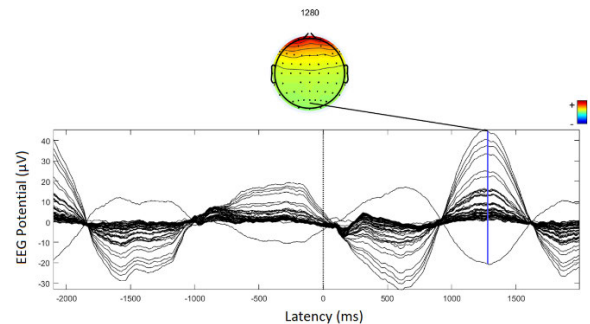


FIGURE 16. EEG voltage for different frequency and number of trails per second.

regions of the brain. Figure 10 indicates the electrode placement positions used for testing the proposed system.

Figure 11 shows the EEG signal for different postures with the placement of electrodes from positions CP5 to LO1,

and figure 12 shows the EEG for different postures with the placement of electrodes from CP5 to PO2 positions and figure 13 shows the EEG for different postures with the placement of electrodes from CP5 to P6 positions. Figure 14 shows the EEG voltage for different frequencies and also the number of trials per second.

Figure 15 shows the number of trials carried out with time, and figure 16 shows the EEG potential with varying latency using the proposed system. The proposed system achieves excellent performance in all real-time scenarios. Results confirm that the proposed method provides adequate assistance and rehabilitation for paralyzed patients.

V. CONCLUSION

To overcome the constraints of weight, flexibility, and adaptability faced by the existing exoskeletons used for assisting the paralyzed people, we proposed an adaptive and flexible Brain Energized Full Body Exoskeleton (BFBE). The brain signals captured by the EEG sensors are used for controlling the movements of the exoskeleton. The flexibility is incorporated into the system by a modular design approach. The parts and joints can be attached and detached easily, allowing it to be used by people with different levels of paralysis. For the fully paralyzed, the full-body exoskeleton structure can be used. The processing happens at the edge, thus reducing delay in decision making, and the system is further integrated with an IoT module that helps to send an alert message to multiple caregivers in case of an emergency. The potential energy harvesting is used in the system to solve the power issues related to the exoskeleton. The stability in the gait cycle is ensured by using adaptive sensory feedback. The system was by using six natural movements on ten different paralyzed persons and received very good results.

REFERENCES

- [1] Multiple Sclerosis News Today. *Mobility Devices for Lower-Limb Paralysis Flawed, Survey Reveals*. Accessed: Jun. 20, 2019. [Online]. Available: <https://multiplesclerosisnewstoday.com/2018/06/08/mobility-devices-lower-limb-paralysis-flawed-survey>
- [2] S. Alqahtani, J. Joseph, B. Dicianno, N. A. Layton, M. L. Toro, E. Ferretti, Y. A. Tuakli-Wosornu, H. Chhabra, H. Neyedli, C. R. Lopes, M. M. Alqahtani, P. Van de Vliet, S.-I. Kumagaya, J.-B. Kim, V. McKinney, Y.-S. Yang, M. Goldberg, and R. Cooper, "Stakeholder perspectives on research and development priorities for mobility assistive-technology: A literature review," *Disab. Rehabil. Assistive Technol.*, pp. 1–15, Dec. 2019, doi: [10.1080/17483107.2019.1650300](https://doi.org/10.1080/17483107.2019.1650300).
- [3] D. Ao, R. Song, and J. Gao, "Movement performance of human-robot cooperation control based on EMG-driven hill-type and proportional models for an ankle power-assist exoskeleton robot," *IEEE Trans. Neural Syst. Rehabil. Eng.*, vol. 25, no. 8, pp. 1125–1134, Aug. 2017, doi: [10.1109/TNSRE.2016.2583464](https://doi.org/10.1109/TNSRE.2016.2583464).
- [4] Q. Ma, L. Ji, and R. Wang, "The development and preliminary test of a powered alternately walking exoskeleton with the wheeled foot for paraplegic patients," *IEEE Trans. Neural Syst. Rehabil. Eng.*, vol. 26, no. 2, pp. 451–459, Feb. 2018.
- [5] T. Zhang, M. Tran, and H. Huang, "Design and experimental verification of hip exoskeleton with balance capacities for walking assistance," *IEEE/ASME Trans. Mechatronics*, vol. 23, no. 1, pp. 274–285, Feb. 2018, doi: [10.1109/TMECH.2018.2790358](https://doi.org/10.1109/TMECH.2018.2790358).
- [6] J. C. Perry, J. Rosen, and S. Burns, "Upper-limb powered exoskeleton design," *IEEE/ASME Trans. Mechatronics*, vol. 12, no. 4, pp. 408–417, Aug. 2007, doi: [10.1109/TMECH.2007.901934](https://doi.org/10.1109/TMECH.2007.901934).
- [7] A. Sutrisno and D. J. Braun, "Enhancing mobility with quasi-passive variable stiffness exoskeletons," *IEEE Trans. Neural Syst. Rehabil. Eng.*, vol. 27, no. 3, pp. 487–496, Mar. 2019, doi: [10.1109/TNSRE.2019.2899753](https://doi.org/10.1109/TNSRE.2019.2899753).
- [8] P. G. Vinoj, S. Jacob, V. G. Menon, S. Rajesh, and M. R. Khosravi, "Brain-controlled adaptive lower limb exoskeleton for rehabilitation of post-stroke paralyzed," *IEEE Access*, vol. 7, pp. 132628–132648, 2019, doi: [10.1109/access.2019.2921375](https://doi.org/10.1109/access.2019.2921375).
- [9] M. Sarac, M. Solazzi, and A. Frisoli, "Design requirements of generic hand exoskeletons and survey of hand exoskeletons for rehabilitation, assistive, or haptic use," *IEEE Trans. Haptics*, vol. 12, no. 4, pp. 400–413, Oct. 2019, doi: [10.1109/toh.2019.2924881](https://doi.org/10.1109/toh.2019.2924881).
- [10] F. Patane, S. Rossi, F. D. Sette, J. Taborri, and P. Cappa, "WAKE-up exoskeleton to assist children with cerebral palsy: Design and preliminary evaluation in level walking," *IEEE Trans. Neural Syst. Rehabil. Eng.*, vol. 25, no. 7, pp. 906–916, Jul. 2017, doi: [10.1109/tnsre.2017.2651404](https://doi.org/10.1109/tnsre.2017.2651404).
- [11] H.-J. Lee, S. Lee, W. H. Chang, K. Seo, Y. Shim, B.-O. Choi, G.-H. Ryu, and Y.-H. Kim, "A wearable hip assist robot can improve gait function and cardiopulmonary metabolic efficiency in elderly adults," *IEEE Trans. Neural Syst. Rehabil. Eng.*, vol. 25, no. 9, pp. 1549–1557, Sep. 2017, doi: [10.1109/tnsre.2017.2664801](https://doi.org/10.1109/tnsre.2017.2664801).
- [12] A. Agrawal, O. Harib, A. Hereid, S. Finet, M. Masselin, L. Praly, A. D. Ames, K. Sreenath, and J. W. Grizzle, "First steps towards translating HZD control of bipedal robots to decentralized control of exoskeletons," *IEEE Access*, vol. 5, pp. 9919–9934, 2017, doi: [10.1109/access.2017.2690407](https://doi.org/10.1109/access.2017.2690407).
- [13] M. K. Shepherd and E. J. Rouse, "Design and validation of a torque-controllable knee exoskeleton for Sit-to-Stand assistance," *IEEE/ASME Trans. Mechatronics*, vol. 22, no. 4, pp. 1695–1704, Aug. 2017, doi: [10.1109/tmech.2017.2704521](https://doi.org/10.1109/tmech.2017.2704521).
- [14] M. Cenciari and M. A. Dollar, "Biomechanical considerations in the design of lower limb exoskeletons," in *Proc. IEEE Int. Conf. Rehabil. Robot.*, Zürich, Switzerland, Jun./Jul. 2011, pp. 1–6, doi: [10.1109/ICORR.2011.5975366](https://doi.org/10.1109/ICORR.2011.5975366).
- [15] H. Herr, "Exoskeletons and orthoses: Classification, design challenges and future directions," *J. NeuroEng. Rehabil.*, vol. 6, no. 1, p. 21, Dec. 2009, doi: [10.1186/1743-0003-6-21](https://doi.org/10.1186/1743-0003-6-21).
- [16] A. Agrawal, A. N. Dube, D. Kansara, S. Shah, and S. Sheth, "Exoskeleton: The friend of mankind in context of rehabilitation and enhancement," *Indian J. Sci. Technol.*, vol. 9, no. S1, pp. 1–8, Dec. 2016, doi: [10.17485/ijst/2016/v9is1/100889](https://doi.org/10.17485/ijst/2016/v9is1/100889).
- [17] C. Chen, X. Wu, D.-X. Liu, W. Feng, and C. Wang, "Design and voluntary motion intention estimation of a novel wearable full-body flexible exoskeleton robot," *Mobile Inf. Syst.*, vol. 2017, pp. 1–11, Jun. 2017, doi: [10.1155/2017/8682168](https://doi.org/10.1155/2017/8682168).
- [18] A. Singla, S. Dhand, A. Dhawad, and G. S. Virk, "Toward human-powered lower limb exoskeletons: A review," in *Harmony Search and Nature Inspired Optimization Algorithms. Advances in Intelligent Systems and Computing*, vol. 741. Singapore: Springer, 2019, pp. 783–795, doi: [10.1007/978-981-13-0761-4_75](https://doi.org/10.1007/978-981-13-0761-4_75).
- [19] S. Federici, F. Meloni, M. Bracalenti, and M. L. De Filippis, "The effectiveness of powered, active lower limb exoskeletons in neurorehabilitation: A systematic review," *NeuroRehabilitation*, vol. 37, no. 3, pp. 321–340, Nov. 2015, doi: [10.3233/nre-151265](https://doi.org/10.3233/nre-151265).
- [20] G. Menga and M. Ghirardi, "Lower limb exoskeleton for rehabilitation with improved postural equilibrium," *Robotics*, vol. 7, no. 2, p. 28, Jun. 2018, doi: [10.3390/robotics7020028](https://doi.org/10.3390/robotics7020028).
- [21] H. Kazerooni and R. Steger, "The berkeley lower extremity exoskeleton," *J. Dyn. Syst., Meas., Control*, vol. 128, no. 1, pp. 14–25, Mar. 2006, doi: [10.1115/1.2168164](https://doi.org/10.1115/1.2168164).
- [22] V. G. Menon, S. Jacob, S. Joseph, and A. O. Almagrabi, "SDN powered humanoid with edge computing for assisting paralyzed patients," *IEEE Internet Things J.*, early access, Dec. 2019, doi: [10.1109/JIOT.2019.2963288](https://doi.org/10.1109/JIOT.2019.2963288).
- [23] S. Jacob, V. G. Menon, F. Al-Turjman, V. P. G., and L. Mostarda, "Artificial muscle intelligence system with deep learning for post-stroke assistance and rehabilitation," *IEEE Access*, vol. 7, pp. 133463–133473, 2019, doi: [10.1109/ACCESS.2019.2941491](https://doi.org/10.1109/ACCESS.2019.2941491).

- [24] L. Jiang, A. Stocco, D. M. Losey, J. A. Abernethy, C. S. Prat, and R. P. N. Rao, "BrainNet: A multi-person brain-to-brain interface for direct collaboration between brains," *Sci. Rep.*, vol. 9, no. 1, pp. 1–11, Dec. 2019, doi: [10.1038/s41598-019-41895-7](https://doi.org/10.1038/s41598-019-41895-7).
- [25] W. Lee, S. Kim, B. Kim, C. Lee, Y. A. Chung, L. Kim, and S.-S. Yoo, "Non-invasive transmission of sensorimotor information in humans using an EEG/focused ultrasound brain-to-brain interface," *PLoS ONE*, vol. 12, no. 6, Jun. 2017, Art. no. e0178476, doi: [10.1371/journal.pone.0178476](https://doi.org/10.1371/journal.pone.0178476).
- [26] S. Rajesh, V. Paul, V. G. Menon, S. Jacob, and P. Vinod, "Secure brain-to-brain communication with edge computing for assisting post-stroke paralyzed patients," *IEEE Internet Things J.*, vol. 7, no. 4, pp. 2531–2538, Apr. 2020, doi: [10.1109/JIOT.2019.2951405](https://doi.org/10.1109/JIOT.2019.2951405).



SUNIL JACOB (Member, IEEE) received the Ph.D. degree in electronics and communication engineering from Bharathiar University, India, in 2015. He is currently the Director with the Centre for Robotics and a Professor with the Department of Electronics and Communication Engineering, SCMS School of Engineering and Technology, India. He is also doing postdoctoral research with the Lincoln University College, Malaysia. His project Muscles to Machine Interface for Paralyzed has been funded by the IEEE EPICS, USA, and other funded projects include bionic haptic arm, rejuvenating the cells of human body, deaddiction coil for drug addicts, smart keyboard for disabled person, low cost 3-D printer, and wearable device for detection and prevention of heart failure. He was a recipient of the AICTE Chhatra Vishwakarma Award, in electronics, in 2017, and the Young Gandhian Technological Innovation Appreciation Award, in 2018.



MUKIL ALAGIRISAMY received the bachelor's degree in electronics and communication engineering, the M.Eng. degree in communication systems, and the Ph.D. degree in engineering, in 2005, 2007, and 2012, respectively. She completed her PDF, in 2015. She started her career as a Lecturer with the Hindustan Engineering College, India. She was working as an Assistant Professor with B. S. Abdur Rahman University, India. Later, she joined the Stamford College, Malaysia, as a Lecturer. She is currently an Associate Professor with the Department of Electrical and Electronics and Engineering, Lincoln University College, Malaysia. She is also working as an Assistant Professor and a Coordinator of the Master of Science in Electrical, Electronics and Telecommunication Engineering Programs, Lincoln University College. She has 12 years of experience in teaching subjects like data communication, analog and digital communications, digital signal processing, and satellite communications. Her research interests include sink mobility patterns, clustering, modulation, data aggregation, and compressive sensing techniques for wireless sensor networks.



VARUN G. MENON (Senior Member, IEEE) received the Ph.D. degree in computer science and engineering from Sathyabama University, India, in 2017. He is currently an Associate Professor with the Department of Computer Science and Engineering, SCMS School of Engineering and Technology, India. His research interests include sensors, the Internet of Things (IoT), fog computing, and underwater acoustic sensor networks. He is also serving as the Guest Editor for the IEEE

SENSORS JOURNAL, the IEEE Internet of Things Magazine, and the IEEE TRANSACTIONS ON INDUSTRIAL INFORMATICS. He is an Associate Editor of IET Quantum Communications and also an Editorial Board Member of IEEE Future Directions: Technology Policy and Ethics. He is also a Distinguished Speaker of ACM.



B. MANOJ KUMAR received the Ph.D. degree in mechanical engineering from Karpagam University, India. He is currently an Associate Professor and the Head of the Department of Automobile Engineering, SCMS School of Engineering and Technology, India. His research interests include sensor networks and industrial engineering.



N. Z. JHANJHI is currently working as an Associate Professor with Taylor's University, Malaysia. He has great international exposure in academia, research, administration, and academic quality accreditation. He worked with Ilma University and King Faisal University (KFU), Saudi Arabia, for a decade. He has 20 years of teaching and administrative experience. He has an intensive background of academic quality accreditation in higher education. Besides scientific research activities,

he had worked a decade for academic accreditation and earned ABET accreditation twice for three programs at CCSIT, KFU. He also worked for the National Commission for Academic Accreditation and Assessment (NCAAA), the Education Evaluation Commission Higher Education Sector (EECHES), formerly NCAAA, Saudi Arabia, for institutional level accreditation. He also worked for the National Computing Education Accreditation Council (NCEAC). He was awarded as a top Reviewer 1% globally by WoS/ISI (Publons) recently for the year 2019. He has edited or authored more than 13 research books with international reputed publishers, earned several research grants, and a great number of indexed research articles on his credit. He has supervised several postgraduate students, including the master's and Ph.D. students. He is an Associate Editor of the IEEE ACCESS, a Moderator of the IEEE TechRxiv, a keynote speaker for several IEEE international conferences globally, an External Examiner or an Evaluator for Ph.D. and master's students for several universities, a Guest editor of several reputed journals, a member of the editorial board of several research journals, and an active TPC Member of reputed conferences around the globe.



VASAKI PONNUSAMY received the bachelor's and M.Sc. degrees in computer science from the University of Science, Malaysia, and the Ph.D. degree in IT from Universiti Teknologi PETRONAS (UTP), Malaysia, in 2013. She is currently an Assistant Professor with Universiti Tunku Abdul Rahman, Malaysia. She is also the Head of the Department of Computer and Communication Technology, Faculty of Information and Communication Technology. She is also working

on cybersecurity, the Internet-of-Things (IoT) security trends, and digital governance. She has great international exposure as a Keynote Speaker, a Visiting Professor, and several Fellowships. She has edited or authored several research books with international reputed publishers, earned several research grants, and supervising postgraduate students. She is also a Human Resource Development Fund Certified Trainer and a Master Trainer for computational thinking and computer science teaching. Her career in academia started, in 1999. She has been teaching information and network security, wireless security, and data communication and networking. She is specialized in handling Cisco devices for routing and security. Her passion is to share her technical knowledge with the community. Her area of specializations are networking, communication, penetration testing, and cybersecurity. She has worked on several projects on IoT intrusion detection systems, cybersecurity governance, social engineering attacks mitigation/awareness, and human behavior-based authentication systems.



include deep learning, cloud security and privacy, *ad hoc* networks, and big data.

P. G. SHYNU received the Ph.D. degree in computer science from the Vellore Institute of Technology (VIT), Vellore, India, and the master's degree in computer science and engineering from the College of Engineering, Anna University, Chennai, India. He is currently working as an Associate Professor with the School of Information Technology and Engineering, VIT. He has published over 30 research papers in refereed international conferences and journals. His research interests



applications. He is the Founder of Anidra Tech Ventures Pty Ltd., a smart remote patient monitoring company. He contributed immensely to eResearch software research and development that uses cloud-based infrastructure and a core member for the project sponsored by Nectar Australian research cloud provider. He contributed heavily in the field of healthcare informatics, sensor networks, and cloud computing.

VENKI BALASUBRAMANIAN (Member, IEEE) received the Ph.D. degree in body area wireless sensor network (BAWSN) for remote healthcare monitoring applications. He is the Pioneer in building (pilot) remote healthcare monitoring application (rHMA) for pregnant women for the New South Wales Healthcare Department. His research establishes a dependability measure to evaluate rHMA that uses BAWSN. His research opens up a new research area in measuring time-critical

• • •

PAPER • OPEN ACCESS

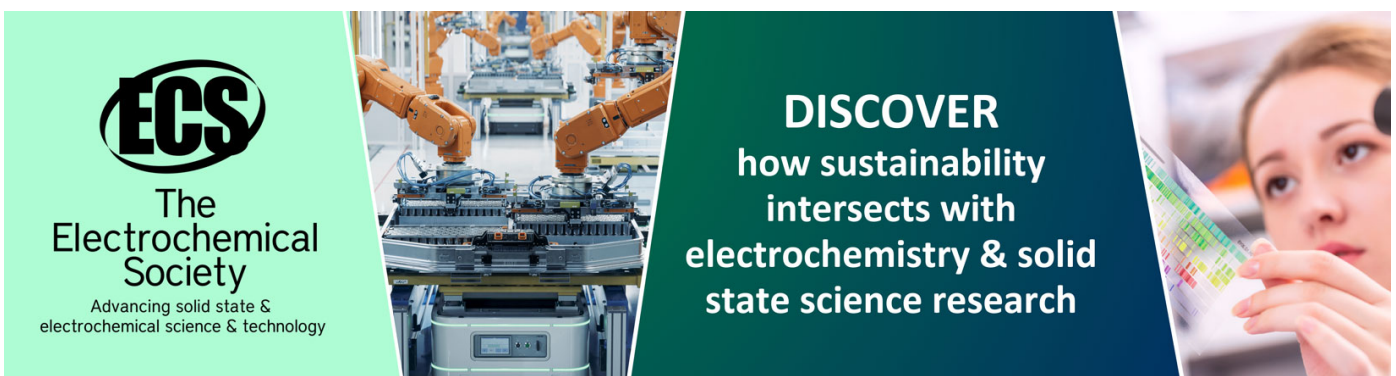
Soft morphological filtering using hypergraphs

To cite this article: Nuja M Unnikrishnan *et al* 2021 *IOP Conf. Ser.: Mater. Sci. Eng.* **1085** 012038

View the [article online](#) for updates and enhancements.

You may also like

- [Planted hitting set recovery in hypergraphs](#)
Ilya Amburg, Jon Kleinberg and Austin R Benson
- [Symmetric hypergraph states: entanglement quantification and robust Bell nonlocality](#)
Jan Nöller, Otfried Gühne and Mariami Gachechiladze
- [Analysis of quantum error correction with symmetric hypergraph states](#)
T Wagner, H Kampermann and D Bruß



ECS
The
Electrochemical
Society
Advancing solid state &
electrochemical science & technology

DISCOVER
how sustainability
intersects with
electrochemistry & solid
state science research

Soft morphological filtering using hypergraphs

Nuja M Unnikrishnan¹, Mini Tom², V Bino Sebastian³ and K V Thomas⁴

¹Research Scholar, Mathematics Department, Bharata Mata College, Thrikkakara, Kerala, India, nuja.mu@gmail.com

²Professor, Basic Science and Humanities Department, SCMS School of Engineering and Technology, Karukutty, Kerala, India, minitom@scmsgroup.org

³Assistant Professor, Mathematics Department, Mar Athanasius College, Kothamangalam, Kerala, India, binosebastianv@gmail.com

⁴Associate Professor, Mathematics Department, Nirmala College, Muvattupuzha, Kerala, India, kvtbmc@gmail.com

Abstract. A new framework of soft mathematical morphology on hypergraph spaces is studied. Application in image processing for filtering objects defined in hypergraph spaces are illustrated using several soft morphological operators- openings, closings, granulometries and ASF acting (a) on the subset of vertex and hyperedge set of a hypergraph and (b) on the subhypergraphs of a hypergraph. Experimental results dealing with the extension of soft morphological operators to gray scale images are presented in this paper. The results obtained are promising and is a better substitute for the prevailing methods.

1. Introduction and Related Works

Mathematical morphology is an emerging area of image processing. In the area where image processing can be applied, mathematical morphology have provided solutions to different tasks. Soft mathematical morphology is another approach to mathematical morphology that was introduced by Koskinen et al. [1]. In this method, weighted order statistics are used instead of minima and maxima [3]. Soft morphological operators show better performance than primitive morphological operators as they are less sensitive to additive noise and to small variations in object shape [4]. Soft mathematical morphology have also been extended to fuzzy sets [3].

Morphological operators can be defined on graphs and hypergraphs. In this paper a new context is introduced that lengthens the perceptions of soft morphological filters into hypergraphs. This work is an extension of our preliminary work [2].

2. Preliminaries

In this section, we see some important definitions and properties that will be needed in the sequel.

2.1. Soft mathematical morphology using hypergraphs [2]

Hypergraph [5], [6] is defined as a pair $H = (H^*, H^X)$, where H^* is a set of points called vertices and H^X is a family of subsets of H^* called hyperedges ie; $H^X = (e_i), i \in I$ where I is a finite set of indices. The sets H^* ,



H^X and H^\bullet are the subsets of H , subsets of H^X and subhypergraphs of H respectively. Here H^X and H^\bullet are Boolean lattices. The set H of all sub hypergraphs of H forms a complete lattice [5], [6]. Morphological operators are defined on these lattices. In soft mathematical morphology, the structural element is divided into two subsets- the core and the soft boundary. In the development of the final output, weightage of core is more than the soft boundary. Hence we subdivide the hyperedges (along with the vertices belonging to it) into core B_1 and soft boundary B_2 .

2.1.1. Definition 1 [2]

The operators $\delta^\bullet, \epsilon^\bullet$ are defined from H^X into H^\bullet and the operators δ^X, ϵ^X are defined from H^\bullet into H^X as follows: For any $X^\bullet \subseteq H^\bullet$ and $X^X \subseteq H^X$, where $X^X = e_i \cup e_i^*$; $e_i \in B_1$ and $e_i^* \in B_2$, $i \in J$ such that $J \subseteq I$,

$$\delta^\bullet: H^X \rightarrow H^\bullet \text{ is defined as } \delta^\bullet(X^X) = k^{th} \text{ largest of } [\cup_{j \in J} \{k \diamond v(e_j), v(e_j^*)\}; e_j \in B_1, e_j^* \in B_2]$$

$$\epsilon^X: H^\bullet \rightarrow H^X \text{ is defined as } \epsilon^X(X^\bullet) = k^{th} \text{ smallest of } \{k \diamond e_i, e_i^*, i \in I \mid v(e_i), v(e_i^*) \subseteq X^\bullet, e_i \in B_1, e_i^* \in B_2\}$$

$$\epsilon^\bullet: H^X \rightarrow H^\bullet \text{ is defined as } \epsilon^\bullet(X^X) = k^{th} \text{ smallest of } [\cap_{j \notin J} \{k \diamond \overline{v(e_j)}, \overline{v(e_j^*)}\}; e_j \in B_1, e_j^* \in B_2]$$

$$\delta^X: H^\bullet \rightarrow H^X \text{ is defined as } \delta^X(X^\bullet) = k^{th} \text{ largest of } \{k \diamond e_i, e_i^*, i \in I \mid v(e_i) \cap X^\bullet \neq \emptyset \text{ and } v(e_i^*) \cap X^\bullet \neq \emptyset; e_i \in B_1, e_i^* \in B_2\}.$$

Here, $k \diamond x$ is read as x is repeated k times. Vertex soft dilation (δ) and vertex soft erosion (ϵ) that act on H^\bullet , also hyper edge soft erosion (ϵ), hyper edge soft dilation (Δ) that act on H^X are defined as follows: The operators δ and ϵ that act on H^\bullet are defined by $\delta = \delta^\bullet \circ \delta^X$ and $\epsilon = \epsilon^\bullet \circ \epsilon^X$ and the operators Δ and ϵ that act on H^X are defined by $\Delta = \delta^X \circ \delta^\bullet$ and $\epsilon = \epsilon^X \circ \epsilon^\bullet$. Furthermore the operators $[\delta, \Delta]$ and $[\epsilon, \epsilon]$ are defined as

$$[\delta, \Delta](X) = (\delta(X^\bullet), \Delta(X^X)) \text{ and } [\epsilon, \epsilon](X) = (\epsilon(X^\bullet), \epsilon(X^X)) \text{ for any } X \in H.$$

These operators are called the soft dilation and soft erosion acting on the lattice (H, \subseteq)

3. Property

- Operators ϵ^X and δ^\bullet are dual of each other. Similar duality concept hold for ϵ^\bullet and δ^X .
- $(\epsilon^X, \delta^\bullet)$ and $(\epsilon^\bullet, \delta^X)$ are adjunctions.
- δ^\bullet and δ^X are soft dilations.
- ϵ^\bullet and ϵ^X are soft erosions.

Proof (a): This property is proved in [2].

(b): Let $X^X \subseteq \epsilon^X(Y^\bullet)$. Then,

$$\begin{aligned} x \in \delta^\bullet(X^X) &\Rightarrow x \in k^{th} \text{ largest of } [\cup_{j \in J} \{k \diamond v(e_j), v(e_j^*)\}] \\ &\Rightarrow x \in v(e_j), x \in v(e_j^*) \text{ for some } j \in J \\ &\Rightarrow \exists e \in X^X \text{ such that } x \in v(e) \\ &\Rightarrow e \in \epsilon^X(Y^\bullet) \quad \{\text{Since } X^X \subseteq \epsilon^X(Y^\bullet)\} \\ &\Rightarrow e \in k^{th} \text{ smallest of } \{k \diamond e_i, e_i^*, i \in I \mid v(e_i), v(e_i^*) \subseteq Y^\bullet\} \\ &\Rightarrow v(e) \subseteq Y^\bullet \\ &\Rightarrow x \in Y^\bullet \quad \{\text{Since } x \in v(e)\} \end{aligned}$$

Thus, $\delta^\bullet(X^X) \subseteq Y^\bullet$.

Conversely, if $\delta^\bullet(X^X) \subseteq Y^\bullet$.

$$\begin{aligned} \text{Then, } e \in X^X &\Rightarrow v(e) \subseteq \delta^*(X^X) \\ &\Rightarrow v(e) \subseteq Y^* && \{\text{Since } \delta^*(X^X) \subseteq Y^*\} \\ &\Rightarrow e \in \in^X(Y^*) \end{aligned}$$

Therefore, $X^X \subseteq \in^X(Y^*)$.

Hence, (\in^X, δ^*) is an adjunction.

In a similar manner, (\in^*, δ^X) is an adjunction can be proved using the information that operators \in^X and δ^X are dual of each other, also \in^* and δ^* are dual of each other and (\in^X, δ^*) is an adjunction. Properties (c) and (d) follows directly using property (b).

4. Soft morphological filters

A morphological filter [5], [8] is an operator α acting on a lattice \mathcal{L} , which is increasing and idempotent. If (α, β) is an adjunction [5], [8] then α is an erosion, β is a dilation. Also, $\beta \circ \alpha$ is called an opening and $\alpha \circ \beta$ is called a closing on \mathcal{L} . Opening and closing are two commonly used filters.

4.1. Definition 2

- Soft opening $\gamma_1 = \delta \circ \varepsilon$ and closing $\Phi_1 = \varepsilon \circ \delta$.
- Soft half opening $\gamma_{1/2} = \delta^* \circ \in^X$ and half closing $\Phi_{1/2} = \in^* \circ \delta^X$.

5. Soft flat morphological Operators on weighted hypergraphs

In real phase, gray-scale soft morphological operations are difficult to work with. Threshold decomposition and stacking principle can be successfully applied on gray-scale soft morphological operations. This property allows the gray scale signals to be decomposed into binary signals and the results so obtained by processing are combined to obtain the desired gray-scale output [7]. By threshold decomposition, [8] the lattice of all subhypergraphs of H induces a lattice $\text{Fun}(H^*) \otimes \text{Fun}(H^X)$ of pairs of functions weighting respectively the vertices and the hyperedges of H such that the simultaneous threshold of these two functions at any given level produces a subhypergraph of H and the properties for hypergraph operators on the lattices H^* , H^X , or H also hold for operators on the lattices $\text{Fun}(H^*)$, $\text{Fun}(H^X)$ and $\text{Fun}(H^*) \otimes \text{Fun}(H^X)$. Thus we can define a set of soft operators which are stack analogues to the soft operators \in^X, δ^*, \in^* and δ^X defined in [2].

5.1. Definition 3.

Let $F^* \in \text{Fun}(H^*)$ and let $F^X \in \text{Fun}(H^X)$, we define

$$\begin{aligned} \delta^*(F^X)(x) &= k^{th} \text{ largest of } \{k \diamond F^X(e_i), F^X(e_i^*) \mid e_i \in B_1, e_i^* \in B_2, B_1 \cup B_2 = H^X\} \forall x \in H^* \\ \in^X(F^*)(e) &= k^{th} \text{ smallest of } \{k \diamond F^*(x), F^*(x) \mid x \in v(e), e \in B_1 \cup B_2\} \\ \in^*(F^X)(x) &= k^{th} \text{ smallest of } \{k \diamond F^X(e_i), F^X(e_i^*) \mid e_i \in B_1, e_i^* \in B_2, B_1 \cup B_2 = H^X\} \forall x \in H^* \\ \delta^X(F^*)(e) &= k^{th} \text{ smallest of } \{k \diamond F^*(x), F^*(x) \mid x \in v(e), e \in B_1 \cup B_2\}. \end{aligned}$$

By using soft flat morphology, it is possible to work with gray scale soft dilation, erosion, opening, closing, granulometries and Alternating Sequential Filters.

6. Experimental Result

To represent the hyperedges we use 4-uniform hypergraph illustrated in Figure 1. A hyperedge together with the 4 vertices belonging to it is taken as core, remaining vertices and hyperedges are taken as soft boundary. Using this simple hypergraph structure, experimental result for $k=1$ and $k=2$ are tabulated. Dilated and eroded gray scale image results are obtained to get the soft flat morphological operators defined in the previous section. Composition of these operators generates alternating sequential filters(ASF) which

are capable of removing noise effectively from binary and gray scale images. Figure 2 represent the gray scale image taken for the experimental purpose. The noisy image obtained by adding 5% salt and pepper noise is shown in figure 3. PSNR of noised image with original image is 17.24. Figure 4 and figure 5 shows the noise removed images obtained by applying alternating sequential filters (ASF) $\gamma_1 \circ \Phi_1$ and $\gamma_{1/2} \circ \Phi_{1/2}$ for $k=1$. The resultant PSNR of the noised removed images with the original image are respectively 40.53 and 40.23. Similarly figure 6 and figure 7 shows the results obtained after applying $\gamma_1 \circ \Phi_1$ and $\gamma_{1/2} \circ \Phi_{1/2}$ for $k=2$. In this case, the resultant PSNR of the noised removed images with the original image are 39.79 and 41.82 respectively. Experiment results depicts that $\gamma_{1/2} \circ \Phi_{1/2}$ for $k=2$ is giving better approximations than $\gamma_1 \circ \Phi_1$ and $\gamma_{1/2} \circ \Phi_{1/2}$ for $k=1$.

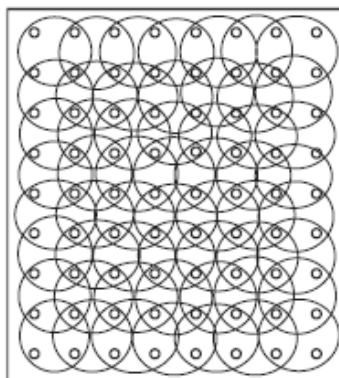

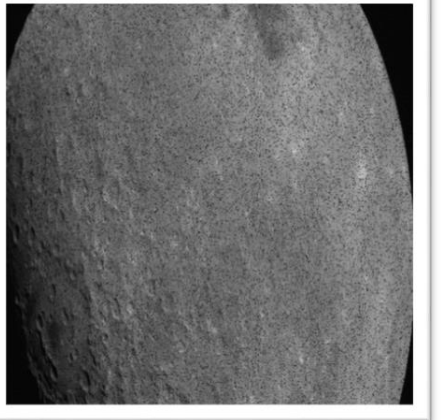






Figure 1 Four Uniform Hypergraph structure used to represent an image

PSNR of noised image with original image : 17.24	
	
Figure 2. Original Image	Figure 3. Noised Image (Added Noise 5%)

Noise Removed Images using Alternating Sequential Filters	
For K =1	
	
Figure 4. $\gamma_1 \circ \Phi_1$ PSNR = 40.53	Figure 5. $\gamma_{1/2} \circ \Phi_{1/2}$ PSNR = 40.23

Noise Removed Images using Alternating Sequential Filters	
For K = 2	
	
Figure 6. $\gamma_1 \circ \Phi_1$ PSNR = 39.79	Figure 7. $\gamma_{1/2} \circ \Phi_{1/2}$ PSNR = 41.82

7. Conclusion

The aim of this work is to recognize the prospects of using soft morphological operators under the framework of hypergraph. In our study a four uniform hypergraph structure was taken. It was then separated into core and soft boundary. But, it's a well-known fact that 3-uniform hypergraph structure gives good result for binary, gray scale and colour image filtering applications [8]. So by the choice of different hypergraph structures along with the suitable choice of core and soft boundary, results of the above method can be improved for different and bigger values of k. The initial results are promising and future work is to be done in this regard using different hypergraph structures.

References

- [1] Koskinen L, Astola J and Neuvo Y 1991 Soft morphological filters *Proc. SPIE- Int. Soc. Opt. Eng.* 262-70.
- [2] Unnikrishnan M Nuja, Sebastian V Bino and Thomas K V 2019 Soft Morphological Operators on Fuzzy Hypergraphs *Mathematical Science International Research Journal (MSIRJ)* 8 Iss.2 72-78.
- [3] Gasteratos A, Andreadis I and Ph. Tsalides 1998 Fuzzy soft mathematical morphology *IEE Proc.-Vis. Image Signal Processing.* 145 41-49.
- [4] Kuosmanen P and Astola J 1995 Soft morphological filtering *J.Math. Imag. Vis.* 5 231-62.
- [5] Sebastian V Bino, Unnikrishnan A, Balakrishnan K and Ramkumar P B 2017 Morphological filtering on hypergraphs *Discrete Applied Mathematics Elsevier* 307-20.
- [6] Sebastian V Bino, Unnikrishnan A, Balakrishnan K, and Ramkumar P B 2014 Mathematical morphology on hypergraphs using vertex-hyperedge correspondence *ISRN Discrete Mathematics.*
- [7] Shih F Y and Mitchell O K 1989 Threshold decomposition of gray-scale morphology into binary morphology *IEEE Trans. Pattern Anal. Mach. Intell.* 11 Iss.1 31-42.
- [8] Sebastian V Bino, Unnikrishnan M Nuja, Sebastian Neenu and Paul Rosebell 2020 Morphological operators on hypergraphs for colour image processing *Advanced Computing and Communication Technologies for High Performance Applications(ACCTHPA)* *IEEE Xplore* 217-20.



RESEARCH ARTICLE

Vol. 7. Issue.1. 2020 (Jan-Mar)

ISSN INTERNATIONAL
STANDARD
SERIAL
NUMBER
INDIA
2395-2628(Print):2349-9451(online)

A STUDY ON WOMEN EDUCATION: EDUCATE AND EMPOWER

DIVYA MS

Assistant Professor, English Department, SCMS School of Engineering and Technology, Ernakulam

Email: divya718@gmail.com



Article information

Received:27/02/2020

Accepted: 15/03/2020

Published online: 21/03/2020

doi: [10.33329/ijelr.7.1.179](https://doi.org/10.33329/ijelr.7.1.179)

ABSTRACT

Education is the key to women's empowerment. When education gets denied there isn't much to happen in her life. As usual she gets married and have children at a young age, work in unpaid or low-paying jobs, and rely on economic support from their husband or family. Without education, their future and their family's future gets limited. According to the Malala Fund, there are over 130 million girls worldwide who are not in school. Has anyone thought about them or their future? There might be an unpolished gem among them. Studies have found that if every girl completes 12 years of education, child marriage would drop by 64% and health complications from early pregnancy, like early births and child deaths, would drop by 59% and 49%, respectively. Educating women and girls also improve the economic status of a nation, which will reduce the risk of war and terrorism and can be a better harbinger of future. There are still many barriers preventing girls and women to pursue and complete their education like fees, distance or lack of transportation, being forced to work and provide for their families, being forced to marry and have children, or conflict in their hometown or country. The most difficult obstacle is the mentality of the family towards a girl child. They are denied education only because she is born as a girl. The United Nations found that as girls reach secondary school, their enrolment rates decline significantly. Only 39% of the countries have equal proportions of boys and girls enrolled in secondary education. In developing countries, 35% to 85% of girls are forced to stay at home from school to take care of their younger siblings and to manage the house while their brothers are provided with higher education. To reach the competition level and to expand their professional opportunities, women need the same experiences and skills, making post-secondary education an essential part of women's empowerment. Higher education instils them with the knowledge, competence and experience that are necessary to get involved in government, business, or even in a civil society. With higher education, women and girls have better access to health information and other beneficial services which in turn will only help the family or generation to grow and develop. We need more and more sheers to be the torch bearers of future.

Key words: Empowerment, Post-secondary education, Shero, Professional opportunities

“You educate a man; You educate a man.

You educate a woman; You educate a generation”-Brigham Young

We are living in a highly competitive world where survival is the only mantra to be focused. Such a fast growing world hardly differentiates between men and women. Education is the only key factor that brought towards such a change. Even when women have access to education, there can be many other factors that can make it difficult for her to take full advantage of those opportunities. It's women who still carries the cultural burden of being the primary homemakers and caregivers. This unpaid “second shift” means that they have less time and energy to dedicate to their studies. Family responsibilities doesn't become burden for them but that is the prime factor that is delimiting them from their higher education or carrier growth. When women become the sole providers for their families, they need to fulfil it with many other factors like being victims of domestic violence, threats like financial and from profession which becomes much more difficult for them to handle. The immense pressure that she is handling becomes worthless when it is labelled under the synonym ‘mother’ or ‘wife’. Today's era has witnessed a lot of change when it comes to single girl child nuclear family. Deciding voices are only that of their parents. Thus providing wings for them to fly high and capture their aim. Their dreams can't be in fetters and who knows there might be an unpolished gem that is being soiled. Women in India have been treated with utmost respect and dignity since time immemorial. For a nation to advance, empowering women is crucial. India was blessed with visionary women who broke the fetters of gender norms in every sector. Its long back we heard about the denial of education to women. A girl child was considered curse than a boon. Never to live in a world where mothers and sisters are dragged out of their homes and raped. Wherein she becomes both the victim and accused and its said by “them”, it's all because of her “out of the box” attitude that caused her this. Is this the caring that we need to give to our sisters, rather than rending a helping hand? We can't even skim through the news heads that is going on these days. What if such an accusation comes out, it needs to face a frequent trail from the social medias and channels who will make them even worse? Is the only solution, to remain silent and bear the tragic effects or to have a prolonged grudge and to end up in depression throughout the life? It's an open ended question towards the secularist nation. Here I would like to quote the famous wording of Michelle Obama,

“When girls are educated, their countries become stronger and more prosperous”

Let the nation realize her power of golden touch. She is to succeed where ever she goes, don't curtail her from her doing what is right. Listen to her inner voice that itself will keep the nation going. We do respect our mothers and all woman is an incarnation of her, our mother Earth. Its only she who can protect, provide, love, sacrifice selflessly. Split of the moment can we see her incarnations of a loving Sita, ready to sacrifice everything for her love and family, Durga the fearest of all who battle against evil for good. For us this is our mother, both deities in one, who loves and cares us with one hand and get furious with another. Still we love her and keep no grudges. Then how can we ever think of harming her. Where has our brains and minds gone, ready to stab the same womb from where we came? Is this what we call progression? Are we the real citizens bearing torches for a future developing nation? How can we sustain by spiting on our own veins? When will all these quires be dissolved? The only solution for all this is only education, it opens the eyes to a new world of realities and hopes for a better nation. It's clearly evident that the only means to attain empowerment is through education. Change should begin from her and its only she who can bring changes. Here I would like to cite the story of Rani Padmini a legendary 13th – 14th century Queen (Rani) of the Mewar kingdom of present day India. She was the wife of King Ratan Sen, captured and imprisoned by Delhi's sultan Alauddin Khalji. Alauddin Khalji became enamoured with Padmavati's beauty and decided to siege Chittor to obtain Padmavati. Before Chittor was captured they had to face defeat against Khalji, she and her companions committed Jauhar (self-immolation) thereby defeating Khalji's aim and protecting their honour. Coupled to the *Jauhar*, the Rajput men died fighting on the battlefield. Throughout the novel *Padmini: The Spirited Queen of Chittoor*, Mridula Behari tried to explain the immense beauty and knowledge that Padmavati possessed. It's only because of her education and knowledge, she had the courage to face such a situation where her husband the Rana itself was helpless. She was bold enough to convince everyone and to equip them for a war against the evils. There are many instances in the novel where we find her indulged in reading the ancient scriptures and getting mesmerised by that. It's the education that

brought her into a new world where she understands that action speaks more than words. There is always an urge for action than mere talks, that won't lead you anywhere. Education delimits the boundaries of caste, creed, gender, finance and what not. How true it is to quote Malala Yousafzai's wordings here,

"If one man can destroy everything, why can't one girl change it?"

As Prime Minister Narendra Modi said on the launch of the expanded 'Beti Bachao Beti Padhao' (March 8, 2018): "Daughters are not a burden but the pride of the whole family. We realise the power of our daughters when we see a woman fighter pilot. The country feels proud whenever our daughters bag gold medals, or for that matter any medal, in the Olympics." This is the time only when we think oh! are they capable of bagging a gold and that too for the nation? When they come to lime light we find applauds and cheering from all over the nation. But have ever we imagined the trials or pains that they have gone through to achieve that? Same is the case with the other gender, but they are always on safe side of the scrutiny eyes of the society. It's a boy, no matter if he is alone or late to home or traveling late or alone. The world is always open to him than to her. We need more Sheros to be an inspiration and to motivate others to come out from their shells that is encircling them towards darkness. Engaged in a combat to the march for equality with our sisters and mothers, let us understand the theme of Women's Day: "An Equal world is an enabled world: realizing women's power." After the adoption of the Beijing Agenda for Action, UN has set the year 2020 as a key year for assessing international progress towards achieving gender equality and human rights for all women and girls. The Ministry of Human Resource Development (MHRD) has much triggered up their progression under the leadership of PM Modi in providing equal opportunities. It is with immense happiness we can say that due to the Swachh Bharat Mission, 14,67,679 schools now have a functioning girl's toilet, an increase of 4.17 percentage points in comparison to 2013-14. The impact of the mission has resulted in an increase in enrolment of girls by 25 percentage points in 2018-19 from 2013-14. These figures get dimmed in a society which is indulging much more in a political game for their sustenance. We living in the safe shelters haven't ever thought about our sisters who is being victimized and marginalized. Minister of Finance Nirmala Sitharaman applauded the performance of Beti Bachao Beti Padhao in her speech on the budget: "Gross enrolment ratio of girls across all levels of education is now higher than boys. At the elementary level it is 94.32 per cent as against 89.28 per cent for boys, at the secondary level it is 81.32 per cent as compared to 78 per cent and at the higher secondary level girls have achieved a level of 59.7 per cent compared to only 57.54 per cent." The MHRD has approved 5,930 Kasturba Gandhi Balika Vidyalayas, which are girls' residential schools and have an enrolment of 6,18 lakh students, to increase equality of access and opportunity for girls. The National Incentive Scheme for Girls for Secondary Education has approved an incentive sum of Rs 8,56 crore for the 28,547 beneficiaries. According to the scheme Rs 3,000 is being deposited under the age of 16 in the name of deserving unmarried girls and entitles them to withdraw it along with interest in reaching 18 years of age and passing Class X. Besides an improvement in the girl's gross enrolment rate in schools, the educational outcomes and accomplishments have also improved.

Let's go ahead with this initiative for our sisters than to get involved in the cheap political drama that is being happening in our nation. There is considerable evidence that women's education and literacy tend to reduce the mortality rates of children. It's indeed true what Malala Yousafzai pointed out:

"We realize the importance of our voice only when we are silenced"

In accordance with the celebration of India's success in improving gender equality in the education system, much greater and collective efforts are needed to achieve the Sustainable Development Goal of eliminating gender disparities in education and ensure equal access to all levels of education and vocational training for the vulnerable, including persons with disabilities, indigenous peoples and children in vulnerable situations. History of Indian women is full of pioneers, who broke gender barriers and worked hard for their rights and made advances in politics, arts, science, law, etc. Let us cite few examples of our pioneers who made us think beyond Anandibai Gopalrao Joshi, who became the first Indian female physician in the year 1887. She was also the first Indian woman who get training in Western medicine and the first woman to travel to the United States of America. Arunima Sinha, is the first female amputee to climb Mount Everest. She is also the first Indian amputee to climb the Everest. She was a national level volleyball player who in 2011 was pushed by

robbers from a running train as she defied them. After meeting this accident, one of her legs was amputated below the knee. Arati Saha became the first Indian and Asian woman to swim across English Channel in the year 1959. She also became the first female sportsperson awarded with Padma Shri in 1960. Mother Teresa founded many Missionaries of Charity, a Roman Catholic religious congregation, giving her life to social work. Indira Gandhi became the first woman Prime Minister of India and served from 1966 to 1977. Indira Gandhi renowned as the "Woman of the Millennium" in a poll which was organised by BBC in 1999. In 1971, she became the first woman to receive the Bharat Ratna award. Justice M. Fathima Beevi became the first female judge to be appointed in the Supreme Court of India in the year 1989. In her autobiography she had said about the immense suffering that she had faced to reach such a highest peak. Her father was the only person who supported her thorough out her journey. Kalpana Chawla, the first Indian woman who reached in space. As a mission specialist and a primary robotic arm operator, she went into space in 1997.

We can move to our present Sheros starting with Mithali Raj, the first woman to score a double hundred in Test Cricket against New Zealand at Wellington, 2004. She was the first to achieve this landmark in the world. Pratibha Patil became the first woman President of India and held office from July 2007 to July 2012. Kiran Bedi, joining Indian Police Service (IPS) in 1972, she became the first woman officer in India. Moreover, later in 2003, Kiran Bedi also became the first woman to be appointed as the United Nations Civil Police adviser. Anjali Gupta is the first female flying officer in the Indian Air Force to be court martialled. She used to work for the Aircraft Systems and Testing Establishment unit in Bangalore. Anjali completed her Masters of Philosophy in Sociology from the Delhi University and was first posted at Belgaum in 2001. Sania Mirza, a professional tennis player, became the first ever Indian woman to win the Women's Tennis Association (WTA) title in 2005. Later in 2015, Sania Mirza became the first Indian woman titled as rank number one in WTA's double rankings. Saina Nehwal became the first Indian women to win a medal in Badminton at 2012 Olympic Games. Later in 2015, she became the first Indian woman to secure no. 1 position in world rankings. Mary Kom, is the only woman boxer who has won a medal in each of the six World Championships. She was the only Indian woman boxer who qualified for the 2012 Olympics and became the first Indian woman boxer to win a gold medal in Asian Games in 2014. Cited just a few but more hands of achievements are behind which are yet to be recognised and appreciated. They have set a model for us to think and act beyond.

Our government has also taken much initiative for protecting the rights of education for girls. India Post or Department of Posts, the postal system of the country, offers several savings schemes with different interest rates. The **Sukanya Samriddhi Yojana**, one such savings scheme offered by India Post, is a deposit scheme for the girl child that can be opened in any of the leading banks and post offices across the country. In such schemes the child is getting the benefit for future education and for her marriage or future life. There is a platform called WE, that is an empowerment program through which woman are trained to form self-organized and self-managed savings groups, each consisting of 15-25 members. Their aim is to develop individual empowerment and increase their access to financial resources which is the prime element for eradicating poverty. All the members meet weekly to make decisions and interact in life-skills training, discuss various issues of mutual interest. They not only give a platform for awareness but also make an effort to join together and take action to improve their lives and communities. We too need to make more and more efforts than *ME TOO* to raise our voice against the inhuman oppression and injustices that is happening worldwide. Amendments to laws are must as Judiciary is the ultimate power which we believe and rely on. For a common man judiciary is the only hope or last and final resort. We all need to respect our law than fearing it. If the administrators of law are more channelized and less corrupted, we don't have to wait for justice. It's absolutely true to say the famous phrase "Justice delayed is justice denied". Let us be the harbingers of a brighter future that initiates the slogan justice and tranquility. Let the coming era witness a world devoid of corruption, discrimination, poverty, illiteracy.

"Empower yourselves with a good education, then get out there and use that education to build a country worthy of your boundless promise"

-Michelle Obama

Bibliography

“Women empowerment”. Indian Express article. <https://indianexpress.com/article/opinion/columns/beti-bachao-beti-padhao/article/6297784>.

“First Indian Women”. India Today. <https://www.indiatoday.in/education-today/gk-current-affairs/story/the-first-indian-women-312243-2016-03-08>

“One Health and Disease: Tick-Borne.” *National Park Service*, U.S. Department of the interior, <https://www.nps.gov/articles/one-health-disease-ticks-borne.htm>.

Behari, Mridula . <https://www.amazon.in/Padmini-Spirited-Chittor-Mridula-Behari-ebook/dp/B0774NH95V>

Behari, Mridula. *Padmini: The Spirited Queen of Chittor*: Penguin publishers, 2017.

Received May 10, 2020, accepted May 22, 2020, date of publication May 26, 2020, date of current version June 9, 2020.

Digital Object Identifier 10.1109/ACCESS.2020.2997727

An Adaptive and Flexible Brain Energized Full Body Exoskeleton With IoT Edge for Assisting the Paralyzed Patients

SUNIL JACOB^{1,2}, (Member, IEEE), MUKIL ALAGIRISAMY³,
VARUN G. MENON⁴, (Senior Member, IEEE), B. MANOJ KUMAR⁵, N. Z. JHANJHI⁶,
VASAKI PONNUSAMY⁷, P. G. SHYNU⁸, AND VENKI BALASUBRAMANIAN^{9,10}, (Member, IEEE)

¹Department of Electronics and Communication Engineering, Lincoln University College, Petaling Jaya 47301, Malaysia

²Department of Electronics and Communication Engineering, SCMS School of Engineering and Technology, Ernakulam 683576, India

³Department of Electrical and Electronics and Engineering, Lincoln University College, Petaling Jaya 47301, Malaysia

⁴Department of Computer Science and Engineering, SCMS School of Engineering and Technology, Ernakulam 683576, India

⁵Department of Automobile Engineering, SCMS School of Engineering and Technology, Ernakulam 683576, India

⁶School of Computer Science and Engineering, Taylor's University, Subang Jaya 47500, Malaysia

⁷Faculty of Information and Communication Technology, Universiti Tunku Abdul Rahman, Kampar 31900, Malaysia

⁸School of Information Technology and Engineering, Vellore Institute of Technology, Vellore 632014, India

⁹School of Science, Engineering and Information Technology, Federation University, Mount Helen, VIC 3350, Australia

¹⁰Anidra Tech Ventures Pvt Ltd., Wyndham Vale, VIC 3024, Australia

Corresponding authors: Sunil Jacob (sunil@scmsgroup.org) and Vasaki Ponnusamy (vasaki@utar.edu.my)

This work was supported in part by the Institute of Electrical and Electronics Engineers (IEEE) EPICS, USA, under Grant 2016-12.

ABSTRACT The paralyzed population is increasing worldwide due to stroke, spinal cord injury, post-polio, and other related diseases. Different assistive technologies are used to improve the physical and mental health of the affected patients. Exoskeletons have emerged as one of the most promising technology to provide movement and rehabilitation for the paralyzed. But exoskeletons are limited by the constraints of weight, flexibility, and adaptability. To resolve these issues, we propose an adaptive and flexible Brain Energized Full Body Exoskeleton (BFBE) for assisting the paralyzed people. This paper describes the design, control, and testing of BFBE with 15 degrees of freedom (DoF) for assisting the users in their daily activities. The flexibility is incorporated into the system by a modular design approach. The brain signals captured by the Electroencephalogram (EEG) sensors are used for controlling the movements of BFBE. The processing happens at the edge, reducing delay in decision making and the system is further integrated with an IoT module that helps to send an alert message to multiple caregivers in case of an emergency. The potential energy harvesting is used in the system to solve the power issues related to the exoskeleton. The stability in the gait cycle is ensured by using adaptive sensory feedback. The system validation is done by using six natural movements on ten different paralyzed persons. The system recognizes human intentions with an accuracy of 85%. The result shows that BFBE can be an efficient method for providing assistance and rehabilitation for paralyzed patients.

INDEX TERMS Artificial intelligence, assistive technologies, brain-computer interface, edge computing, Internet of Things (IoT), rehabilitation.

I. INTRODUCTION

A recent survey carried out by Toyota Foundations revealed that 30% of the paralyzed population is disappointed with the assistive devices in the market. The outdated design of assistive devices is causing constant pain and frustration. Survey participants also recommended that future assistive

The associate editor coordinating the review of this manuscript and approving it for publication was Zhenyu Zhou¹⁰.

devices should be easy to handle and help in daily activities. The respondents also indicated that the design should be natural, like an extension of their body, providing them freedom and independence [1], [2]. Currently, exoskeletons are the most popular solution used in rehabilitation and assistance of the paralyzed people [3]–[8]. Numerous types of exoskeletons are designed for purposes ranging from rehabilitation and assistance to transportation and handling heavy load in industries.

In rehabilitation, the exoskeletons are used to work in parallel with the human legs and carry out the desired actions with ease. These devices are specifically designed to treat disabilities of patients in a clinical setting. The rehabilitation exoskeleton helps paralyzed patients to engage with real-world things and to monitor the movement of body parts. Exoskeletons are also designed for healthy subjects, enabling them to interact with a virtual environment [9]. As healthy people use these haptic exoskeletons, ease of wearability is not a major issue, but portability and efficient finger tracking are highly required. In recent times, to assist children having cerebral palsy disorders, exoskeletons have been designed [10]. The architecture of the control unit, the mechanical system, and feature extraction is discussed in detail. In [11], a wearable hip assist robot is discussed, which is used to improve the gait function and reduce muscle effort and metabolic activities. The device can reduce knee and ankle muscle activity along with a decrease in hip movements. The robot can stabilize the trunk during walking in adults. But the system has not investigated the effectiveness of gait rehabilitation.

In [12], the translation of gait without using crutches gait in a biped robot is demonstrated. The mathematical hybrid model analysis is carried out to find different gait and walking speeds. The walking gaits are stabilized using a centralized controller. A knee exoskeleton that can be used for sit to stand assistance is discussed in [13]. Here, the torque control is improved using a unique transmission configuration, also with reduced output impedance. Design specifications of the current lower limb exoskeletons are reviewed, and the human biomechanical consideration in lower limb design is analyzed in [14]. The classification and design challenges in the field of Exoskeleton and Orthoses are discussed in [15]. In [16], the classification of exoskeletons into the palm, upper limb, and lower limb exoskeleton is discussed. Further, the paper discusses various exoskeletons proposed for rehabilitation and enhancement purposes. The paper also puts forward the concept of developing a full-body exoskeleton.

In [17], a wearable full-body exoskeleton is designed for a mobile cyber-physical system. Here, the design of a new technique for identifying the gate phase is also discussed. Energy harvesting using human's daily actions is proposed to charge the battery of exoskeleton in [18]. Conventional and alternative methods for providing power to exoskeletons are discussed. A systematic review of various types of exoskeletons for using with the lower limb in neurorehabilitation is presented in [19]. In [20], an exoskeleton to aid patient rehabilitation with postural equilibrium is designed. Multi-variable robust control with the patient's Electro Myographical (EMG) signals is utilized to achieve equilibrium. Berkeley Lower Limb Exoskeleton (BLEEX) [21] is designed to transfer load and body weight into the ground, which reduces the metabolic cost of the wearer. This parallel exoskeleton is able to enhance the endurance of the user. The exoskeleton, which augments the torque and power of the user during lifting and daily activities, is discussed.

Software-Defined Network (SDN) assisted solutions with exoskeletons for use in rehabilitation are also proposed recently [22]. The majority of the existing exoskeletons have weight, flexibility, and adaptability constraints. Easy wearability and portability are other significant limitations experienced by current assistive exoskeleton-based solutions for rehabilitation [23]–[25].

To overcome the current issues existing with exoskeletons, we propose an adaptive and flexible Brain Energized Full Body Exoskeleton (BFBE) for assisting the paralyzed people. In the BFBE system, the brain signals captured by the EEG sensors are used for controlling the movements of the exoskeleton. The flexibility is incorporated into the system by a modular design approach. The BFBE system has a BCI module, a Control Unit (CU), and a Body-Part Actuation Module (BAM). BCI module captures the brain signal and transforms it into a signal that can be used by the CU. The processing happens at the edge, thus reducing delay in decision making, and the system is further integrated with an IoT module that helps to send an alert message to multiple caregivers in case of an emergency. The system is non-invasive, and the fabricated EEG sensor is used to collect the signals from the scalp. An instrumentation amplifier is used to enhance the strength of the obtained signals. The output signal from the amplifier is subjected to filtering and pre-processing. The signals are generated for different basic human actions (sitting, standing, sleeping) and then after the pre-processing is stored in a database. When the paralyzed person has an intention to make a particular movement, the microcontroller in the CU uses this database and produces the signal for activating the particular body part. The generated EEG pattern of the person is mapped into the corresponding action. The BAM then uses the motor driver circuit to pass the activation signal to the corresponding part of the body. The potential energy harvesting is used in the system to solve the power issues related to the exoskeleton. The stability in the gait cycle is ensured by using adaptive sensory feed-back.

The paper is arranged into 4 sections. The proposed work is discussed in Section 2. The system architecture is discussed initially, and then the theoretical analysis is presented. Section 3 presents and discusses the system working and testing details and the results obtained. Finally, the paper concludes in section 4. The list of abbreviations is listed in table 1.

II. PROPOSED SYSTEM

A. SYSTEM ARCHITECTURE

The architecture of the Brain Energized Full Body Exoskeleton (BFBE) system is shown in Figure 1. The BFBE system has three major modules 1) BCI module, 2) Control Unit, and 3) Body-Part Actuation Module. The primary function of the BCI module is to collect the EEG signals from the scalp and then convert it into a form that can be used by the CU. We have fabricated a sixteen-electrode based EEG sensor, which is used in the proposed system for collecting the signals and also for analyzing the brain activity. For removing the

TABLE 1. List of abbreviations.

Abbreviation	Description
BFBE	Brain Energized Full Body Exoskeleton
DoF	Degrees of Freedom
EEG	Electroencephalogram
EMG	Electro Myographical
BLEEX	Berkeley Lower Limb Exoskeleton
SDN	Software-Defined Network
CU	Control Unit
BAM	Body-Part Actuation Module
IoT	Internet of Things
BCI	Brain Computer Interface
WHT	Walsh Hadamard Transform

TABLE 2. Body parts of BFBE and its corresponding joints.

Different modules of the exoskeleton	Joints used to control the movements
Lower limb (Left & Right)	Knee Joint Left, Foot Joint Left, Knee Joint Right, Foot Joint Right
Upper limb (Left & Right)	Elbow Joint Right, Elbow Joint Left, Hand Joint Left, Hand Joint Right
Head & Neck	Head Joint, Neck Joint
Shoulder (Left & Right)	Shoulder Joint Left, Shoulder Joint Right
Hip	Torso Joint, Hip Joint Left, Hip Joint Right
Lower limb (Left & Right)	Knee Joint Left, Foot Joint Left, Knee Joint Right, Foot Joint Right

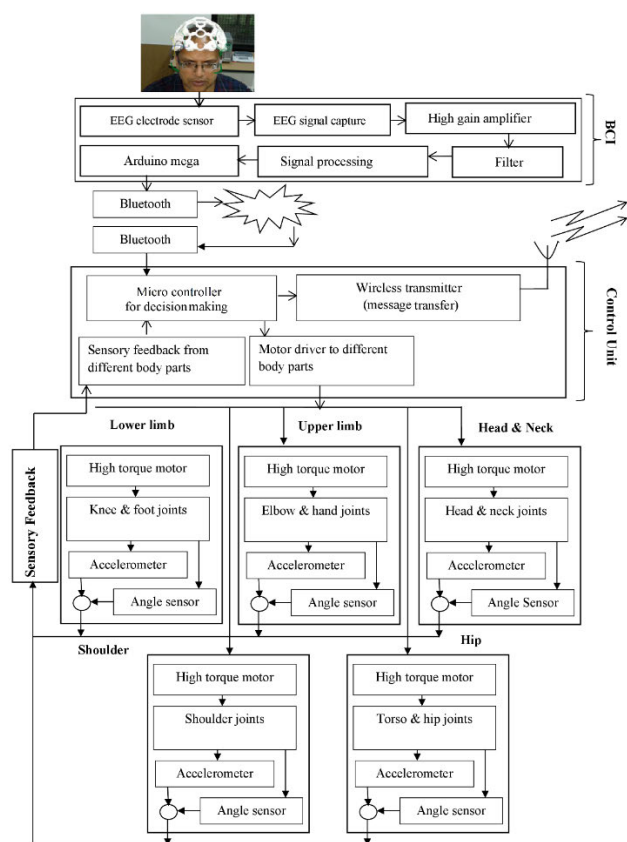


FIGURE 1. System architecture: Brain Energized Full Body Exoskeleton (BFBE).

high-frequency noise, we use a bandpass. Walsh Hadamard Transform (WHT) is then used to transform the signals into the frequency domain.

The signals are further transformed into a digital form and provided to the Arduino Mega, which transmits the signal via Bluetooth to the Control Unit. The signals are generated for different basic human actions (sitting, standing, sleeping) and then after the pre-processing is stored in a database. When the paralyzed person has an intention to make a particular movement, the microcontroller in the CU uses this

database and produces the signal for activating the particular part of the body. The generated EEG pattern of the person is mapped into the corresponding action. The BAM then uses the motor driver circuit to pass the activation signal to the corresponding part of the body. The potential energy harvesting is used in the system to solve the power issues related to the exoskeleton. The stability in the gait cycle is ensured by using adaptive sensory feed-back. The feedback to the CU is provided using a multi-level sensing technique so that corrections can be made in the process. Required corrections for producing the actuation signals are done by the microcontroller using this feedback and thus improving the decision-making accuracy. An accelerometer is used on the backside for detecting accidental falls. The processing happens at the edge, thus reducing delay in decision making, and the system is further integrated with an IoT module that helps to send an alert message to multiple caregivers in case of an emergency. If the measured tilt passes a particular threshold, a similar emergency message will be given to the caregiver via a wireless transmitter. The secure communication is ensured between paralyzed persons and caregivers using a double encrypted NTSA algorithm [26]. The material used for the development is carbon fiber, so that it can easily replicate various body movements with ease. The BFBE has a total of 15 degrees of freedom spread across different joints of the body, as indicated in Table 2.

Each of these joints is realized using high torque motors. Controlling the angle of rotation of the motors enables the system to make different movements. The exoskeleton is easy to wear due to its flexible and detachable components. The straps are used to tie the exoskeleton to different body parts. To further improve the stability of the person, support is provided on the backside and ankle region. In order to check if the applied force is sufficient to make the exoskeleton stable, angle sensors are placed on the joints.

B. SYSTEM DESIGN AND METHODOLOGY

The full-body structure of the exoskeleton mainly consists of five different body parts, which are lower limb, upper limb, head & neck, shoulder, and hip. The BFBE structured is designed by integrating these parts. The modular design provides BFBE with the highly required flexibility. The system can thus be used by people with different degrees of paralysis.

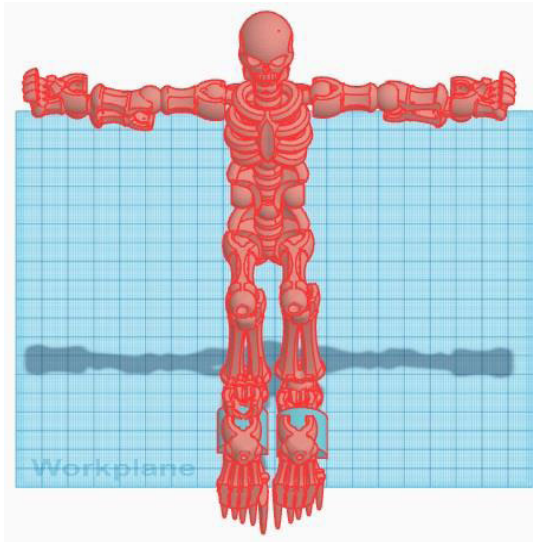


FIGURE 2. Sitting posture of BFBE (3D model).

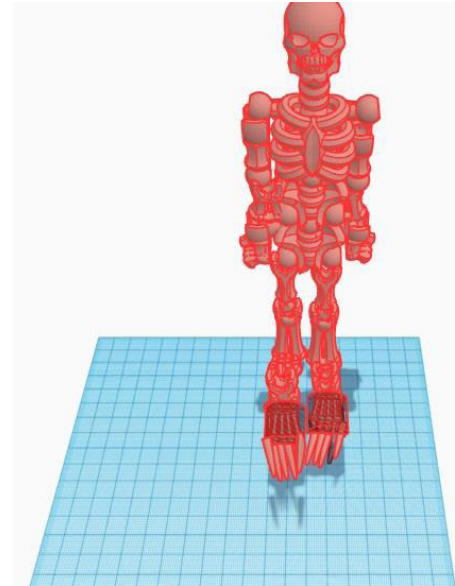


FIGURE 3. Standing posture of BFBE (3D model).

1) EXOSKELETON DESIGN FOR DIFFERENT POSTURES

In this section, we discuss the design generated for the exoskeleton in different body postures. BFBE exoskeleton is constructed to mirror the anatomy of the human body. Figure 2 illustrates the full-body exoskeleton designed using 3D software to emulate sitting posture. The major advantage of the exoskeleton system is that the various parts and the joints can be attached and detached easily. The system can thus be used by people with different degrees of paralysis. The full-body exoskeleton can be used by a completely paralyzed person. paralysis can be provided with a customized exoskeleton. People experience the ease of wearability and mobility because of the development of the exoskeleton with carbon fiber material. To further improve the stability of the person, on the backside and in the ankle region, a support is provided with the system. Actuating the motors placed at the corresponding joints helps to move from sleeping to the sitting posture.

Figure 3 shows the standing posture of the full-body exoskeleton. The system translates from sleeping to standing based on the acquired human intentions. The high torque motors placed at the different joints help in lifting the human weight. If the actuation signals produced are not sufficient, more accurate signals will be generated based on the feedback received. A customized execution pattern is used to maintain stability and reduce errors. The design also ensures that no direct transition from sleeping to standing or vice versa.

III. MATHEMATICAL ANALYSIS OF THE PROPOSED SYSTEM

The mathematical analysis is done on the full-body exoskeleton to identify the desired torque proportional to the mass. The joints used to provide 15 degrees of freedom are utilized to control the different bones of the human skeleton. Figure 4 presents the exoskeleton structure used for the analysis. Here, *A* is the head joint (HJ), *b* is the neck joint (NJ),

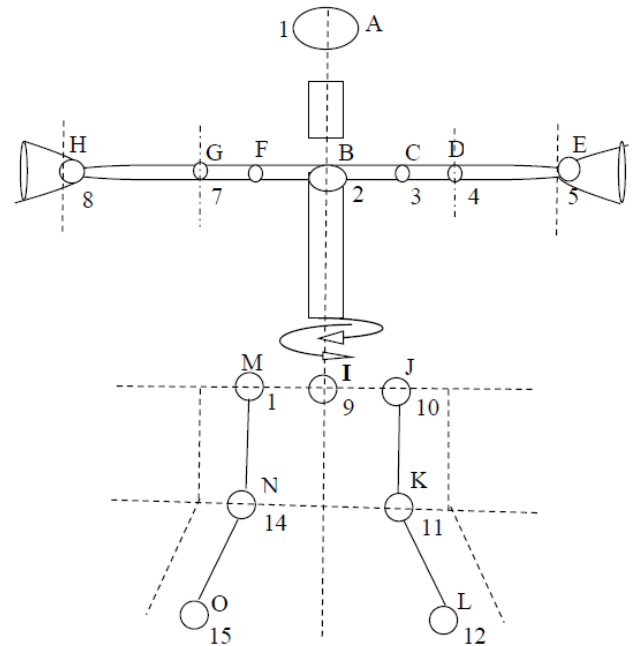


FIGURE 4. Exoskeleton structure used for analysis.

c is the left shoulder joint left (SJL), *d* is the elbow joint left (EJL), *e* is the hand joint left (HJL), *f* is the shoulder joint right (SJR), *g* is the elbow joint right (EJR), *h* is the hand joint right (HJR), *lr* and *lh* are the links for humanoid limbs.

Let the angle of the limb with respect to vertical and horizontal axis is denoted by ' θ ', the masses of the element by m_i , the length of the elements by l_i , and the center of gravity of the system by G_i . The spring of the element is represented by spring coefficient K_i . The angles are referenced with horizontal and vertical axis where *L* denotes the kinetic and *P* denotes

the potential energy, and \in is the force to be applied to the joint.

Let the different control signals to be applied at hip and knee joint of human and exoskeleton be defined as \hat{A} for the angular acceleration of knee, $\hat{\dot{A}}$ for the angular velocity of the knee, \hat{A} for the angular position of the knee, \hat{J} for the total torque applied on the knee and the ankle, \hat{I} for the inertia on the foot and the shank. Let the length of the shank is $\hat{L}m$, length of the foot is $\hat{L}m$, the mass of the shank is \hat{O} kg, mass of the foot is \hat{O} kg and let the torque be proportional to mass.

Consider the upper part of the body. The driving motor is located at the head joint driven by V_{HJ} , V_{NJ} is the neck joint motor driving voltage, V_{SJL} is the shoulder joint left motor driving voltage, V_{SJR} is the shoulder joint right motor driving voltage. Because of the DC voltage, we have currents I_{HJ} , I_{NJ} , I_{SJL} , I_{SJR} , entering the exoskeleton upper part. The current flowing from the neck joint to the head joint is denoted by I_{NH} . We have $I_{NJ} = I_{NH}$, $I_{SJL} = 0$, $I_{SJR} = 0$, $I_{HJ} = -I_{NH}$ and $I_{NH} = S_M(V_{NJ}, V_{SJR}, V_{SJL}, V_{HJ})$, where S_M is a function classified based on the portion at the exoskeleton. Also ' \in ' is the force to be applied to the joint to move from an initial position or angle ' θ ' to final position angle ' θ' '. The length of the exoskeleton part be l_i and the width is w_i and the initial position of the exoskeleton is ' x ' along the axis. The net force applied to the head joint movement will be,

$$\in_{HJ} = \int_0^{<\theta} \in_{HJ}^1 W_i dx \quad (1)$$

With \in^1 as the force applied per unit area, the width W_i becomes constant, thus we have,

$$\in_{HJ} = W_i \int_0^{<\theta} \in_{HJ}^1 dx \quad (2)$$

Similarly, we obtain other values of force applied on shoulder joint left and shoulder joint right as,

$$\in_{SJL} = W_i \int_0^{<\theta} \in_{SJL}^1 dx \quad (3)$$

$$\in_{SJR} = W_i \int_0^{<\theta} \in_{SJR}^1 dx \quad (4)$$

We can say that the net force applied to the head joint, shoulder joint left and shoulder joint right movement as a function of different voltages given by,

$$\in_{HJ} = f_{HJ}(V_{NJ}, V_{SJL}, V_{SJR}, V_{HJ}) \quad (5)$$

$$\in_{SJL} = f_{SJL}(V_{NJ}, V_{SJL}, V_{SJR}, V_{HJ}) \quad (6)$$

$$\in_{SJR} = f_{SJR}(V_{NJ}, V_{SJL}, V_{SJR}, V_{HJ}) \quad (7)$$

If we consider a time-varying voltage V_{NJ} , V_{SJL} , V_{SJR} , V_{HJ} to move the exoskeleton at any position at any time, the neck to head force, shoulder joint left and shoulder joint right, as a function of time t is given by,

$$\in_{NH}^{(t)} = f_{HJ}(V_{NJ}(t), V_{SJL}(t), V_{SJR}(t), V_{HJ}(t)) \quad (8)$$

$$\in_{SJL}^{(t)} = f_{SJL}(V_{NJ}(t), V_{SJL}(t), V_{SJR}(t), V_{HJ}(t)) \quad (9)$$

$$\in_{SJR}^{(t)} = f_{SJR}(V_{NJ}(t), V_{SJL}(t), V_{SJR}(t), V_{HJ}(t)) \quad (10)$$

Here 'f' is the function taking the time-varying force into consideration. Now we have current acting at shoulder joint left and shoulder joint right given by,

$$I_{SJL}(t) = \frac{d}{dt} \in_{SJL} \quad (11)$$

$$I_{SJR}(t) = \frac{d}{dt} \in_{SJR} \quad (12)$$

As the incoming current is equal to the outgoing current, we have, $I_{NJ}(t) + I_{HJ}(t) = \frac{d}{dt} \in_{NH}$. With $I_{NJD}(t)$ as the initial position, we have $I_{NJ}(t) = I_{\mu}(t) + I_{NJD}(t)$, $I_{HJ}(t) = -I_{\mu}(t) + I_{HJD}(t)$ and $I_{NJD}(t) + I_{HJD}(t) = \frac{d}{dt} \in_{NH}$.

Here, $I_{\mu}(t)$ is fully responsible for the exact movement at the exact time and I_{NJD} and I_{HJD} for the correct initial position. We can call them as the returned coordinates. If $I_{NJD}(t)$ is causing the change in the movement of exoskeleton by an angle θ' in the given time Δt , then $I_{NJD}(t) = \frac{d}{dt} \in'_{\theta}$, and if $I_{HJD}(t)$ is causing the change in the movement of exoskeleton by θ'' in the given time Δt , then $I_{HJD} = \frac{d}{dt} \in''_{\theta}$.

Change in the variation between the neck and the head joint is given by $\frac{d}{dt} \in'_{\theta} + \frac{d}{dt} \in''_{\theta} = \frac{d}{dt} \in_{NH}$ that is $\in'_{\theta} + \in''_{\theta} = \in_{NH}$. Assuming two different movement angle force at $<\in'_{\theta}$ and $<\in''_{\theta}$ we have the force, variations given by,

$$\in'_{\theta'} = W_i \int_0^{<\theta'} \frac{x}{l_i} \in'_{HJ} dx \quad (13)$$

$$\in''_{\theta''} = W_i \int_0^{<\theta''} \left(1 - \frac{x}{l_i}\right) \in'_{HJ} dx \quad (14)$$

The net force applied is written as a function of different voltages given by,

$$\in'_{\theta'} = f_{\theta'}(V_{NJ}, V_{SJL}, V_{SJR}, V_{HJ}) \quad (15)$$

$$\in''_{\theta''} = f_{\theta''}(V_{NJ}, V_{SJL}, V_{SJR}, V_{HJ}) \quad (16)$$

Considering the time-varying voltage V_{NJ} , V_{SJL} , V_{SJR} , V_{HJ} to move the exoskeleton at any position at any time, the neck to head force, shoulder joint left and shoulder joint right, as a function of time t is given by,

$$\in'_{\theta'}(t) = f_{\theta'}(V_{NJ}(t), V_{SJL}(t), V_{SJR}(t), V_{HJ}(t)) \quad (17)$$

$$\in''_{\theta''}(t) = f_{\theta''}(V_{NJ}(t), V_{SJL}(t), V_{SJR}(t), V_{HJ}(t)) \quad (18)$$

Considering the 'f' function takes time varying force into considerations, we have the current acting as,

$$I_{HJD}(t) = \frac{d}{dt} \in_{\theta'} \quad (19)$$

$$I_{HJD}(t) = \frac{d}{dt} \in_{\theta''} \quad (20)$$

$$I_{SJL}(t) = \frac{d}{dt} \in_{SJL} \quad (21)$$

$$I_{SJR}(t) = \frac{d}{dt} \in_{SJR} \quad (22)$$

The net current flowing through the exoskeleton is zero and given by,

$$I_{NJ}(t) + I_{HJ}(t) + I_{SJL}(t) + I_{SJR}(t) = 0 \quad (23)$$

$$I_{NJD}(t) + I_{HJD}(t) + I_{SJL}(t) + I_{SJR}(t) = 0 \quad (24)$$

Using the chain value of differentiation on the current values we obtain,

$$I_{NJD}(t) = \frac{\partial \epsilon_{\theta'}}{\partial V_{NJ}} \frac{d}{dt} V_{NJ} + \frac{\partial \epsilon_{\theta'}}{\partial V_{SJL}} \frac{d}{dt} V_{SJL} + \frac{\partial \epsilon_{\theta'}}{\partial V_{SJR}} \frac{d}{dt} V_{SJR} + \frac{\partial \epsilon_{\theta'}}{\partial V_{HJ}} \frac{d}{dt} V_{HJ} \quad (25)$$

$$I_{HJD}(t) = \frac{\partial \epsilon_{\theta''}}{\partial V_{NJ}} \frac{d}{dt} V_{NJ} + \frac{\partial \epsilon_{\theta''}}{\partial V_{SJL}} \frac{d}{dt} V_{SJL} + \frac{\partial \epsilon_{\theta''}}{\partial V_{SJR}} \frac{d}{dt} V_{SJR} + \frac{\partial \epsilon_{\theta''}}{\partial V_{HJ}} \frac{d}{dt} V_{HJ} \quad (26)$$

$$I_{SJL}(t) = \frac{\partial \epsilon_{SJL}}{\partial V_{NJ}} \frac{d}{dt} V_{NJ} + \frac{\partial \epsilon_{SJL}}{\partial V_{SJL}} \frac{d}{dt} V_{SJL} + \frac{\partial \epsilon_{SJL}}{\partial V_{SJR}} \frac{d}{dt} V_{SJR} + \frac{\partial \epsilon_{SJL}}{\partial V_{HJ}} \frac{d}{dt} V_{HJ} \quad (27)$$

$$I_{SJR}(t) = \frac{\partial \epsilon_{SJR}}{\partial V_{NJ}} \frac{d}{dt} V_{NJ} + \frac{\partial \epsilon_{SJR}}{\partial V_{SJL}} \frac{d}{dt} V_{SJL} + \frac{\partial \epsilon_{SJR}}{\partial V_{SJR}} \frac{d}{dt} V_{SJR} + \frac{\partial \epsilon_{SJR}}{\partial V_{HJ}} \frac{d}{dt} V_{HJ} \quad (28)$$

With dx as a small incremental moment for an incremental time $d\tau$ we obtain,

$$dx = \frac{-K_i W_i}{\tilde{A}} \epsilon'_{HJ} d\tau \quad (29)$$

Substituting the above value of dx in (2) and (3) we obtain,

$$\epsilon_{SJL} = W_i \int_{\theta'}^{\theta''} \epsilon'_{SJL} \left(\frac{-K_i W_i}{\tilde{A}} \epsilon'_{HJ} d\tau \right) \quad (30)$$

$$\epsilon_{SJL} = \frac{-K_i W_i^2}{\tilde{A}} \int_{\theta'}^{\theta''} \epsilon'_{SJL} \epsilon'_{HJ} d\tau \quad (31)$$

$$\epsilon_{SJR} = \frac{-K_i W_i^2}{\tilde{A}} \int_{\theta'}^{\theta''} \epsilon'_{SJR} \epsilon'_{HJ} d\tau \quad (32)$$

$$\epsilon_{HJ} = \frac{-K_i W_i^2}{\tilde{A}} \int_{\theta'}^{\theta''} (\epsilon'_{HJ})^2 d\tau \quad (33)$$

Substituting the above value of dx in (12) and (13) we obtain,

$$\epsilon'_{\theta'} = \frac{-K_i W_i^2}{\tilde{A}} \int_{\theta'}^{\theta''} \frac{x}{l_i} (\epsilon'_{HJ})^2 d\tau \quad (34)$$

$$\epsilon''_{\theta''} = \frac{-K_i W_i^2}{\tilde{A}} \int_{\theta'}^{\theta''} \left(1 - \frac{x}{l_i} \right) (\epsilon'_{HJ})^2 d\tau \quad (35)$$

Calculating 'x' in terms of torque we integrate 'x' from initial angle θ' to final angle θ'' .

$$x = \frac{-K_i W_i}{\tilde{A}} \int_{\theta'}^{\theta''} \epsilon'_{HJ} d\tau \quad (36)$$

The V_{NJ} value for which we reach the maximum limit is V_{max} . If the value of V_{NJ} is raised above V_{max} , the exoskeleton movements will remain unaltered and practically constant. The human body parts will act as the dielectric of the capacitor with the exoskeleton acting as the plate of the capacitor. Here V_{OI} is the voltage applied between outer and inner exoskeleton, P_{limb} is the potential drop across the thickness of the limb, P_{IX} is the potential drop across the inner

surface of the exoskeleton, and P_{CM} is the potential at all the contact point across the exoskeleton and human limb. We now have,

$$VOJ = P_{limb} + PIX + PCM \quad (37)$$

The variation in the voltage is given by, $\Delta V_{OJ} = \Delta P_{limb} + \Delta PIX + P_{CM}$ where, P_{CM} is constant.

Now there are three potential charges across the exoskeleton and the limb, φ_{OE} is the charge on the outer exoskeleton, φ_{limb} is the charge on the limb, φ_{IE} is the charge on the inner exoskeleton, and we have $\varphi_{OE} + \varphi_{limb} + \varphi_{IE} = 0$ and $\tilde{\varphi}_{OE} + \tilde{\varphi}_{limb} + \tilde{\varphi}_{IE} = 0$. The charges per unit area are given by $\Delta \tilde{\varphi}_{OE} + \Delta \tilde{\varphi}_{IE} = 0$ with $\tilde{\varphi}_{limb}$ as constant.

To analyze the effect of external voltage on the exoskeleton, and the human limb, we are defining a threshold voltage depending on the EEG signal V_{th} . The minimum voltage required to trigger the movement is, if $VOI < V_{th}$ then $\tilde{\varphi}_{IE} > 0$ and $PIX < 0$, if $VOI \geq V_{th}$ then $\tilde{\varphi}_{IE} < 0$ and $PIX > 0$, if $VOI = V_{th}$ then $\tilde{\varphi}_{IE} = 0$ and $PIX = 0$. The signal from EEG headset to limb is defined as $R_{surface-limb}$, ST is the potential depending on the thickness of limb, and L_T is the length of the limb. The ratio of the potential drop across the inner surface of the exoskeleton to the length of the limb is given by P_{IX}/L_T . The signal transferred from EEG headset to the limb is given by,

$$R_{surface-limb} = S_T e^{P_{IX}/L_T} \quad (38)$$

The potential depending on the thickness of the limb is calculated as,

$$S_T = S_L e^{-P_{RX}/L_T} \quad (39)$$

Substituting the value of ST in (39), we obtain,

$$R_{surface-limb} = S_L e^{(P_{IX} - P_{RX})/L_T} \quad (40)$$

The capacitance coefficient variation in the direction of x and capacitance coefficient variation in the opposite direction of x given by,

$$K(x) = K_0 e^{P(x)/L_T} \quad (41)$$

$$K(y) = L_0 e^{-P(x)/L_T} \quad (42)$$

Potential is at its local maximum, which indicates that the system in the equilibrium state is unstable. We apply a small displacement to the exoskeleton and move it to a random small distance from its equilibrium state, and the total force of the exoskeleton makes it to move even farther. Mobility displacement along the x direction is given by,

$$\mu(x) = \vartheta (K(y) - K(x) - P_A) \quad (43)$$

$$\frac{d^2 P}{dy^2} = \frac{-\vartheta}{\mu_s} \left[L_0 e^{-P(x)/L_T} - K_0 e^{P(x)/L_T} - P_A \right] \quad (44)$$

The charge on the inner skeleton is given by,

$$\tilde{\varphi}_{IE} = \frac{\mp \sqrt{2\vartheta \mu_s P_A} \sqrt{L_T e^{-P(x)/L_T} + P_{IX}}}{\sqrt{-L_T + e^{-P_{RX}/L_T} (L_T e^{P/L_T} - P_{IX} - L_T)}} \quad (45)$$

$$\tilde{\varphi}_{IE} = \tilde{C}_{limb} P_{limb} \quad (46)$$

$$\tilde{\varphi}_{IE} = -\sqrt{2\vartheta \mu_s P_A} \sqrt{P_{IX} + L_T e^{(P_{IX} - P_{RX})/L_T}} \quad (47)$$

$$\tilde{\varphi}_{IE} = \tilde{\varphi}_{RL} + \tilde{\varphi}_{SL} \quad (48)$$

The charge on the right-side outer skeleton to the limb is calculated as,

$$\tilde{\varphi}_{RL} = \int_{initial\theta}^{final} (\vartheta) K(x) (Adx) \quad (49)$$

The charge on the left-side outer skeleton to the limb is calculated as,

$$\tilde{\varphi}_{SL} = -\vartheta \int_{initial}^{final} K(x) dx \quad (50)$$

The body parameter constant with static exoskeleton movement is given by,

$$T_B = \sqrt{\frac{2\mu_s}{\vartheta P_A}} \sqrt{P_{IX}} \quad (51)$$

The small variation in the charge on the inner skeleton is given by, $\Delta\tilde{\varphi}_{IE} = \Delta\tilde{\varphi}_{RL} + \Delta\tilde{\varphi}_{SL}$ where $\tilde{\varphi}_{RL} = \tilde{\varphi}_{RL}(P_{IX})$ and $\tilde{\varphi}_{SL} = \tilde{\varphi}_{SL}(P_{IX})$. The voltage applied between the outer and inner exoskeleton is given by,

$$V_{OI} = V_{th} + P_{IX} - \frac{\tilde{\varphi}_{SL}(P_{IX}) + \tilde{\varphi}_{RL}(P_{IX})}{\tilde{limb}} \quad (52)$$

IV. RESULTS AND DISCUSSION

The designed system is tested on six different subjects, three healthy and three paralyzed persons. The collection of data is done in the offline and online phases. The experiments are carried out for three different human intentions like sleeping, standing, and sitting. To maintain stability, the movements are executed based on the designed pattern. In the offline training phase, the brain patterns corresponding to each of these intended movements are acquired using the 64 channel EEG sensor. Figure 5 presents the EEG Sensor manufactured with 16 Electrodes for collecting the signals.

Signal analysis is carried out using WHT, and the unique features required for the classification are extracted. Large amount of EEG signals is compressed using WHT, and a faster computation is also provided. The database is designed using the extracted information corresponding to each human thought obtained during the training phase. In the online phase, the WHT coefficients, along with extracted information, are transmitted from the brain to the full-body exoskeleton for the reconstruction of the original signal.

The EEG signals corresponding to human intentions of sitting and standing are depicted in figure 6. Here, the original signal and the reconstructed signal for both the postures are presented. Figure 7 shows the area matching of EEG patterns obtained for the sitting and standing postures. The original and reconstructed signal is correlated at the receiver side to identify the movement to be executed. Based on the classification results, the required joints are actuated to produce the desired movement by the exoskeleton system.

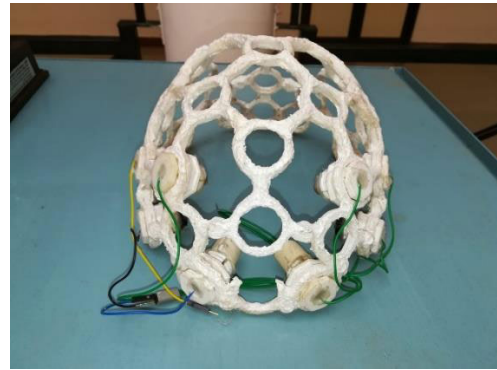


FIGURE 5. EEG sensor manufactured with 16 electrodes.

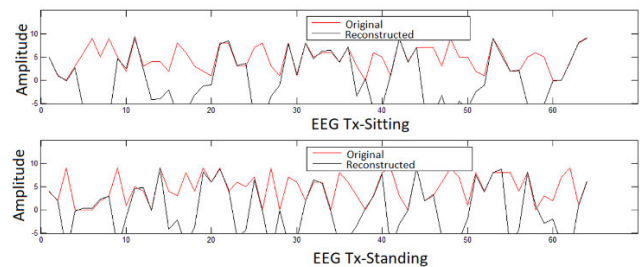


FIGURE 6. Original and reconstructed EEG signal in sitting and standing positions with BFBE.

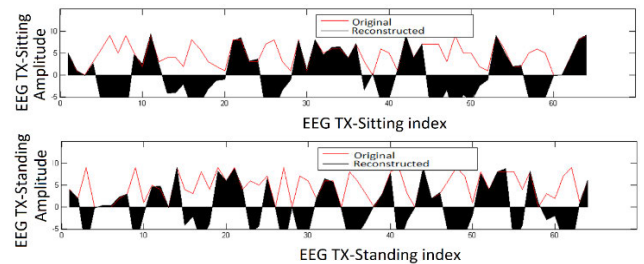


FIGURE 7. Area matching of EEG patterns obtained for sitting and standing posture.

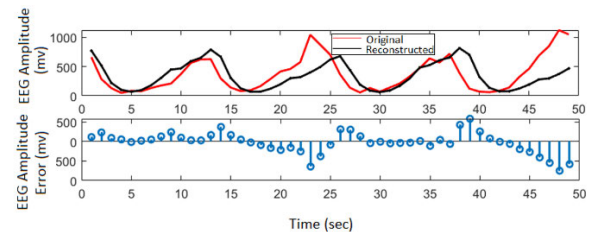


FIGURE 8. EEG amplitude and EEG amplitude error for original and reconstructed signals.

Figure 8 shows the varying of the EEG signal captured by the brain headset with time. The error in EEG amplitude for the signal is also shown in the figure. Figure 9 presents the brain pattern variations at different frequencies using the proposed system. The voltage spectral density variations at frequencies 6 Hz, 10 Hz and 22 Hz are presented and highlighted in the figure.

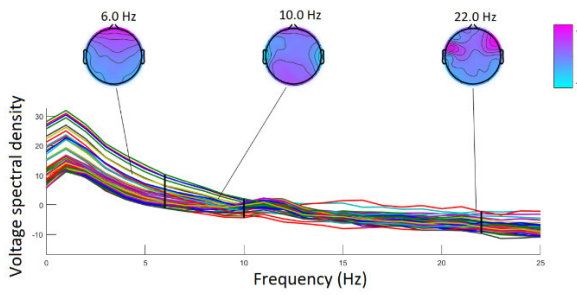


FIGURE 9. Brain pattern variations at different frequencies.

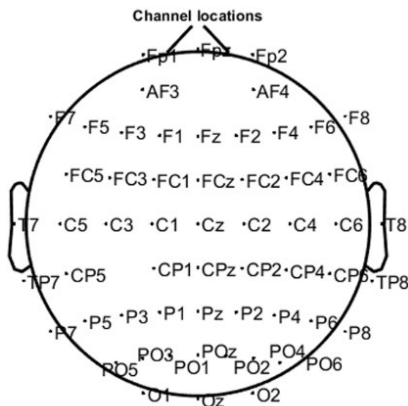


FIGURE 10. Electrode placement locations in the EEG headset.

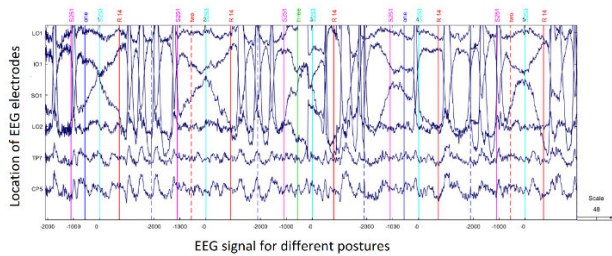


FIGURE 11. EEG for different postures with placement of electrodes from CP5 to LO1.

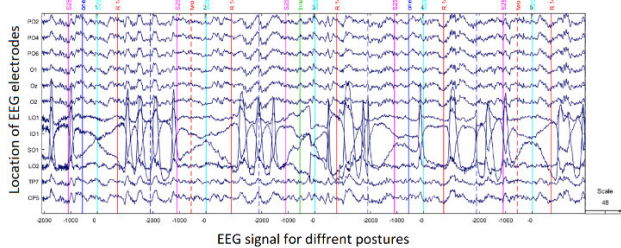


FIGURE 12. EEG for different postures with the placement of electrodes from CP5 to PO2.

In the proposed system, EEG analysis is carried out using realistic head models to identify the unique EEG signal features and to validate the brain network connectivity. Here, a 64-electrode placement scheme is used in the proposed system. The electrodes are placed in the frontal and parietal

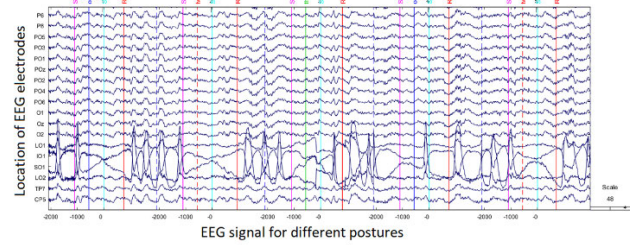


FIGURE 13. EEG for different postures with the placement of electrodes from CP5 to P6.

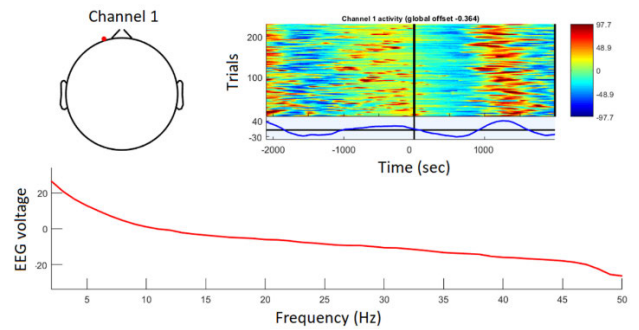


FIGURE 14. EEG voltage for different frequency and number of trials per second.

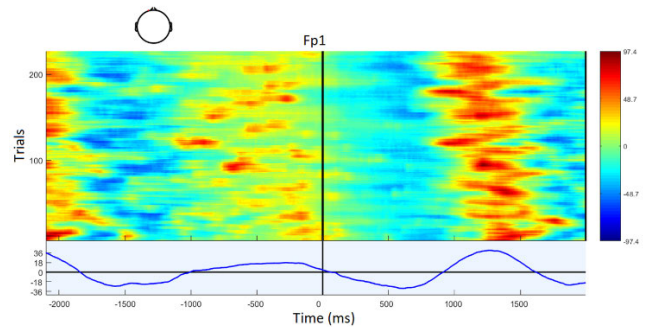


FIGURE 15. Number of trials with time.

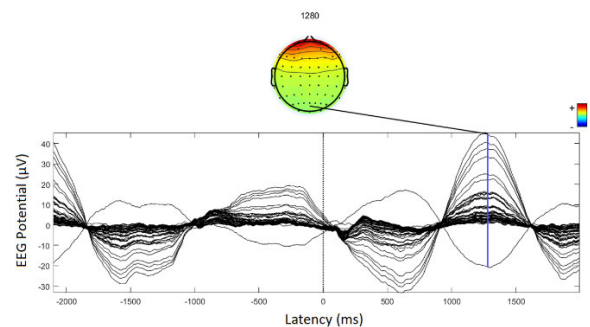


FIGURE 16. EEG voltage for different frequency and number of trails per second.

regions of the brain. Figure 10 indicates the electrode placement positions used for testing the proposed system.

Figure 11 shows the EEG signal for different postures with the placement of electrodes from positions CP5 to LO1,

and figure 12 shows the EEG for different postures with the placement of electrodes from CP5 to PO2 positions and figure 13 shows the EEG for different postures with the placement of electrodes from CP5 to P6 positions. Figure 14 shows the EEG voltage for different frequencies and also the number of trials per second.

Figure 15 shows the number of trials carried out with time, and figure 16 shows the EEG potential with varying latency using the proposed system. The proposed system achieves excellent performance in all real-time scenarios. Results confirm that the proposed method provides adequate assistance and rehabilitation for paralyzed patients.

V. CONCLUSION

To overcome the constraints of weight, flexibility, and adaptability faced by the existing exoskeletons used for assisting the paralyzed people, we proposed an adaptive and flexible Brain Energized Full Body Exoskeleton (BFBE). The brain signals captured by the EEG sensors are used for controlling the movements of the exoskeleton. The flexibility is incorporated into the system by a modular design approach. The parts and joints can be attached and detached easily, allowing it to be used by people with different levels of paralysis. For the fully paralyzed, the full-body exoskeleton structure can be used. The processing happens at the edge, thus reducing delay in decision making, and the system is further integrated with an IoT module that helps to send an alert message to multiple caregivers in case of an emergency. The potential energy harvesting is used in the system to solve the power issues related to the exoskeleton. The stability in the gait cycle is ensured by using adaptive sensory feedback. The system was by using six natural movements on ten different paralyzed persons and received very good results.

REFERENCES

- [1] Multiple Sclerosis News Today. *Mobility Devices for Lower-Limb Paralysis Flawed, Survey Reveals*. Accessed: Jun. 20, 2019. [Online]. Available: <https://multiplesclerosisnewstoday.com/2018/06/08/mobility-devices-lower-limb-paralysis-flawed-survey>
- [2] S. Alqahtani, J. Joseph, B. Dicianno, N. A. Layton, M. L. Toro, E. Ferretti, Y. A. Tuakli-Wosornu, H. Chhabra, H. Neyedli, C. R. Lopes, M. M. Alqahtani, P. Van de Vliet, S.-I. Kumagaya, J.-B. Kim, V. McKinney, Y.-S. Yang, M. Goldberg, and R. Cooper, "Stakeholder perspectives on research and development priorities for mobility assistive-technology: A literature review," *Disab. Rehabil. Assistive Technol.*, pp. 1–15, Dec. 2019, doi: [10.1080/17483107.2019.1650300](https://doi.org/10.1080/17483107.2019.1650300).
- [3] D. Ao, R. Song, and J. Gao, "Movement performance of human-robot cooperation control based on EMG-driven hill-type and proportional models for an ankle power-assist exoskeleton robot," *IEEE Trans. Neural Syst. Rehabil. Eng.*, vol. 25, no. 8, pp. 1125–1134, Aug. 2017, doi: [10.1109/TNSRE.2016.2583464](https://doi.org/10.1109/TNSRE.2016.2583464).
- [4] Q. Ma, L. Ji, and R. Wang, "The development and preliminary test of a powered alternately walking exoskeleton with the wheeled foot for paraplegic patients," *IEEE Trans. Neural Syst. Rehabil. Eng.*, vol. 26, no. 2, pp. 451–459, Feb. 2018.
- [5] T. Zhang, M. Tran, and H. Huang, "Design and experimental verification of hip exoskeleton with balance capacities for walking assistance," *IEEE/ASME Trans. Mechatronics*, vol. 23, no. 1, pp. 274–285, Feb. 2018, doi: [10.1109/TMECH.2018.2790358](https://doi.org/10.1109/TMECH.2018.2790358).
- [6] J. C. Perry, J. Rosen, and S. Burns, "Upper-limb powered exoskeleton design," *IEEE/ASME Trans. Mechatronics*, vol. 12, no. 4, pp. 408–417, Aug. 2007, doi: [10.1109/TMECH.2007.901934](https://doi.org/10.1109/TMECH.2007.901934).
- [7] A. Sutrisno and D. J. Braun, "Enhancing mobility with quasi-passive variable stiffness exoskeletons," *IEEE Trans. Neural Syst. Rehabil. Eng.*, vol. 27, no. 3, pp. 487–496, Mar. 2019, doi: [10.1109/TNSRE.2019.2899753](https://doi.org/10.1109/TNSRE.2019.2899753).
- [8] P. G. Vinoj, S. Jacob, V. G. Menon, S. Rajesh, and M. R. Khosravi, "Brain-controlled adaptive lower limb exoskeleton for rehabilitation of post-stroke paralyzed," *IEEE Access*, vol. 7, pp. 132628–132648, 2019, doi: [10.1109/access.2019.2921375](https://doi.org/10.1109/access.2019.2921375).
- [9] M. Sarac, M. Solazzi, and A. Frisoli, "Design requirements of generic hand exoskeletons and survey of hand exoskeletons for rehabilitation, assistive, or haptic use," *IEEE Trans. Haptics*, vol. 12, no. 4, pp. 400–413, Oct. 2019, doi: [10.1109/toh.2019.2924881](https://doi.org/10.1109/toh.2019.2924881).
- [10] F. Patane, S. Rossi, F. D. Sette, J. Taborri, and P. Cappa, "WAKE-up exoskeleton to assist children with cerebral palsy: Design and preliminary evaluation in level walking," *IEEE Trans. Neural Syst. Rehabil. Eng.*, vol. 25, no. 7, pp. 906–916, Jul. 2017, doi: [10.1109/tnsre.2017.2651404](https://doi.org/10.1109/tnsre.2017.2651404).
- [11] H.-J. Lee, S. Lee, W. H. Chang, K. Seo, Y. Shim, B.-O. Choi, G.-H. Ryu, and Y.-H. Kim, "A wearable hip assist robot can improve gait function and cardiopulmonary metabolic efficiency in elderly adults," *IEEE Trans. Neural Syst. Rehabil. Eng.*, vol. 25, no. 9, pp. 1549–1557, Sep. 2017, doi: [10.1109/tnsre.2017.2664801](https://doi.org/10.1109/tnsre.2017.2664801).
- [12] A. Agrawal, O. Harib, A. Hereid, S. Finet, M. Masselin, L. Praly, A. D. Ames, K. Sreenath, and J. W. Grizzle, "First steps towards translating HZD control of bipedal robots to decentralized control of exoskeletons," *IEEE Access*, vol. 5, pp. 9919–9934, 2017, doi: [10.1109/access.2017.2690407](https://doi.org/10.1109/access.2017.2690407).
- [13] M. K. Shepherd and E. J. Rouse, "Design and validation of a torque-controllable knee exoskeleton for Sit-to-Stand assistance," *IEEE/ASME Trans. Mechatronics*, vol. 22, no. 4, pp. 1695–1704, Aug. 2017, doi: [10.1109/tmech.2017.2704521](https://doi.org/10.1109/tmech.2017.2704521).
- [14] M. Cenciari and M. A. Dollar, "Biomechanical considerations in the design of lower limb exoskeletons," in *Proc. IEEE Int. Conf. Rehabil. Robot.*, Zürich, Switzerland, Jun./Jul. 2011, pp. 1–6, doi: [10.1109/ICORR.2011.5975366](https://doi.org/10.1109/ICORR.2011.5975366).
- [15] H. Herr, "Exoskeletons and orthoses: Classification, design challenges and future directions," *J. NeuroEng. Rehabil.*, vol. 6, no. 1, p. 21, Dec. 2009, doi: [10.1186/1743-0003-6-21](https://doi.org/10.1186/1743-0003-6-21).
- [16] A. Agrawal, A. N. Dube, D. Kansara, S. Shah, and S. Sheth, "Exoskeleton: The friend of mankind in context of rehabilitation and enhancement," *Indian J. Sci. Technol.*, vol. 9, no. S1, pp. 1–8, Dec. 2016, doi: [10.17485/ijst/2016/v9is1/100889](https://doi.org/10.17485/ijst/2016/v9is1/100889).
- [17] C. Chen, X. Wu, D.-X. Liu, W. Feng, and C. Wang, "Design and voluntary motion intention estimation of a novel wearable full-body flexible exoskeleton robot," *Mobile Inf. Syst.*, vol. 2017, pp. 1–11, Jun. 2017, doi: [10.1155/2017/8682168](https://doi.org/10.1155/2017/8682168).
- [18] A. Singla, S. Dhand, A. Dhawad, and G. S. Virk, "Toward human-powered lower limb exoskeletons: A review," in *Harmony Search and Nature Inspired Optimization Algorithms. Advances in Intelligent Systems and Computing*, vol. 741. Singapore: Springer, 2019, pp. 783–795, doi: [10.1007/978-981-13-0761-4_75](https://doi.org/10.1007/978-981-13-0761-4_75).
- [19] S. Federici, F. Meloni, M. Bracalenti, and M. L. De Filippis, "The effectiveness of powered, active lower limb exoskeletons in neurorehabilitation: A systematic review," *NeuroRehabilitation*, vol. 37, no. 3, pp. 321–340, Nov. 2015, doi: [10.3233/nre-151265](https://doi.org/10.3233/nre-151265).
- [20] G. Menga and M. Ghirardi, "Lower limb exoskeleton for rehabilitation with improved postural equilibrium," *Robotics*, vol. 7, no. 2, p. 28, Jun. 2018, doi: [10.3390/robotics7020028](https://doi.org/10.3390/robotics7020028).
- [21] H. Kazerooni and R. Steger, "The berkeley lower extremity exoskeleton," *J. Dyn. Syst., Meas., Control*, vol. 128, no. 1, pp. 14–25, Mar. 2006, doi: [10.1115/1.2168164](https://doi.org/10.1115/1.2168164).
- [22] V. G. Menon, S. Jacob, S. Joseph, and A. O. Almagrabi, "SDN powered humanoid with edge computing for assisting paralyzed patients," *IEEE Internet Things J.*, early access, Dec. 2019, doi: [10.1109/JIOT.2019.2963288](https://doi.org/10.1109/JIOT.2019.2963288).
- [23] S. Jacob, V. G. Menon, F. Al-Turjman, V. P. G., and L. Mostarda, "Artificial muscle intelligence system with deep learning for post-stroke assistance and rehabilitation," *IEEE Access*, vol. 7, pp. 133463–133473, 2019, doi: [10.1109/ACCESS.2019.2941491](https://doi.org/10.1109/ACCESS.2019.2941491).

- [24] L. Jiang, A. Stocco, D. M. Losey, J. A. Abernethy, C. S. Prat, and R. P. N. Rao, "BrainNet: A multi-person brain-to-brain interface for direct collaboration between brains," *Sci. Rep.*, vol. 9, no. 1, pp. 1–11, Dec. 2019, doi: [10.1038/s41598-019-41895-7](https://doi.org/10.1038/s41598-019-41895-7).
- [25] W. Lee, S. Kim, B. Kim, C. Lee, Y. A. Chung, L. Kim, and S.-S. Yoo, "Non-invasive transmission of sensorimotor information in humans using an EEG/focused ultrasound brain-to-brain interface," *PLoS ONE*, vol. 12, no. 6, Jun. 2017, Art. no. e0178476, doi: [10.1371/journal.pone.0178476](https://doi.org/10.1371/journal.pone.0178476).
- [26] S. Rajesh, V. Paul, V. G. Menon, S. Jacob, and P. Vinod, "Secure brain-to-brain communication with edge computing for assisting post-stroke paralyzed patients," *IEEE Internet Things J.*, vol. 7, no. 4, pp. 2531–2538, Apr. 2020, doi: [10.1109/JIOT.2019.2951405](https://doi.org/10.1109/JIOT.2019.2951405).



SUNIL JACOB (Member, IEEE) received the Ph.D. degree in electronics and communication engineering from Bharathiar University, India, in 2015. He is currently the Director with the Centre for Robotics and a Professor with the Department of Electronics and Communication Engineering, SCMS School of Engineering and Technology, India. He is also doing postdoctoral research with the Lincoln University College, Malaysia. His project Muscles to Machine Interface for Paralyzed has been funded by the IEEE EPICS, USA, and other funded projects include bionic haptic arm, rejuvenating the cells of human body, deaddiction coil for drug addicts, smart keyboard for disabled person, low cost 3-D printer, and wearable device for detection and prevention of heart failure. He was a recipient of the AICTE Chhatra Vishwakarma Award, in electronics, in 2017, and the Young Gandhian Technological Innovation Appreciation Award, in 2018.



MUKIL ALAGIRISAMY received the bachelor's degree in electronics and communication engineering, the M.Eng. degree in communication systems, and the Ph.D. degree in engineering, in 2005, 2007, and 2012, respectively. She completed her PDF, in 2015. She started her career as a Lecturer with the Hindustan Engineering College, India. She was working as an Assistant Professor with B. S. Abdur Rahman University, India. Later, she joined the Stamford College, Malaysia, as a Lecturer. She is currently an Associate Professor with the Department of Electrical and Electronics and Engineering, Lincoln University College, Malaysia. She is also working as an Assistant Professor and a Coordinator of the Master of Science in Electrical, Electronics and Telecommunication Engineering Programs, Lincoln University College. She has 12 years of experience in teaching subjects like data communication, analog and digital communications, digital signal processing, and satellite communications. Her research interests include sink mobility patterns, clustering, modulation, data aggregation, and compressive sensing techniques for wireless sensor networks.



VARUN G. MENON (Senior Member, IEEE) received the Ph.D. degree in computer science and engineering from Sathyabama University, India, in 2017. He is currently an Associate Professor with the Department of Computer Science and Engineering, SCMS School of Engineering and Technology, India. His research interests include sensors, the Internet of Things (IoT), fog computing, and underwater acoustic sensor networks. He is also serving as the Guest Editor for the IEEE

Sensors Journal, the IEEE Internet of Things Magazine, and the IEEE TRANSACTIONS ON INDUSTRIAL INFORMATICS. He is an Associate Editor of IET Quantum Communications and also an Editorial Board Member of IEEE Future Directions: Technology Policy and Ethics. He is also a Distinguished Speaker of ACM.



B. MANOJ KUMAR received the Ph.D. degree in mechanical engineering from Karpagam University, India. He is currently an Associate Professor and the Head of the Department of Automobile Engineering, SCMS School of Engineering and Technology, India. His research interests include sensor networks and industrial engineering.



N. Z. JHANJHI is currently working as an Associate Professor with Taylor's University, Malaysia. He has great international exposure in academia, research, administration, and academic quality accreditation. He worked with Ilma University and King Faisal University (KFU), Saudi Arabia, for a decade. He has 20 years of teaching and administrative experience. He has an intensive background of academic quality accreditation in higher education. Besides scientific research activities,

he had worked a decade for academic accreditation and earned ABET accreditation twice for three programs at CCSIT, KFU. He also worked for the National Commission for Academic Accreditation and Assessment (NCAAA), the Education Evaluation Commission Higher Education Sector (EECHES), formerly NCAAA, Saudi Arabia, for institutional level accreditation. He also worked for the National Computing Education Accreditation Council (NCEAC). He was awarded as a top Reviewer 1% globally by WoS/ISI (Publons) recently for the year 2019. He has edited or authored more than 13 research books with international reputed publishers, earned several research grants, and a great number of indexed research articles on his credit. He has supervised several postgraduate students, including the master's and Ph.D. students. He is an Associate Editor of the IEEE Access, a Moderator of the IEEE TechRxiv, a keynote speaker for several IEEE international conferences globally, an External Examiner or an Evaluator for Ph.D. and master's students for several universities, a Guest editor of several reputed journals, a member of the editorial board of several research journals, and an active TPC Member of reputed conferences around the globe.



VASAKI PONNUSAMY received the bachelor's and M.Sc. degrees in computer science from the University of Science, Malaysia, and the Ph.D. degree in IT from Universiti Teknologi PETRONAS (UTP), Malaysia, in 2013. She is currently an Assistant Professor with Universiti Tunku Abdul Rahman, Malaysia. She is also the Head of the Department of Computer and Communication Technology, Faculty of Information and Communication Technology. She is also working

on cybersecurity, the Internet-of-Things (IoT) security trends, and digital governance. She has great international exposure as a Keynote Speaker, a Visiting Professor, and several Fellowships. She has edited or authored several research books with international reputed publishers, earned several research grants, and supervising postgraduate students. She is also a Human Resource Development Fund Certified Trainer and a Master Trainer for computational thinking and computer science teaching. Her career in academia started, in 1999. She has been teaching information and network security, wireless security, and data communication and networking. She is specialized in handling Cisco devices for routing and security. Her passion is to share her technical knowledge with the community. Her area of specializations are networking, communication, penetration testing, and cybersecurity. She has worked on several projects on IoT intrusion detection systems, cybersecurity governance, social engineering attacks mitigation/awareness, and human behavior-based authentication systems.



include deep learning, cloud security and privacy, *ad hoc* networks, and big data.

P. G. SHYNU received the Ph.D. degree in computer science from the Vellore Institute of Technology (VIT), Vellore, India, and the master's degree in computer science and engineering from the College of Engineering, Anna University, Chennai, India. He is currently working as an Associate Professor with the School of Information Technology and Engineering, VIT. He has published over 30 research papers in refereed international conferences and journals. His research interests



applications. He is the Founder of Anidra Tech Ventures Pty Ltd., a smart remote patient monitoring company. He contributed immensely to eResearch software research and development that uses cloud-based infrastructure and a core member for the project sponsored by Nectar Australian research cloud provider. He contributed heavily in the field of healthcare informatics, sensor networks, and cloud computing.

VENKI BALASUBRAMANIAN (Member, IEEE) received the Ph.D. degree in body area wireless sensor network (BAWSN) for remote healthcare monitoring applications. He is the Pioneer in building (pilot) remote healthcare monitoring application (rHMA) for pregnant women for the New South Wales Healthcare Department. His research establishes a dependability measure to evaluate rHMA that uses BAWSN. His research opens up a new research area in measuring time-critical

• • •

Depth Information Enhancement Using Block Matching and Image Pyramiding Stereo Vision Enabled RGB-D Sensor

Sunil Jacob^{1b}, Member, IEEE, Varun G. Menon^{1b}, Senior Member, IEEE, and Saira Joseph, Member, IEEE

Abstract—Depth sensing devices enabled with an RGB camera, can be used to augment conventional images with depth information on a per-pixel basis. Currently available RGB-D sensors include the Asus Xtion Pro, Microsoft Kinect and Intel RealSense™. However, these sensors have certain limitations. Objects that are shiny, transparent or have an absorbing matte surface, create problems due to reflection. Also, there can be an interference in the IR pattern due to the use of multiple RGB-D cameras and the depth information is correctly interpreted only for short distances between the camera and the object. The proposed system, block matching stereo vision (BMSV) uses an RGB-D camera with rectified/non-rectified block matching and image pyramiding along with dynamic programming for human tracking and capture of accurate depth information from shiny/transparent objects. Here, the IR emitter generates a known IR pattern and the depth information is recovered by comparing the multiple views of the focused object. The depth map of the BMSV RGB-D camera and the resultant disparity map are fused. This fills any void regions that may have emerged due to interference or because of the reflective transparent surfaces and an enhanced dense stereo image is obtained. The proposed method is applied to a 3D realistic head model, a functional magnetic resonance image (fMRI) and the results are presented. Results showed an improvement in speed and accuracy of RGB-D sensors which in turn provided accurate depth information density irrespective of the object surface.

Index Terms—Block matching, depth sensing, disparity estimation, image pyramiding, RGB-D sensor, stereo vision.



I. INTRODUCTION

DDEPTH sensing is a challenging task and is the core behind numerous indoor and outdoor applications. Various sensing devices have been employed recently for capturing accurate depth information. Precision of captured information is vital for many biomedical applications and helps in the detection and in-depth analysis of diseases like tumors [1]. RGB-D cameras are one of the few preferred modern

sensing systems that capture RGB images along with per-pixel depth information [2]–[4]. Currently available RGB-D sensors capture depth information at reasonable accuracy with good data transfer rates [5]– [6]. The depth range, field of view (FoV) of depth, depth resolution and frame rate of existing RGB-D sensors are presented in table IV. The depth range accuracy depends on the distance of an object in the frame from the sensor. The accuracy of the depth information is the difference between the measured depth data and the actual depth of the reference object. The precision depends on the continuous measurement of the subsequent depth information in static condition. The accuracy and precision of the depth frame of an object also depends on the distance, colour and temperature. RGB-D cameras employ a mechanism in which they project the IR radiation in an irregular pattern of dots using an IR projector and then utilize the IR cameras to detect the infrared light bounced off the object of interest. The required depth information is captured using the offset observed on comparing the projected pattern and the recorded image. Although depth information is captured with relatively good accuracy, these devices suffer from few major limitations.

Manuscript received December 7, 2019; revised January 22, 2020; accepted January 22, 2020. Date of publication January 24, 2020; date of current version April 16, 2020. This work was supported by IEEE EPICS under Grant 2016-12. The associate editor coordinating the review of this article and approving it for publication was Dr. Amitava Chatterjee. (Corresponding author: Varun G. Menon.)

Sunil Jacob is with the Center for Robotics, SCMS School of Engineering and Technology, Karukutty 683576, India (e-mail: suniljacob@scmsgroup.org).

Varun G. Menon is with the Department of Computer Science and Engineering, SCMS School of Engineering and Technology, Karukutty 683576, India (e-mail: varunmenon@ieee.org).

Saira Joseph is with the Department of Electronics and Communication Engineering, SCMS School of Engineering and Technology, Karukutty 683576, India (e-mail: saira_joseph@scmsgroup.org).

Digital Object Identifier 10.1109/JSEN.2020.2969324

One of the major constraints with RGB-D devices is in the accurate capturing of depth information with shiny or transparent objects or objects that have an absorbing matte surface [7]– [8]. Also, there can be an interference in the IR pattern due to the use of multiple RGB-D cameras and the depth information is correctly interpreted only for short distances between the camera and the object. When multiple RGB-D sensors are used with overlapping views, IR patterns of different RGB-D cameras overlap, generating IR interference. Here, each RGB-D sensor will sense and align the pattern of other RGB-D cameras with its own IR pattern and will not be able to differentiate its own IR pattern from the other. Further, the depth quality degrades creating invalid depth pixel or black pixel with no depth information. The depth map of the image can be reconstructed comparing the RGB and the IR image. Recently, few deep learning-based methods have also been proposed with RGB-D images for human motion detection and tracking [9]. Some works have also focused on improving the clarity of image and video conversions [10]. Most of the proposed methods focus on reducing the cost of the deployed system and also on enhancement of captured images. Very few methods have focused on accurate capture of depth information especially in biomedical images [3], [11]– [13].

This paper presents a novel system, block matching stereo vision (BSMV) RGB-D that utilizes the advantages offered by block matching [14] and image pyramiding along with dynamic programming [15] for accurate capture of depth information from shiny/transparent objects. Here, an IR emitter generates a known IR pattern and the depth information is recovered by comparing multiple views of the focused object. The depth map of the block matching stereo vision RGB-D camera and the resultant disparity map are fused. This fills any void regions that may have emerged due to interference or because of reflective transparent surfaces and an enhanced dense stereo image is obtained. The proposed method is applied on a 3D realistic head model and the results are presented.

The paper is organized into three sections. Related works are presented in the next section. The proposed system along with the mathematical analysis is presented in section 3. The proposed system integrated with disparity estimation, block matching, image pyramiding and dynamic programming is explained in this section. The next section presents the results obtained from the application of the proposed method on a 3D realistic head model [16]–[19]. Conclusion and future work are presented in the final section.

II. RELATED WORKS

Few techniques have been proposed in recent years for depth information enhancement of images captured by various camera sensors. In [11], authors present an interesting technique that estimates the depth of positions that are too far away and irrelevant to any objects or plans. This is enabled with the help of an RGB-D camera and a gyroscope. An advanced and flexible color-guided autoregressive model for depth recovery from low quality images captured by

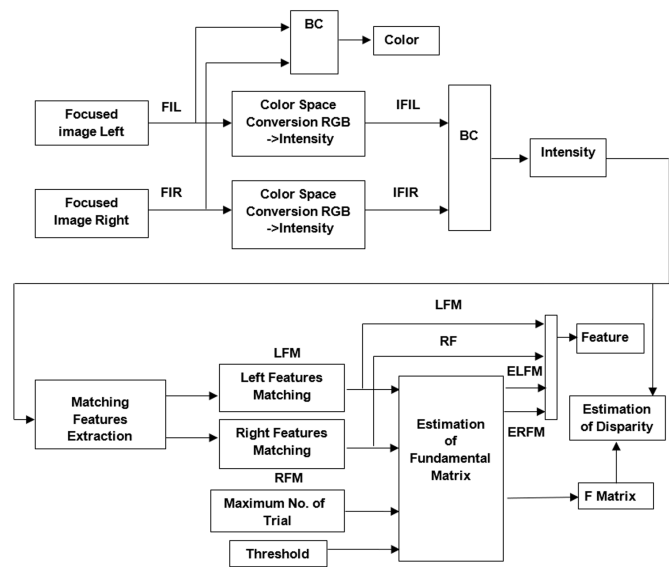


Fig. 1. System architecture.

cameras is proposed in [3]. The authors analyze the stability of the method using a linear system view. Further a parameter adapting scheme is discussed by the author for recovery of depth information. Recently, the application of RGB-D cameras has become prominent in biomedical field. Authors discuss the application of RGB-D cameras in the study of soft tissue deformation due to the bicep’s muscular activity in [12]. In [13], a depth propagation method using bilateral filtering and motion estimation is proposed. Most of the methods have certain limitations, especially in accurate detection of shiny and transparent objects. Also, some of them suffer from interference in the IR pattern due to the use of multiple RGB-D cameras and also accuracy of depth information restoration is limited. The proposed work overcomes these limitations using an RGB-D camera with rectified/non rectified block matching and image pyramiding for high speed stereo vision.

III. PROPOSED SYSTEM

Initially, the working of the system is explained with the help of an architecture diagram. Then, the mathematical modelling and analysis of the system is presented.

A. System Architecture

The architecture of the proposed system is presented in figure 1. Initially, the object of interest is captured from two different viewpoints using two RGB cameras. The focused color image pair consists of a left and right image. The focused image left (FIL) and focused image right (FIR) are connected via a bus connector (BC) and the color is extracted. Also, the color space conversion is carried out for FIL and FIR and the intensity value is extracted. Then, the matching features in each focused image is extracted using the corner detection blocks. The sum of the square difference algorithm is used to identify pixels that are common to both the focused images. The corresponding epipolar line is computed in the focused right image compared to each position in the focused left

image. On the epipolar line of the right image, the pixel that matches the pixel on the left image is identified. A quadratic polynomial is drawn such that it fits to the position of the accurately matched pixel. The polynomial curve minimum value is the final pixel location.

Here, all the matching points in left feature matching (LFM) and right feature matching (RFM) are used to compute the fundamental matrix. The maximum number of trials and the threshold value is provided for the estimation of the fundamental matrix. Eight pairs of points selected randomly from LFM and RFM along with the normalized eight-point algorithm is used to obtain the fundamental matrix. The fitness of the fundamental matrix for all points in LFM and RFM is then calculated. This value then replaces the initial fundamental matrix value. The fundamental matrix along with the calculated intensity is then used to calculate the disparity values. All the values of disparity are collected and assembled to form the disparity map.

B. Disparity Estimation

Stereo vision works on the principle of retrieving the 3D image of a structure using information of images captured from two different viewpoints. A computer compares the images while shifting the two images over each other to find the parts that match. For this, color images are first converted to gray scale using the built in `rgb2gray` function with MATLAB R2018a [20]. The shift in the pixel intensity is called the disparity and the computation output of this process is called a disparity map. The epipolar geometry of the stereo vision image is used to retrieve the relative depth information in disparity map between the two images. This gives the range between the image and the camera. However, for non-rectified images, the analysis along epipolar lines is not always aligned on the horizontal axis. The stereo images are rectified through linear transformation so that corresponding points of the two images will have same row coordinates. Rectification is a standard step used with the proposed algorithm. This step ensures that the search for matching blocks needs to be done only horizontally and not vertically during block matching.

C. Working of BSMV-RGBD

The overall working of the proposed BSMV-RGBD is discussed in three steps,

1) *Read Focused Image Left/Right Pair*: First, the object of interest is captured from two different viewpoints using two RGB cameras. The focused color image pair consists of a left and right image. From these images, color and intensity are extracted to form a grayscale image so that we have only one value (0 - 255) for each pixel. This image is used to analyze disparity map.

2) *4 × 4 Feature Block Matching*: Block matching selects a region in one image and tries to find the most similar region in the other image, using sum of absolute difference as the metric. A lower value corresponds to more similarity between the two regions. Two parameters are needed to implement block matching algorithm: size of the block and maximum disparity. In the focused left image, a 4 × 4 sub pixel feature block is

TABLE I
FREQUENTLY USED NOTATIONS

Notation	Definition
N_D	array of optimal noise disparity
I	intensity
R	optimal noise solution for $[I, d]$.
I	intrinsic matrix
$[l, d]$	boolean array threshold
D^{S-B}	baseline distance between the two RGB-D cameras from S to B
f_L	focal length_left
f_R	focal length_right
C_L	camera center_left
C_R	camera center_right
S_L	skew left
L_c	left camera
R_c	right camera
Z_d	Z depth
C_1, C_2	origin of the RGB-D camera
P_1, P_2	projection of the cross-point P on the two images

TABLE II
LIST OF ABBREVIATIONS

Abbreviation	Description
BSMV	Block Matching Stereo Vision
fMRI	Functional Magnetic Resonance Image
FoV	Field of View
IR	Infrared
RoI	Region of Interest
BC	Bus Connector
FIL	Focused Image Left
FIR	Focused Image Right
LFM	Left Features Matching
RFM	Right Features Matching
IFIL	Intensity of Focused Image Left
IFIR	Intensity of Focused Image Right
ELFM	Estimated Left Features Matching
ERFM	Estimated Right Features Matching
DP	Dynamic Programming
RHM	Realistic Head Model
NFT	Neuroelectromagnetic Forward Head Modelling Toolbox
BEM	Boundary Element Method

formed around a pixel. Then a search is done in the right-hand direction starting at the same coordinates in the right image. The search is carried out for the best match of the 4 × 4-pixel block. The bigger the block size, the less noisy the disparity map will be and results will be more accurate. However, it is computationally more expensive. In the proposed method, search is carried out for ±7 pixels surrounding the pixel of the focused left image. Column-wise searching is done for the rectified images.

3) *Dynamic Programming*: In the block matching process, the selected pixel has noise disparity with its own location and thus produces an image with noisy disparity. Smoothing is done to reduce noise disparity. By increasing the noise disparity sharing with surrounding sub pixels, the selected pixel shares the disparity with its surrounding sub pixel. By using four intra 16 × 16 modes we can predict one whole 16 × 16 macro block. The 16 × 16 macro block has 4 × 4 sub-blocks. These 4 × 4 sub-blocks can be predicted independently using nine intra 4 × 4 blocks. The individual prediction at intra 4 × 4 block is advantageous when the correlation at the block level is localized. 16 pixels are available in 4 × 4 sub

pixel block. This 4×4 sub pixel block helps to form the 4×4 predictive block. The 16 pixels in the 4×4 predictive block is generated using prediction mode in all the different directions using the information of all adjacent pixels. The optimal estimation of noise disparity along the noise disparity path from one block of image to another block of image can be efficiently solved using dynamic programming (DP).

The result of dynamic programming is applied individually to each block such that the optimal noise disparity structure is decomposed into suboptimal noise disparity problems. Then the optimal noise disparity value is to be expressed in terms of suboptimal noise disparity problem. The value of optimal noise disparity is then computed using a matrix structure with a bottom to up approach. This computed information is used to construct optimal noise disparity map. Next subsection presents the theoretical analysis of dynamic programming in the proposed BSMV RGB-D method.

4) *Mathematical Analysis of Dynamic Programming in BSMV-RGBD*: Initially, the optimal noise disparity structure has to be decomposed to suboptimal noise disparity problems. Here, the array of optimal noise disparity is $N_D[0 \dots n, 0 \dots n_1]$. For $1 \leq d \leq n$ and $0 \leq d \leq n_1$, the value of entry $N_D[l, d]$ will have the suboptimal noise subset with maximum combined values. The suboptimal noise subset $\{1, 2 \dots l\}$ consists of the weighting factors for intensity 'l'. Hence, the array of optimal noise disparity is given by,

$$N_D[l, d] = \max \left\{ \sum_{p \in R} n_p : R \subseteq \{1, 2 \dots d\} \sum_{p \in R} d_p \leq d \right\} \quad (1)$$

The computation of all the entries in the array $N_D[l, d]$ will lead to the $N_D[n, n_1]$ array as the suboptimal noise solution. For $[l, d]$, 'R' is a solution. If $R \subseteq \{1, 2 \dots l\}$ and $\sum_{p \in R} d_p \leq d$, then 'R' is an optimal noise solution for $[l, d]$. If 'R' is an optimal noise solution, then $\sum_{p \in R} n_p = N_D[l, d]$. Now the optimal noise disparity value in terms of suboptimal noise disparity problem is to be obtained. The initial setting for this scenario is $N_D[0, d] = 0$ for $0 \leq d \leq n_1$ and $N_D[l, d] = -\infty$ for $d < 0$. The recursive step is given by $N_D[l, d] = \max(N_D[l-1, d], n_l + N_D[l-1, d-d_l])$ for $1 \leq l \leq n, 0 \leq d \leq n_1$. The optimal noise disparity would select or not select 'l'. Now the value of optimal noise disparity is computed using a matrix structure in bottom to up approach. The array is computed using $N_D[l, d] = \max(N_D[l-1, d], n_l + N_D[l-1, d-d_l])$ row by row.

The first stage of dynamic programming in BSMV RGB-D is given by,

$$BSMV \ RGB-D(v, d, n, n_1) \left\{ \begin{array}{l} \text{for } (d=0 \text{ to } n_1) \ N_D[0, d]=0 \text{ for } (l=1 \text{ to } n) \\ \text{for } (d=0 \text{ to } n_1) \ \text{of } (d[l] \leq d \\ N_D[l, d]=\max\{N_D[l-1, d], v[l]+N_D[l-1, d-d[l]]\} \\ \text{else} \\ N_D[l, d]=N_D[l-1, d] \ \text{return } N_D[n, n_1] \end{array} \right\} \quad (2)$$

The algorithm is given below,

The next stage is to compute the suboptimal noise disparity. For this the auxiliary Boolean array $threshold[l, d]$ is 1, if the

l^{th} pixel in the $N_D[l, d]$ is selected, otherwise zero. Also, the optimal solution is to be formulated. The $threshold[l, d]$ is used for finding the suboptimal nose 'R' having maximum computation time. If $threshold[l, d]$ is 1 then $n \in R$, continuously repeating the process for $threshold[n-1, n_1-d_n]$. If $threshold[n, n_1]$ is 0 then $n \notin R$, continuously repeating the process for $threshold[n-1, n_1]$. The following partial code will compute the value of 'R'. Assigning n_1 to T for ($l = n$, down to 1) if $threshold[l, T] == 1$, output 1 and $T = T - d[l]$. The stage 2 of dynamic programming in BSMV RGB-D is given by $BSMV \ RGB - D(v, d, n, n_1)$, is shown at the top of the next page,

The algorithm is given below,

The application of DP completely removes the noise around the image border and the foreground object appears in better reconstructed form.

D. Pyramiding the Image

Pyramiding technique is used for the image with telescopic search to ease block matching. Given the full-scale image to detect the noise disparity, the process has to be carried over ± 7 -pixel block. By pyramiding, the image is downsized by a factor of 2. The process will reduce to ± 1 -pixel block. The noise disparity is then estimated on this down sized block. This down sized block act as the seed to the larger image. This enables search of the noise disparity only in smaller pixel block ranges and the process becomes at least five time faster compared to normal block matching. Here, three level image pyramiding is used.

Dynamic programming executed on noise disparity at every pyramidal level reduces the computational burden drastically. The depth map of the stereo image, the intrinsic parameters of the RGB-D camera and the concerned image are back projected on a pixel to pixel basis to form the 3D points. The

$$\text{intrinsic matrix I for RGB-D camera is, } I = \begin{bmatrix} f_L & S_L & C_L \\ 0 & f_R & C_R \\ 0 & 0 & 1 \end{bmatrix}$$

and the 3D image coordinates aligned with the homogenized stereo camera coordinates is $[L_c \ R_c]^T = I[L_c, R_c, Z_d]^T$. The intrinsic matrix describes all the pixels in the image which can be back projected into a 3D pixel. However, the distance of the concerned pixel to the camera is unknown. Considering S-B as the distance between the two RGB-D cameras, 'f' is the focal length, the noise disparity estimation of the depth map is given,

$$Z_d = \frac{f + D^{S-B}}{N_D} \quad (4)$$

The result of the re-projection shows the surrounding of the images appearing mutually orthogonal and the image is reconstructed accurately. Now performing a BSMV RGBD Gaussian N level pyramiding, a cascaded low pass filter produces down sampled images represented as $\vec{G}_p = [\vec{G}_0, \vec{G}_1, \vec{G}_2, \dots, \vec{G}_T]$. The separable N-dimensional kernel 't' = $[t_1 \ t_2 \ t_3 \ t_4 \ t_5]$ is used for construction of the down sampled images. In each direction a down sampling value of 2 is used.

$$\begin{aligned}
 & \text{BSMV RGB} - D(v, d, n, n_1) \\
 & \left. \begin{aligned}
 & \text{for } (d = 0 \text{ to } D) N_D[0, n_1] = 0; \text{ for } (l = 1 \text{ to } n) \text{ for } (d = 0 \text{ to } n_1) \\
 & \text{if } ((d[l] \leq d) \text{ and } (n[l] + N_D[l-1, d-d[l]] > N_D[l-1, d])) \\
 & \quad \{N_D[l, d] = n[l] + N_D[l-1, d-d[l]]; \text{Threshold}[l, T] = 1\} \\
 & \quad \text{else} \\
 & \quad \quad \{N_D[l, d] = N_D[l-1, d]; \text{Threshold}[l, T] = 0\} \\
 & \quad \quad T = n_1; \text{ for } (l = n \text{ down to } 1) \\
 & \text{If } (\text{Threshold}[l, T] == 1 \{ \text{output } l; T = T - d[l]; \} \text{ return } N_D[n, n_1] \}
 \end{aligned} \right\} \quad (3)
 \end{aligned}$$

Algorithm 1 To Calculate Optimal Noise Disparity

```

1: procedure BSMV RGB-D (v, d, n, n1)
2:   for d ← 0 to n1 ∧ ND[0, n1] == 0 do
3:     for l ← 1 to n do
4:       for d ← 0 to n1 do
5:         if (d[l] ≤ d) then
6:           ND[l,d] ← max{(ND[l-1,d], v[l] + ND[l-1,d-d[l]})}
7:         else
8:           ND[l,d] ← ND[l-1,d]
9:         end if
10:      end for
11:    end for
12:  end for
13:  return ND[n, n1]
14: end procedure
  
```

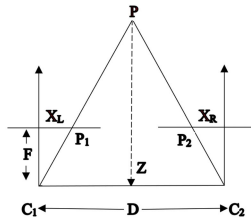


Fig. 2. Placement of RGB-D camera.

Mapping the N-dimensional kernel from one face to another is done as,

$$\vec{G}_{P+1} = M \vec{G}_P = \begin{bmatrix} 1 & 0 & 0 & & \\ 0 & 1 & 0 & \dots & \\ 0 & 0 & 0 & & \end{bmatrix} \begin{bmatrix} h & \dots & \cdot \\ \vdots & h & \vdots \\ \cdot & \dots & h \end{bmatrix} \vec{G}_P$$

Down sampling Convolution

IV. RESULTS AND DISCUSSION

This section presents the discussion on the results obtained by applying the proposed technique BSMV RGB-D to a 3D realistic head model and also to a fMRI image. Here the software used for simulation and testing is MATLAB R2018a [20] with neuroelectromagnetic forward head modelling toolbox (NFT) plug in. The 4×4 feature block matching technique has a higher rate of retrieval, as the shape of the focused image is retrieved well. The recovered image shows irregular depth range and spots of noise scattered across the image, especially

Algorithm 2 To Calculate Sub-Optimal Noise Disparity

```

1: procedure BSMV RGB-D (v, d, n, n1)
2:   for d ← 0 to n1 ∧ ND[0, n1] == 0 do
3:     for l ← 1 to n do
4:       for d ← 0 to n1 do
5:         if ((d[l] ≤ d) ∧ (n[l] +
           ND[l-1,d-d[l]] > ND[l-1,d])) then
6:           ND[l,d] ← n[l] + ND[l-1, d-d[l]]
7:           threshold[l,T] ← 1
8:         else
9:           ND[l,d] ← ND[l-1,d]
10:          threshold[l,T] ← 0
11:        end if
12:        T ← n1
13:        for d ← n to 1
14:          if (threshold[l,T]) == 1 then
15:            output l
16:            T ← T-d[l]
17:          end if
18:        end for
19:      end for
20:    end for
21:  end for
22:  return ND[n,n1]
23: end procedure
  
```

on the upper part of the image. There is excess noise scattering on the top of the image as there are no major features of the image available inside the 4×4 sub pixel matrix under comparison. The noise spot occurs because individual sub pixel disparity map is independent of the surrounding pixel.

The RGB-D cameras are kept approximately parallel while capturing multiple views of the image, to ensure that the disparity values are positive. Otherwise, the depth map will have both positive and negative values. The placement of the RGB-D cameras is illustrated in figure 2. Here, P1 and P2 are the projection of the cross-point P on the two images, C1 and C2 are the origin of RGB-D camera, F is the focal length, D is the distance between the two cameras and Z is the depth. The sub pixel estimation and correction are done by taking minimum mismatch of actual pixel and the neighboring pixel. A parabola is drawn considering these values and solved for minimum mismatch of the sub pixel. This results in the removal of the contouring effect and the estimation of disparity

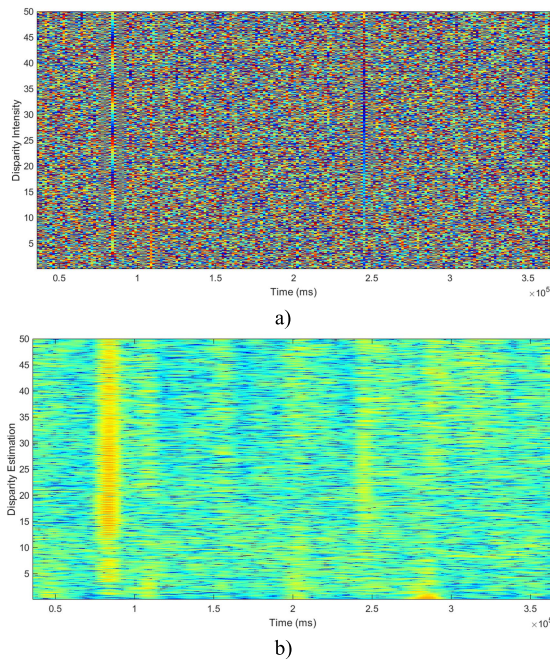


Fig. 3. a) Disparity intensity vs time b) disparity estimation vs time.

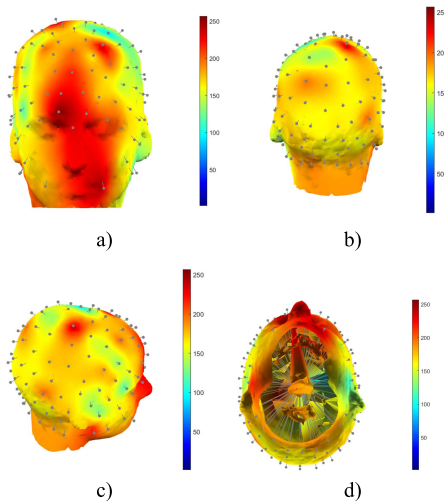


Fig. 4. IR variation in 16-bit RGB-D 3D realistic head model a) front view b) back view c) side view d) pixel mapped depth sensing view.

is fine-tuned. The result can be seen along the surface of the image.

Figure 3 shows the disparity intensity and disparity estimation of the image with varying time. The figure highlights the difference in the intensity of the pixels in the image captured by the RGB-D sensor.

A. BMSV RGB-D Applied on 3D Realistic Head Model

Figure 4 presents the IR variation in 16-bit RGB-D 3D realistic head model. These values are very vital for accurate disparity mapping. The front, back view and side views are obtained. Also, the pixel mapped depth sensing view is also presented. Figure 5 presents the IR variation in 64-bit RGB-D 3D realistic head model with various views. The significance

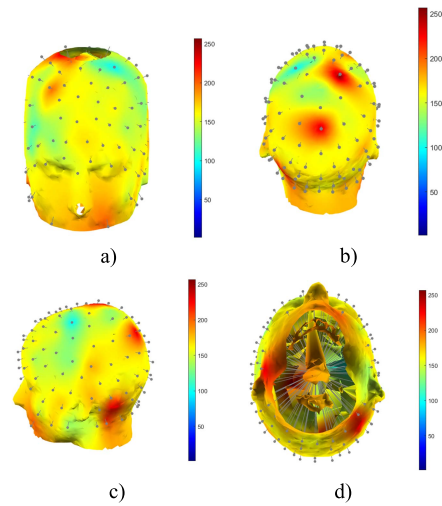


Fig. 5. IR variation in 64-bit RGB-D 3D realistic head model a) front view b) back view c) side view d) pixel mapped depth sensing view.

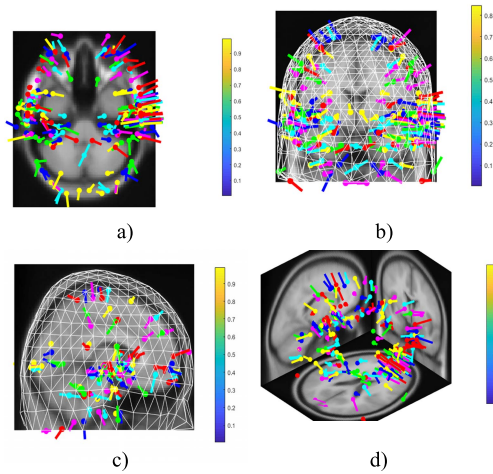


Fig. 6. 3D fMRI image a) top view b) sagittal view c) coronal view d) combined 3D view.

TABLE III
PSNR VARIATION FOR 8, 16 AND 32-bit SUB BLOCK FOR DIFFERENT BLOCK MATCHING METHOD

TSS (Three Step Search)	NTSS (New Three Step Search)	Four Step Search (FSS)	ARPS (Adaptive Rood Pattern Search)	BMSV RGB-D
35.52	36.44	36.87	37.79	39.81
35.17	35.55	36.39	37.12	38.09
35.01	35.50	36.10	37.02	38.17

of 16-bit and 64-bit is in the size of the physical memory support for RGB-D camera.

B. BMSV-RGBD applied on fMRI image

The top view, sagittal view and coronal view with mesh of 3D fMRI image is presented in figure 6. The weighted

TABLE IV
COMPARISON OF BSMV RGB-D WITH EXISTING CAMERA

Sensors (R) & Parameters (C)	Xtion Pro Live [21]	Orbbec Astra S [22]	Microsoft Kinect ii [23]	RS SR300 [24]	Intel D435 [25]	Proposed BSMV RGB-D
Technology	Infrared pattern	Structured light technology	Time of Flight (ToF)	Infrared pattern	Active stereoscopy	Infrared-Block Matching, Image Pyramiding and Dynamic Programming
Depth Range (m)	0.7 to 3.5	0.4 to 2	0.5 to 4.5	0.3 to 2	0.2 to 8	0.2 to 8
Field of View of Depth	58° H, 45° V, 70° D	60°H, 49.5°V, 73°D	70°H, 60°V	73° H, 59° V, 90° D	85.2 ° H, 58° V,	93.2° H, 68.5° V, 100.6° D
Frame rate (fps)	30, 60	30	30	30	30, 60, 90	30, 60, 90
Depth resolution (pixel)	628 × 468	640 × 480	512 × 424	640 x 480	1280×720	1280 × 720 pixel, 848 × 480, 640 × 480
Power consumption	< 2.5W	< 2.4W	~ 15W	1.8	600–1900 mW	600-1500 mW
RGB Resolution (pixel)	1280 × 1024	640 × 480	1920 × 1080	1920 × 1080	1920 × 1080	1920 × 1080, 1280 × 720, 848 × 480, 640 × 480

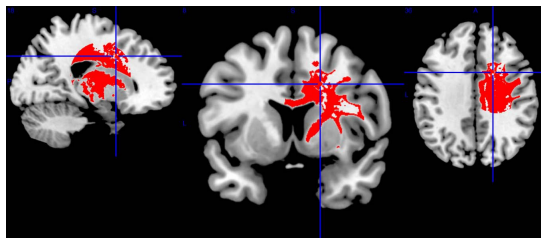


Fig. 7. Depth analysis of 3D fMRI image with BSMV-RGB-D.



Fig. 8. Image of an object with transparent surface (spectacles) captured and reconstructed using BSMV RGB-D method.

magnetic resonance images are analysed for cerebrospinal fluid, segmenting the skull, scalp and brain tissue. For the forward problem numerical solution, boundary element method (BEM) is used. The BEM meshes is generated once the segmented tissue volume is extracted. The individual realistic head model is wrapped by template head model electrode location if magnetic resonance image is not available. Here, the coordinates are aligned with the homogenized stereo camera. The intrinsic matrix describes all the pixels in the image which can be back projected into a 3D pixel. The result of the re-projection shows the surrounding of the images appears mutually orthogonal and the image is reconstructed accurately.

Figure 7 presents the depth analysis of 3D fMRI image with BSMV RGB-D. The cross point on the fMRI image indicates the seed pixel. The RGB-D image enabled with telescopic search is analysed using pyramiding technique for block matching. The noise disparity is detected for the full-scale image and it is applied over the 7-pixel block. Pyramiding will downsize the image by a factor of 2, which will further scale down to 1-pixel block. For this down sized block, the noise disparity is calculated. The down sized block will be the seed for the scaled up RGB-D image. The noise disparity is enabled for the search of the down sized smaller

pixel block. The search process is fivefold faster compared to existing block matching. The dynamic programming is run on the noise disparity which reduces the computational burden substantially. The IR projector emits the predefined pattern and the concerned RGB-D image is back projected on a pixel to pixel basis to form depth information.

The seed point in the image is identified initially and mapped to 3D space for the depth information. To identify the edge and mark it automatically, canny edge detection algorithm is used. Then the noise disparity is calculated from the cross mark on the two images. The placement of camera is shown in figure 2. The camera A is displaced to the right direction, that is in the X-direction positive D_x . The 3D coordinates of the left camera (X_1, Y_1, Z_1) would have ($X_1 - D_x, Y_1, Z_1$) coordinates in the right camera. This would project different image point X coordinates for the left and right camera creating noise disparity. The noise disparity value will be positive, negative or zero depending upon the position of the object compared to the cross point. This noise disparity is used to calculate the information of an object. The depth is then calculated by using the equation 4. The calibrated depth range obtained here is 0.2 m to 8 m for 16-bit and 64-bit realistic head models. Figure 8 presents the results obtained with the BSMV RGB-D with objects having transparent surface. Here,

the human face is sensed by the RGB-D camera and with the accurate depth information captured using the proposed method, the 3D image is reconstructed. The spectacle on the face is correctly decoded and shows a nullifying effect on the actual 3D object.

Table III presents the comparison of the proposed method with other existing block matching methods in terms of PSNR for varying sub block sizes. The proposed method BSMV RGB-D has better PSNR value compared to all the other existing block matching techniques and this signifies better performance. In block matching BMSV-RGBD, each pixel is having a very high correlation with its neighbors. This makes it easy to assign motion vector to a sub pixel block compared to individual pixels. In the BSMV-RGBD the RGB-D frame is segmented into $n \times n$ blocks. The current block of subsequent frame is aligned and matched with the corresponding subblock in the same coordinates of the previous frame for the pixel having a very large motion displacement. The optimized alignment and matching give the correct displacement.

V. CONCLUSIONS

This paper presents and discusses a novel system for object tracking and capturing of accurate depth information from shiny/transparent objects using RGB-D camera with rectified/non-rectified block matching and image pyramiding along with dynamic programming. The architecture and the working of the proposed system is presented and discussed in detail. Theoretical analysis of the BSMV dynamic programming algorithm is presented. The results achieved by the proposed method in simulations using MATLAB 2018a are presented. The results from the depth information analysis carried out on a 3D realistic head model and an fMRI image illustrate the accuracy of the proposed method. The advantages and better performance of the proposed method is also highlighted using a comparison with the existing RGB-D sensors and block matching techniques. Finally, the capture and accurate reconstruction of an object with transparent surface is demonstrated using the proposed method.

REFERENCES

- [1] D. Riahi, W. Bouachir, Y. Ouakrim, and N. Mezghani, "Depth imaging system for human posture recognition," in *Proc. IEEE 4th Middle East Conf. Biomed. Eng. (MECBME)*, Tunis, Tunisia, Mar. 2018, pp. 177–181.
- [2] C.-C. Sun, Y.-H. Wang, and M.-H. Sheu, "Fast motion object detection algorithm using complementary depth image on an RGB-D camera," *IEEE Sensors J.*, vol. 17, no. 17, pp. 5728–5734, Sep. 2017.
- [3] J. Yang, X. Ye, K. Li, C. Hou, and Y. Wang, "Color-guided depth recovery from RGB-D data using an adaptive autoregressive model," *IEEE Trans. Image Process.*, vol. 23, no. 8, pp. 3443–3458, Aug. 2014, doi: 10.1109/tip.2014.2329776.
- [4] M. Gao, J. Jiang, G. Zou, V. John, and Z. Liu, "RGB-D-based object recognition using multimodal convolutional neural networks: A survey," *IEEE Access*, vol. 7, pp. 43110–43136, 2019.
- [5] P. Henry, M. Krainin, E. Herbst, X. Ren, and D. Fox, "RGB-D mapping: Using Kinect-style depth cameras for dense 3D modeling of indoor environments," *Int. J. Robot. Res.*, vol. 31, no. 5, pp. 647–663, Apr. 2012.
- [6] Z. Cai, Y. Long, and L. Shao, "Adaptive RGB image recognition by visual-depth embedding," *IEEE Trans. Image Process.*, vol. 27, no. 5, pp. 2471–2483, May 2018.

- [7] C. Jing, J. Potgieter, F. Noble, and R. Wang, "A comparison and analysis of RGB-D cameras' depth performance for robotics application," in *Proc. 24th Int. Conf. Mechatronics Mach. Vis. Pract. (M2VIP)*, Auckland, New Zealand, Nov. 2017, pp. 1–6.
- [8] Y. W. Kuan, N. O. Ee, and L. S. Wei, "Comparative study of intel R200, Kinect v2, and primesense RGB-D sensors performance outdoors," *IEEE Sensors J.*, vol. 19, no. 19, pp. 8741–8750, Oct. 2019.
- [9] P. S. Santoso and H.-M. Hang, "Learning-based human detection applied to RGB-D images," in *Proc. IEEE Int. Conf. Image Process. (ICIP)*, Beijing, China, Sep. 2017, pp. 3365–3369.
- [10] D. K. Jain, S. Jacob, J. Alzubi, and V. Menon, "An efficient and adaptable multimedia system for converting PAL to VGA in real-time video processing," *J. Real-Time Image Process.*, pp. 1–13, 2019, doi: 10.1007/s11554-019-00889-4.
- [11] T.-H. Chien, Y.-H. Lu, J.-W. Lin, and R.-G. Chang, "An enhanced depth estimation system using RGB-D cameras and gyroscopes," in *Proc. Int. Conf. Appl. Syst. Innov. (ICASI)*, Sapporo, Japan, May 2017, pp. 1554–1557, doi: 10.1109/ICASI.2017.7988224.
- [12] M. Goffredo *et al.*, "Shape analysis of bicipital contraction by means of RGB-D sensor, parallel transport and trajectory analysis," in *Proc. XIV Medit. Conf. Med. Biol. Eng. Comput.*, Cyprus, Middle East, 2016, pp. 634–639.
- [13] H. Wang, Y. Tian, and Y. Zhang, "A novel depth propagation algorithm with color guided motion estimation," in *Proc. 2013 Vis. Commun. Image Process. (VCIP)*, Kuching, Malaysia, Nov. 2013, pp. 1–5, doi: 10.1109/VCIP.2013.6706419.
- [14] F. Liu, "3D block matching algorithm in concealed image recognition and E-commerce customer segmentation," *IEEE Sensors J.*, to be published.
- [15] A. A. Altahir *et al.*, "Optimizing visual surveillance sensor coverage using dynamic programming," *IEEE Sensors J.*, vol. 17, no. 11, pp. 3398–3405, Jun. 2017.
- [16] P. G. Vinoj, S. Jacob, V. G. Menon, S. Rajesh, and M. R. Khosravi, "Brain-controlled adaptive lower limb exoskeleton for rehabilitation of post-stroke paralyzed," *IEEE Access*, vol. 7, pp. 132628–132648, 2019, doi: 10.1109/ACCESS.2019.2921375.
- [17] S. Rajesh, V. Paul, V. G. Menon, S. Jacob, and P. Vinod, "Secure brain to brain communication with edge computing for assisting post-stroke paralyzed patients," *IEEE Internet Things J.*, to be published, doi: 10.1109/JIOT.2019.2951405.
- [18] S. Jacob, V. G. Menon, F. Al-Turjman, V. P. G., and L. Mostarda, "Artificial muscle intelligence system with deep learning for post-stroke assistance and rehabilitation," *IEEE Access*, vol. 7, pp. 133463–133473, 2019.
- [19] V. G. Menon, S. Jacob, S. Joseph, and A. O. Almagrabi, "SDN powered humanoid with edge computing for assisting paralyzed patients," *IEEE Internet Things J.*, to be published, doi: 10.1109/JIOT.2019.2963288.
- [20] Accessed: Apr. 10, 2019. [Online]. Available: https://in.mathworks.com/products/new_products/release2018a.html
- [21] Accessed: Apr. 17, 2019. [Online]. Available: https://www.asus.com/3D-Sensor/Xtion_PRO_LIVE/specifications/
- [22] Accessed: Apr. 17, 2019. [Online]. Available: <https://orb3d.com/product-astra-pro/>
- [23] E. Lachat, H. Macher, T. Landes, and P. Grussenmeyer, "Assessment and calibration of a RGB-D camera (Kinect v2 Sensor) towards a potential use for close-range 3D modeling," *Remote Sens.*, vol. 7, no. 10, pp. 13070–13097, Oct. 2015.
- [24] Accessed: Apr. 17, 2019. [Online]. Available: <https://ark.intel.com/content/www/us/en/ark/products/92329/intel-realsense-camera-sr300.html>
- [25] Accessed: Apr. 17, 2019. [Online]. Available: <https://ark.intel.com/content/www/us/en/ark/products/128255/intel-realsense-depth-camera-d435.html>



Sunil Jacob (Member, IEEE) received the Ph.D. degree in electronics and communication engineering from Bharathiar University, India, in 2015. He is currently the Director with the Center for Robotics, and also a Professor with the Department of Electronics and Communication Engineering, SCMS School of Engineering and Technology, India. His research interests include SDN, edge computing, brain computer interface, and signal processing.



Varun G. Menon (Senior Member, IEEE) received the Ph.D. degree in computer science and engineering from Sathyabama University, India, in 2017. He is currently an Associate Professor with the Department of Computer Science and Engineering, SCMS School of Engineering and Technology, India. His research interests include sensors, IoT, fog computing, and underwater acoustic sensor networks. He is currently serving as the Guest Editor for the IEEE SENSORS JOURNAL, the *IEEE Internet of Things Magazine*,

and the IEEE TRANSACTIONS ON INDUSTRY INFORMATICS. He is also a Distinguished Speaker of ACM.



Saira Joseph (Member, IEEE) received the M.Tech. and Ph.D. degrees in electronics and communication engineering from the Cochin University of Science and Technology, Kerala, India, in 2006 and 2017, respectively. She is currently an Associate Professor and the Head of Department of Electronics and Communication Engineering, SCMS School of Engineering and Technology, Kerala, India. Her interests include sensors, edge computing, fractal antennas, UWB, RADAR, and metamaterials.

Secure Brain-to-Brain Communication With Edge Computing for Assisting Post-Stroke Paralyzed Patients

Sreeja Rajesh, Varghese Paul, Varun G. Menon^{1b}, Member, IEEE, Sunil Jacob, and P. Vinod

Abstract—Stroke affects 33 million individuals worldwide every year and is one of the prime causes of paralysis. Due to partial or full paralysis, most of the patients affected by stroke depend on caregivers for the rest of their lives. Easy and efficient communication from the patient to the caregiver is a vital parameter determining the quality of life during rehabilitation. Several solutions, such as brain-computer interface (BCI) systems and exoskeletons, are proposed for post-stroke rehabilitation. But, most of these devices are expensive, sophisticated, and put an additional burden on the patient. Also, the communication between the patient and the caregiver is insecure. In this article, the brain-to-brain interface technique is integrated with an efficient encryption algorithm to enable secure transmission of information from the patient's brain to the caregiver. When a patient thinks of a word or a number, the thought is transmitted with the help of an electroencephalogram (EEG) headset through a wireless medium to the recipient, who correctly interprets the thoughts conveyed by the sender and types the same alphabet on the keyboard at his/her end. The transmitted message at the edge is encrypted with a lightweight novel tiny symmetric algorithm (NTSA), which can only be decrypted at the edge receiver. The Internet of Things integrated system is also flexible to send signals to multiple caregivers at the same time. The proposed method tested on ten users gave an average effective concentration percentage of 78.9% along with the secure transmission, which is a significant result compared with existing solutions.

Index Terms—Brain-to-brain interface, edge computing, electroencephalogram (EEG), Internet of Things, post-stroke paralysis, secure communication, security and privacy, TMS.

Manuscript received June 22, 2019; revised August 26, 2019, September 18, 2019, and October 22, 2019; accepted October 30, 2019. Date of publication November 5, 2019; date of current version April 14, 2020. This work was supported in part by EPICS in IEEE under Grant 2016-12. (Corresponding author: Varun G. Menon.)

S. Rajesh is with the Department of Computer Science, Bharathiar University, Coimbatore 641046, India (e-mail: m.sreeja79@gmail.com).

V. Paul is with the Department of Information Technology, Rajagiri School of Engineering and Technology, Ernakulam 682039, India (e-mail: vp.itcusat@gmail.com).

V. G. Menon and P. Vinod are with the Department of Computer Science and Engineering, SCMS School of Engineering and Technology, Karukutty 683576, India (e-mail: varunmenon@scmsgroup.org; vinodp@scmsgroup.org).

S. Jacob is with the Center for Robotics, SCMS School of Engineering and Technology, Karukutty 683576, India (e-mail: suniljacob@scmsgroup.org).

Digital Object Identifier 10.1109/JIOT.2019.2951405

I. INTRODUCTION

STROKE is a major cause of full or partial paralysis among people, especially, prevalent in developing countries. Thirty five percent of survivors have permanent disability one year after a stroke [1] and all of them need care in a nursing home or other long-term assistance. Communicating ideas and requests from the patient to the caregiver is a significant challenge in these conditions. Communicating the feelings can often be unclear and hard to understand, depending on how a person describes or expresses them in words. It is more challenging when the patient and the caregiver are far apart. Exoskeletons have been proposed in recent years as a possible solution to this issue. Regaining the ability to walk has been major focus of most of the exoskeleton systems. Progressive, task-specific, and repetitive training based on the principles of motor learning and neuroplasticity is carried out with the help of exoskeletons. Wearable robots strapped onto legs, and actuated motors are also used for rehabilitation in many scenarios [2]. Numerous alternate brain-computer interface (BCI) [3], [4] systems have also emerged for stroke rehabilitation. Most of the proposed solutions are expensive, sophisticated, put an additional burden on the patient, and also do not ensure secure and efficient communication between the patient and the caregiver [5].

Recently, the brain-to-brain interface systems [6]–[9] have opened numerous possibilities in efficient post-stroke rehabilitation, including provision for direct communication of the ideas and thoughts between the patient and the caregiver. This technology involves the transmission of information from one person's brain to another using a wireless medium. The significant advantage of this technology is that it is noninvasive and does not have the complications of using bulky devices like exoskeletons and comes with less cost. This technology is still in its early stages and has numerous limitations and challenges. The recent research in post-stroke rehabilitation has thus focused on developing efficient systems using the brain-to-brain interface. Most of the existing brain-to-brain interface systems work only with simulations and fail to deliver in real-time environments. Another major limitation of current systems is the lack of security in the transmitted message. Whenever the information is transmitted through a wireless medium or any public medium like the Internet, it is essential to have a suitable security mechanism. Securing the sensitive data transferred between the patient and the caregiver is vital for regaining the confidence during the rehabilitation phase.

Very few works have been done in this article direction, and this article focuses on proposing an efficient solution to this problem.

In the proposed system, the secrecy of information transferred is attained using cryptography wherein the transferred file is scrambled into a nonreadable form by the sender. The recipient on receiving the scrambled message from the sender de-scrambles it into a readable form. The tiny encryption algorithm (TEA) [10]–[12], which is one of the most widely used symmetric algorithms due to the ease of implementation and less memory utilization, is improved and used in the system as the novel tiny symmetric algorithm (NTSA). It enhances the security features of TEA by introducing more key confusions [13]–[15]. The keys are altered dynamically, thus making it secure from the intruders. Since the key is computed dynamically, the key values change during execution time and cannot be precomputed. This algorithm is then used in the proposed system for the secure transmission of information from the patient to the caregiver. As the computation happens at the edge of the network, it eliminates the delay in transmission and processing of the data that exists in systems with centralized data processing centers. The contributions of this article are as follows.

- 1) A simple, noninvasive, and efficient brain-to-brain thought transfer system that helps to share the thoughts between the patient and the caregiver with electroencephalogram (EEG) headset at the transmitting end and magnetic stimulation at the receiving end.
- 2) Edge computing powered secured transmission of message between the patient and the caregiver using an efficient and lightweight symmetric encryption algorithm.
- 3) Real-time implementation with analysis of the results obtained is provided.

The remainder of this article is organized into six sections. Section II reviews the related work in brain-to-brain communication. Section III describes the theoretical analysis of the proposed system. Section IV provides the details of the proposed system, its working, and discussion. Section V presents the results obtained with experiments and proves that the proposed method achieves secured data transmission between the patient and the caregiver. Finally, Section VI summarizes the findings and presents the conclusion and future work.

II. RELATED WORKS

This section presents the discussion on few latest related works in the brain-to-brain communication and BCI. The usage of BCI facilitates a person to communicate without the intervention of the brain's normal output pathways of peripheral nerves and muscles. The EEG features are used to identify the message or commands from the brain. The two methods used in BCI are invasive and noninvasive BCI. The invasive BCI uses implanted electrodes in brain tissue, and noninvasive uses EEG recordings obtained by placing electrodes at various points on the scalp of a person. In [16], multiple

TABLE I
FREQUENTLY USED NOTATIONS

Notation	Definition
T_X	transmitter headset
R_X	receiver headset
L_B	height of T_X from ground
β_B	angle of incidence
β_D	angle of reflection
D_{Total}	total distance between T_X and R_X
ϵ_{B-D}	signal strength of the directly transmitted signal
ϵ'_{B-D}	signal strength of the reflected part
ϵ_{Total}	total transmitted signal energy
ΔD	difference of the distance travelled by the reflected and line of sight waves
μ_F	propagation loss in the environment
β_{LU}	incident and reflection loss of the transmitted signal
$\gamma(L_B)$	T_X side gain
$\gamma(L_D)$	R_X side gain
μ_{env}	environmental gain factor

variations of using BCI in communication and motor control are discussed. Wolpaw *et al.* [17] conducted a survey and identified that the BCI systems were efficient in providing communication and controls the options to those with a disability. Mason and Birch [18] discussed a prototype of an asynchronous switch known as LF-ASD. For people who are paralyzed and have no voluntary muscle control, a BCI might give the ability to answer simple questions quickly and control the environment [19]. Zhang *et al.* [20] proposed a brain interface system to control a rat implanted with micro-electrodes. Maksimenko *et al.* [21] proposed a system for distributing the cognitive load among all members of the group toward achieving a common task. In [22]–[24], user authentication and other security mechanism that can be introduced in the transmission of signals from the brain to other devices are discussed.

Most of the existing systems have minimal works only with simulations and fail to deliver in real-time environments. Another major limitation with most of the methods is the lack of adequate security in the transmitted message. Also, the privacy of the information transmitted from the patient to the caregiver is not provided. The proposed system is designed to overcome all the above limitations. Using the concept of brain-to-brain interface, edge computing, and a novel lightweight symmetric encryption algorithm [13], [25], [26], secure transmission of information from the patient's brain to the caregiver using wireless medium is achieved with EEG and TMS. The Internet of Things module can be further integrated into the system to transfer information securely to multiple receivers.

III. MATHEMATICAL ANALYSIS

In this section, the theoretical analysis of the transmitted signal strength is presented and discussed. Table I presents the summary of frequently used notations in this article.

Analysis of the thought transfer signal along with the range estimation is presented in Fig. 1. The total transmitted signal from T_X is calculated from the above deployment scenario of the proposed system. The total transmitted signal is the sum of the signal that is directly transmitted and the part of the signal that is reflected from the surface. Hence, the total transmitted

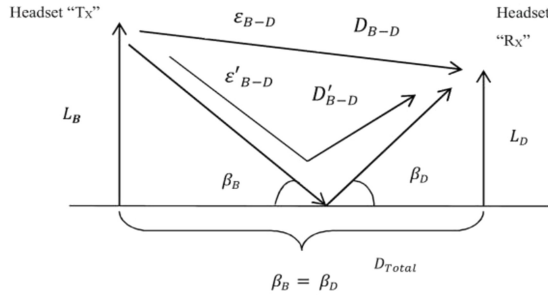


Fig. 1. Signal analysis for thought transfer.

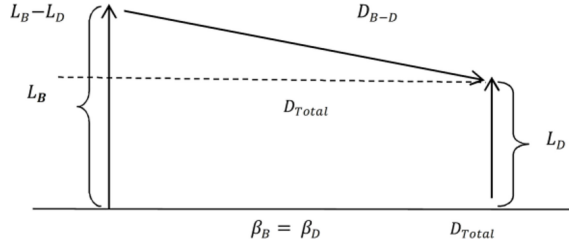


Fig. 2. Range analysis of thought processing.

signal energy is given by

$$\varepsilon_{\text{Total}} = \varepsilon_{B-D} + \varepsilon'_{B-D}. \quad (1)$$

A reference signal strength of ε_0 at a distance D_0 is assumed by the system, which is given by

$$\varepsilon_{B-D} = \frac{\varepsilon_0 D_0}{D_{\text{Total}}} e^{j2\pi F_c \left(t_0 - \frac{D_{B-D}}{c} \right)} \quad (2)$$

$$\varepsilon'_{B-D} = \frac{-\varepsilon_0 D_0}{D_{\text{Total}}} e^{j2\pi F_c \left(t_0 - \frac{D'_{B-D}}{c} \right)}. \quad (3)$$

Here, the negative sign in (3) is due to the phase inversion of the signal. Substituting (2) and (3) into (1) gives

$$\varepsilon_{\text{Total}} = \frac{\varepsilon_0 D_0}{D_{\text{Total}}} e^{j2\pi F_c \left(t_0 - \frac{D_{B-D}}{c} \right)} - \frac{\varepsilon_0 D_0}{D_{\text{Total}}} e^{j2\pi F_c \left(t_0 - \frac{D'_{B-D}}{c} \right)} \quad (4)$$

$$\varepsilon_{\text{Total}} = \frac{\varepsilon_0 D_0}{D_{\text{Total}}} e^{j2\pi F_c \left(t_0 - \frac{D_{B-D}}{c} \right)} \left(1 - e^{j2\pi F_c \frac{\Delta D}{c}} \right) \quad (5)$$

where $\Delta D = D'_{B-D} - D_{B-D}$ that gives the difference of the distance traveled by the reflected wave and the distance traveled by the direct line-of-sight wave

$$\varepsilon_{\text{Total}} = \frac{\varepsilon_0 D_0}{D_{\text{Total}}} e^{-j2\pi F_c \left(t_0 - \frac{D_{B-D}}{c} \right)} \left(1 - e^{j2\pi \frac{\Delta D}{\lambda_0}} \right) \quad (6)$$

where $(C/F_c) = \lambda_0$

$$\varepsilon_{\text{Total}} = \frac{\varepsilon_0 D_0}{D_{\text{Total}}} e^{-j2\pi F_c \left(t_0 - \frac{D_{B-D}}{c} \right)} e^{j2\pi \frac{\Delta D}{2\lambda_0}} e^{-j2\pi \frac{\Delta D}{2\lambda_0}} \quad (7)$$

$$\varepsilon_{\text{Total}} = -\frac{\varepsilon_0 D_0}{D_{\text{Total}}} e^{-j2\pi F_c \left(t_0 - \frac{D_{B-D}}{c} \right)} e^{j2\pi \frac{\Delta D}{2\lambda_0}} \sin \left(2\pi \frac{\Delta D}{2\lambda_0} \right). \quad (8)$$

The magnitude of the total signal strength is obtained as

$$|\varepsilon_{\text{Total}}| = \frac{\varepsilon_0 D_0}{D_{\text{Total}}} \left| \sin \left(2\pi \frac{\Delta D}{2\lambda_0} \right) \right|. \quad (9)$$

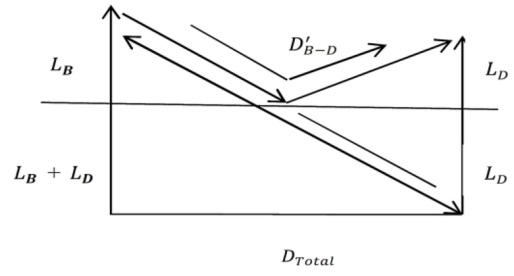


Fig. 3. Range estimation using mirror image analysis.

Fig. 2 presents the range analysis of the thought processing signal. The actual range of the line-of-sight signal is given by D_{B-D} which is obtained as

$$D_{B-D} = \sqrt{(L_B - L_D)^2 + (D_{\text{Total}})^2}. \quad (10)$$

Fig. 3 presents the range estimation of the signal using the mirror image analysis. The reflected signal in the system is given by

$$D'_{B-D} = \sqrt{(L_B + L_D)^2 + (D_{\text{Total}})^2}. \quad (11)$$

Using (11), the value of ΔD is estimated, where $\Delta D = D'_{B-D} - D_{B-D}$

$$\Delta D = \sqrt{(L_B + L_D)^2 + (D_{\text{Total}})^2} - \sqrt{(L_B - L_D)^2 + (D_{\text{Total}})^2} \quad (12)$$

$$\Delta D = D_{\text{Total}} \left\{ \sqrt{1 + \left(\frac{L_B + L_D}{D_{\text{Total}}} \right)^2} - \sqrt{1 + \left(\frac{L_B - L_D}{D_{\text{Total}}} \right)^2} \right\} \quad (13)$$

where $L_B, L_D \ll D_{\text{Total}}$.

Approximating the ΔD value with respect to L_B, L_D , and D_{Total}

$$\Delta D \approx D_{\text{Total}} \left\{ \left(1 + \frac{1}{2} \left(\frac{L_B + L_D}{D_{\text{Total}}} \right)^2 \right) - \left(1 + \frac{1}{2} \left(\frac{L_B - L_D}{D_{\text{Total}}} \right)^2 \right) \right\}. \quad (14)$$

Reducing the above equation, we obtain

$$\Delta D \approx 2 \frac{L_B L_D}{D_{\text{Total}}}. \quad (15)$$

Substituting the value of ΔD in (9), the magnitude of the total signal strength is obtained as

$$|\varepsilon_{\text{Total}}| = \frac{2\varepsilon_0 D_0}{D_{\text{Total}}} \sin \left(2\pi \frac{\Delta D}{2\lambda_0} \right). \quad (16)$$

Considering a very small value of sine, the magnitude of the total signal strength is approximated as

$$|\varepsilon_{\text{Total}}| \approx \frac{2\varepsilon_0 D_0}{D_{\text{Total}}} 2\pi \frac{\Delta D}{2\lambda_0} \quad (17)$$

$$|\varepsilon_{\text{Total}}| \approx \frac{2\varepsilon_0 D_0}{D_{\text{Total}}} \frac{2\pi}{2\lambda_0} \frac{2L_B L_D}{D_{\text{Total}}}. \quad (18)$$

Finally, the approximated total strength of the thought processes signal is obtained as

$$|\varepsilon_{\text{Total}}| \approx 4\pi \frac{\varepsilon_0 D_0}{\lambda_0 (D_{\text{Total}})^2} L_B L_D. \quad (19)$$

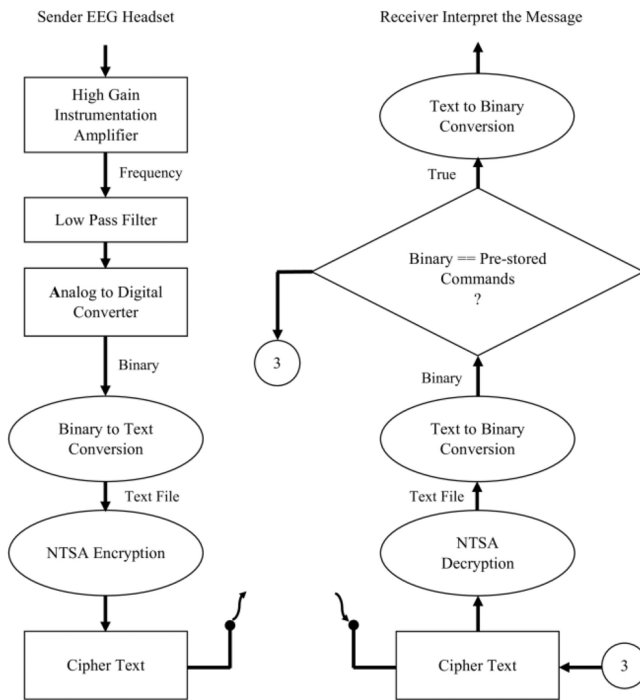


Fig. 4. System architecture.

The correctness factor introduced in the signal is discussed below. The 50th percentile loss in dB is given by

$$\mu_{50}(dB) = \mu_F + \beta_{LU} - \gamma(L_B) - \gamma(L_D) - \mu_{env}. \quad (20)$$

Here, μ_F is the propagation loss in the environment, β_{LU} is the incident and reflection loss of the transmitted signal, $\gamma(L_B)$ is the T_X side gain factor, $\gamma(L_D)$ is the R_X side gain factor, and μ_{env} is the environmental gain factor.

IV. PROPOSED SYSTEM

This article aims to securely transfer the thoughts between the paralyzed patient and the caregiver with the help of EEG headsets. The idea is to share the thoughts with EEG headset at the transmitting end and use magnetic stimulation at the receiving end. The EEG recordings from the brain are taken by placing a cap of electrodes on a person's scalp, using a 10–20 placement scheme. The electrical stimulation from the brain's cortex region is then recorded and transmitted wirelessly through the cloud. At the receiving end, the machine converts the message into the equivalent electrical signal. This electrical signal produces equivalent magnetic stimulation in the form of TMS and the receiver interprets the information based on the flashes he/she sees. Fig. 4 shows the detailed block diagram of the proposed system.

A. At the Sender Side

Sender wears the EEG headset which is shown in Fig. 5. Then, using the 10–20 probe placement scheme on the person's scalp, the electric impulses at the neural synapses from the brain cortex region is fetched and recorded. Fig. 5 shows the EEG headset to which EEG electrodes are attached and also the placement of electrodes on the brain. This EEG

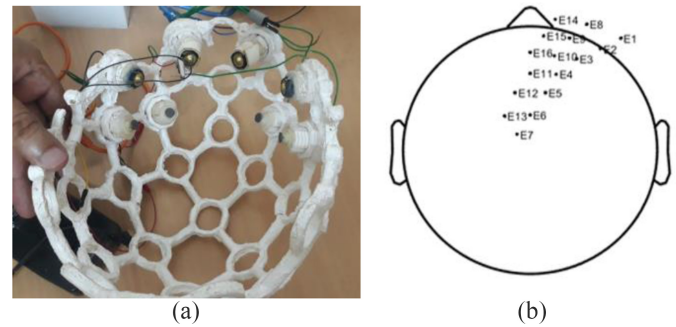


Fig. 5. (a) EEG headset. (b) Electrode placement on the brain [23].



Fig. 6. Electromagnetic coil.

recording obtained is feeble, and hence amplified using the high-gain instrumentation amplifier. The noise in the signal is mitigated by passing the signal through a low-pass filter. The resulting analog signal is digitized using the analog-to-digital convertor (ADC). This digitized signal is converted to text and can be securely sent through the public medium using the proposed NTSA encryption algorithm.

B. At the Receiver Side

The ciphertext transmitted by the sender reaches the receiver through the wireless medium. On reception of the ciphertext, it is decrypted using the NTSA decryption algorithm and the text file is obtained. The text file is converted into binary which is compared with the prestored commands. If it matches with the prestored commands, the TMS circuit is triggered correspondingly to generate the TMS flashes which will be interpreted by the receiver. The TMS circuit is designed with an external source of 230-V ac signal and is step down to 24-V ac signal using the step-down transformer and is passed to the coil via Triac switch. The 12-V step-down transformer is used to trigger the timer circuit. The Triac is used as a high-power switching device and is controlled by the binary value. Depending on 0s and 1s, TMS creates flash (binary 1 for vibration with flash and binary 0 for no vibration and flash). The helmet at the receiver side has two coils inside it and each coil has 30 000 turns. One coil is used to control the activity of left part of the brain and the other to control the right part of the brain. Based on the excitation signal from the coil, the brain gets stimulated to create a flash or equivalent vibration. Fig. 6 shows the electromagnetic coil with the circuit.

Algorithm 1 Encryption

```

1: procedure E(n)encryption (plaintext[64], key[128],  $\emptyset$ )
2:   // Initialize subkeys  $sk_i$  and plaintexts  $P_i$ 
3:    $sk_0 \leftarrow key[i : i+32]$ 
4:    $sk_1 \leftarrow key[i+33 : i+64]$ 
5:    $sk_2 \leftarrow key[i+65 : i+96]$ 
6:    $sk_3 \leftarrow key[i+97 : i+128]$ 
7:    $C_0 \leftarrow plaintext[i : i+32]$ 
8:    $C_1 \leftarrow plaintext[i+33 : i+64]$ 
9:    $ksc \leftarrow (2^{31}) / \emptyset$ 
10:   $kc \leftarrow 0$ 
11:  // The loop generates cipher text  $C_0$  and  $C_1$  and the keys  $sk_1$ 
    and  $sk_3$ 
12:  for cycle  $\leftarrow 0$  to 32 do
13:     $kc \leftarrow kc + ksc$ 
14:     $C_0 \leftarrow C_0 + ((C_1 << 4 \wedge sk_0) \oplus (C_1 \wedge kc) \oplus$ 
       $((C_1 >> 5) \wedge sk_1))$ 
15:     $sk_1 \leftarrow sk_1 + (sk_0 \oplus (xtract(C_0)))$ 
16:     $C_1 \leftarrow C_1 + ((C_0 << 4 \wedge sk_2) \oplus (C_0 \wedge kc) \oplus ((C_0$ 
       $>> 5) \wedge sk_3))$ 
17:     $sk_3 \leftarrow sk_3 + (sk_2 \oplus (xtract(C_1)))$ 
18:  end for
19:   $newk1 \leftarrow sk_1$ 
20:   $newk3 \leftarrow sk_3$ 
21: end procedure

// Details of key confusion xtract function
1: procedure xtract(a)
2: while  $i = \text{lal}$  do
3:   if  $a[i] = 32$  then
4:      $a[i] \leftarrow a[i] \bmod 32$ 
5:   end if
6:    $i \leftarrow i + 1$ 
7: end while
8: return a

```

C. Novel Tiny Symmetric-Key Algorithm

The proposed NTSA is a symmetric cryptographic algorithm that follows the Feistel structure, having 64 rounds and 32 cycles, each cycle comprising of an odd and even round. The pseudocode for encryption and decryption is presented in Algorithms 1 and 2, respectively, and Fig. 7 presents the illustration of the encryption process. During encryption, in steps 1–8, the plain text with 64 bits is divided into two halves of 32 bit each and the key 128 bits is divided into four subkeys sk_0 , sk_1 , sk_2 , and sk_3 of 32 bit each. Subkey sk_1 is applied to odd round and subkey sk_3 is applied to even round. Different multiples of magic constant are used for each round. The value of magic constant is chosen to be floor $(2^{31}/\emptyset)$, where \emptyset is the golden ratio. In steps 12–18, a loop generates ciphertext C_0 and C_1 and the keys sk_1 and sk_3 .

An xtract function is used to generate additional key confusions in encryption. The xtract function given above (lines 1–8) returns the array indices value between 0 and 31. The value from the array is then selected dynamically to recompute the subkey values, thus making the algorithm secure. The decryption algorithm has the same initialization procedure and preliminary steps as in encryption which is depicted in lines 1–12. In lines 13–19, the loop generates the plain text P_0 and P_1 and keys sk_1 and sk_3 .

D. Security and Privacy Enabled at the Edge

The transmitted EEG signal is amplified and digitized, and encrypted at the edge using the NTSA algorithm. Instead of recording and processing the data with centralized cloud

Algorithm 2 Decryption

```

1: procedure D(e)decryption ( $C_0, C_1, key[128], newk_1, newk_3, \emptyset$ )
2:   // Initialize
3:    $sk_0 \leftarrow key[i : i+32]$ 
4:    $sk_1 \leftarrow key[i+33 : i+64]$ 
5:    $sk_2 \leftarrow key[i+65 : i+96]$ 
6:    $sk_3 \leftarrow key[i+97 : i+128]$ 
7:    $ksc \leftarrow (2^{31}) / \emptyset$ 
8:    $kc \leftarrow 0xC6EF3720$ 
9:    $sk_1 \leftarrow newk_1$ 
10:   $sk_3 \leftarrow newk_3$ 
11:   $P_0 \leftarrow C_0$ 
12:   $P_1 \leftarrow C_1$ 
13:  for cycle  $\leftarrow 0$  to 32 do // The loop generates plaintext  $P_0$ 
    and  $P_1$ 
14:     $sk_3 \leftarrow sk_3 - (sk_2 \oplus (xtract(P_1)))$ 
15:     $P_1 \leftarrow P_1 - ((P_0 << 4) \wedge sk_2) \oplus (P_0 \wedge kc) \oplus ((P_0$ 
       $>> 5) \wedge sk_3))$ 
16:     $sk_1 \leftarrow sk_1 - (sk_0 \oplus (xtract(P_0)))$ 
17:     $P_0 \leftarrow P_0 - ((P_1 << 4) \wedge sk_0) \oplus (P_1 \wedge kc) \oplus ((P_1 >>$ 
       $5) \wedge sk_1))$ 
18:     $kc \leftarrow kc - ksc$ 
19:  end for
20: end procedure

```

centers, the proposed system encrypts and decrypts the EEG signals at the edge of the network. Only encrypted data is available in the network and without the key, decryption is not possible. Hence, the security of information is ensured at the edge of the network.

V. RESULTS AND DISCUSSION

The sender is hooked up to an electroencephalography machine, to examine the brain signals, while the receiver has a TMS coil, attached to the side of the head to control the right side of the body. The sender watches an on-screen keyboard and urges to press a key using the right hand. The machine transmits this information securely as an encrypted file through the wireless medium. The wireless reception transfers it to the TMS, which prompts the distant located receiver's brain to do the same action of the sender.

A. Sender Side

The EEG signal extraction and transmission by the sender are depicted in Fig. 8. The unit comprises: 1) EEG signal extraction headset; 2) EEG signal processing unit; and 3) signal encryption and wireless transmission unit.

B. Sender Side

The EEG signal extraction and transmission by the sender is depicted in Fig. 8. The unit comprises: 1) EEG signal extraction headset; 2) EEG signal processing unit; and 3) signal encryption and wireless transmission unit.

C. EEG Signal Extraction Headset

The EEG headset is worn by the sender. The sender chooses a specific key of the onscreen keyboard by concentrating his/her thoughts on it. The electrodes on contact with the scalp extract these EEG signals from the brain. This EEG signal is passed to the EEG signal processing unit.

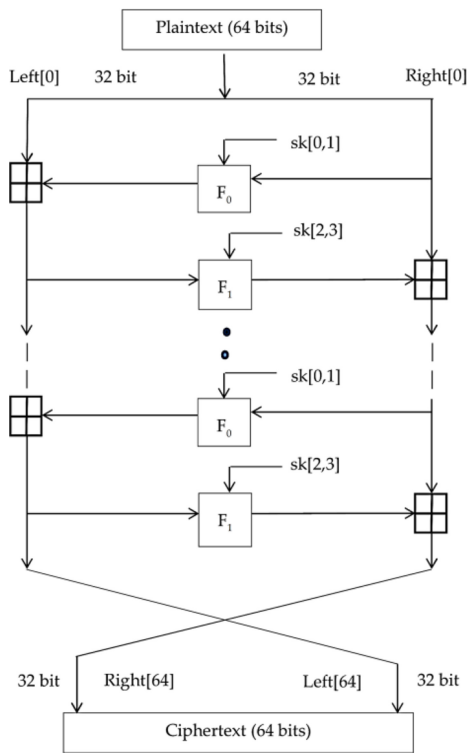


Fig. 7. Encryption in the NTSA algorithm [13].

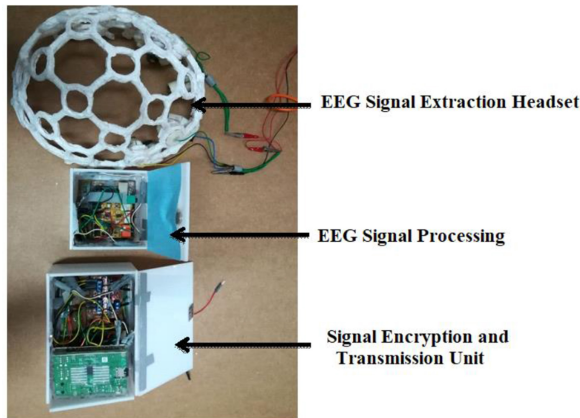


Fig. 8. Signal extraction and transmission unit.

D. EEG Signal Processing and Wireless Transmission Unit

Here, the EEG signals undergo high gain amplification and noise filtering for further processing. The analog signals are then converted to digitized format using the ADC. This digital data is then converted to text which is encrypted using the NTSA algorithm. The obtained ciphertext is then sent to the receiver through the Internet using the wireless transmission unit.

E. Receiver Side

Fig. 9 shows the ciphertext reception and decoding at the receiver side. This unit comprises: 1) wireless reception and decryption unit; 2) brain excitation control system; and 3) brain excitation headset.

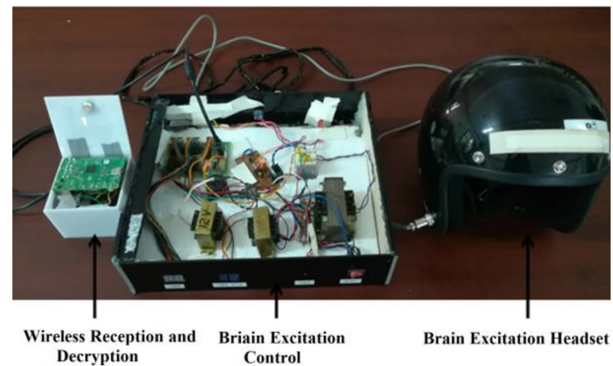


Fig. 9. Signal reception and end user.

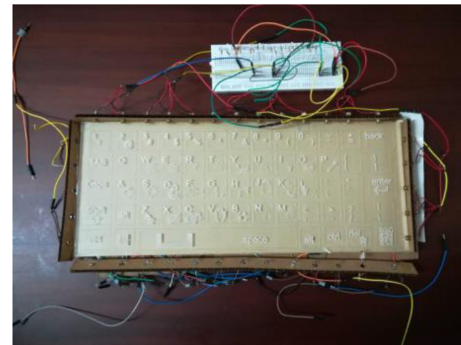


Fig. 10. End user interface.

F. Wireless Reception and Decryption and Signal Processing Unit

On reception of the ciphertext by the wireless receiver unit, decoding is performed using the NTSA decryption algorithm to get the text message which is then digitized. This digitized code is compared with the prestored commands stored in the data library. If there is a match, then the corresponding command is passed to the brain excitation control system.

G. Brain Excitation Control System

The exciter circuit (TMS) will generate the signal corresponding to the command passed. This signal will reach the receiver who will be wearing the helmet connected to TMS. The excitation impulses prompt the receiver (end user) to press the specific key on the customized keyboard (shown in Fig. 10) that was chosen by the sender.

H. EEG Signal Extraction and Reception

The brain pattern generated by concentrating on the virtual keyboard for letter ‘‘A’’ and the stimulated pattern of the transmitted character A received at the receiver end is shown in Fig. 8. It is observed that the pattern transmitted at the sender side and the pattern received at the receiver end are the same. Similarly, brain pattern generated for single character B, combination of characters AN, combination of numbers 12 are depicted in Figs. 11–13, respectively.

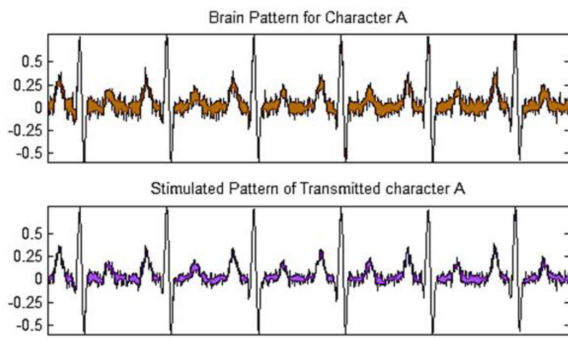


Fig. 11. Brain pattern transmitted and received for character A.

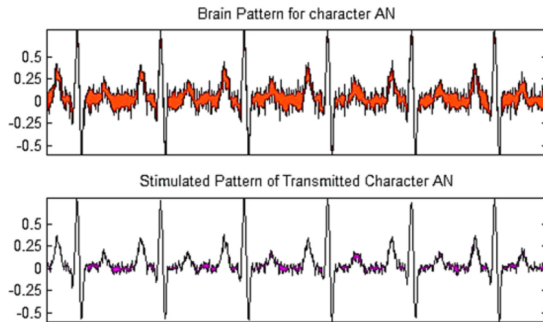


Fig. 12. Brain pattern transmitted and received for character AN.

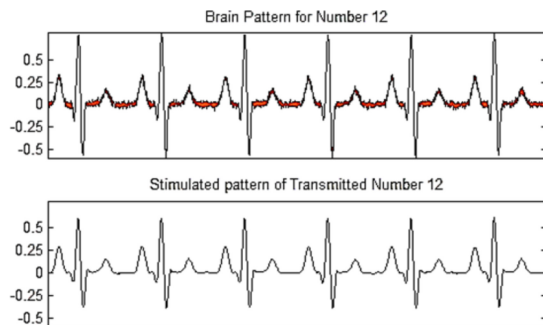


Fig. 13. Brain pattern transmitted and received for number 12.

I. NTSA Avalanche Effect

Additionally, the strength of the proposed encryption algorithm is evaluated using the concept of the avalanche effect. It is one of the desired properties of a block cipher algorithm, in that a very small change in the input creates a significant change in the output. The NTSA and TEA encryption algorithms were executed with varying key sizes of 48, 64, and 128 bits as one input and same plaintext as another input. The same experiment is repeated with the same key but by changing only one bit of it. The observation made was that for every 64-bit block, one-bit change in key produces a significant change on the ciphertext for NTSA when compared to TEA. Fig. 14 shows for every 64-bit block a change in one-bit of key with various key sizes and the corresponding change in ciphertext for NTSA and TEA.

The same experiment is repeated, but now one-bit change is made on the plaintext. The observations made are: NTSA shows drastic changes in the ciphertext than the TEA algorithm. Fig. 15 shows that for every 64-bit block

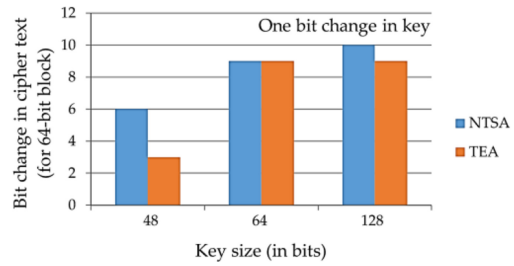


Fig. 14. One-bit change in key and the corresponding change in ciphertext for 64-bit block.

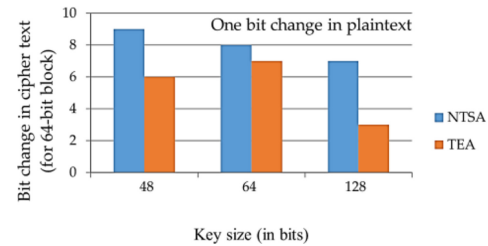


Fig. 15. One-bit change in plaintext and the corresponding change in ciphertext for 64-bit block.

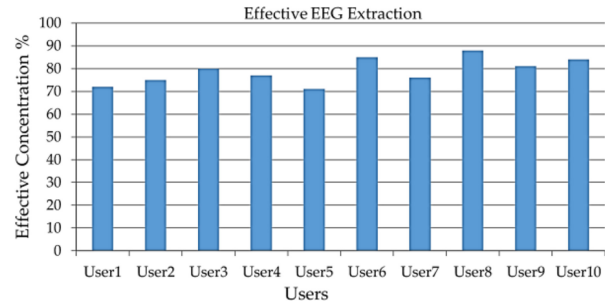


Fig. 16. Effective EEG extraction from test users.

a change in one bit of key with various key sizes and corresponding change in the ciphertext for NTSA and TEA.

J. Effective Concentration Percentage

The proposed system was tested on ten users and their effective concentration percentages were obtained. The results are presented in the graph as shown in Fig. 16. The result shows that the average effective concentration percentage is 78.9% which is really significant and higher value compared to most of the existing methods.

VI. CONCLUSION

This article analyzed the possibilities of brain-to-brain communication and highlighted the limitations with the existing systems. The proposed system enabled secure transmission of information from the patient’s brain to the caregiver using the wireless medium with EEG and TMS and a novel lightweight symmetric encryption algorithm, NTSA. This easy to use and secure system will be of great assistance to the paralyzed in the rehabilitation phase and will enable efficient and easy communication from the patient to the caregiver with less cost and without the help of any complex devices. In the future, the size of the system could be reduced so that it can be much more easily handled by the patients. Furthermore, the possibilities of using deep learning strategies to make the system efficient could be studied.

ACKNOWLEDGMENT

The authors would like to thank the Principal and Management of SCMS School of Engineering and Technology, Dr. S. Joseph and Ms. A. Jacob for the valuable support extended to this article.

REFERENCES

- [1] A. E. Hillis and D. C. Tippett, "Stroke recovery: Surprising influences and residual consequences," *Adv. Med.*, vol. 2014, pp. 1–10, Oct. 2014, doi: [10.1155/2014/378263](https://doi.org/10.1155/2014/378263).
- [2] D. R. Louie and J. J. Eng, "Powered robotic exoskeletons in post-stroke rehabilitation of gait: A scoping review," *J. Neuroeng. Rehabil.*, vol. 13, no. 1, p. 53, 2016, doi: [10.1186/s12984-016-0162-5](https://doi.org/10.1186/s12984-016-0162-5).
- [3] A. Rezeika, M. Benda, P. Stawicki, F. Gembler, A. Saboor, and I. Volosyak, "Brain-computer interface spellers: A review," *Brain Sci.*, vol. 8, no. 4, p. 57, 2018, doi: [10.3390/brainsci8040057](https://doi.org/10.3390/brainsci8040057).
- [4] F. Pichiorri *et al.*, "Brain-computer interface boosts motor imagery practice during stroke recovery," *Ann. Neurol.*, vol. 77, no. 5, pp. 851–865, 2015, doi: [10.1002/ana.24390](https://doi.org/10.1002/ana.24390).
- [5] R. Ramele, A. J. Villar, and J. M. Santos, "EEG waveform analysis of P300ERP with applications to brain computer interfaces," *Brain Sci.*, vol. 8, no. 11, p. 199, 2018, doi: [10.3390/brainsci8110199](https://doi.org/10.3390/brainsci8110199).
- [6] L. Jiang, A. Stocco, D. M. Losey, J. A. Abernethy, C. S. Prat, and R. P. N. Rao, "BrainNet: A multi-person brain-to-brain interface for direct collaboration between brains," *Sci. Rep.*, vol. 9, no. 1, p. 6115, 2019, doi: [10.1038/s41598-019-41895-7](https://doi.org/10.1038/s41598-019-41895-7).
- [7] R. P. N. Rao *et al.*, "A direct brain-to-brain interface in humans," *PLoS ONE*, vol. 9, no. 11, 2014, Art. no. e111332, doi: [10.1371/journal.pone.0111332](https://doi.org/10.1371/journal.pone.0111332).
- [8] P. G. Vinoj, S. Jacob, and V. G. Menon, "Hybrid brain-actuated muscle interface for the physically disabled," *Basic Clin. Pharmacol. Toxicol.*, vol. 123, no. 1, pp. 8–9, 2019, doi: [10.1111/bcpt.13100](https://doi.org/10.1111/bcpt.13100).
- [9] S. Jacob, V. G. Menon, F. Al-Turjman, P. G. Vinoj, and L. Mostarda, "Artificial muscle intelligence system with deep learning for post-stroke assistance and rehabilitation," *IEEE Access*, vol. 7, pp. 133463–133473, 2019, doi: [10.1109/ACCESS.2019.2941491](https://doi.org/10.1109/ACCESS.2019.2941491).
- [10] D. J. Wheeler and R. M. Needham, "TEA, a tiny encryption algorithm," in *Proc. Fast Softw. Encryption Workshop*, vol. 1008, 1994, pp. 363–366, doi: [10.1007/3-540-60590-8_29](https://doi.org/10.1007/3-540-60590-8_29).
- [11] A. A. George, M. Riyadh, and M. V. Prajitha, "Secure image transferring using KBRP and TEA algorithms," in *Proc. Int. Conf. Innov. Inf. Embedded Commun. Syst. (ICIECS)*, Coimbatore, India, 2015, pp. 1–5, doi: [10.1109/ICIECS.2015.7193117](https://doi.org/10.1109/ICIECS.2015.7193117).
- [12] R. L. Rivest, A. Shamir, and L. Adleman, "A method for obtaining digital signatures and public-key cryptosystems," *Commun. ACM*, vol. 26, no. 1, pp. 96–99, 1983, doi: [10.1145/357980.358017](https://doi.org/10.1145/357980.358017).
- [13] S. Rajesh, V. Paul, V. G. Menon, and M. R. Khosravi, "A secure and efficient lightweight symmetric encryption scheme for transfer of text files between embedded IoT devices," *Symmetry*, vol. 11, no. 2, p. 293, 2019, doi: [10.3390/sym11020293](https://doi.org/10.3390/sym11020293).
- [14] A. Jolfaei, A. Matinfar, and A. Mirghadri, "Preserving the confidentiality of digital images using a chaotic encryption scheme," *Int. J. Electron. Security Digit. Forensics*, vol. 7, no. 3, p. 258, 2015, doi: [10.1504/ijesdf.2015.070389](https://doi.org/10.1504/ijesdf.2015.070389).
- [15] A. Jolfaei, A. Vizandan, and A. Mirghadri, "Image encryption using HC-128 and HC-256 stream ciphers," *Int. J. Electron. Security Digit. Forensics*, vol. 4, no. 1, p. 19, 2012, doi: [10.1504/ijesdf.2012.045388](https://doi.org/10.1504/ijesdf.2012.045388).
- [16] N. Birbaumer, "Breaking the silence: Brain computer interfaces (BCI) for communication and motor control," *Psychophysiology*, vol. 43, no. 6, pp. 517–532, 2006, doi: [10.1111/j.1469-8986.2006.00456.x](https://doi.org/10.1111/j.1469-8986.2006.00456.x).
- [17] J. R. Wolpaw *et al.*, "Brain-computer interface technology: A review of the first international meeting," *IEEE Trans. Rehabil. Eng.*, vol. 8, no. 2, pp. 164–173, Jun. 2000, doi: [10.1109/tre.2000.847807](https://doi.org/10.1109/tre.2000.847807).
- [18] S. G. Mason and G. E. Birch, "A brain-controlled switch for asynchronous control applications," *IEEE Trans. Biomed. Eng.*, vol. 47, no. 10, pp. 1297–1307, Oct. 2000, doi: [10.1109/10.871402](https://doi.org/10.1109/10.871402).
- [19] A. Kübler, B. Kotchoubey, J. Kaiser, J. Wolpaw, and N. Birbaumer, "Brain-computer communication: Unlocking the locked in," *Psychol. Bull.*, vol. 127, no. 3, pp. 358–375, 2001, doi: [10.1037/0033-2909.127.3.358](https://doi.org/10.1037/0033-2909.127.3.358).
- [20] S. Zhang *et al.*, "Human mind control of rat cyborg's continuous locomotion with wireless brain-to-brain interface," *Sci. Rep.*, vol. 9, no. 1, p. 1321, 2019, doi: [10.1038/s41598-018-36885-0](https://doi.org/10.1038/s41598-018-36885-0).
- [21] V. A. Maksimenko *et al.*, "Increasing human performance by sharing cognitive load using brain-to-brain interface," *Front. Neurosci.*, vol. 12, p. 949, Dec. 2018, doi: [10.3389/fnins.2018.00949](https://doi.org/10.3389/fnins.2018.00949).
- [22] A. Jolfaei, X. Wu, and V. Muthukkumarasamy, "On the feasibility and performance of pass-thought authentication systems," in *Proc. 4th Int. Conf. Emerg. Security Technol.*, Cambridge, MA, USA, 2013, pp. 33–38.
- [23] P. G. Vinoj, S. Jacob, V. G. Menon, S. Rajesh, and M. R. Khosravi, "Brain-controlled adaptive lower limb exoskeleton for rehabilitation of post-stroke paralyzed," *IEEE Access*, vol. 7, pp. 132628–132648, 2019, doi: [10.1109/ACCESS.2019.2921375](https://doi.org/10.1109/ACCESS.2019.2921375).
- [24] J. F. Valenzuela-Valdes, M. A. Lopez, P. Padilla, J. L. Padilla, and J. Minguillon, "Human neuro-activity for securing body area networks: Application of brain-computer interfaces to people-centric Internet of Things," *IEEE Commun. Mag.*, vol. 55, no. 2, pp. 62–67, Feb. 2017, doi: [10.1109/mcom.2017.1600633cm](https://doi.org/10.1109/mcom.2017.1600633cm).
- [25] A. Jolfaei and A. Mirghadri, "Substitution-permutation based image cipher using chaotic Henon and Baker's maps," *Int. Rev. Comput. Softw.*, vol. 6, no. 1, pp. 40–54, 2011.
- [26] A. Jolfaei, X. Wu, and V. Muthukkumarasamy, "A secure lightweight texture encryption scheme," in *Proc. Workshops Image Video Technol. (PSIVT)*, vol. 9555, 2015, pp. 344–356.



Sreeja Rajesh is currently pursuing the Ph.D. degree with the Department of Computer Science, Bharathiar University, Coimbatore, India.

Her research interests are in cryptography, security and privacy, Internet of Things, fog computing, and secure communication protocols.



Varghese Paul received the Ph.D. degree in computer science from the Cochin University of Science and Technology (CUSAT), Kochi, India.

He was the Head of information technology with CUSAT. He is currently a Professor with the IT Department, Rajagiri School of Engineering and Technology, Ernakulam, India. His research interests are in security and privacy, cryptography, data compression, data mining, image processing, and Internet of Things.



Varun G. Menon (M'16) received the Ph.D. degree in computer science and engineering from Sathyabama University, Chennai, India.

He is currently an Associate Professor with the Department of Computer Science and Engineering, SCMS School of Engineering and Technology, Karukutty, India. His research interests include Internet of Things, brain signal analysis, fog computing and networking, and underwater acoustic sensor networks.

Prof. Menon is currently serving as the Guest Editor for the *IEEE Internet of Things Magazine* and the *Journal of Supercomputing*. He is an ACM Distinguished Speaker.



Sunil Jacob received the Ph.D. degree in electronics and communication engineering from Bharathiar University, Coimbatore, India.

He is currently the Director of the Centre for Robotics, SCMS School of Engineering and Technology, Karukutty, India, where he is a Professor with the Department of Electronics and Communication Engineering.

Prof. Jacob is the recipient of the Young Gandhian Technological Innovation Appreciation Award in 2018 and the AICTE Chhatra Vishwakarma Award in 2017.



P. Vinod received the Ph.D. degree in computer engineering from MNIT, Jaipur, India.

He is currently a Professor with the Department of Computer Science and Engineering and the Dean Research with the SCMS School of Engineering and Technology, Karukutty, India. He is also a Postdoctoral Fellow with the Department of Mathematics, University of Padua, Padua, Italy. His area of interest is adversarial machine learning, malware analysis, context-aware privacy preserving data mining, ethical hacking, and natural language processing.



Contents lists available at ScienceDirect

Groundwater for Sustainable Development

journal homepage: <http://www.elsevier.com/locate/gsd>

Research paper

Development of a novel groundwater iron removal system using adsorptive Fe(II) process

Nitha Abraham^a, Jency James^a, Tuhin Banerji^b, Ratish Menon^{a,*}^a SCMS Water Institute, SCMS School of Engineering and Technology Campus, Karukutty, Ernakulam, India^b National Environmental Engineering Research Institute, Mumbai Zonal Centre, 89/B, Dr. A.B. Road, Worli, Mumbai, 400018, India

ARTICLE INFO

Keywords:

Adsorptive process
 Ferric hydroxide flocs
 Groundwater treatment
 Iron removal

ABSTRACT

Potential of Ferric Hydroxide[Fe(OH)₃] flocs to be used as a media for the adsorptive removal of Fe(II) in water was explored in detail. It was found that this removal mechanism created new adsorption sites as the adsorption process continued. Batch experiment studies were conducted to determine the effect of contact time, adsorbent dosage, pH and competitive ions on the removal mechanism. Contact time and adsorbent dosage emerged as the dominating factors in the adsorption process, and the adsorption occurred effectively in the pH range 6.5–7. The Fe(II) adsorption was slightly hindered by calcium and manganese ions present in the groundwater, while the effects of other competitive ions such as sulphate, chloride and fluoride on the adsorptive removal mechanism were less pronounced. The kinetic process of the Fe(II) adsorption on Fe(OH)₃ was indicated to be a pseudo second order reaction that relied on the assumption of chemisorption as the rate limiting step. Based on the kinetic study, a new batch mode adsorption unit was recommended for domestic and industrial applications.

1. Introduction

Groundwater is the major source of drinking water in most parts of the world. In India, 50% of urban water requirement and 85% of rural domestic water requirement are met by ground water use (World Bank, 2010). Groundwater is considered as the primary source of drinking water because of its convenient availability, naturally good quality and its relatively low capital cost. However, it is also vulnerable to all sorts of contaminations due to natural causes or various anthropogenic activities such as agricultural, domestic and industrial (Sharma, 2001). One of the major concerns regarding the contamination of groundwater is the precipitation and accumulation of heavy metals. Natural sources of heavy metals may include weathering and erosion of bed rocks and ore deposits (Chakraborti et al., 2010). Due to the rich availability of laterite soil, iron content in Indian states such as Kerala is high (DMG, 2016). When leaching occurs, the iron enters the aquifer affecting the water quality of the aquifer. As per the Central Groundwater Board status, about 13 districts of Kerala have iron content in the aquifers at a concentration exceeding the permissible limit of 1.0 mg/l (CPCB, 2007a, b). The presence of iron results in a reddish colour and undesirable odour (Kulkarni, 2016). Fe(II) is colourless in the dissolved form, but in contact with air it is converted into the insoluble Fe(III) form, precipitates of

which cause the reddish colour, metallic taste and unpleasant odour of the water. This impairs the organo-leptix properties of water and may promote the growth of certain types of chlorine-tolerant microorganisms (Vidovic et al., 2014). A dose of 1500 mg/l iron can damage blood tissues in children while among adults, it can cause digestive disorders, skin diseases and dental problems (Khurana and Sen, 2008). As per the drinking water standards in India, desirable limit of iron is 0.3 mg/l (IS 10500:2012). High levels of iron make large volumes of water unavailable for drinking, and water scarcity ensues.

In ground water, iron exists mainly as Fe(II) due to lack of oxygen (Redman et al., 2002; Buschmann et al., 2006; Palmer et al., 2006; Benner and Fendorf, 2010). The water solubility of Fe(II) make its removal from groundwater a key concern for most water supply companies who use groundwater as their source. Researchers have attempted to develop advanced technologies for the treatment of water, more effective and economic than the prevailing ones (Sheng et al., 2017; Sharma et al., 2005; Tekerlekopoulou et al., 2006, 2013). Though many technologies currently exist, they are either expensive to maintain or require high energy for their operation, thereby reducing their affordability for low income households (Chaturvedi and Dave, 2012). Adsorptive filtration has been considered a promising alternative to different conventional iron removal mechanisms (Sharma et al., 2001).

* Corresponding author.

E-mail address: ratishmenon@scmsgroup.org (R. Menon).

<https://doi.org/10.1016/j.gsd.2019.100318>

Received 3 March 2019; Received in revised form 25 November 2019; Accepted 13 December 2019

Available online 19 December 2019

2352-801X/© 2020 Elsevier B.V. All rights reserved.

Access through your institution

Purchase PDF

Article preview

Abstract

Introduction

Section snippets

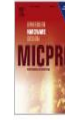
References (23)

Cited by (2)



Microprocessors and Microsystems

Volume 73, March 2020, 102951



Interfaced circuit using a non-destructive method for moisture measurement

Divya Nath K^a, Prabhu Ramanathan^b

Show more

Add to Mendeley Share Cite

<https://doi.org/10.1016/j.micpro.2019.102951>

Get rights and content

Abstract

Divya Nath K

View in Scopus

SCMS School of Engineering & Technology, Karukutty, Ernakulam, Kerala 683582, India

Corresponding author.

divyanathk@gmail.com



Divya Nath K. completed her Ph.D. in Electrical Engineering from VIT University, Vellore, Tamil Nadu, India. In 2007 she is

FEEDBACK

Access through your institution

Purchase PDF

Search ScienceDirect

Article preview

Abstract

Introduction

Section snippets

References (23)

Cited by (2)

Abstract

Analysing the moisture in stored products like harvested cereal grains and their products, peas, beans, oil-seeds, copra, cocoa beans, spices etc. is very much important to avoid the fungi growth. Moisture can be present in grain in more than one state, i.e. as bound, adsorbed or absorbed water. A designed, integrated circuit was interfaced with personal computer to measure the capacitance which in turn help to calculate the moisture content of rice. The interfaced circuit was tested by measuring the capacitance of different ceramic capacitor. This technique is fast, reliable, accurate and gives hundred set of readings in few seconds. Moisture contents are measured in percentage. The error correction was done with the help of mat - lab programming.

Introduction

Agriculture is a main source of income in a developing country like India. The moisture content of grains depends upon the humidity and the temperature of the atmosphere. As the humidity and temperature of the atmosphere varies, it is very much necessary to measure the moisture content of grains frequently. Moisture content is a factor critical to the shelf life. The moisture content in food grains like paddy, rice, etc. should be known by the farmers for its trading, processing and

Microprocessors and Microsystems, Volume 73, 20... Sakthivel B., Padma A.

A robust wire crossing design for thermostability and fault tolerance in...

Microprocessors and Microsystems, Volume 74, 20... Yongqiang Zhang, ..., Jie Han

Design of low power multi-ternary digit multiplier in CNTFET technology

Microprocessors and Microsystems, Volume 73, 20... Trapti Sharma, Laxmi Kumre

Show 3 more articles

Article Metrics

Citations

Citation Indexes: 2

Activate Windows Go to Settings to activate Windows.

Readers: FEEDBACK

[Log in](#)[Register](#)[Cart](#)[IETE Technical Review >](#)

Volume 38, 2021 - Issue 4

854 | 23

Views | CrossRef citations to date | 0 | Altmetric

Articles

Blockchain For Intelligent Transport System

Anandkumar Balasubramaniam, Malik Junaid Jami Gul , Varun G. Menon & Anand Paul 

Pages 438-449 | Published online: 31 May 2020

 [Download citation](#)  <https://doi.org/10.1080/02564602.2020.1766385> [Full Article](#) [Figures & data](#) [References](#) [Citations](#) [Metrics](#) [Reprints & Permissions](#)[Read this article](#)

ABSTRACT

Intelligent Transportation System (ITS) is gaining attention but at the same time, road accidents, congestion, delays, etc. have also increased. Relative information about such events is vital. Such information can be presented in legal processes as digital proof. Availability of the information is not a problem as multidimensional data have been recorded all the time by ITS. Recording all the information in ITS arises the problem of fetching relevant information and removing other facts and figure that are not required to describe certain situations such as an accident. To

address this issue, we analyze road accident data and reduce various dimensions with Principal Component Analysis (PCA). Linear Discriminant Analysis (LDA) and

[Home](#) ▶ [All Journals](#) ▶ [IETE Technical Review](#) ▶ [List of Issues](#) ▶ [Volume 38, Issue 4](#)
▶ [Blockchain For Intelligent Transport Sys ...](#)

three datasets where error rate for PCA is 32% with Dataset1. Likewise, error rate for LDA and NMF are 36% and 35%, respectively. While keeping in mind that such reduced data is helpful in many legal processes, we introduce Blockchain in the framework. Blockchain can make data immutable thus can be considered as digital proof. Blockchain also requires a smart contract in this situation between insurance companies to collect data in case of any uncertain situation. Such analysis can offer a different point of views and trends in data. Information can be more explainable to define the situation and helps to develop a friendly environment for day-to-day customers. The proposed framework provides dimensionality reduction of data that eventually reduce the data dimension to store in Blockchain.

Q KEYWORDS: Accident analysis Blockchain ITS Principal component analysis
Smart transportation system Traffic surveillance

Acknowledgements

This study was supported by the National Research Foundation of Korea (NRF) grant funded by the Korean government (NRF2017R1C1B5017464).

Disclosure statement

No potential conflict of interest was reported by the author(s).

Additional information

Funding

This study was supported by the National Research Foundation of Korea (NRF) grant funded by the Korean government [grant number 2020R1A2C1012196].

Notes on contributors



Anandkumar Balasubramaniam

Anandkumar Balasubramaniam received his bachelors in electronics and communication engineering under Anna University, Chennai, India in 2012. Currently, he is pursuing his masters combined PhD program under the supervision of Prof Anand Paul at Kyungpook National University, Daegu, South Korea. His research areas include intelligent transportation systems, internet of vehicles, smart city and smart vehicles. **Email:** bsanandkumar@gmail.com



Malik Junaid Jami Gul

Malik Junaid Jami Gul received his master's degree in computer science and information technology, Pakistan in 2015. Currently, he is pursuing his PhD with Dr Anand Paul at Kyungpook National University, Daegu, South Korea. His research interests include big data analytics, internet of things, smart systems, network traffic analysis and monitoring, smart city, operating system security, intrusion detection, and computer and network security. **Email:** junaidgul@live.com.pk



Varun G. Menon

Varun G Menon (SM'19) is currently an associate professor with the

[Home](#) ▶ [All Journals](#) ▶ [IETE Technical Review](#) ▶ [List of Issues](#) ▶ [Volume 38, Issue 4](#)

▶ [Blockchain For Intelligent Transport Sys](#)



Engineering and Technology, India. He has completed his PhD in computer science and engineering from Sathyabama University, India in 2017. His research interests include sensors, IoT, fog computing, brain computer interface and underwater acoustic sensor networks. He is a distinguished speaker of ACM. He is currently associate editor for *IET Quantum Communications Journal*, Editorial Member of *IEEE Technology Policy and Ethics* and a guest editor for *IEEE Sensors Journal*, *IEEE Internet of Things Magazine*, *IEEE Transactions on Industry Informatics*, *Computer Communications Journal* and the *Journal of Supercomputing*. **Email:** varunmenon@ieee.org



Anand Paul

Anand Paul received the PhD degree in electrical engineering from the National Cheng Kung University, Tainan, Taiwan, in 2010. He is currently working as an associate professor in the School of Computer Science and Engineering, Kyungpook National University, South Korea. He is a delegate representing South Korea for M2M focus group and for MPEG. His research interests include algorithm and architecture reconfigurable embedded computing. He is IEEE Senior member and has guest edited various international journals and he is also part of Editorial Team for *Journal of Platform Technology*, *ACM Applied Computing review and Cyber-Physical Systems*. He serves as a reviewer for various IEEE /IET/Springer and Elsevier journals. He is the track chair for Smart human computer interaction in ACM SAC 2015, 2014. He was the recipient of the Outstanding International Student Scholarship Award in 2004–2010, the Best Paper Award in National Computer Symposium and in 2009, and organized an International Conference on Soft computing and Network Security, India in 2015.

Related research

People also read

Recommended articles

Cited by

[Home](#) ▶ [All Journals](#) ▶ [IETE Technical Review](#) ▶ [List of Issues](#) ▶ [Volume 38, Issue 4](#)
▶ [Blockchain For Intelligent Transport Sys ...](#)

[Blockchain in transport and logistics – paradigms and transitions](#) >

Lenny Koh et al.

International Journal of Production Research

Published online: 6 Apr 2020

[Blockchain applications in supply chains, transport and logistics: a systematic review of the literature](#) >

Mehrdokht Pournader et al.

International Journal of Production Research

Published online: 11 Aug 2019

[A comprehensive view of intelligent transport systems for urban smart mobility](#) >

Riccardo Mangiaracina et al.

International Journal of Logistics Research and Applications

Published online: 13 Oct 2016

[View more](#)

[Home](#) ▶ [All Journals](#) ▶ [IETE Technical Review](#) ▶ [List of Issues](#) ▶ [Volume 38, Issue 4](#)
▶ [Blockchain For Intelligent Transport Sys ...](#)

[Home](#) ▶ [All Journals](#) ▶ [IETE Technical Review](#) ▶ [List of Issues](#) ▶ [Volume 38, Issue 4](#)
▶ [Blockchain For Intelligent Transport Sys ...](#)

[Home](#) ▶ [All Journals](#) ▶ [IETE Technical Review](#) ▶ [List of Issues](#) ▶ [Volume 38, Issue 4](#)
▶ [Blockchain For Intelligent Transport Sys ...](#)

[Authors](#)

[R&D professionals](#)

[Editors](#)

[Librarians](#)

[Societies](#)

[Opportunities](#)

[Reprints and e-prints](#)

[Advertising solutions](#)

[Accelerated publication](#)

[Corporate access solutions](#)

[Overview](#)

[Open journals](#)

[Open Select](#)

[Dove Medical Press](#)

[F1000Research](#)

[Help and information](#)

[Help and contact](#)

[Newsroom](#)

[All journals](#)

[Books](#)

Keep up to date

Register to receive personalised research and resources by email

 [Sign me up](#)

[Copyright © 2023 Informa UK Limited](#) [Privacy policy](#) [Cookies](#) [Terms & conditions](#) [Accessibility](#)





Taylor & Francis Group
Informa UK Limited

Registered in England & Wales No. 3099067
5 Howick Place | London | SW1P 1WG

Chapter 6

Automated Detection of Retinal Hemorrhage Based on Supervised Classifiers and Implementation in Hardware



K. A. Sreeja , S. S. Kumar , and Arun Pradeep 

Abstract Supervised machine learning algorithm based retinal hemorrhage detection and classification is presented. For developing an automated diabetic retinopathy screening system, efficient detection of retinal hemorrhage is important. Splat, which is a high level entity in image segmentation is used to mark out hemorrhage in the pre-processed fundus image. Here, color images of retina are portioned into different segments (splats) covering the whole image. With the help of splat level and GLCM features extracted from the splats, two classifiers are trained and tested using the relevant features. The ground-truth is established with the help of a retinal expert and using dataset and clinical images the validation was done. The trained classifier's output is evaluated and the classifier with the best output is chosen for implementation in hardware.

Keywords Retinal hemorrhage · Diabetic retinopathy · Fundus image · Splat feature classification · GLCM features · Raspberry Pi

6.1. Introduction

The World Health Organization estimated that by 2030, there will be nearly 366 million people with Diabetic Mellitus (DM) [1]. A microvascular complication of DM that is responsible for a major share of cases of blindness in the world is the Diabetic Retinopathy (DR). The severe complications like Microaneurysms, Exudates,

K. A. Sreeja (✉)

SCMS School of Engineering and Technology, Ernakulam, India

e-mail: ka.sreeja@gmail.com

S. S. Kumar · A. Pradeep

Noorul Islam University, Kanyakumari, India

e-mail: kumarss@live.com

A. Pradeep

e-mail: arunpradeep@msn.com



SysDroid: a dynamic ML-based android malware analyzer using system call traces

Ananya A.¹ · Aswathy A.¹ · Amal T. R.¹ · Swathy P. G.¹ · Vinod P.¹ · Mohammad Shojafar^{2,3}

Received: 10 August 2019 / Revised: 29 November 2019 / Accepted: 31 December 2019 / Published online: 13 January 2020
© Springer Science+Business Media, LLC, part of Springer Nature 2020

Abstract

Android is a popular open-source operating system highly susceptible to malware attacks. Researchers have developed machine learning models, learned from attributes extracted using static/dynamic approaches to identify malicious applications. However, such models suffer from low detection accuracy, due to the presence of noisy attributes, extracted from conventional feature selection algorithms. Hence, in this paper, a new feature selection mechanism known as *selection of relevant attributes for improving locally extracted features using classical feature selectors* (SAILS), is proposed. SAILS, targets on discovering prominent system calls from applications, and is built on the top of conventional feature selection methods, such as mutual information, distinguishing feature selector and Galavotti–Sebastiani–Simi. These classical attribute selection methods are used as local feature selectors. Besides, a novel global feature selection method known as, weighted feature selection is proposed. Comprehensive analysis of the proposed feature selectors, is conducted with the traditional methods. SAILS results in improved values for evaluation metrics, compared to the conventional feature selection algorithms for distinct machine learning models, developed using Logistic Regression, CART, Random Forest, XGBoost and Deep Neural Networks. Our evaluations observe accuracies ranging between 95 and 99% for dropout rate and learning rate in the range 0.1–0.8 and 0.001–0.2, respectively. Finally, the security evaluation of malware classifiers on adversarial examples are thoroughly investigated. A decline in accuracy with adversarial examples is observed. Also, SAILS recall rate of classifier subjected to such examples estimate in the range of 24.79–92.2%. However, prior to the attack, the true positive rate obtained by the classifier is reported between 95.2 and 99.79%. The results suggest that the hackers can bypass detection, by discovering the classifier blind spots, on augmenting a small number of legitimate attributes.

Keywords Android malware · Machine learning (ML) · Deep learning (DL) · Feature selection · Adversarial machine learning (AML) · Attacks

✉ Mohammad Shojafar
mohammad.shojafar@unipd.it; m.shojafar@surrey.ac.uk

Ananya A.
ananya@scmsgroup.org

Aswathy A.
aswathy@scmsgroup.org

Amal T. R.
amal@scmsgroup.org

Swathy P. G.
swathy@scmsgroup.org

Vinod P.
vinodp@scmsgroup.org

¹ Department of Computer Science & Engineering, SCMS School of Engineering and Technology, Ernakulam, Kerala, India

² ICS/5GIC, University of Surrey, Guildford GU27XH, UK

³ University of Padua, 35131 Padua, Italy

1 Introduction

The number of Android users has exponentially increased over the past decade, and this has opened the doors for the attackers to innovate methods, to compromise devices through vulnerable Android applications. The rise in the number of malware variants, constraint the anti-virus vendors in the signature update process, thereby adversely affecting the security of smartphones and tablets. According to Symantec's Internet Security Threat Report 2018, there was an increase of 54% Android malware variants with the figures reported in 2017 [9]. Symantec's report also mentions that third-party app stores hosted 99.9% of malicious apps. Kaspersky Lab products detected 5,321,142 malicious installation packages, 151,359 new mobile banking Trojans and 60,176 new mobile ransomware Trojans for the year 2018 [22].

Conventional mechanisms of Android malware analysis are based on three approaches which are static, dynamic and hybrid analysis. The static analysis incorporates signature-based, permission-based, and component-based investigation. Dynamic analysis involves the execution of the application in real-time and observing the behaviour of the application. The hybrid analysis consists of combining static and dynamic features [24]. In literature, several researchers have developed machine learning (ML) techniques [17–19] to resolve the problems of Android malware attacks. Previous works have focused on evasion attacks, which results in misclassification of the sample [6]. Zhou and Jiang [37] have worked on detecting Android malware by AV vendors. DroidAPIMiner [1] performs extraction of API call frequency from android applications and performs malware detection using supervised learning algorithms.

Contributions Static analysis alone cannot be used to identify malware applications as malware hide payload in the encrypted form, installed on execution. To cope with this problem, it is essential to develop methods based on dynamic analysis. Hence, some questions arises: Is it possible to adopt strategies employing dynamics analysis to detect Android malware using different features? How can the proposed dynamic method be guaranteed, to swiftly update itself to dynamically changing real-time Android samples (applications)? The main aim of the paper is to respond to these queries by devising a new feature selection method, and evaluate the robustness of the classifier against adversarial attacks. Hence, a novel system call analysis is proposed to detect Android malware at run time. In this way, a new feature selection method called *SAILS* is proposed, which improves the performance of classifiers over the conventional feature selection methods. The classical identified by us in this paper are mutual

information (MI), Galavotti–Sebastiani–Simi (GSS) and Distinguishing Feature Selector (DFS), to extract relevant attributes representative of the target class. Experiments are conducted on benchmark dataset consisting of 2474 Drebin malware and 2475 benign apps. In summary, the main contributions of our work are listed as follows:

- A new feature selection mechanism known as Selection of relevant Atttributes for Improving Locally extracted features using classical feature Selectors (SAILS) is proposed.
- An extensive analysis of ML and deep learning (DL) algorithms under diverse classifier parameters is conducted.
- One of the key observation is that XGBoost has a higher prediction capability in comparison to other classification algorithms.
- The performance of the classification algorithms when subjected to adversarial examples is performed. It is experimentally verified that classifiers are mislead even to small modification in attributes introduced by augmenting malware samples with few prominent benign features.

The rest of the paper is organised as follows. In Sect. 2, the related works proposed in the field of Android malware detection. Section 3 presents the methodology. The attack model is presented in Sect. 4. The experiments, results, and its analysis has been discussed in Sect. 5. Finally Sect. 6 discusses about the conclusion and future work.

2 Related work

Several anti-malware techniques have been introduced to detect malware on Android devices. These techniques can be broadly classified as static and dynamic analysis. In static analysis, malicious behaviour is analyzed by scanning the source code of the application, instead of executing an application/program. The source code of the program is investigated to identify the trigger of malicious event. On disassembling the apps, different features such as permissions, hardware components, intents, broadcast receivers, data flow, APIs, control flow, etc. can be derived. Dynamic analysis is performed during run time. Here, the malware scanners monitor the response generated by the operating system, on the execution of the program. Commonly used features include network connections, system calls, etc. To bridge the gap between static and dynamic analysis, hybrid anti-malware techniques were also developed to improve the performance of malware detector. In the following subsections, the background is categorized into static methods presented in Sect. 2.1, solutions based

on dynamic malware analysis approach presented in Sect. 2.2, and hybrid techniques presented in Sect. 2.3.

2.1 Static feature based approaches

The authors in [11] propose a method to evaluate the security of machine learning-based android malware detector. Classifiers were trained using API calls extracted from the smali files. To explore the security of the classifier, the authors considered evasion attacks on diverse threat models. They propose a robust secure-learning paradigm that can be applied to other security tasks like fraud detection. The goal of the research work was to improve the robustness of online malware scanners against adversarial examples created at test time.

Another group of authors in [14] designed a method that worked in discrete and binary input domains. For malware detection, they train the neural network on the Drebin dataset and achieve classification performance against similar works in literature. They use an AML algorithm to mislead the ML model to about 63% of all malware samples in the Drebin dataset.

2.2 Dynamic feature selection methods

Bhandari et al. [5] proposed a malware detection tool capable of handling code injection during runtime. This approach binds semantics of the program and a classification engine. A sequence of system calls demonstrates the semantics of the app. To capture the actual behaviour of the apps, the order of the system calls were conserved. They apply Markov property on the acquired system call traces and construct a sequential system call graph (SSG). The authors compute all the acyclic paths by considering the first, and the last system calls as the start and end node in SSG. They develop feature vectors from the typical sets by applying asymptotic equipartition property on each path. After that, they perform statistical analysis by finding the average logarithmic branching factor of each path to train the model. Further, they use the histogram binning technique to form the feature vector table and train them using supervised learning algorithms. They conduct experiments on dataset containing 2000 applications (1000 Benign and 1000 malware apps). Benign apps were collected from the Google play store, and malware apps belonged to 119 different families. The proposed system obtains a detection accuracy of 94.2%.

The authors in [12] have designed a two-step learning strategy named *KuafuDet*, that used adversarial detection to learn malware patterns. It is composed of an offline training step that could select and extract features from the samples and further use this model to compromise the online tool. An automated camouflage detector is used to

filter the false negatives and feed them back into the training phase. *KuafuDet* reduces false negatives and improves detection accuracy by 15%. This method was tested on more than 250,000 mobile applications to demonstrate the scalability of *KuafuDet*.

Additionally, in another work, the authors [35] propose a method that transforms the packed malware variant detection problem, to a system calls classification problem. They generated a sequence of sensitive system calls and further applied principal component analysis to extract relevant attributes. Then, multi-layer neural networks were utilized to classify benign and malicious applications. The proposed system was reported to achieve a detection accuracy of 95.6%.

The authors in [8] used strace tool to extract the system calls. Each invocation of system calls was mapped to a frequency-based feature vector. Experiments were performed on self-made 60 apps, and the proposed work reported accuracy between 85 and 100%. Later authors, in [2] proposed an ML-based dynamic malware detection method. They extracted API calls and system call traces. In particular, 74 API functions and 90 system calls were considered as features. For classification, Random Forest classifier was utilized. Experiments were conducted on the dataset comprising of 7520 apps, of 3780 samples were used for training and remaining (3740 application) were considered in the testing phase. The study demonstrated an accuracy of 96.66%.

The authors in [10] introduced an ML approach that helped in increasing the user effectiveness in handling system data to improve security and privacy. The proposed approach was evaluated on different ML algorithms deployed on real-world systems, and it showed better efficiency. Suci et al. [29] developed a Fail Attacker Model. The model effectiveness was evaluated on adversaries having limited capabilities. A poisoning attack was subjected on different ML algorithms. Consequently, the fail model exhibited better resilience on generalized transferability.

2.3 Hybrid feature selection methods

The authors in [25] propose a novel malware detection method called *HADM*—hybrid analysis for detection of malware. The set of features were represented as vectors fed to Deep Neural Network (DNN) with different kernels. To apply graph kernels onto the graph sets, they converted dynamic information into graph-based representations. Further, output from various vector were combined with graph feature sets using hierarchical multiple kernel learning (MKL), to build a final hybrid classifier. The authors in [4] propose a three-level hybrid model called *SAMADroid* for Android malware detection. By

combining the benefits of three levels, SAMADroid provides more detection accuracy on static and dynamic analysis, deployed on local and remote host. For static analysis, attributes from the manifest files and the dex code files were considered. For dynamic analysis, they generate system call logs based on the local inputs and send it to the remote server. Remote servers analyze the extracted static features and the logs. Finally, ML algorithms are used to classify malware and benign apps. They present that the SAMADroid can provide detection accuracy of 82.76% with Random Forest (RF). Also, the authors in [30] designed a novel hybrid approach and utilized the NetLink technology to generate patterns of system calls related to file and network access. They compare the pattern of malware and benign apps, to build a malicious pattern set. They aim to collect system calls and in offline compares both the malicious and normal pattern sets to identify the unknown app.

Besides, the paper [15] explains a hybrid method called *MalDAE* that combines the dynamic and static API sequences into one hybrid sequence based on semantics mapping. *MalDAE* experiments show that the system achieved accuracy in the range of 94.39% and 97.89%. Also, *MalDAE* provides an overall idea about the common types of malware and predictive support for understanding and resisting malware. Another novel hybrid method is [32] which consists of deep Autoencoder (DAE) and convolutional neural network (CNN). They reconstruct high-dimensional features of Android applications and use multiple CNN to detect Android malware. To increase sparseness, nonlinear activation function *Relu* was utilized to prevent overfitting in the serial CNN architecture *CNN-S*. To increase the capability of feature extraction, they bound the convolutional layer and pooling layer with the full-connection layer. Later, deep Autoencoder as a pre-training method of CNN was employed to reduce the training time. They tested their hybrid approach on 10,000 legitimate and 13,000 malicious apps. This resulted in 5% increase in the accuracy compared with SVM. Further, training time using the DAE-CNN model reduces by 83% compared with the CNN-S model. A hybrid scheme designed by Zhenlong Yuan et al. [34] aims to introduce an online deep-learning-based malware detection method called *DroidDetector*. *DroidDetector* performs prediction on thousands of Android apps and also thoroughly perform an in-depth study of the features and declares an accuracy of 96.76%.

3 Methodology

In this section, our proposed system is presented. Figure 1 describes the architecture and the working of our system. A clear description of the steps involved in the identification and evaluation of malware samples, is discussed in the subsequent sections.

3.1 Data collection

The data collection phase involves the collection of two types of Android applications, malware applications as well as trusted applications. A total of 4949 samples comprising of 2475 benign and 2474 Drebin applications [3, 23] were downloaded. In particular, legitimate application were considered from diverse app categories. Categories comprised of lifestyle, education, medical, comics, etc. from 9Apps site [38]. All these apps were scanned using VirusTotal [31], which is a web service that examines files or URLs to check whether they are malicious or not. Finally, samples labelled as benign were included for carrying out experiments.

3.2 Feature extraction

A system call sequence presents how an application requests a service from the kernel of the operating system. System calls generated during the execution of an application, are used as features to identify samples as malware or benign. The intention of using system calls is to deduce the behaviour of the application and to understand its interaction with the Android operating system. System calls have been logged using strace utility. Further, to mimic human interactions, Android Monkey Runner [20], a utility in sdk is periodically accessed. Specifically, Android Monkey was configured to direct 200 random UI events in a minute. Some events generated are: (i) reception of SMS (ii) answer and make call, (iii) change geolocation, (iv) swipes and (v) update the battery charge status These set of events were selected as it generalizes the operations performed on the smartphones. To collect the call traces, the following procedures were adopted:

1. Install the app (using ADB install command)
2. Extract the package name and class of the application
3. Gets the process id (PID) corresponding to each application
4. Invoke strace command, and at each timestamp log system calls
5. Start Monkey command with application package name as the parameter
6. Suspend the application for ten seconds
7. Kill the app

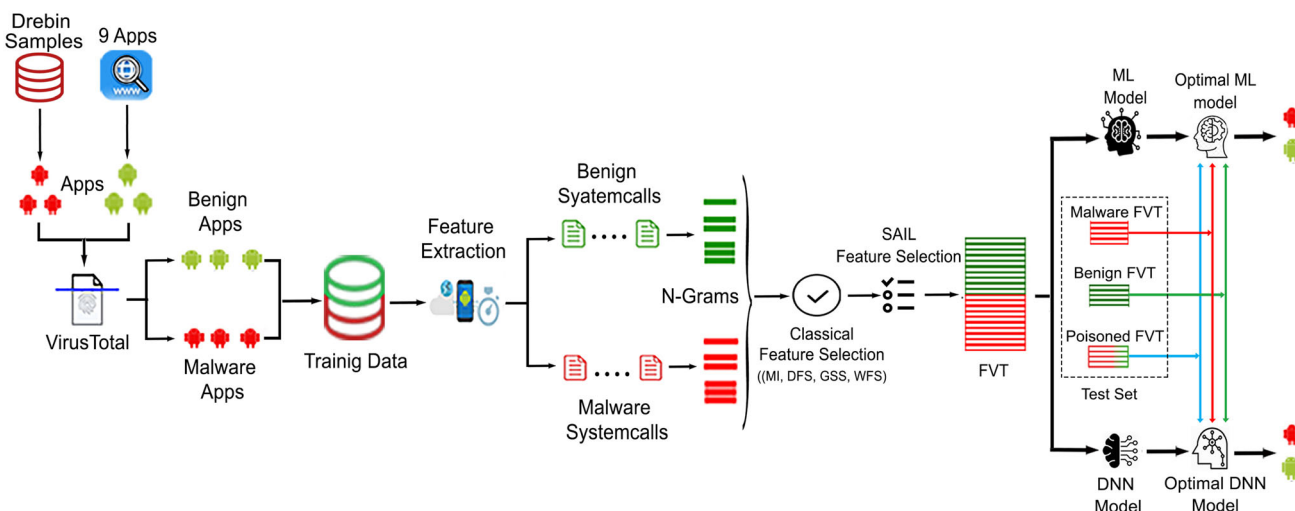


Fig. 1 The proposed architecture

8. Uninstall the app (using ADB uninstall command)
9. Delete app from device, finally reset the emulator clean state

Alternatively, in-order to extract system calls a human expert well versed in Android programming also interacted with the installed applications. In the feature extraction phase, initially, an emulator or an Android virtual device is created by specifying the basic configuration details such as device name, memory size, OS version, storage area, skins, screen resolution etc. Subsequently the .apk file, is installed into the emulator using the command: `adb -s emulator-id install sample_app.apk`.

Likewise, all other applications on the emulator are installed, and the system calls (`strace -p process_id -o output_path`) are recorded. Simultaneously, the Android monkey continuously interacts with the app during (`adb shell monkey -p pkg_name -v 200`). Once the specified events are completed, the process stops, and finally, the emulator is restored back into its clean state.

3.3 N-gram generation

In this part of the paper, the process of generation of *N-grams* is discussed. *N-gram* is a sequence of *n* items from a given sample. In *N-gram* model, the occurrence of an item is predicted based on the occurrence of its previous *n - 1* items. They are used to store the context of the words and can be used to make the next word predictions. *N-gram* for any range usually perform the best, and is shown to be applied in the domain of malware detection [27]. Since *N-grams* overlap, they not only capture the statistics about substrings of length but also implicitly capture frequencies of longer substrings as well.

Experiments on unigrams, bigrams, and trigrams are performed. Consider for an example a set of extracted features and the corresponding unigrams, bigrams, and trigrams generated:

- (i) **Features:** read prctl openat epoll_ct socketpair recvform
- (ii) **Unigram:** read, prctl, openat, epoll_ct, socketpair, recvform
- (iii) **Bigram:** read:prctl, prctl:openat, openat:epoll_ct, epoll_ct:socketpair, socketpair:recvform
- (iv) **Trigram:** read:prctl:openat, prctl:openat:epoll_ct, openat:epoll_ct:socketpair, epoll_ct:socketpair:recvform

Once the features are obtained, the corresponding bigrams and trigrams are generated, and analysis is performed on all *N-grams* to investigate the effect of *N-gram* size on classification accuracy.

3.4 Feature selection

Feature selection is one of the most crucial phase of ML, which has a huge impact on the classification model generated. Irrelevant and redundant features must be removed or else they may negatively impact the classification. Irrelevant are variables/attributes which have less correlation with a class, and redundant features have correlation with one or more attributes in the feature space. Thus, feature selection allows us to filter out attributes so that only the important features which help in classification is left out. Some of the conventional feature selection methods previously applied in the domain of malware detection are MI [21], GSS [36] and DFS [33]. Mutual information (MI) is a measure between two random variables quantifying the amount of information obtained from one random variable compared to the other random variable. DFS method exploits the hypothesis that certain term

appearing in more number of documents are highly relevant for categorization. GSS coefficient is a simplified variant of the Chi-square statistics proposed by Galavotti et al. In this approach, Chi-square is used to measure the correlation between the attribute and class. Thus, if a variable carries more information about a target class, such attributes are known as a characteristic feature, also have a high value. Thus, in summary, the benefits of performing feature selection improve accuracy reduce overfitting, and reduces training time. The following subsection highlights the feature selection methods employed in our experiment.

3.4.1 SAILS: selection of relevant attributes for improving locally extracted features using classical feature selectors

We propose *SAILS* as a novel feature selection method. The following steps outline the proposed feature selection methods through a simple example.

Step 1 Set of malware and benign system calls are listed. Let S_i denote a system call.

	S_1	S_2	S_3	S_4
M	bind	munmap	capget	ioctl
B	fcntl	lseek	writew	prctl

Step 2 Feature selection algorithms such as MI, GSS and DFS are used to give score for the samples.

Let $FS = \{f_1, f_2, \dots, f_n\}$
 $f_i(a_j) = \text{Malware/Benign score}$

Step 3 System calls are sorted based on the malware and benign scores.

	S_1	S_2	S_3	S_4
M	bind	munmap	capget	ioctl
B	fcntl	lseek	writew	prctl

Sorted list containing system calls is arranged in descending order of prominence.

M	S_2	S_4	S_3	S_1
B	S_1	S_4	S_2	S_3

Step 4 System calls are added to the new list

To do so, first, system calls from both malware and benign list are taken. Then, a check is performed to identify whether the system call already exists in the final list, if it is not present, it is augmented to the final result.

M	S_2	S_4	S_3	S_1
B	S_1	S_4	S_2	S_3

S_2	S_1		
-------	-------	--	--

Next, the second system call from both malware and benign list is picked and their presence in the final list is

checked. Here S_4 appears in both malware and benign list, hence it is added once in the final list.

M	S_2	S_4	S_3	S_1
B	S_1	S_4	S_2	S_3

S_2	S_1	S_4	
-------	-------	-------	--

Similarly, the third system call is chosen, i.e., S_3 and S_2 . Here, S_2 is already present in the final list, hence only S_3 is added in the final list.

M	S_2	S_4	S_3	S_1
B	S_1	S_4	S_2	S_3

S_2	S_1	S_4	S_3
-------	-------	-------	-------

Here, both S_1 and S_3 are already present in the final list, hence no need to add these two system calls again.

M	S_2	S_4	S_3	S_1
B	S_1	S_4	S_2	S_3

S_2	S_1	S_4	S_3
-------	-------	-------	-------

This method is built over the conventional feature selection methods such as MI, GSS, and DFS. Initially, the malware and benign score of the union of malware and benign system calls are computed using the conventional feature selection methods. Then the features are ranked in the descending order of scores for the target classes. Once two separate lists of system calls are obtained, the new list of attributes based on SAILS are derived. For this purpose, the alternate system calls are selected, one each from the malware score ranked list and the other from the benign score ranked list and these system calls, are added into the new list provided, they are not the same and are not already present in the list. If the two calls are similar, only one instance of the feature is added to the list.

Algorithm 1 gives a brief description of the steps involved in SAILS. The input to the algorithm is the list of system calls, $S = \{s_1, s_2, \dots, s_N\}$; where m is the set of malware system calls and b is the set of benign system calls (line 1). In lines 2–3, call present in the applications are sorted. Lists, u and v consist of system calls arranged in the descending order of precedence of malware and benign score, respectively. X is the set of system calls that forms the final output. In the following steps, it is first checked whether the current sorted malware system call from u is present in X , if not, then, the presence of the benign system call from v is checked in X . If absent, both malware and benign system calls are added to X at positions j and $j + 1$ respectively (lines 7–8). Similarly, if the benign system call is already found in X then only the malware system call is added (line 10). Alternatively, if the malware system call is already present in X , then the presence of benign system call is checked, if not present, only the benign call is added

into X . Finally, if the benign system call from v is already present in X then there is no need to add either the malware (u) or the benign (v) system call into X . Finally, the list X is returned as output, as shown in line number 20.

The implementation of SAILS was performed using binary Max-Heap tree. Thus, two heap trees one for malware and another for benign system calls is obtained. Since this tree is populated using identical (union) system calls from both the dataset, hence it contains the same number of system calls, but arranged in different fashion due to the difference in local scores, corresponding to each system call. In this way, the space complexity in worst case is $O(N)$, to be precise as the number of system calls are less (approximately 393 in Linux Kernel 3.7), the space complexity is also less. The time complexity to create Max-Heap tree is $O(\log N)$. Generally, both the trees contain system call with maximum score at the root node. A system call with maximum score is picked and appended to the list X . During this course of action the system call with the highest score is deleted from the tree and a heapify operation is performed. Thus, the time required to undertake heapify operation in the worst case requires $O(N \log N)$. Therefore, in the worst case the total time to arrange the system calls will need $O(N \log N)$.

Algorithm 1 System calls extracted using SAILS

```

1: Procedure SAILS( $S, m, b$ )
2:  $u \leftarrow \text{sort}(m)$ 
3:  $v \leftarrow \text{sort}(b)$ 
4: while  $i \neq |S|$  do
5:   if  $u[i] \notin X$  then
6:     if  $v[i] \notin X$  then
7:        $X[j] \leftarrow u[i]$ 
8:        $X[j + 1] \leftarrow v[i]$ 
9:     else
10:       $X[j] \leftarrow u[i]$ 
11:    end if
12:  else
13:    if  $v[i] \notin X$  then
14:       $X[j] \leftarrow v[i]$ 
15:    else
16:      //do nothing
17:    end if
18:  end if
19: end while
20: return  $X$ 
    
```

3.4.2 Weighted feature selection (WFS)

Another method used in our experiment for feature selection is WFS. Here the weight of system calls are first computed, and then ordered in descending order of the corresponding malware and benign scores separately. The prominent system calls are used to create the feature vector matrix, which is further used to train the model and to evaluate the performance of the generated model.

Algorithm 2 discusses the steps involved in feature selection using WFS. The input to the algorithm is the set of system calls, S , as shown in line number 1. From line number 3 to 6, we compute the weight of system calls in the malware set. In particular, the weight of system call is computed as the product of the ratio of occurrences of system calls in malwares to the total occurrence of system calls in both training samples and the frequency of the calls in malware files, to the total number of malware samples in the training set. The time complexity for computing the weight is $O(1)$. Similarly, line number 8 to 10 depicts the calculation of the weight of system calls for benign examples. Finally, the average weight of system calls is determined (refer to line 12). The steps 3–12 steps are repeated until the weight corresponding to each call in set S is ascertained.

Algorithm 2 System calls extracted using WFS

```

1: Procedure WFS( $S$ )
2:  $S = \{s_1, s_2, \dots, s_N\}$ ; set of system calls.
3: while  $i \neq |S|$  do
4:   //Determine weight of system call in malware set
5:    $T(S_i, M) \leftarrow \frac{\text{occ}(S_i, M)}{\text{occ}(S_i, M) + \text{occ}(S_i, B)}$ 
6:    $U(S_i, M) \leftarrow \frac{\text{freq}(S_i, M)}{|M|}$ 
7:    $wt(S_i, M) \leftarrow T(S_i, M) * U(S_i, M)$ 
8:   //Determine weight of system call in Benign set
9:    $T(S_i, B) \leftarrow \frac{\text{occ}(S_i, B)}{\text{occ}(S_i, M) + \text{occ}(S_i, B)}$ 
10:   $U(S_i, B) \leftarrow \frac{\text{freq}(S_i, B)}{|B|}$ 
11:   $wt(S_i, B) \leftarrow T(S_i, B) * U(S_i, B)$ 
12:   $\text{avg}(S_i) \leftarrow \frac{wt(S_i, M) + wt(S_i, B)}{2}$ 
13: end while
14: return  $\text{avg}(S_i)$ 
    
```

3.5 Feature vector table

The feature vector table is the collection of vectors consisting of n rows and $m + 1$ columns. Here, n represents the number of applications in the dataset, and m is the number of unique system calls invoked by both malware and

	V_1		V_k		V_m	Y
X_1	a_{11}	...	a_{1k}	...	a_{1m}	0
X_2	a_{21}	...	a_{2k}	...	a_{2m}	0

X_j	a_{j1}	...	a_{jk}	...	a_{jm}	1

X_n	a_{n1}	...	a_{n2}	...	a_{nm}	1

Fig. 2 Feature vector table

benign APKs. An example of a feature vector table is depicted in Fig. 2. The columns 1 to m denote the attributes obtained after the feature selection phase. The last column denotes the class label associated with each sample. Here, the class label ‘1’ identifies malware samples, and ‘0’ denotes benign apps. Each row denotes a vector X with dimension m that correspond to samples in the dataset. Lastly, a_{ij} denotes the number of times j th system call was invoked by i th sample.

3.6 Training and testing phases

Once the feature selection phase is concluded, the next step is to train the model and predict new samples. Training phase largely include construction of a feature occurrence matrix, a data structure that record the frequency of attributes obtained after the feature selection process. Eventually, the classification algorithm learns patterns discriminant to the target classes. Later, the test samples are supplied to a trained ML model. The learned model assigns class labels to each apk in the test set. The performance of the classifiers is evaluated using performance metrics, such as accuracy, precision, recall, and F1-score. Models are developed using Logistic Regression (LR), Classification and Regression Tree, RF, XGBoost, and DNNs.

Train-test split method is used in this work. Specifically, 60% samples are assigned to train set and the remaining 40% of the apks are included in the test set. The train-test split method may sometimes result in the overfitted model.

3.7 Classifiers

Classification or predictive modelling is a method of approximating a hypothesis function (f) which maps to discrete output variables (y) for input observations (X). In particular, classification is a supervised approach where a program learns patterns from input examples and predict the class for a new sample. Multiple ML classification algorithms such as RF [7], Classification and Regression Tree (CART) [26], LR [16] and XGBoost [13] were used in our work. DNNs were also used to analyze the performance and to compare the performance obtained with machine learning algorithms.

3.7.1 Classification and regression tree (CART)

A decision tree is a non-parametric ML technique for regression and classification problems. Given the input observation, decision tree forms a hierarchical structure. Each internal node corresponds to attribute and leaf node corresponds to class labels. CART is a Gini index-based

method. Initially, all training samples are put in the root node. Subsequently, the best partition is explored to minimize the Gini impurity. Noisy or impure attributes classify a randomly selected sample into the wrong subset. Besides, gini impurity equals zero if samples belong to one class. The best discovered partition is further divided into parts, each of which is subsequently seen as a new node. This process is repeated until leaf nodes are obtained.

3.7.2 Random forest (RF)

Random Forest (RF) consists of a large number of decision trees which can function as an ensemble. Each tree is created from the set of a randomly selected subset of training examples. The individual tree generates a class prediction, further, the class that receives maximum votes is the outcome of the entire classification process.

RF hyper-parameters are used to improve the model’s predictive ability. Commonly used hyper-parameters include a number of trees that the algorithm builds before taking the maximum vote or considers the average prediction. A higher number of trees generally increases performance and makes predictions more stable, however, suffers from speed. Alternatively, Random Forest can be configured with another hyperparameter like split criterion, min/max number of leaf nodes, the height of the tree etc.

3.7.3 Logistic regression (LR)

Logistic Regression is used when the target variable (i.e., dependent variable) is a categorical/binary response. A sigmoid function is used as a logistic function which outputs real value for the corresponding input feature vector. The obtained output value is subsequently converted to binary based on the threshold, in particular, the output is the estimated probability. Additionally, the coefficients also help in predicting the importance of each input variable.

3.7.4 XGBoost

XGBoost is a scalable and precise implementation of gradient boosting, developed solely for improving model performance and speed. Gradient Boosting is an ensemble learner, it creates a final model based on a prediction obtained from the collection of individual models. As the predictive power of individual models is weak and susceptible to overfitting, hence ensembles of weak models improve the overall result. Newly generated models can predict error of prior models. XGBoost utilizes gradient descent approach to reduce the error while combining the models

3.7.5 Deep neural network (DNN)

A DNN is a network contain multiple layers in between the input and output layer. In DNN, nodes in each layer are trained on a set of features of the previous output layer. As the number of layers increases, the complexity of the network increases, and it learns complex attributes. At higher dimensions, traditional ML algorithms such as LR, KNN, etc. exhibit poor performance, whereas in the case of neural networks, as the size of the data increases, the performance of the model increases. Additionally, hyperparameters like drop out, and the learning rate may be altered to improve the model performance.

Drop out is a regularization technique for neural networks, to avoid overfitting. It is an approach in which randomly selected neurons are ignored during training. Thus, in the forward pass, the contribution to the activation of the neurons in subsequent layers are ignored, and any updates in weights are also not applicable in the backward phase. Dropout enables a model to learn more robust features. Learning rate indicates the amount of change made to the model during each step of the search process.

3.8 Evaluation of the classifiers

In this paper, evaluation metrics considered are accuracy (see Eq. (1)), precision (see Eq. (2)), recall (or true positive rate) (see Eq. (3)) and F1-score (see Eq. (4)) to identify the classifier performance. *True negative* (α), is the number of truly classified benign samples. *True positive* (β) is the number of correctly classified malware files. The number of mis-classified legitimate applications are referred as *false positive* (γ). Malicious applications wrongly classified as benign are called as *False negative* (θ). Using TP (β), TN (α), FP (γ) and FN (θ), accuracy, recall, precision and F1-score is computed.

$$\text{Accuracy}(\mathcal{A}) = \frac{\alpha + \beta}{\alpha + \beta + \gamma + \theta} \quad (1)$$

$$\text{Precision}(\mathcal{PRC}) = \frac{\beta}{\beta + \gamma} \quad (2)$$

$$\text{Recall}(\mathcal{REC}) = \frac{\beta}{\beta + \theta} \quad (3)$$

$$\text{F1 - Score}(\mathcal{F}_1) = 2 * \left(\frac{\mathcal{PRC} * \mathcal{REC}}{\mathcal{PRC} + \mathcal{REC}} \right) \quad (4)$$

4 Attack model

Adversarial machine learning involves techniques, where the malicious samples injected with attributes of legitimate applications, forces machine learning system to misclassify such perturbed malware apps. The modified(perturbed) examples are also known as adversarial examples.

Adversarial examples can be broadly classified as (a) poisoning attack-performed during the training phase and (b) evasion attack-perturbed samples created in the prediction phase to mislead detection. Additionally, an adversary may use one/more, threat models. These threat model are related to the knowledge an attacker possesses, with reference to a machine learning system. In a white-box threat model, an adversary has complete knowledge of training samples and classifier parameters. Such attack models are used to evaluate the performance of a machine learning system in the worst case. Moreover, in a black-box attack model, the adversary does not have access to classifier and the training set. She can make a limited number of attempts to fool the classification system.

4.1 Evasion attack

In evasion attack, an attackers feed adversarial input to the classifier to increase misclassification. To accomplish this task and adversary create synthetic malware samples, imitating the properties of the benign applications. To start with, 10% (247 apps) of the total malware samples (2474 samples) are chosen. Then, prominent system calls invoked by benign samples absent in malware applications are appended to it at a varied concentration (1%, 2%, 3%, etc.). Such modified malware samples form the test set, which are later used to predict the performance of the models.

Algorithm 3 Evasion attack

```

1: Procedure Poisoning ( $M, S, j$ )
2:  $V \leftarrow j(M)$  //extract  $j$  percentage of samples from
   malware set
3:  $X \leftarrow S(M)$  //percentage of Unique system calls present
   only in benign set are extracted
4: for each file in  $V$  do
5:   append  $X$  at the end of file
6: end for
7: return file

```

Algorithm 3 gives a brief description of the evasion attack. The input to the algorithm includes M , which is the set of malware files and $S = \{s_1, s_2, \dots, s_N\}$, a set of prominent benign system calls which are absent in malware files, to be injected into the malware samples, at the specified concentration for creating adversarial examples. In particular, system calls in benign Max-Heap tree, are referred to as prominent calls which are absent in the first half of the malware Max-Heap tree. Thus, in the worst-case half the number of nodes in malware Max-Heap tree (half the height of tree) is searched. Hence, in worst case the time complexity to search legitimate system call in malware Max-Heap require $O(\log N)$, where N is the total number of system calls. In line 2, $j\%$ of the malware samples from original malware set are extracted. To be

precise, j is the percentage of malware files that needs to be poisoned (line 1). Next, prominent system calls invoked by benign APKs at the required concentration, i.e. (1%, 2%, ...) are selected (line 3). In lines 4 to 7, for each in file V , the system calls from X are added to samples in V depending on the supplied concentration rate. Finally, the output is a set of perturbed malware instances, injected with a sequence of the calls from benign apps (line 7).

5 Performance analysis

In this section, the experiments along with results are detailed. The experiments are conducted on Ubuntu 18.04 platform with the support of Intel Core i5-8250U CPU @ 1.80 GHz with 8GB RAM. The dataset consisted of 2475 benign and 2474 malware applications. Benign applications are downloaded from 9Apps site and verified for benignness by scanning samples using VirusTotal. The apps from Drebin dataset constituted malware set. This dataset contain malware samples belonging to 179 families. An automated tool, i.e., Android Monkey which is a part of the Android SDK, along with `strace` utility are used to record the system calls. On the completion of system calls extraction, the emulator process is killed and clean snapshot of the emulator is loaded for the analysis of subsequent samples. Comprehensive experiments were performed for evaluating the following:

- Performance of machine learning classifiers using proposed feature selection methods.
- Investigation of optimal feature category and feature length.
- Performance comparison of machine learning and deep learning algorithms.
- Investigation of the effect of drop out and learning rate in the performance of deep learning neural network.

5.1 Experiment-I: feature selection method

A novel feature selection method (SAILS) was developed on the top of classical feature selection approaches. Traditional feature selection methods like MI, GSS and DFS were employed as local feature selectors to estimate the score of each system call. These calls were further ranked using our proposed attribute ranking approach, yielding an enhanced outcome, both in terms of evaluation metrics and feature-length.

Table 1 depicts the comparison of accuracies obtained with proposed feature selectors and the conventional approaches. In this experiment, classification models were developed using RF, CART, LR and XGBoost. On observing the results, it is noted that the accuracy obtained

for our proposed system is higher in most of the cases, and for remaining experiments, the performance was at least equal to the conventional approach. It was observed that the highest accuracy was recorded for RF with unigrams, and for bigrams, the best outcome was achieved using XGBoost. In the case of trigrams, LR exhibited the highest accuracy. It is worth mentioning that the results obtained with the proposed methods exceed with fewer feature-length.

5.2 Experiment II: robustness of N-grams

Figure 3 illustrates the malware and benign scores of 20 system calls which were predominant in benign samples. From Fig. 3a, for unigrams, it can be seen that scores are identical or marginally differ. This suggests statistical similarity in the feature vectors for both malware and benign examples. Considering Fig. 3b and c it seen that the benign system call score is lesser when compared to the malware call score. Similar trend is observed in case of GSS^* , WFS^* and MI^* as shown in Appendix Figs. 11, 12 and 13 respectively.

5.3 Experiments-III: comparison of classification algorithms

In this experiment, the effectiveness of different ML algorithms in identifying malware applications is evaluated. In particular LR, Classification and Regression Tree (CART), Random Forest (RF), eXtreme Gradient Boost (XGBoost) and DNN are chosen. Additionally, a comprehensive analysis on the performance of DNN is performed by determining optimal values of dropout and learning rate.

From Fig. 4 it is clear that for GSS feature selection, the accuracy and F1-Score obtained with SAILS is better compared to the conventional approach.

Further, the average score of each system call was computed, the system calls were then arranged in the descending order of the average scores. Finally, sorted calls using the aforesaid approach was utilized in the training phase. For unigram, it was observed that Random Forest achieved the highest accuracy of 95.85% with F1-score of 95.87%. In the case of bigram, XGBoost showed better results with an accuracy of 99.4% and F1-score of 99.4%. Figure 4c depicts that for trigram, LR shows the highest accuracy of 99.34% and F1-score of 99.34%, which was higher than other classifiers.

A similar pattern of results was obtained with Random Forest and XGBoost employing DFS and MI feature selectors as depicted in Figs. 5 and 6. In the case of DFS feature selector, with Random Forest, the highest accuracy and F1-score obtained for unigram was 96.31% and

Table 1 Performance of classification algorithms with proposed feature selection approach and classical feature selectors

Classifier	Feature selectors	Unigram		Bigram		Trigram	
		FL	\mathcal{A}	FL	\mathcal{A}	FL	\mathcal{A}
LR	MI*	100(98)	97.66	100(2212)	97.16	90(18318)	99.44
	AVG-MI	100(98)	91.05	100(2212)	96.41	90(18318)	96.75
	GSS*	50(47)	88.58	80(1769)	99.13	80(16283)	99.34
	AVG-GSS	90(88)	88.43	100(2212)	99.08	100(20354)	99.34
	DFS*	100(98)	91.96	90(1990)	97.61	100(20354)	99.34
	AVG-GSS	90(88)	88.43	100(2212)	99.08	100(20354)	99.34
	WFS*	40(37)	89.3	100(2212)	98.0	100(20354)	99.4
CART	MI*	100(98)	96.5	100(2212)	96.65	100(20354)	98.83
	AVG-MI	100(98)	92.26	100(2212)	94.94	100(20354)	94.78
	GSS*	90(88)	92.67	80(1769)	97.77	80(16283)	98.58
	AVG-GSS	90(88)	92.57	80(1769)	95.08	100(20354)	98.17
	DFS*	90(88)	92.32	70(1548)	96.7	90(18318)	98.22
	AVG-DFS	90(88)	92.02	90(1990)	95.39	90(18318)	97.89
	WFS*	40(37)	93.1	100(2212)	96.7	100(20354)	98.7
RF	MI*	100(98)	96.75	80(1769)	97.21	100(20354)	98.23
	AVG-MI	100(98)	96.1	80(1769)	97.21	100(20354)	96.8
	GSS*	90(88)	95.85	90(1990)	98.78	80(16283)	98.17
	AVG-GSS	100(98)	95.5	100(2212)	98.53	100(20354)	97.77
	DFS*	100(98)	96.31	100(2212)	97.66	100(20354)	97.82
	AVG-DFS	100(98)	96.11	100(2212)	97.21	100(20354)	97.97
	WFS*	90(88)	97.2	20(442)	97.6	100(20354)	97.5
XGBoost	MI*	100(98)	95.6	90(1990)	99.3	100(20354)	99.2
	AVG-MI	100(98)	95.5	90(1990)	99.3	100(20354)	99.2
	GSS*	80(78)	95.75	70(1548)	99.44	80(16283)	98.32
	AVG-GSS	80(78)	92.65	70(1548)	97.67	80(16283)	97.72
	DFS*	90(88)	95.7	100(2212)	99.4	80(16283)	98.2
	AVG-DFS	90(88)	95.4	100(2212)	97.3	80(16283)	98.2
	WFS*	70(68)	96.6	40(884)	97.9	20(4070)	97.7

FL denotes feature length at which best outcomes were obtained. FL is represented in the form of $P(Q)$, where P denote the percentage of features extracted from the feature space and Q denote the number of attributes used to create model

Asterisks indicate a revised feature set after the application of SAILS

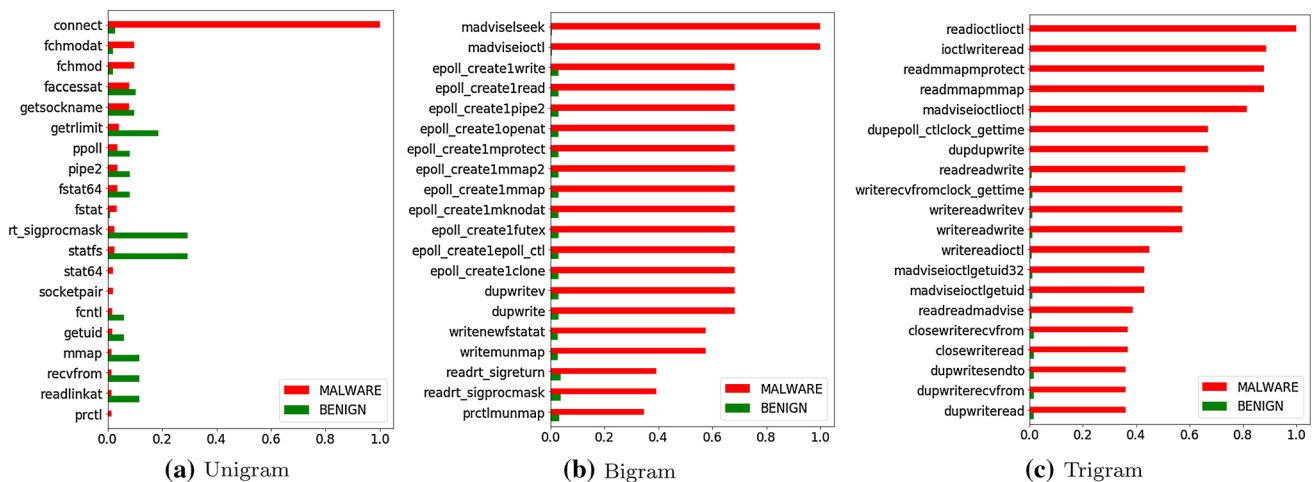


Fig. 3 Score difference of N-grams for DFS*

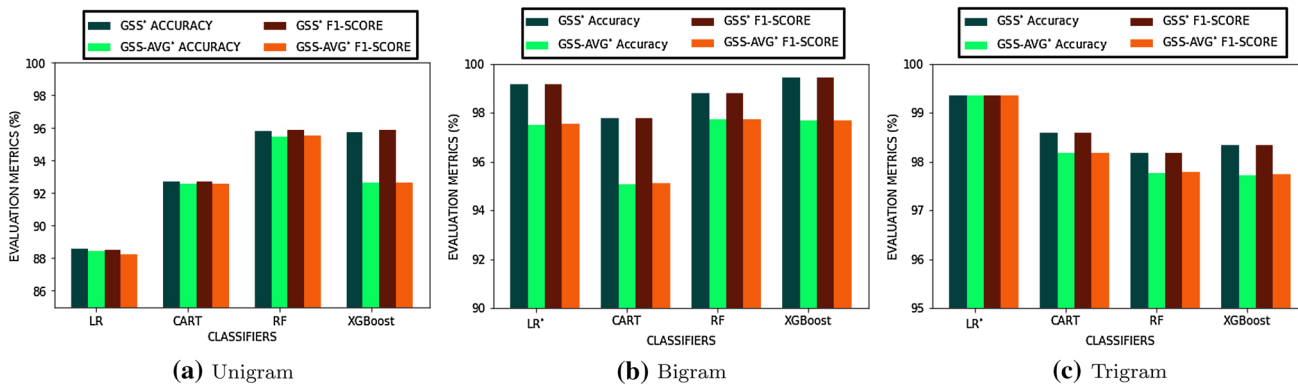


Fig. 4 Performance of GSS* feature selection on unigram, bigram, trigram

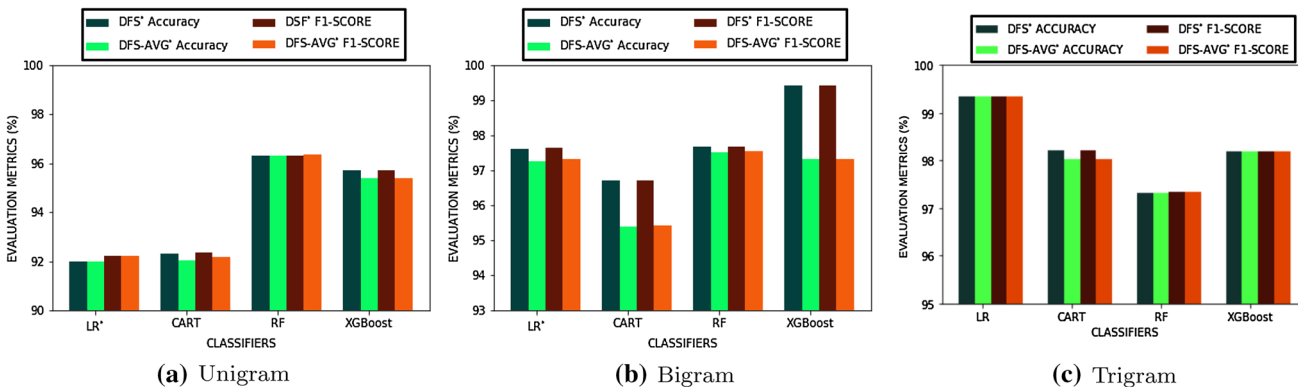


Fig. 5 Performance of DFS* feature selection on unigram, bigram, and trigram

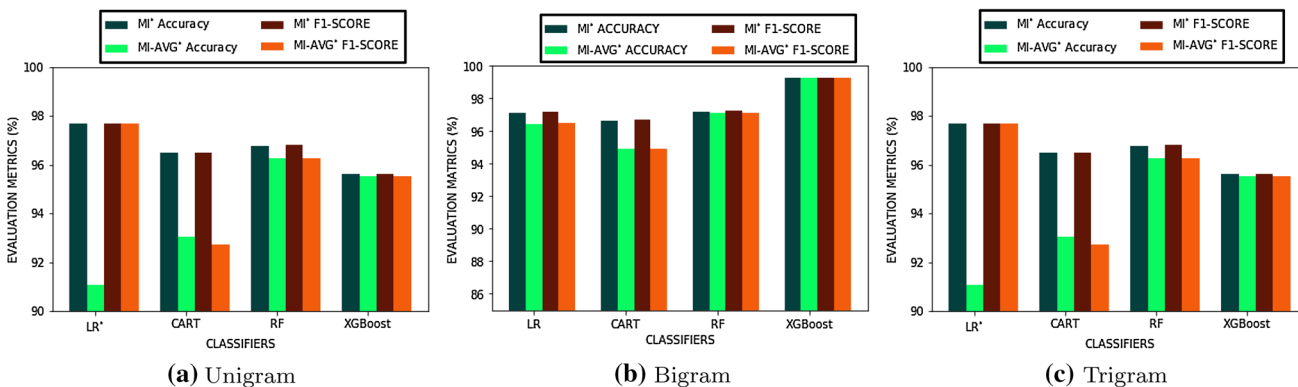


Fig. 6 Performance of MI* feature selection on unigram, bigram, and trigram

96.32%. In the case of bigram with XGBoost, accuracy and F1-score were 99.4% and 99.4% respectively.

Further, considering system call trigram with LR, the best accuracy achieved was 99.34% along with F1-score of 99.34%. Considering MI feature selector for unigram with Random Forest, the best accuracy attained was 96.75% and obtained F1-score of 96.79%. In the case of bigram, the best accuracy and F1-score obtained with XGBoost was 98% and 97.9% respectively. Whereas with LR, trigram

achieved accuracy and F1-score of 99.4% and 99.5% respectively.

Summary The results lead to the conclusion that the proposed feature selection method could derive attributes that had a higher correlation with the target class. Thus, resulting in improved outcome. In the case of unigram, Random Forest achieved higher accuracy and F1-score comparing other classifiers. Further for bigram, among all four classifiers, XGBoost exhibited better accuracy and F1-score. Comparing the results of trigram, LR achieved better

accuracy and F1-score compared to other classifiers. This is because, LR exhibited improved results as the feature vectors become linear in higher dimensional attribute space. The trend was clearly evident for the three Logistic regression model (i.e., unigram, bigram and trigram). Intuitively, in all cases of classification algorithms trained using bigrams and trigrams reported better performance compared to unigram.

5.4 Experiment IV: performance with DL classifier

In this experiment, DL was used to distinguish malware and legitimate applications. This experiment was conducted to analyze the performance of DNN compared to conventional ML approaches. A DNN model named DNN-2L with two hidden layers was designed. The first hidden layer consisted of 50% of attributes of the input feature space, as the number of neurons. Subsequently, the second layer contained 50% of the neurons, that were present in the previous layer. For example, if the feature set contained 1000 attributes, then the first layer will be created with 500 neurons and the second layer will be formed using 250 neurons. In DNN-2L, all layers contained Rectified Linear Unit (ReLU) activation function. Sigmoid activation function was used in the output layer, as malware identification is a binary classification problem. For faster convergence and to avoid overfitting, Adam optimization algorithm and cross entropy loss function was utilized respectively. Employing DNN-2L comprehensive analysis was conducted under following experimental settings and we investigated: (i) effect of dropout rate in the performance of model (Sect. 5.4.1) and (ii) effect of learning rate in the performance of model (Sect. 5.4.2).

5.4.1 Effect of dropout rate in the performance of model

To avoid overfitting on training data, dropout was proposed by Srivastava et al. [28]. Dropout is a regularization technique in which randomly selected neurons are removed during the training phase. This indicates that, the contribution of such neurons will be temporarily removed, during the forward pass and weight update will be ignored, in the backward pass. During the learning phase, a neuron specific to a particular layer relies on the neighbouring neurons. In a fully connected topology, a neuron tuned to specific feature was passed on to the upstream neurons. Thus, the network becomes more specific to the training data. On the contrary, if certain neurons were randomly eliminated, then the predictions are performed with the existing neurons. This suggests that many new patterns/representations, will be created and subsequently learned by the network. Thus, the network would be less sensitive

to the weights of neurons and less likely to overfit the training data.

To study the impact of dropout rate, a diverse classification model learned with attributes derived by our proposed feature selection method was created. In particular, the well known feature selectors were improved by deriving the call/sequence of calls having the ability to identify target classes. The outcome of the results are shown in Fig. 7. The results in Fig. 7a indicates that dropout rates of 0.2, 0.5 and 0.6 gave the best results for all three categories of features (i.e., unigram, bigram and trigram). An identical trend can be observed in Fig. 7b and c, i.e., better results are obtained at dropout rate of 0.3, 0.5 and 0.6. Finally, it was observed that DNN-2L learned with unigram, bigram and trigram at dropout rate of 0.2, 0.5 and 0.7 respectively, attained the best results as depicted in Fig. 7d. A similar observation has been observed when considering the F1-score as the evaluation metric, to evaluate the performance of the DL classifiers as show in Fig. 8.

5.4.2 Effect of learning rate in the performance of model

Further the importance of learning rate on the results of classification was explored. Learning rate is a hyper-parameter which denotes how much a model needs to be modified each time, by adjusting the weight. Lower value of learning rate indicates more time spent on training or in particular more steps needed to reach local minima. Conversely, large gradient descent learning rate would overshoot, besides missing local minima. Specifically, the model would fail to converge. In this study, the learning rate was varied such that it began with a small value (i.e. 0.001) and progressively increased by 0.01 until the maximum value of learning rate (i.e., 0.3) was reached (refer to Table 2).

5.5 Experiment V: evaluation against adversarial examples

The performance of any ML based system might degrade over time, eventually fortifying the system. In order to evaluate the detection capability of the classifier in the presence of adversarial samples, synthetic malware's mimicking statistical properties of legitimate set were created. In this context, adversarial malware samples were developed, by injecting varied proportion of prominent system calls, frequently invoked by the benign applications. The point of argument here is that, the classification algorithms fail to detect adversarial malware samples. The results show that as the proportion of system calls injected into each of the samples was increased, the recall declined dramatically, indicating that the classification algorithms fail to detect the malware samples (refer Table 3).

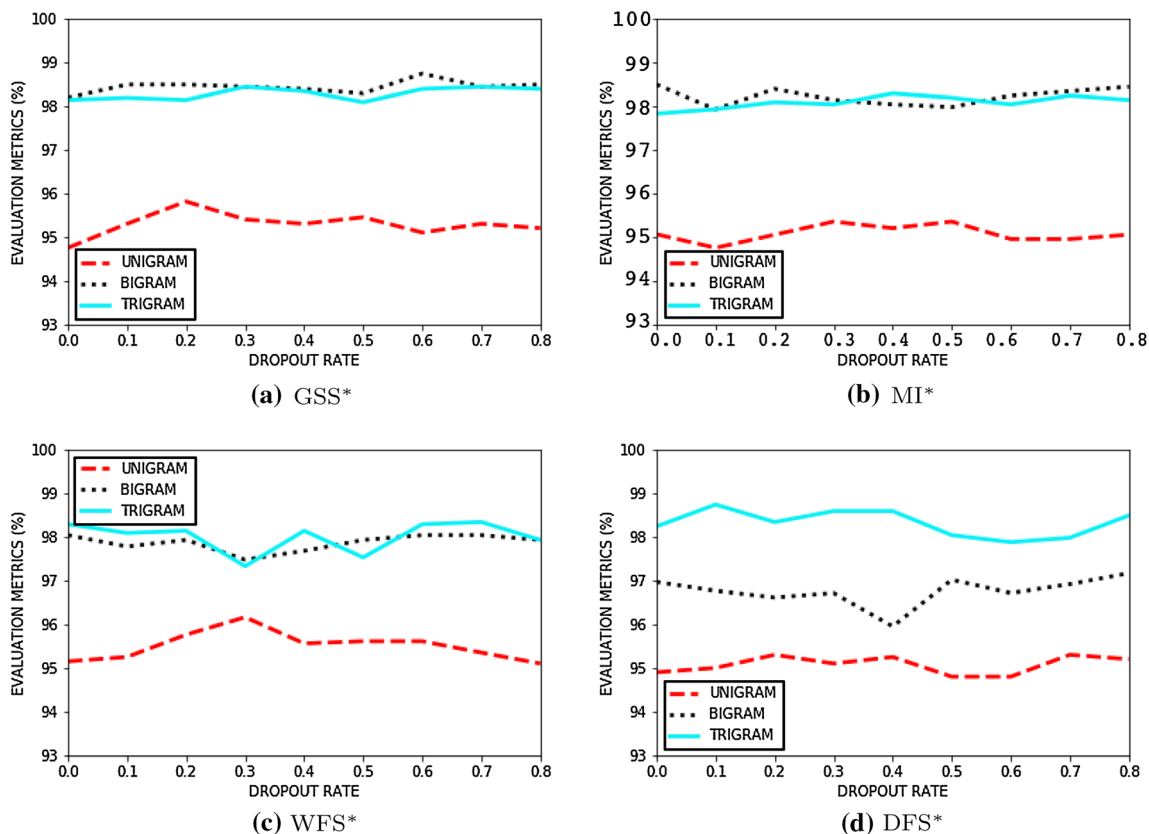


Fig. 7 Accuracy comparisons for different DL classifiers of proposed feature selection approach using dropout rate

In this experiment, adversarial samples for five detection models were generated. For each model, the recall rate was evaluated for 1%, 2% and 3% of prominent Benign system calls that were used to poison the malware samples. Figure 9a shows that the recall rate for Unigram in CART prior to the attack was 96.55% and after the attack, it got reduced to 33.73%. This was the case of 1% of prominent benign system calls that were appended to the malware samples for poisoning and the trend continued for both 2% and 3% of prominent benign system calls. Considering 2% of benign system calls, after poisoning the recall rate was minimized to 58.94% and for 3% of benign system calls it dropped to 30.89%. In case of a bigram, the recall rate reduced from 97.26 to 29.26% for 1% of benign system calls and for 2% benign system calls, the recall rate diminished to 30.0%. Likewise, for 3% of benign system calls, recall was minimized to 24.79%. Further for trigram, the recall rate for 1% of benign system calls reduced from 98.88 to 45.93%. Whereas for 2% of benign system calls, the rate minimized to 57.48% and for 3% of benign system calls, the rate reduced to 39.67 %.

Figure 9b depicts that for 1% benign system calls of unigram, LR shows a recall rate of 98.68% prior to poisoning, and after poisoning it was reduced to 50.4%. In case of 2% and 3% of system calls, the true positive rate

was reduced to 68.29% and 66.66% respectively. For bigram after poisoning, the recall rate was reduced from 98.78 to 77.64%, 81.3% and 69.1% for 1%, 2% and 3% of benign system calls. Considering trigram, from 99.79% of recall rate, it diminished to 86.17%, 86.6% and 85.02% for 1% 2% and 3% of prominent benign system calls respectively.

Figure 9c shows that in case of Random Forest, for unigram the true positive rate declined from 97.89 to 61.38%, 74.79% and 35.77% for 1%, 2% and 3% of benign system calls respectively. Considering 1%, 2% and 3% of benign system calls of bigram, the recall rate reduced from 98.38 to 79.26%, 83.33%, and 74.39% respectively. Further, for poisoned trigram, the recall rate diminished from 98.58 to 82.11%, 84.61% and 84.61% for 1%, 2% and 3% of benign system calls.

From Fig. 9d it is clear that with XGBoost, the recall rate of unigram reduced from 95.8 to 80.01% for 1%, 2% and 3% of benign system calls after poisoning. Considering 1%, 2% and 3% of benign system calls in Bigram after poisoning, the recall rate reduced from 98.7 to 92.22%. In case of Trigram, for 1%, 2% and 3% of benign system calls, the recall rate of 99% diminished to 91.9%.

Figure 10 depicts that for unigram, the recall rate diminished from 95.2 to 44.53% in case of 1% of

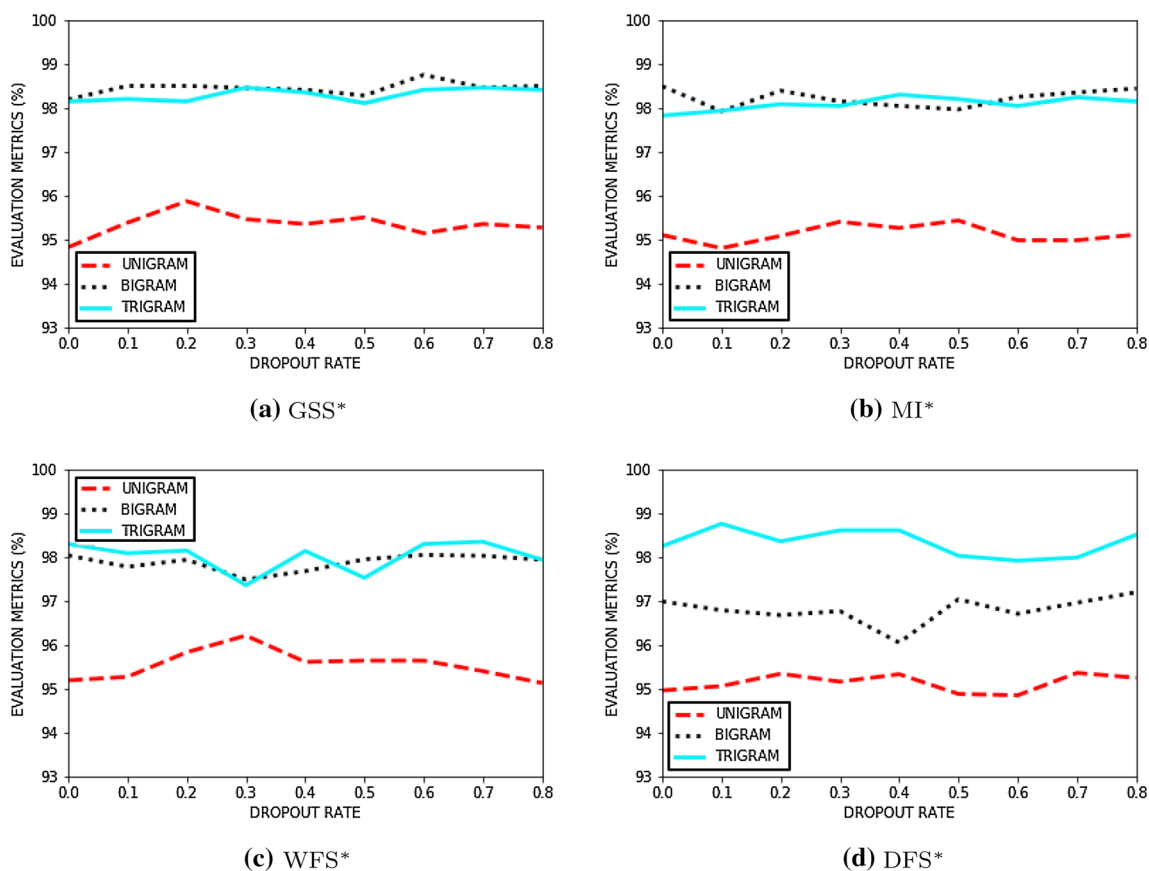


Fig. 8 F1-Score comparisons for different DL classifiers of proposed feature selection approach using dropout rate

Table 2 Performance of DL classifier with proposed feature selection approaches using dropout rate and learning rate

Feature selectors	Category	Drop out	LR	\mathcal{A}	\mathcal{F}_1	\mathcal{PRC}	\mathcal{REC}
GSS*	UNIGRAM	0.2	0.1	0.952	0.952	0.950	0.956
	BIGRAM	0.6	0.2	0.990	0.990	0.990	0.994
	TRIGRAM	0.8	0.1	0.980	0.980	0.980	0.990
DFS*	UNIGRAM	0.7	0.001	0.950	0.950	0.953	0.943
	BIGRAM	0.8	0.1	0.990	0.990	0.984	0.992
	TRIGRAM	0.1	0.1	0.980	0.981	0.970	0.991
MI*	UNIGRAM	0.5	0.001	0.952	0.952	0.952	0.952
	BIGRAM	0.8	0.1	0.980	0.980	0.980	0.982
	TRIGRAM	0.4	0.001	0.987	0.987	0.986	0.989

Asterisks indicate a revised feature set after the application of SAILS

prominent benign system calls and for 2% and 3% of benign system calls, the recall rate reduced to 43.3% and 42.1%. Considering 1% of injected bigram, the recall rate minimized from 98.2 to 40.48%, the recall at 2% and 3% injection rate reduced to 34.81% and 32.39% respectively. Further for trigram, in case of 1% injected calls, the recall declined from 98.58 to 48.18%, moreover, for 2% to 3%, the recall dropped from 42.51 and 37.65% respectively.

6 Conclusion and future directions

In this paper, a new feature selection method, SAILS, is designed, which can provide better results compared to conventional feature selection approaches. Also, the classifier performance of different N -grams is studied. We performed parallel analysis of the Android malware detector using deep learning network and machine learning algorithms. Further, the performance of the model was evaluated by analysing the change in dropout and learning rate.

Table 3 Performance comparison of WFS feature selection method with other approaches

Classifier	Feature selectors	Unigram		Bigram		Trigram	
		FL	\mathcal{A}	FL	\mathcal{A}	FL	\mathcal{A}
LR	WFS*	40(37)	89.3	100(2212)	98.0	100(20354)	99.4
	MI-AVG	100(98)	91.05	100(2212)	96.41	90(18318)	96.75
	GSS-AVG	90(88)	88.43	100(2212)	99.08	100(20354)	99.34
	DFS-AVG	100(98)	91.96	90(1990)	97.16	100(20354)	99.34
CART	WFS*	40(37)	93.1	100(2212)	96.7	100(20354)	98.7
	MI-AVG	100(98)	92.26	100(2212)	94.94	100(20354)	94.78
	GSS-AVG	90(88)	92.57	80(1769)	95.08	100(20354)	98.17
	DFS-AVG	90(88)	92.02	90(1990)	95.39	90(18318)	97.89
RF	WFS*	90(88)	97.2	20(442)	97.6	100(20354)	97.5
	MI-AVG	100(98)	96.1	80(1769)	97.21	100(20354)	96.8
	GSS-AVG	100(98)	95.5	100(2212)	98.53	100(20354)	97.77
	DFS-AVG	100(98)	96.11	100(2212)	97.21	100(20354)	97.97
XGBoost	WFS*	70(68)	96.6	40(884)	97.9	20(4070)	97.7
	MI-AVG	100(98)	95.5	90(1990)	99.3	100(20354)	99.2
	GSS-AVG	80(78)	92.65	70(1548)	97.67	80(16283)	97.72
	DFS-AVG	90(88)	95.4	100(2212)	97.3	80(16283)	98.2

FL denotes feature length at which the best outcomes were obtained. FL is expressed in the form of $P(Q)$, where P denotes the percentage of features extracted from the feature space and Q denote the number of attributes used to create the model

Asterisks indicate a revised feature set after the application of SAILS

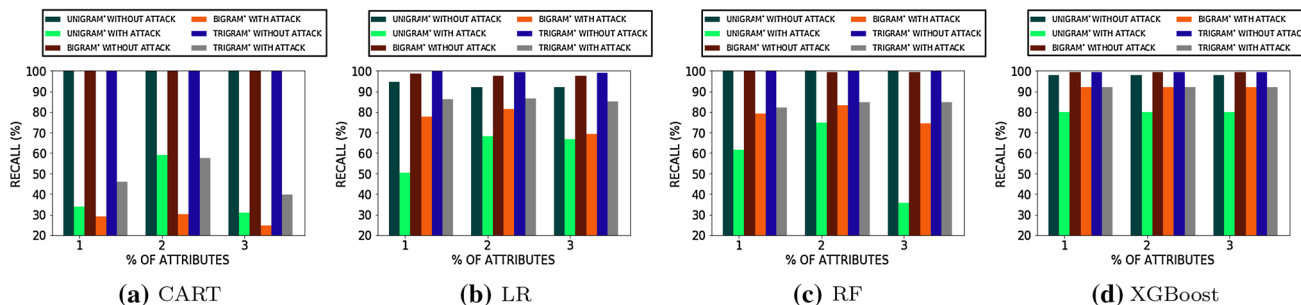


Fig. 9 Performance evaluation of unigram, bigram and trigram after poisoning using ML

Adversarial attacks are also performed on the ML models. It is observed that the adversary could deceive the current ML based malware detectors. A drop in performance is observed when the trained models were given evasive examples as input. Thus, it is important to develop robust ML models trained with adversarial patterns, such that Android malware detectors are capable of recognizing tainted samples.

Our current work focuses on dynamic analysis of Android malware. In future work, we envisage the use hybrid analysis on a larger dataset. It is also planned to

include features relating to network packets (packet size, packet payload size, packet inter-arrival time, TCP flag status, the total number of bytes in packets, packet direction, protocols, etc.), to train ML algorithms. The collection of these features along-with systems calls would undoubtedly reveal promising patterns for identifying malware. We also plan to model new feature selection techniques having high correlation with class, but loosely correlated with other features. Finally, we plan to carry out attacks on classifier ensembles, and develop

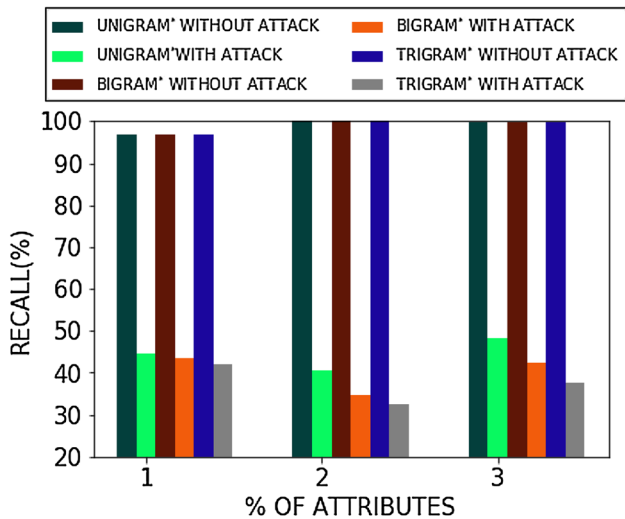


Fig. 10 Performance evaluation of unigram, bigram and trigram after poisoning using DL

countermeasures to harden classifier for minimizing misclassification rate.

Compliance with ethical standards

Conflicts of interest There is no conflict of interest for the paper.

Appendix

In this section, different scores of N-gram for GSS, WFS, and MI are presented to illustrate the malware and benign samples for various features (see the Figs. 11, 12 and 13).

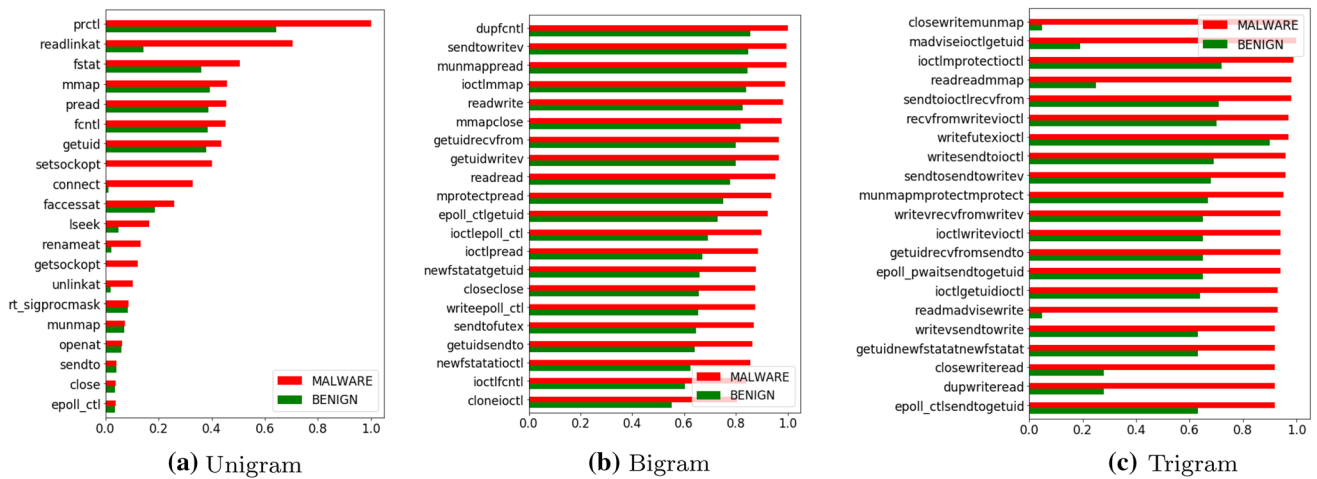


Fig. 11 Score difference of N-grams for GSS*

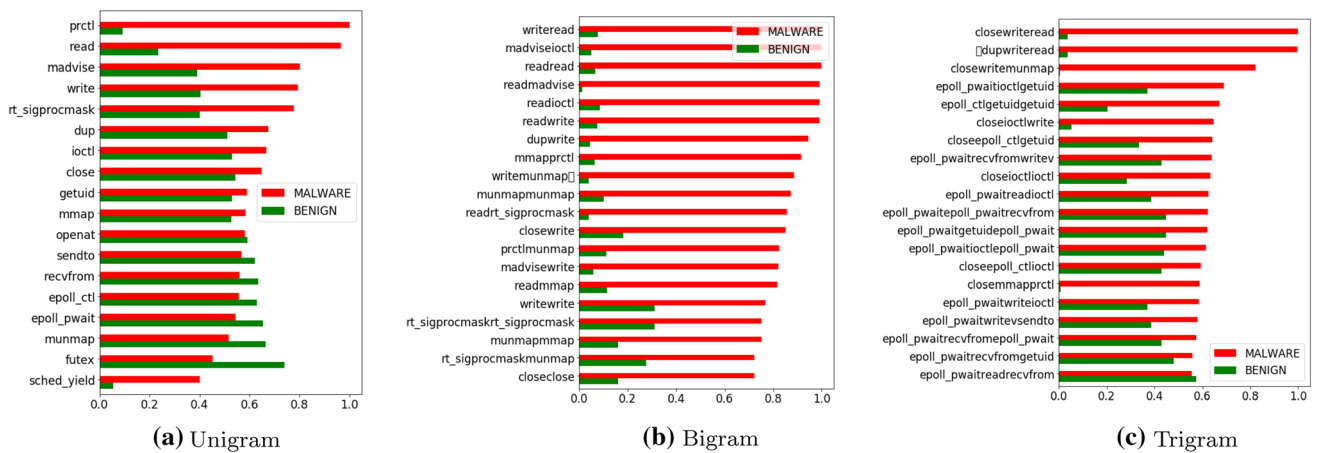


Fig. 12 Score difference of N-grams for WFS*

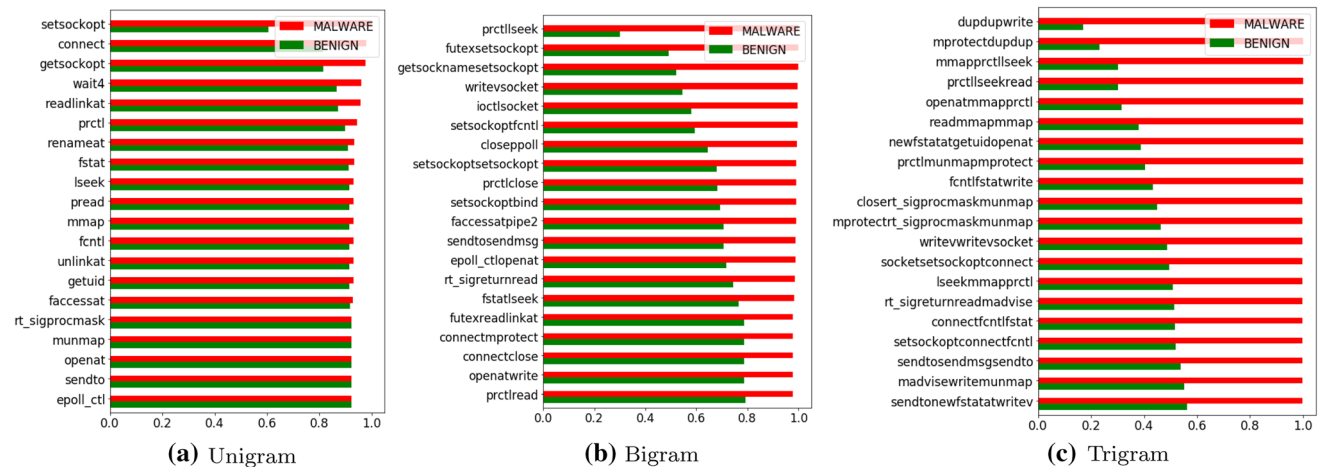


Fig. 13 Score difference of N-grams for MI*

References

1. Aafer, Y., Du, W., Yin, H.: Droidapiminer: mining api-level features for robust malware detection in android. In: International Conference on Security and Privacy in Communication Systems, pp. 86–103. Springer, Berlin (2013)
2. Afonso, V.M., de Amorim, M.F., Grégio, A.R.A., Junquera, G.B., de Geus, P.L.: Identifying android malware using dynamically obtained features. *J. Comput. Virol. Hacking Tech.* **11**(1), 9–17 (2015)
3. Arp, D., Spreitzenbarth, M., Hubner, M., Gascon, H., Rieck, K., Siemens, C.: Drebin: effective and explainable detection of android malware in your pocket. *Ndss* **14**, 23–26 (2014)
4. Arshad, S., Shah, M.A., Wahid, A., Mehmood, A., Song, H., Yu, H.: Samadroid: a novel 3-level hybrid malware detection model for android operating system. *IEEE Access* **6**, 4321–4339 (2018)
5. Bhandari, S., Panihar, R., Naval, S., Laxmi, V., Zemmari, A., Gaur, M.S.: Sword: semantic aware android malware detector. *J. Inf. Secur. Appl.* **42**, 46–56 (2018)
6. Biggio, B., Corona, I., Maiorca, D., Nelson, B., Šmrdić, N., Laskov, P., Giacinto, G., Roli, F.: Evasion attacks against machine learning at test time. In: Joint European Conference on Machine Learning and Knowledge Discovery in Databases, pp. 387–402. Springer, Berlin (2013)
7. Breiman, L.: Random forests. *Mach. Learn.* **45**(1), 5–32 (2001)
8. Burguera, I., Zurutuza, U., Nadjm-Tehrani, S.: Crowddroid: behavior-based malware detection system for android. In: Proceedings of the 1st ACM Workshop on Security and Privacy in Smartphones and Mobile Devices, pp. 15–26. ACM (2011)
9. Cyber security facts and statistics for 2019. <https://us.norton.com/internetsecurity-emerging-threats-10-facts-/about-todays-cybersecurity-landscape-that-you-should-know.html> (2019). Accessed 10 Aug 2019
10. Cao, Y., Yang, J.: Towards making systems forget with machine unlearning. In: 2015 IEEE Symposium on Security and Privacy, pp. 463–480. IEEE (2015)
11. Chen, L., Hou, S., Ye, Y., Chen, L.: An adversarial machine learning model against android malware evasion attacks. In: Asia-Pacific Web (APWeb) and Web-Age Information Management (WAIM) Joint Conference on Web and Big Data, pp. 43–55. Springer, Berlin (2017)
12. Chen, S., Xue, M., Fan, L., Hao, S., Xu, L., Zhu, H., Li, B.: Automated poisoning attacks and defenses in malware detection systems: an adversarial machine learning approach. *Comput. Secur.* **73**, 326–344 (2018)
13. Chen, T., Guestrin, C.: Xgboost: a scalable tree boosting system. In: Proceedings of the 22nd ACM SIGKDD International Conference on Knowledge Discovery and Data Mining, pp. 785–794. ACM (2016)
14. Grosse, K., Papernot, N., Manoharan, P., Backes, M., McDaniel, P.: Adversarial examples for malware detection. In: European Symposium on Research in Computer Security, pp. 62–79. Springer, Berlin (2017)
15. Han, W., Xue, J., Wang, Y., Huang, L., Kong, Z., Mao, L.: Maldae: detecting and explaining malware based on correlation and fusion of static and dynamic characteristics. *Comput. Secur.* **83**, 208–233 (2019)
16. Hosmer Jr., D.W., Lemeshow, S., Sturdivant, R.X.: Applied Logistic Regression, vol. 398. Wiley, New York (2013)
17. Hou, S., Saas, A., Chen, L., Ye, Y.: Deep4maldroid: a deep learning framework for android malware detection based on linux kernel system call graphs. In: 2016 IEEE/WIC/ACM International Conference on Web Intelligence Workshops (WIW), pp. 104–111. IEEE (2016)
18. Hou, S., Saas, A., Ye, Y., Chen, L.: Droiddelver: an android malware detection system using deep belief network based on API call blocks. In: International Conference on Web-Age Information Management, pp. 54–66. Springer, Berlin (2016)
19. Hou, S., Ye, Y., Song, Y., Abdulhayoglu, M.: Hindroid: an intelligent android malware detection system based on structured heterogeneous information network. In: Proceedings of the 23rd ACM SIGKDD International Conference on Knowledge Discovery and Data Mining, pp. 1507–1515. ACM (2017)
20. Ishibashi, H., Hihara, S., Iriki, A.: Acquisition and development of monkey tool-use: behavioral and kinematic analyses. *Can. J. Physiol. Pharmacol.* **78**(11), 958–966 (2000)
21. Largeton, C., Moulin, C., Géry, M.: Entropy based feature selection for text categorization. In: Proceedings of the 2011 ACM Symposium on Applied Computing, pp. 924–928. ACM (2011)
22. Mobile malware evolution 2019. <https://securelist.com/mobile-malware-evolution-2018/89689/> (2019). Accessed 10 Aug 2019
23. Michael, S., Florian, E., Thomas, S., Felix, C.F., Hoffmann, J.: Mobilesandbox: looking deeper into android applications. In: Proceedings of the 28th International ACM Symposium on Applied Computing (SAC) (2013)
24. Naway, A., Li, Y.: A review on the use of deep learning in android malware detection. arXiv preprint arXiv:1812.10360 (2018)

25. Roundy, K.A., Miller, B.P.: Hybrid analysis and control of malware. In: International Workshop on Recent Advances in Intrusion Detection, pp. 317–338. Springer, Berlin (2010)
26. Safavian, S.R., Landgrebe, D.: A survey of decision tree classifier methodology. *IEEE Trans. Syst. Man Cybern.* **21**(3), 660–674 (1991)
27. Santos, I., Peña, Y.K., Devesa, J., Bringas, P.G.: N-grams-based file signatures for malware detection. *ICEIS* **2**(9), 317–320 (2009)
28. Srivastava, N., Hinton, G., Krizhevsky, A., Sutskever, I., Salakhutdinov, R.: Dropout: a simple way to prevent neural networks from overfitting. *J. Mach. Learn. Res.* **15**(1), 1929–1958 (2014)
29. Suci, O., Marginean, R., Kaya, Y., Daume III, H., Dumitras, T.: When does machine learning FAIL? Generalized transferability for evasion and poisoning attacks. In: 27th USENIX Security Symposium (USENIX Security 18), pp. 1299–1316 (2018)
30. Tong, F., Yan, Z.: A hybrid approach of mobile malware detection in android. *J. Parallel Distrib. Comput.* **103**, 22–31 (2017)
31. VirusTotal. <http://virustotal.com/> (2019). Accessed 10 Aug 2019
32. Wang, W., Zhao, M., Wang, J.: Effective android malware detection with a hybrid model based on deep autoencoder and convolutional neural network. *J. Ambient Intell. Humaniz. Comput.* **10**(8), 3035–3043 (2019)
33. Yang, Y., Shen, H.T., Ma, Z., Huang, Z., Zhou, X.: L2, 1-norm regularized discriminative feature selection for unsupervised. In: Twenty-Second International Joint Conference on Artificial Intelligence (2011)
34. Yuan, Z., Lu, Y., Xue, Y.: Droiddetector: android malware characterization and detection using deep learning. *Tsinghua Sci. Technol.* **21**(1), 114–123 (2016)
35. Zhang, J., Zhang, K., Qin, Z., Yin, H., Wu, Q.: Sensitive system calls based packed malware variants detection using principal component initialized multilayers neural networks. *Cybersecurity* **1**(1), 10 (2018)
36. Zheng, Z., Wu, X., Srihari, R.: Feature selection for text categorization on imbalanced data. *ACM SIGKDD Explor. Newslett.* **6**(1), 80–89 (2004)
37. Zhou, Y., Jiang, X.: Dissecting android malware: characterization and evolution. In: 2012 IEEE Symposium on Security and Privacy, pp. 95–109. IEEE (2012)
38. 9apps: Android app website. <https://www.9apps.com/> (2019). Accessed 10 Aug 2019

Publisher's Note Springer Nature remains neutral with regard to jurisdictional claims in published maps and institutional affiliations.



Ananya Asok graduated from SCMS School of Engineering and Technology, Kochi, Kerala in May 2019 with a Bachelor's of Technology in Computer Science and Engineering. She has keen interests in the area of machine learning. Her main research interest is Android Mobile security and privacy and machine learning.



Aswathy A. graduated from SCMS School of Engineering & Technology in July 2019 with a bachelor's of technology in Computer Science and Engineering. She has a keen interest in the field of machine learning and her involvement in the developer community ecosystem had made a great impact on the lives of many aspiring women engineers. Her main research interest is Android Mobile security and privacy and machine learning.



Amal T.R. received his Bachelor of Science in Mathematics from Calicut University in 2016. Also, he received a Master's degree in Computer Applications from APJ Abdul Kalam Technical University in 2019. His main research interest is Android Mobile security and privacy and machine learning.



Swathy P.G. graduated from SCMS School of Engineering and Technology in July 2019 with a Master's in Computer Science and Information Systems. Her main research interest is Android Mobile security and privacy and machine learning.



Vinod P. is Professor in Department of Computer Science & Engineering at SCMS School of Engineering and Technology, Kerala, India. He was Post Doc at Department of Mathematics, University of Padua, Italy. During his Post Doctoral research he was actively involved in executing EU-H2020 project TagitSmart. He holds his Ph.D in Computer Engineering from Malaviya National Institute of Technology, Jaipur, India. He has more

than numerous research articles published in peer reviewed Journals and International Conferences. He is reviewer of number of security journals, and has also served as programme committee member in the

International Conferences related to Computer and Information Security. His current research is involved in the development of malware scanner for mobile application using machine learning techniques. Vinod's area of interest is Adversarial machine learning, Malware analysis, context aware privacy persevering data mining, ethical hacking and natural language processing.



Mohammad Shojafar is an Intel Innovator, a Senior IEEE member, a Senior Researcher and a Marie Curie Fellow in the SPRITZ Security and Privacy Research group at the University of Padua, Italy. Also, he was CNIT Senior Researcher at the University of Rome Tor Vergata contributed to 5G PPP European H2020 “SUPERFLUIDITY” project. He is a PI on PRISE-NODE project, a 275,000 euro Horizon 2020 Marie Curie project in the areas of network

security and Fog computing and resource scheduling collaborating

between the University of Padua and University of Melbourne. He also was a PI on an Italian SDN security and privacy (60,000 euro) supported by the University of Padua in 2018. He also contributed to some Italian projects in telecommunications like GAUChO—A Green Adaptive Fog Computing and Networking Architecture (400,000 euro), and SAMM-Clouds- Secure and Adaptive Management of Multi-Clouds (30,000 euro) collaborating among Italian universities. He received a Ph.D. in ICT from Sapienza University of Rome, Italy, in 2016 with an “Excellent” degree. His main research interests are in the area of Computer Networks, Network Security, and Privacy. In this area, he published more than 100+ papers in topmost international peer-reviewed journals and conferences, e.g., IEEE TCC, IEEE TNSM, IEEE TGCN, IEEE TSUSC, IEEE Network, IEEE SMC, IEEE PIMRC, and IEEE ICC/GLOBECOM. He served as a PC member of several prestigious conferences, including IEEE INFOCOM Workshops in 2019, IEEE GLOBECOM, IEEE ICC, IEEE UCC, IEEE ScalCom, and IEEE SMC. He was GC in FMEC 2019, INCoS 2019, INCoS 2018, and a Technical Program Chair in IEEE FMEC 2020. He served as an Associate Editor in IEEE Transactions on Consumer Electronics, IET Communication, Springer Cluster Computing, and Ad Hoc & Sensor Wireless Networks Journals.

1-1-2020

A secure and energy-efficient opportunistic routing protocol with void avoidance for underwater acoustic sensor networks

Varun Menon

DIVYA Midhunchakkaravarthy

SONALI JOHN

SUNIL JACOB

AMRIT Mukherjee

Follow this and additional works at: <https://journals.tubitak.gov.tr/elektrik>



Part of the [Computer Engineering Commons](#), [Computer Sciences Commons](#), and the [Electrical and Computer Engineering Commons](#)

Recommended Citation

Menon, Varun; Midhunchakkaravarthy, DIVYA; JOHN, SONALI; JACOB, SUNIL; and Mukherjee, AMRIT (2020) "A secure and energy-efficient opportunistic routing protocol with void avoidance for underwater acoustic sensor networks," *Turkish Journal of Electrical Engineering and Computer Sciences*: Vol. 28: No. 4, Article 34. <https://doi.org/10.3906/elk-2001-51>

Available at: <https://journals.tubitak.gov.tr/elektrik/vol28/iss4/34>

This Article is brought to you for free and open access by TÜBİTAK Academic Journals. It has been accepted for inclusion in Turkish Journal of Electrical Engineering and Computer Sciences by an authorized editor of TÜBİTAK Academic Journals. For more information, please contact academic.publications@tubitak.gov.tr.

A secure and energy-efficient opportunistic routing protocol with void avoidance for underwater acoustic sensor networks

Varun MENON^{1,2*} , Divya MIDHUNCHAKKARAVARTHY³ , Sonali JOHN² , Sunil JACOB^{4,5} ,
Amrit MUKHERJEE^{6,7} 

¹Department of Computer Science and Engineering, Lincoln University College, Petaling Jaya, Malaysia

²Department of Computer Science and Engineering, SCMS School of Engineering and Technology, Cochin, India

³Center of Postgraduate Studies, Lincoln University College, Petaling Jaya, Malaysia

⁴Department of Electronics and Communication Engineering, Lincoln University College, Petaling Jaya, Malaysia

⁵Center for Robotics, SCMS School of Engineering and Technology, Cochin, India

⁶Department of Computer Science and Communication Engineering, Jiangsu University, Jiangsu, P.R. China

⁷School of Electronics Engineering, KIIT University, Bhubaneswar, India

Received: 11.01.2020

Accepted/Published Online: 04.05.2020

Final Version: 29.07.2020

Abstract: Recently, underwater acoustic sensor networks (UASNs) have gained wide attention due to their numerous applications in underwater surveillance, oil leakage detection, assisted navigation, and disaster prevention. With unique characteristics like increased propagation delay, constant mobility of sensor nodes, high error rate, and limitations in energy and interference, efficient routing of data packets from the source node to the destination is a major challenge in UASNs. Most of the protocols proposed for traditional sensor networks do not work well in UASNs. Although many protocols have been specifically proposed for underwater environments, the aim of most of them is to improve only the quality of service (QoS) in the network. The security of the transmitted data, energy efficiency of the participating nodes, and handling of communication voids are three significant challenges that need to be adequately addressed in UASNs. In this research work, a secure and energy-efficient opportunistic routing protocol with void avoidance (SEEORVA) is proposed. This protocol uses the latest opportunistic routing strategy for reliable data delivery in the network and also provides priority to the nodes having energy above a specific threshold in the forwarding process, thereby increasing the lifetime and energy efficiency in the network. The transmitted messages are encrypted using a secure lightweight encryption technique. The protocol is also integrated with a strategy to handle the communication voids in the network. Simulation results with Aqua-Sim validate the better performance of the proposed system compared to the existing ones.

Key words: Energy efficiency, communication voids, routing protocols, secure data transmission, QoS, underwater acoustic sensor networks

1. Introduction

The ocean covers about 70% of the Earth's surface and is the most abundant source of rare and valuable resources. Due to various constraints, knowledge about the underwater environment is limited, and most of these resources are still unexplored. Underwater acoustic sensor networks (UASNs) [1] have given us hope as a possible solution to this problem. A UASN is a group of self-driven sensor nodes and autonomous vehicles connected underwater to perform different collective tasks based on user applications [2]. Sensor nodes placed at various locations and depths sense and record data and transfer them through the network of nodes to the

*Correspondence: varungmenon46@gmail.com

destination sinks placed at the surface. The collection centers are usually on buoys or ships on the water's surface. Integrating with the most popular Internet of Things (IoT) [3, 4] technology, this smart network of interconnected underwater devices forms the Internet of Underwater Things (IoUT) [5].

Recently, the IoUT and UASNs have gained wide popularity due to their numerous research, industrial, and military applications. They are currently deployed for underwater monitoring and surveillance, oil leakage detection, assisted navigation, and disaster prevention. UASNs are different from the traditional sensor networks (TSNs) and use acoustic signals instead of radio signals. Routing of data packets in UASN is an exceedingly challenging task due to the unique features of the transmission medium such as long propagation delay, constant mobility of sensor nodes, high error rate, limitations in energy, increased error rate, interference caused by animals, and limited bandwidth. Reliable communication and efficient transfer of data from the source to the destination node are vital factors determining the success of various user applications deploying UASNs with multiple objectives. Routing protocols proposed for TSNs do not work well in the underwater environment [6–8]. In the last few years, many techniques have been discussed for efficient data transfer in UASNs, with opportunistic routing protocols (ORPs) [9, 10] being the latest and most efficient among them. ORPs use a broadcasting strategy to increase the number of forwarder nodes and create a prioritized list of available forwarder nodes. They then select the node that has maximum progress to the destination for forwarding the data packet. If that node is unable to forward the data packet within a specified time limit, the next forwarder node in the list forwards the data packet, thus ensuring reliable data delivery in the network. Although the ORPs proposed for UASNs offer several advantages, most of them are designed primarily for improving the quality of service (QoS) in the network.

One of the main limitations in UASNs is the difficulty in periodic recharging of the sensor nodes. If the energy available in the sensor nodes gets exhausted very quickly, the nodes cannot participate in future data transmission. Hence, it is essential to optimize the energy usage in data packet forwarding and conserve energy to extend the lifetime of each sensor node [11–13]. This issue is very inadequately addressed by most of the routing protocols proposed for UASNs [14–16]. Security in data transmission is another major issue to be addressed in UASNs. Sensor nodes in many military and industrial applications collect and record sensitive data. These sensitive data have to be securely stored and transmitted to the sink nodes and any leakage can be very harmful [17]. Moreover, it is found that numerous communication voids [18] occur in underwater environments. Communication voids occur when a source node is unable to find any suitable forwarder node in its transmission range and located in the direction of the destination. Communication voids are also called communication gaps or the unreachability problem. Failure of intermediate nodes due to energy drainage, wrong deployment, intrusions, attacks, etc. are some of the reasons contributing to the occurrence of voids in the network. As most of the latest routing protocols use a position-based greedy forwarding mechanism, this issue has become a major concern. Lack of proper mechanisms to handle voids can lead to huge data loss and loss of energy with retransmissions. Our proposed protocol, the secure and energy-efficient opportunistic routing protocol with void avoidance (SEEORVA), addresses all three issues and also supports good QoS for data transmission in the underwater environment.

In SEEORVA, the sensed and collected data are encrypted using a lightweight security protocol, the novel tiny symmetric encryption algorithm (NTSA) [19]. These encrypted packets are sent to the destination nodes through the network of sensor nodes. Only the collection and processing centers located at the surface are capable of decrypting these data packets, hence ensuring the security of transmitted data. The proposed protocol uses an opportunistic routing strategy but considers the remaining energy in each sensor node as a

significant factor determining the selection of the next best forwarder node. Nodes that have less energy are given less priority to participate in the forwarding process, thus extending the lifetime of each sensor node. SEEORVA is also integrated with a unique strategy to handle the communications voids in the network. Simulation results using Aqua-Sim [20] validated the better performance of SEEORVA compared to the existing protocols in the underwater environment.

The paper is arranged as follows. Section 2 presents the discussion on a few related works. Section 3 discusses the proposed work. Theoretical analysis of energy-efficient data transfer in the network is also presented. Section 4 presents a discussion on the results achieved through simulations. Here the performance of the proposed work is compared with existing protocols in the underwater environment. Section 5 presents the future research directions in UASNs. Finally, the paper concludes in section 6 with future research directions. Table 1 presents the notations and Table 2 presents the abbreviations used in the article. Table 3 lists the differences between TSNs and UASNs.

Table 1. Frequently used notations.

19 Notation	Definition
\bar{x}	Transmission signal coefficient
\bar{h}	Fading signal coefficient
\bar{n}	Noise coefficient
$y_1, y_2 \dots y_L$	Signal received at the receiving node
\bar{y}	Receiving signal coefficient
\bar{w}	Beamforming coefficient
B_f	Beamformer output
P_s	Signal power
P_n	Noise power
N_e	Effective noise at the output of beamformer
SNR_{B_f}	SNR at the output of the beamformer
\bar{w}	Beamforming vector

Table 2. List of abbreviations.

Abbreviation	Description
UASN	Underwater acoustic sensor networks
QoS	Quality of Service
SEEORVA	Secure and energy-efficient opportunistic routing protocol with void avoidance
IoT	Internet of things
IoUT	Internet of underwater things
TSN	Traditional sensor networks
ORP	Opportunistic routing protocols
NTSA	Novel tiny symmetric encryption algorithm
PDR	Packet delivery ratio
PFL	Priority forwarder list

Table 3. Difference between TSNs and UASNs.

TSN	UASN
Sensor nodes are deployed densely	Sparse deployment of sensor nodes
The Communication medium is radio waves	The Acoustic channel is the medium used
Data transfer rate is comparatively high	Data transfer rate is low
Less delay in data transmission	High delay is communication and data transmission
Lower energy consumption	High energy consumption
Higher number of static nodes	Higher number of dynamic nodes
Low error rate	High error rate

2. Related work

This section presents and discusses a few of the existing protocols proposed for UASNs. The security of the transmitted data, energy efficiency of the nodes, and handling of communication voids are three major challenges that need to be adequately addressed in UASNs. Several protocols are proposed to improve the QoS and energy efficiency in UASN. In Su et al. [21], a technique is discussed to increase the network lifetime of the sensor nodes in UASNs using the concept of Deep Q-Network. The technique is also aimed at reducing the delay in data transmission in the network. Another method [22] uses the fuzzy-based relay selection approach to select the node with the maximum energy for forwarding the data packets. Furthermore, the holding time is set for each group of forwarding nodes to avoid collision and save energy. Many protocols work on reducing the collision between the nodes in the network, like the multichannel MAC protocol discussed in Bouabdallah et al. [23]. Although many protocols have tried to improve the energy efficiency and QoS in UASNs, most of them have given very little importance to security in data transmission. A reliable security framework for UASNs is proposed in Ateniese et al. [24]. Common security measures and threats faced in UASNs are discussed in detail in that work. It aims to provide data confidentiality, integrity, and authentication for applications deploying UASNs. A comprehensive discussion on the security attacks faced in UASNs is presented in Shahapur and Khanai [25]. A technique to improve the secrecy of block transmissions based on the half-duplex nature of the underwater transceivers in underwater acoustic channels is presented in Huang et al. [26]. A few protocols are designed to handle the communication voids in the network [27, 28]. However, most of the existing protocols focus primarily on improving the QoS. Lack of an efficient technique for energy efficiency and void avoidance with adequate security in data transmission is still a major problem. The proposed method, secure and energy-efficient opportunistic routing protocol with void avoidance (SEEORVA), uses the latest opportunistic routing strategy for reliable data delivery in the network. The protocol considers only the nodes having energy above a specific threshold in the forwarding process, thereby increasing the lifetime and energy efficiency in the network. The transmitted messages are encrypted using a lightweight encryption technique and the protocol is integrated with a strategy to handle the communication voids in the network. The next section discusses the proposed method.

3. Proposed system

3.1. Theoretical analysis

In this section, the theoretical analysis of the proposed work in efficient energy utilization of a UASN is presented and discussed. Emphasis is given on optimizing the beamforming between the sender and the receiver nodes

such that minimum energy is utilized during the transmission process. Here, assuming \bar{x} as the transmission signal coefficient, \bar{h} as the fading signal coefficient, \bar{n} as the noise coefficient, and y_1, y_2, \dots, y_L as the signal received at the receiving node, the receiving signal coefficient \bar{y} is given by

$$\bar{y} = \bar{h}\bar{x} + \bar{n} \tag{1}$$

Here the beamforming coefficient is assumed to be \bar{w} such that

$$\bar{w} = \begin{bmatrix} w_1 \\ w_2 \\ \cdot \\ \cdot \\ w_l \end{bmatrix} \text{ and } \bar{w}^H = [w_1^* \quad w_2^* \quad w_3^* \quad \dots \quad w_L^*].$$

Combining the received signals with the beamforming coefficient \bar{w} , the beamformer output B_f is obtained as

$$B_f = [w_1^* \quad w_2^* \quad w_3^* \quad \dots \quad w_L^*] \begin{bmatrix} y_1 \\ y_2 \\ \cdot \\ \cdot \\ y_L \end{bmatrix} \tag{2}$$

$$B_f = \bar{w}^H \bar{y} \tag{3}$$

Substituting the value of the received output signal \bar{y} in Eq. 1 into Eq. 2, we obtain

$$B_f = \bar{w}^H (\bar{h}\bar{x} + \bar{n}) \tag{4}$$

$$B_f = \bar{w}^H \bar{h}\bar{x} + \bar{w}^H \bar{n} \tag{5}$$

Here the signal power P_s is given by $\bar{w}^H \bar{h}\bar{x}$ and noise power P_n is given by $\bar{w}^H \bar{n}$. Introducing constant P with signal power, we obtain

$$P_s = |\bar{w}^H \bar{h}|^2 .P \tag{6}$$

Now we have the effective noise at the output of beamformer, $N_e = \bar{w}^H \bar{n}$. Calculating the expectation E of N_e we have

$$N_e = E \left\{ |\bar{w}^H \bar{n}|^2 \right\} \tag{7}$$

$$N_e = E \left\{ (\bar{w}^H \bar{n}) (\bar{w}^H \bar{n})^* \right\} \tag{8}$$

where $\bar{w}^H \bar{n} = w_1^* n_1 + w_2^* n_2 + \dots + w_L^* n_L$ and $(\bar{w}^H \bar{n})^* = w_1 n_1^* + w_2 n_2^* + \dots + w_L n_L^*$

$$N_e = E \left\{ \sum_{i=1}^L |w_i|^2 |n_i|^2 + \sum_i \sum_j w_i w_j^* n_i^* n_j \right\}, \tag{9}$$

where $i \neq j$. Here $E(n_i n_j^*) = E(n_i)E(n_j^*)$, which will become zero. Thus the equation is reduced to

$$N_e = \sum |w_i|^2 E\{n_i\}^2 \tag{10}$$

$$N_e = \sigma_n^2 \sum w_i^2 \tag{11}$$

$$N_e = \sigma_n^2 \bar{w}^2 \tag{12}$$

$$N_e = \sigma_n^2 \bar{w}^H \bar{w} \tag{13}$$

Now the *SNR* at the output of the beamformer is given by

$$(SNR)_{\max} = \frac{|\bar{w}^H h|^2 P}{\sigma_n^2 (\bar{w}^H \bar{w})} \tag{14}$$

The aim is to select the beamforming vector \bar{w} , such that \bar{w} maximizes the *SNR* in multiple diversity receiving nodes,

$$(SNR)_{\max} = \left(\frac{|\bar{w}^H \bar{h}|^2}{\bar{w}^H \bar{w}} \right) * \frac{p}{\sigma_n^2} \tag{15}$$

Let us assume that the optimal \bar{w} is K such that

$$(SNR)_{\max} = \left(\frac{K^2 |\bar{w}^H \bar{h}|^2}{K^2 \bar{w}^H \bar{w}} \right) * \frac{p}{\sigma_n^2} \tag{16}$$

Here the constant K will get canceled, implying that scaling will have no effect. It is scale invariant and we need to select \bar{w} such that its magnitude is one. Select \bar{w} such that $\|\bar{w}\|^2 = 1$, which implies $\bar{w}^H \bar{w} = 1$. Now

$$(SNR)_{\max} = |\bar{w}^H \bar{h}|^2 \cdot \frac{p}{\sigma_n^2} \tag{17}$$

Now we need to find the maximum value for $\left(|\bar{w}^H \bar{h}|^2 \frac{p}{\sigma_n^2} \right)$, for which $\bar{w} = \text{const } \bar{h}$. For this we have $c^2 \|\bar{h}\|^2 = 1$, which gives $C = \frac{1}{\bar{h}}$. Optimal beamforming vector \bar{w} that maximizes the received $SNR = \frac{\bar{h}}{\bar{h}} \|\bar{h}\|^2 = \bar{w}$ (the optimal value that is calculated as maximum ratio combiner). Now we have $SNR = \frac{(\bar{h}^H \bar{h})^2}{\bar{h}} \frac{p}{\sigma_n^2}$, which gives $SNR = h^2 \frac{p}{\sigma_n^2}$. This is the optimal *SNR* at the output of the receiver.

3.2. Best forwarder selection

The proposed method uses the opportunistic routing strategy for the selection of the best relay node. The opportunistic routing strategy enables the presence of more than one forwarder node and hence the chances of data delivery at the destination are high. Thus, our algorithm initially makes sure that the packet delivery ratio (PDR) in the network is high and maximum packets are delivered at the destination. The proposed algorithm used for the best forwarder selection is presented below. At first, the source node that has to transmit data packets creates a virtual vector pipe to the destination node. A list of nodes that are located within the pipe is then compiled. The highest energy of the nodes in the list is then calculated. The nodes that are outside the pipe are not considered in the forwarding process. A threshold energy value based on the calculated highest energy value is set for the forwarder nodes. The node that has energy above the threshold and within the transmission range of the source node and also that has the maximum progress to the destination is chosen as the best forwarder node. If this node cannot forward the packet within a specific period (set by a timer) due to reasons like mobility or damage of the node, the next node in the list forwards the data packet to the destination. Thus, a high rate of data delivery along with energy efficiency is guaranteed by the proposed approach. The working of this technique is illustrated in Figure 1. Here the source ‘s’ wants to transmit the data packets to target node ‘t’. The source node creates a list ‘f’, ‘c’, ‘h’, ‘a’, ‘b’ of the nodes that are located within the vector pipe. Now the source node calculates the highest energy node among the four and sets the threshold value. Nodes ‘h’, ‘c’, and ‘f’ are within the transmission range of the source node. Therefore, a priority forwarder list (PFL) (‘h’,‘c’,‘f’) is generated by the source node based on the maximum progress to the destination. Let us assume that node ‘h’ does not have energy greater than the set threshold. Thus, the node ‘c’ is selected as the best forwarder. If the node ‘c’ is unable to forward the data packet within a particular time, node ‘f’ forwards it.

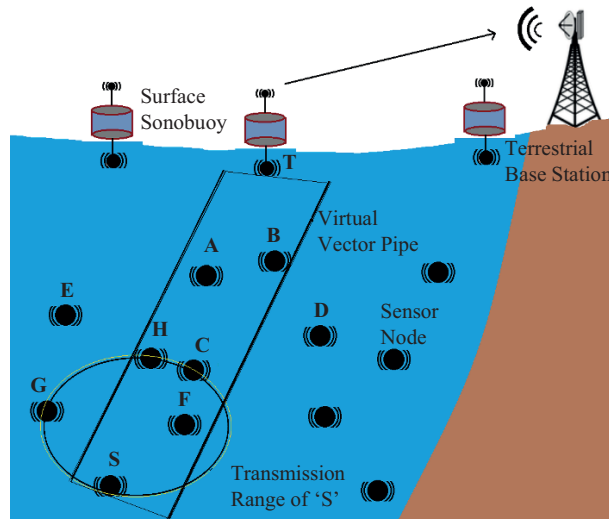


Figure 1. Illustration of the best forwarder selection algorithm using the proposed method.

Algorithm 1: For best forwarder node selection

1. The source node creates a virtual vector pipe to the destination node.
2. The source node checks for the nodes inside the pipe. If true go to step 3, otherwise drop the data packet.
3. Calculate the highest energy among the nodes inside the pipe and go to step 4

4. Set the energy threshold as highest/2.
5. The source node creates a PFL containing the nodes within its transmission range.
6. Sort the list by the distance to the destination. The node having a minimum distance to the destination is assigned the highest priority in the PFL.
7. Check whether the energy $>$ threshold for all the nodes in the PFL. If true keep the node in the list and go to step 9. Otherwise, go to step 8.
8. Drop the packet and label as a low energy node.
9. Call packet forwarding algorithm.
10. Repeat the step until the packet reaches the destination.

Algorithm 2: For packet forwarding

1. Data packet is received by a source node.
2. The node generates the PFL.
3. Forward the packet to the nodes in the PFL.
4. If the best priority forwarder forwards the data packet within a period, go to step 6, else go to step 5.
5. Next node in the PFL forwards the data packet.
6. The received node repeats steps from 1 to 4 until the packet reaches the destination.

3.3. Security and void avoidance in data transmission

One of the major issues to be addressed in UASNs is the security of data transmitted between the sensor nodes. In many UASN applications such as military ones, the security of data is the most important factor. Any leakage of information in such applications can have major consequences. To provide high security for the transmitted data, we integrate a simple, lightweight, and strong encryption technique discussed in Rajesh et al. [19] into our proposed system. It is a symmetric encryption algorithm that follows the Feistel structure. The algorithm has 64 rounds and 32 cycles of operation. In every cycle, there is an odd and even round. The message to be transferred through the network is set as 64-bit blocks. The key used in the algorithm is 128 bits and is divided into 4 subkeys. The subkeys are then dynamically applied to odd and even rounds in encryption. This algorithm is used to encrypt the transmitted data packet, which can only be decrypted by the receiver, thereby protecting the data from intruders. Due to sparse deployment and frequent mobility of sensor nodes, communication voids are a major issue contributing to increased packet drops. An efficient mechanism to handle communications voids is necessary to guarantee good QoS for various applications in UASNs. In the proposed method when a node experiences a communication void, it sends a data packet void_alert to the previous node from which the data have come. The previous node tries to find an alternate route avoiding the void or around the void and routes the data packets to the destination. All the remaining packets through the void node are redirected to this new route until the void node reports that the void is past. This technique gives much better results compared to the major existing techniques used to handle communication voids. The major advantage of this technique is that it is easy to implement with less overhead and delay.

4. Results and discussion

The performance of the proposed method, SEEORVA, is analyzed and compared with that of the existing underwater routing protocols using simulations in Aqua-Sim [20]. Aqua-Sim is an extended version of NS-2 and offers easy implementation of underwater network scenarios. The specifications used for the simulation are presented in Table 4.

The protocols are compared in terms of performance using the packet delivery ratio (PDR) (number of packets delivered at the destination compared to the total packets sent), average end-to-end delay, and normalized energy consumption. The PDR and average end-to-end delay are used to measure the QoS in the network. The number of nodes participating in the network is varied and the performance of the protocols is measured. Comparison is done using vector-based forwarding (VBF) [29] and vector-based void avoidance (VBVA) [30] protocols. Figure 2 presents the comparison of PDR with a varying number of nodes. Here we can see that the proposed technique has a better PDR compared to all the existing techniques with different numbers of nodes. Moreover, in void scenarios the proposed technique achieves a good PDR. This is because, in the proposed technique, the best forwarder is selected using an opportunistic strategy and even if the best forwarder is unable to forward the data packet, the next best forwarder forwards it, thus ensuring reliability and a high packet delivery rate in the network. Figure 3 presents the comparison of average end-to-end delay with varying number of nodes. SEEORVA has less delay in data transmission compared to all other existing techniques like VBF and VBVA. The proposed technique is easy to implement with less complexity. The efficient forwarder priority list in the algorithm aids in less delay in data transmission. Figure 4 presents the normalized energy consumption achieved through various protocols with varying numbers of nodes in the network. It is evident that SEEORVA has better energy efficiency in the network compared to the existing approaches. In addition, the proposed technique is tested in a communication void environment. Both in normal and void scenarios, the proposed technique achieves much better energy efficiency compared to all the existing approaches. This is because the proposed technique considers the residual energy available in the sensor nodes for the forwarder selection process. Thus, the network lifetime is extended with improved energy efficiency in the routing process. The simulation results show the better performance offered by the proposed technique in terms of QoS, energy efficiency, and security compared to the existing techniques in UASNs.

Table 4. Simulation specifications.

Parameter name	Values
Simulator name	NS 2.35 with Aqua-Sim
Dimension of topology	1500 x 1500 x 1500 m
Transmission range	250 m
Antenna-Type	Omni-Directional
Data rate	50 kbps
Packet size	25 to 125 bytes
Number of nodes	100 to 300
Simulation time	200 s
Number of Simulation runs	10
Protocols	SEEORVA, VBF, VBVA

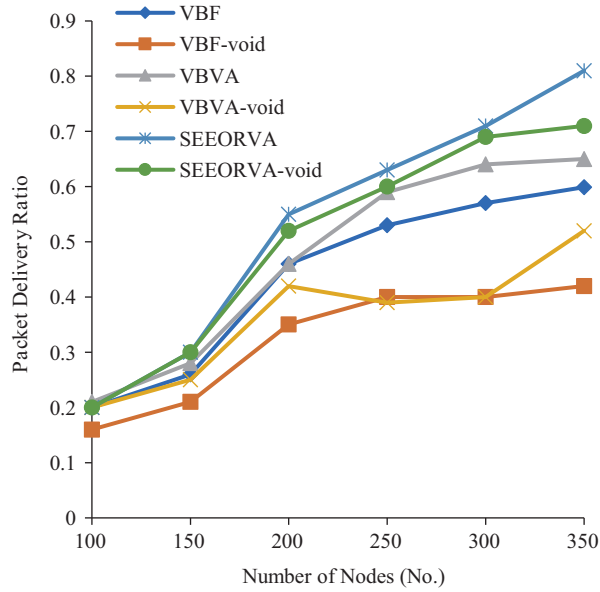


Figure 2. Variation in packet delivery ratio (PDR) with different numbers of nodes.

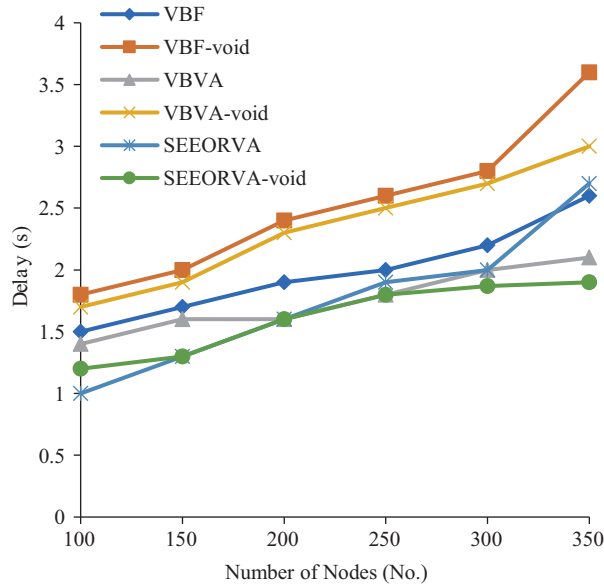


Figure 3. Variation in delay with different numbers of nodes.

5. Future research directions

In this section, we list a few research areas within UASNs that have generated interest among researchers due to the opportunities, issues, and challenges.

- Quality of service: QoS has been one of the major research areas focused on in UASNs. As the success of most of the applications depends on a high delivery rate, less delay, and other QoS parameters, numerous studies have been carried out in this direction. With an increased number of sensor nodes and advancement in sensor technology, new technique for further optimization of QoS in the network is an emerging area of research.
- Energy efficiency: With restrictions and limitations in recharging the deployed sensor node underwater,

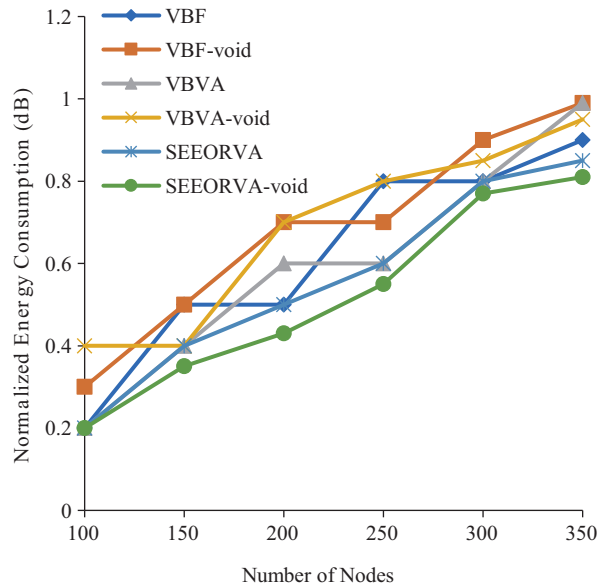


Figure 4. Variation in normalized energy consumption with different numbers of nodes.

the major hindrance behind the success of many applications is related to energy efficiency. Current research focuses on optimizing energy usage in the routing process and preventing energy leakages. This will be a major area of research in the future too.

- **Channel utilization:** Efficient utilization of the channel is another major area of research in UASNs that has gained wide prominence. With numerous challenges like propagation delay, constant mobility of sensor nodes, high error rate, and interference, it is vital to have optimal utilization of the channel.
- **Security:** The security of data transmitted between sensor nodes is a major area of concern. In many UASN applications such as military ones, the security of data is the most important factor. Any leakage of information in such applications can have major consequences. Recently, numerous studies have been carried out to secure the communication between the sensor nodes in UASNs. With increasing attacks and threats, research in security and privacy will be an ongoing and highly challenging task.
- **Reliability:** Many studies have focused on reliable data delivery in the network. This is an important parameter because it provides trust for user applications and helps in its success.
- **Communication voids:** Sparse deployment and frequent mobility of sensor nodes have led to increased communication voids in networks, leading to frequent packet drops. An efficient mechanism to handle communications voids is necessary to guarantee good QoS for various applications deployed with UASNs. This is a major research area in UASNs and will continue to be prominent in the coming years.

6. Conclusion

The security of the transmitted data, energy efficiency of the nodes, and handling of communication voids are three major challenges in UASNs that are not adequately addressed in most of the existing protocols. To address these issues, a secure and energy-efficient opportunistic routing protocol with void avoidance (SEEORVA) is proposed. This protocol uses the latest opportunistic routing strategy for reliable data delivery in the network and considers only the nodes having energy above a specific threshold in the forwarding process, thereby

increasing the lifetime and energy efficiency in the network. The transmitted messages are encrypted using a lightweight encryption technique and the protocol is also integrated with a strategy to handle the communication voids in the network. Simulation results with Aqua-Sim confirmed the better performance of the proposed system compared to the existing ones. The proposed technique needs to be tested in a real-time underwater environment in the future. The design could also be modified to incorporate bulk data coming from numerous sources.

References

- [1] Jouhari M, Ibrahimi K, Tembine H, Ben-Othman J. Underwater wireless sensor networks: A survey on enabling technologies, localization protocols, and internet of underwater things. *IEEE Access* 2019; 7: 96879-96899. doi: 10.1109/ACCESS.2019.2928876
- [2] Menon V. Opportunistic routing protocols in underwater acoustic sensor networks: issues, challenges, and future directions. In: Fei Hu (editor). *Magnetic Communications: From Theory to Practice*. USA: CRC Press, 2017, pp. 127-148.
- [3] Ang K, Seng J. Application specific Internet of Things (ASIoTs): taxonomy, applications, use case and future directions. *IEEE Access* 2019; 7: 56577-56590. doi: 10.1109/ACCESS.2019.2907793
- [4] Anavangot V, Menon V, Nayyar A. Distributed big data analytics in the internet of signals. In: *Proceedings of the IEEE International Conference on System Modelling and Advancement in Research Trends (SMART)*; Moradabad, India; 2018. pp. 73-77. doi: 10.1109/SYSMART.2018.8746983
- [5] Liou EC, Kao CC, Chang CH, Lin YS, Huang CJ. Internet of underwater things: challenges and routing protocols. In: *Proceedings of the IEEE International Conference on Applied System Invention*; Chiba, Japan; 2018. pp. 1171-1174. doi: 10.1109/ICASI.2018.8394494
- [6] Menon V, Joeprathap PM. Comparative analysis of opportunistic routing protocols for underwater acoustic sensor networks. In: *Proceedings of the IEEE International Conference on Emerging Technological Trends (ICETT)*; Kollam, India; 2016. pp. 1-5. doi: 10.1109/ICETT.2016.7873733
- [7] Alzubi JA, Almomani O, Alzubi OA, Al-shugran M. Intelligent and dynamic neighbourhood entry lifetime for position-based routing protocol using fuzzy logic controller. *International Journal of Computer Science and Information Security* 2016; 14(1): 118-128.
- [8] Zorzi M, Casari P, Baldo N, Harris A. Energy-efficient routing schemes for underwater acoustic networks. *IEEE Journal on Selected Areas in Communications* 2008; 26(9): 1754-1766. doi: 10.1109/JSAC.2008.081214
- [9] Coutinho RWL, Boukerche A. Opportunistic routing in underwater sensor networks: potentials, challenges and guidelines. In: *Proceedings of 2017 13th International Conference on Distributed Computing in Sensor Systems (DCOSS)*; Ottawa, Canada; 2017. pp. 1-2. doi: 10.1109/DCOSS.2017.42
- [10] Menon V, Joeprathap PM. Analysing the behaviour and performance of opportunistic routing protocols in highly mobile wireless ad hoc networks. *International Journal of Engineering and Technology* 2016; 8(5): 1916-1924. doi: 10.21817/ijet/2016/v8i5/160805409
- [11] Irandoost A, Taheri S, Movaghar A. PL-MAC: ProLonging network lifetime with a MAC layer approach in wireless sensor networks. In: *Proceedings of the Second International Conference on Sensor Technologies and Applications*; Cap Esterel, France; 2008. pp. 109-114. doi: 109-114.10.1109/SENSORCOMM.2008.120
- [12] Alrabea A, Alzubi OA, Alzubi JA. A task-based model for minimizing energy consumption in WSNs. *Energy Systems* 2019. <https://doi.org/10.1007/s12667-019-00372-w>
- [13] Almomani O, Al-Shugran M, Alzubi JA, Alzubi OA. Performance evaluation of position-based routing protocols using different mobility models in manet. *International Journal of Computer Applications* 2015; 119(3): 43-48.
- [14] Kaur K, Kumar N, Garg S, Rodrigues JPC. EnLoc: data locality-aware energy-efficient scheduling scheme for cloud data centers. In: *Proceedings of the IEEE International Conference on Communications (ICC)*; Kansas City, USA; 2018, pp. 1-6. doi: 10.1109/ICC.2018.8422225

- [15] Kaur K, Garg S, Kaddoum G, Gagnon F, Kumar N et al. An energy-driven network function virtualization for multi-domain software defined networks. In: Proceedings of the IEEE INFOCOM - IEEE Conference on Computer Communications Workshops (INFOCOM WKSHPS); Paris, France; 2019. pp. 121-126. doi: 10.1109/INFOCOMW.2019.8845314
- [16] Kaur K, Garg S, Kaddoum G, Bou-Harb E, Choo KR. A big data-enabled consolidated framework for energy efficient software defined data centers in IoT setups. *IEEE Transactions on Industrial Informatics* 2020; 16(4): 2687-2697. doi: 10.1109/TII.2019.2939573
- [17] Jiang S. On securing underwater acoustic networks: A survey. *IEEE Communications Surveys and Tutorials* 2019; 21(1): 729-752. doi: 10.1109/COMST.2018.2864127
- [18] Menon V, Joeprathap PM. Opportunistic routing with virtual coordinates to handle communication voids in mobile ad hoc networks. In: Proceedings of the Second International Symposium on Signal Processing and Intelligent Recognition Systems; Trivandrum, India; 2015. p. 323-334.
- [19] Rajesh S, Paul V, Menon V G, Khosravi M. A secure and efficient lightweight symmetric encryption scheme for transfer of text files between embedded IoT devices. *Symmetry* 2019; 11(2): 293. doi:10.3390/sym11020293
- [20] Xie P, Zhou Z, Peng Z, Yan H, Hu T et al. Aqua-Sim: An NS-2 based simulator for underwater sensor networks. In: Proceedings of the OCEANS 2009, MTS/IEEE Biloxi - Marine Technology for Our Future: Global and Local Challenges; Biloxi, USA; 2009. pp. 1-7. doi: 10.23919/OCEANS.2009.5422081
- [21] Su Y, Fan R, Fu X, Jin Z. DQELR: An adaptive deep Q-network-based energy and latency-aware routing protocol design for underwater acoustic sensor networks. *IEEE Access* 2019; 7: 9091-9104. doi: 10.1109/ACCESS.2019.289159
- [22] Mulla A, Jadhav V. Energy efficient routing protocol for underwater acoustic sensor network. In: Proceedings of the Second International Conference on Intelligent Computing and Control Systems; Madurai, India; 2018. pp. 1707-1712. doi: 10.1109/ICCONS.2018.8662952
- [23] Bouabdallah F, Zidi C, Boutaba R, Mehaoua A. Collision avoidance energy efficient multi-channel MAC protocol for underwater acoustic sensor networks. *IEEE Transactions on Mobile Computing* 2019; 18(10): 2298-2314. doi: 10.1109/TMC.2018.2871686
- [24] Ateniese G, Caposelle A, Gjanci P, Petrioli C, Spacciniet D. SecFUN: Security framework for underwater acoustic sensor networks. In: Proceedings of OCEANS 2015; Genova, Italy; 2015. pp. 1-9. doi: 10.1109/OCEANS-Genova.2015.7271735
- [25] Shahapur S, Khanai R. Localization, routing and its security in UWSN - A survey. In: Proceedings of the International Conference on Electrical, Electronics, and Optimization Techniques (ICEEOT); Chennai, India; 2016. pp. 1001-1006. doi: 10.1109/ICEEOT.2016.7754836
- [26] Huang Y, Xiao P, Zhou S, Shi Z. A half-duplex self-protection jamming approach for improving secrecy of block transmissions in underwater acoustic channels. *IEEE Sensors Journal* 2016; 16(11): 4100-4109. doi: 10.1109/JSEN.2015.2446465
- [27] Sonali J, Menon V, Nayyar A. Simulation-based performance analysis of location-based opportunistic routing protocols in underwater sensor networks having communication voids. In: Proceedings of Data Management, Analytics and Innovation; New Delhi, India; 2019. pp. 697-711.
- [28] Wang Z, Han G, Qin H, Zhang S, Sui Y. An energy-aware and void-avoidable routing protocol for underwater sensor networks. *IEEE Access* 2018; 6: 7792-7801. doi: 10.1109/ACCESS.2018.2805804
- [29] Peng X, Cui J, Lao L. VBF: vector-based forwarding protocol for underwater sensor networks. In: Proceedings of the International conference on research in networking; Coimbra, Portugal; 2006. pp. 1216-1221. doi: 10.1007/11753810_111
- [30] Peng X, Zhou Z, Peng Z, Cui JZ, Zhi Z. Void avoidance in three-dimensional mobile underwater sensor networks. In: Proceedings of the International Conference on Wireless Algorithms, Systems, and Applications; Boston, MA, USA; 2009. pp. 305-314. doi: 10.1007/978-3-642-03417-6_30

Optimum range of angle tracking radars: a theoretical computing

Sadegh Samadi¹, Mohammad Reza Khosravi², Jafar A. Alzubi³, Omar A. Alzubi⁴, Varun G. Menon⁵

^{1,2}Shiraz University of Technology, Iran

^{3,4}Al-Balqa Applied University, Jordan

⁵SCMS School of Engineering and Technology, India

Article Info

Article history:

Received Mar 7, 2018

Revised Dec 22, 2018

Accepted Jan 3, 2019

Keywords:

Angle error

Angle tracking radars (ATRs)

Optimal range

Radar equation

Signal-to-noise ratio (SNR)

ABSTRACT

In this paper, we determine an optimal range for angle tracking radars (ATRs) based on evaluating the standard deviation of all kinds of errors in a tracking system. In the past, this optimal range has often been computed by the simulation of the total error components; however, we are going to introduce a closed form for this computation which allows us to obtain the optimal range directly. Thus, for this purpose, we firstly solve an optimization problem to achieve the closed form of the optimal range (R_{opt}) and then, we compute it by doing a simple simulation. The results show that both theoretical and simulation-based computations are similar to each other.

Copyright © 2019 Institute of Advanced Engineering and Science.
All rights reserved.

Corresponding Author:

Varun G. Menon,

SCMS School of Engineering and Technology,

Kochi, India.

Email: varunmenon@scmsgroup.org

1. INTRODUCTION

There are different kinds of radar systems for different applications in industries, airports, military organs such as navy and so on. A type of radars is the tracking radars which are applied in fire control and etc [1]. Generally, two classes of tracking radars can be considered as angle tracking and range tracking radars. Our aim in this study attends to the first class. Figure 1 shows a real sample of tracking radar which has been placed on a ground platform for the fire control usages. Tracking radar for finding angle can use several tracking modes (scanning techniques) including sequential lobing, conical scan and monopulse (e.g. in terms of amplitude) [1]. These three techniques are different in terms of the error status. So, the mode used in each angle tracking radar must be considered in computing the error and then the optimal range of radar. Figure 2 shows a schematic which explains the mechanism of angle tracking radars. From step 1 to step 6, a target is seen in PPI display which tracked during these steps. Figure 3 and Figure 4 show the block diagram of two types of angle tracking radars based on monopulse and conical scan techniques, respectively [2], [3]. In [1]-[3], it is explained that in terms of angle error, two techniques of sequential lobing and conical scan are similar to each other. In the next parts, we specify the differences between the impacts of monopulse and conical scan/sequential lobing (non-monopulse) techniques. Computing the optimal range of each angle tracking radar is an optimization problem which depicts one of the main parameters of the radar. In [1], this problem has been represented, but it is only solved by simulation and numerical computation. As a completing approach for [1], we wish to solve this problem theoretically. In addition, we obtain the simulation result to compare to the proposed approach.

In the appendix of this paper, we give the readers a sample MATLAB code in order to the simulation-based computing of the optimal range.



Figure 1. A fire control tracking radar

This paper is organized as follows. In the second part, we have an overview on the resources of the angle error. In the third part, we theoretically solve the problem. In the fourth part, we solve a typical example based on both simulation-based and theoretical approaches which allows us to have a comparison between them. The latest parts are allocated to the conclusions of the work and the appendix.

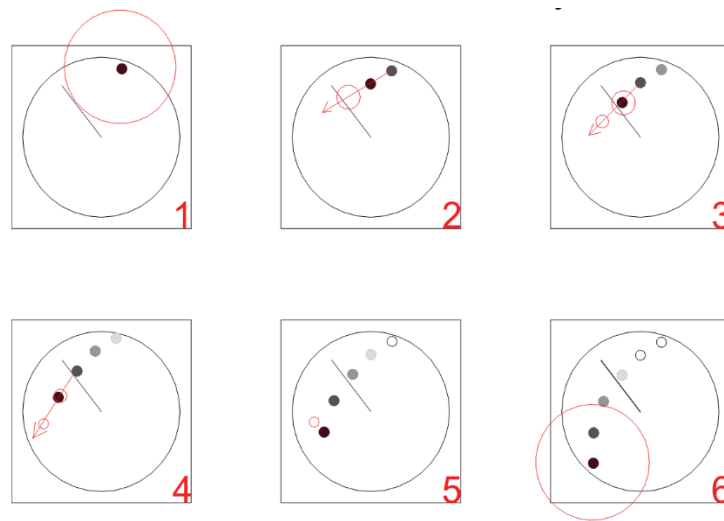


Figure 2. PPI display sequence to illustrate the target tracking process [2]

2. RESOURCES OF ERROR IN ATRS

According to [1], the general standard deviation of the angle error (σ_t) in ATRs is mainly depended on five components (five different standard deviations) including angle fluctuation error related to angle noise and glint phenomena (σ_g), mechanical error ($\sigma_{mech.}$), control loop error ($\sigma_{cont.}$), scintillation error related to amplitude fluctuation and target fading ($\sigma_{sc.}$). And finally the error created by thermal noise of the radar system (σ_n). As follows, we introduce the detailed information about σ_t . (1) shows the general formula of σ_t .

$$\sigma_t = \sqrt{\sigma_{cont.}^2 + \sigma_{mech.}^2 + \sigma_g^2 + \sigma_n^2 + \sigma_{sc.}^2} \quad (1)$$

Where $\sigma_{cont.}$, $\sigma_{mech.}$, σ_g , σ_n and $\sigma_{sc.}$ ($\sigma_{sc.}$ is zero for monopulse mode) are as (2) to (6), respectively ((6) is for non-monopulse modes).

$$\sigma_{cont.} = \begin{cases} \frac{\omega_{max}}{k_v} & \text{for fixed velocity} \\ \frac{\omega_{max}}{k_a} & \text{for fixed acceleration} \end{cases} \quad (2)$$

$$\sigma_{mech.} = q_1 \theta_B \quad (3)$$

where $q_1 \in [0.001, 0.005]$; $q_{1,typical} = 0.002$

$$\sigma_g = \frac{L}{3R} \quad (4)$$

$$\sigma_n = \frac{\theta_B}{q_2 \sqrt{(2 \times SNR) \left(\frac{PRF}{B_s} \right)}} \quad (5)$$

where $q_2 = \begin{cases} 1.3 & \text{non-monopulse} \\ 1.7 & \text{monopulse} \end{cases}$

$$\sigma_{sc.} = 0.01 \theta_B \quad (6)$$

In the equations, B_s , k_v and k_a are some constants related to the status of movement of the target and depended on transform function of the control loop, see more information in [4]. ω_{max} is the highest angle frequency of the target. θ_B is the maximum of beam width in two directions of elevation and azimuth ($\theta_B^\circ = \max\{\theta_{az}^\circ, \theta_{el}^\circ\}$). L is the largest size of the target and R is the distance between radar and target. SNR is signal-to-noise ratio of radar while receiving an echo from the target. SNR is based on the radar equation; we will discuss more about it later. PRF shows the pulse repetition frequency which is equal to the inverse of pulse repetition interval (shown by T_p) in pulse radar-based tracking systems. About SNR and radar equation, we can say that SNR is desired at the input side of the receiver and is therefore computable by the radar equation as (7); for simplicity, we omit some details of radar equation which are reachable in [1], [4].

$$SNR = \frac{P_t \lambda^2 G_a^2 RCS}{(4\pi)^3 P_{noise} R^4} \quad (7)$$

Where P_t the maximum of transmission power of the radar is, λ is the wavelength used in the radar. G_a is antenna gain of the radar (assume that we use a monostatic pulse radar for angle tracking) and described by (8) where $G_o = 32000$, and L_{el} and L_{az} are the size of the radar's antenna for elevation and azimuth, respectively, see more details in [1]. RCS shows the radar cross section of target and is not often fixed, especially in fast maneuvering and high rate fluctuation, however it is usually replaced with an average value which is at most equal to the geometrical cross section of the target (target size). So in here, we suppose that it is a constant. Finally, P_{noise} is power of the thermal noise of radar's receiver which is computed by (9); in this equation B is the noise bandwidth of the radar's receiver in which $B = \tau^{-1}$ (where τ is pulse width), F is the noise figure (NF), k and T_o are two constants; for more information in this regard, see [1].

$$G_a = \frac{G_o L_{el} L_{az}}{(60\lambda)^2} \quad (8)$$

$$P_{noise} = k T_o B F \quad (9)$$

In addition, there is another form for representing the noise power P_{noise} , refer to [1]. It is observable that in a specific example, all values of $P_t, \lambda, G_a, RCS, B, F$ and P_{noise} are fixed, thus the SNR is a function in terms of the radar range (R).

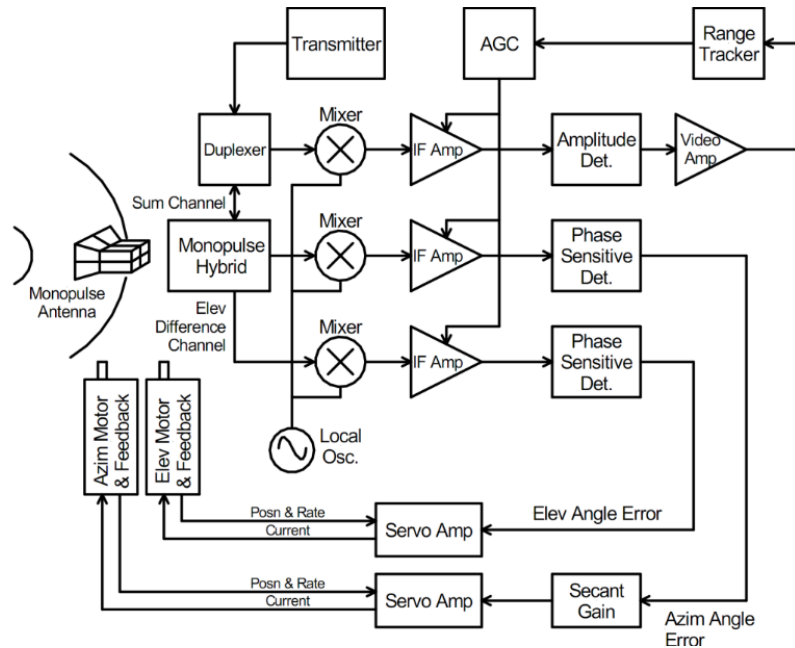


Figure 3. Block diagram of a monopulse tracking radar [2]

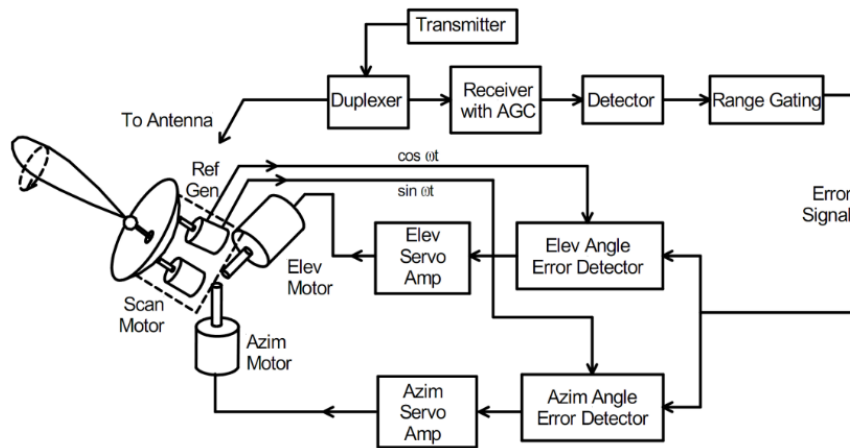


Figure 4. Block diagram of a conical scan radar [3]

3. PROPOSED METHOD

In this part, the proposed method is represented based on solving a mathematical optimization problem. In the previous part, we reviewed all details of angle error. It is noticeable that in an example with the specified parameters, σ_t is only in terms of R (distance to the target). Therefore, if we minimize the general standard deviation for a sample range such as $R=R_{opt}$, then the total angle error becomes the minimum (because the mean of error variable is assumed to be zero, so a minimum variance/standard deviation shows the lowest error). In this case, R_{opt} is the optimal range. The equation of σ_t is rewritten as (10). If the SNR equation is to be rewritten as (11), we accordingly have σ_t as (12).

$$\sigma_t = \left(\frac{\sigma_{cont.}^2 + \sigma_{mech.}^2 + \sigma_{sc.}^2}{K_1} + \left(\frac{L}{3} \times \frac{1}{R} \right)^2 + \left(\frac{\theta_B}{q_2} \right)^2 \times \frac{1}{\left(\frac{2PRF}{B_s} \right) \times SNR} \right)^{\frac{1}{2}} \tag{10}$$

$$SNR = \frac{P_t \lambda^2 G_a^2 RCS}{(4\pi)^3 P_{noise}} \times \frac{1}{R^4} \tag{11}$$

$$\sigma_t = \left(K_1 + \frac{K_2}{K_3} R^4 + \frac{K_4}{R^2} \right)^{\frac{1}{2}} \tag{12}$$

In (12), all K_1 to K_4 coefficients are fixed, so we find the optimal range which can minimize the term for σ_t , as (13). After solving the optimization problem, we see that K_1 has no impact on the R_{opt} .

$$\begin{aligned} \frac{\partial \sigma_t}{\partial R} = 0 &\rightarrow A \cdot B = 0 \\ \text{where } A &= \left(K_1 + \frac{K_4}{R^2} + \frac{K_2}{K_3} R^4 \right)^{-\frac{1}{2}} \\ B &= \frac{-2K_4}{R^3} + \frac{K_2}{K_3} (4R^3) \end{aligned} \tag{13}$$

The roots of (13) include all roots of two new equations of $A = 0$ and $B = 0$. It is provable that the equation $A = 0$ has no acceptable root for R (do it easily), we must solve the equation $B = 0$; (14) shows the single root of this equation.

$$R_{opt} = \left(\frac{K_3 K_4}{2K_2} \right)^{\frac{1}{6}} \tag{14}$$

The achieved relation for the optimal range is a theoretical solution. This recent equation is a generally closed form for all scanning techniques due to the consideration of the coefficient q_2 (embedded in K_2) and the standard deviation of $\sigma_{sc.}$ in terms of different aspects related to the scanning techniques. In order to have a clear approach, we integrate all discussed items through the *Consequence 1*.
 Consequence 1. The optimal range of an angle tracking radar for all scanning techniques is as (15)-(18).

$$R_{opt} = \sqrt[6]{a_1 a_2 a_3} \tag{15}$$

$$a_1 = \frac{P_t \lambda^2 G_a^2 RCS}{(4\pi)^3 P_{noise}} \tag{16}$$

$$a_2 = \frac{L^2}{9} \tag{17}$$

$$a_3 = \frac{K^2 PRF}{\theta_B^2 B_s} \tag{18}$$

$$K \in \{1.3, 1.7\} \quad (=q_2)$$

All angles are in degree(s) and other parameters are in linear space (not in dB) and some of them which have physical dimension are in S.I. units. In the next part, we solve an example based on the proposed approach and then compare it to the simulation result.

4. NUMERICAL EXAMPLE AND SIMULATION

In this part, we firstly use the MATLAB code in the appendix to solve the problem by simulation (classically). Its result is shown in Figure 5. It is clear that the optimal range when the simulation parameters are selected as Table 1 is between 5 and 10 meters.

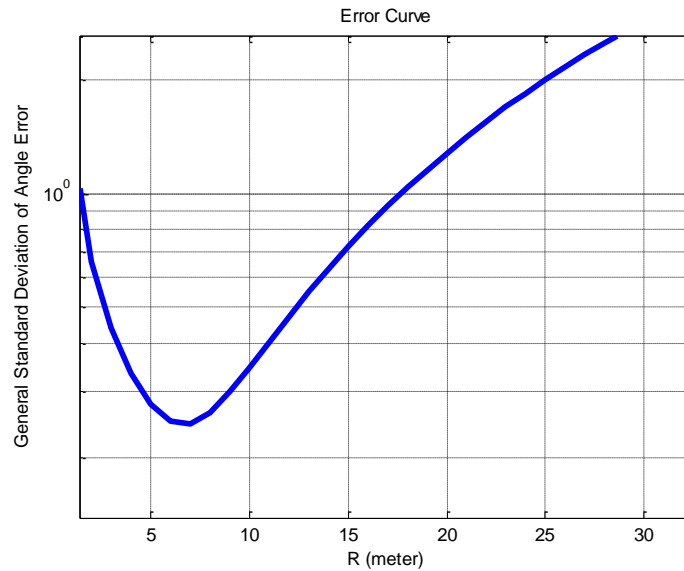


Figure 5. The error curve shows the optimal range obtained from the simulation under the setting in Table 1

Table 1. Settings for simulation

$$\begin{aligned} \omega_{\max} &= 0.1 \text{ m} \\ k_v &= 10 \\ \sigma_v &= \omega_{\max} / k_v = 0.001 \\ \theta_B &= 2^\circ \\ \sigma_{\text{mech.}} &= 0.002 \theta_B = 0.004 \\ L &= 4 \text{ m} \\ \sigma_g &= \frac{L}{3R} = \frac{1.34}{R} \\ B_s &= 30 \\ PRF &= 1000 \\ P_t &= 1000 \\ P_{\text{noise}} &= 1 \\ \lambda &= 0.03 \text{ m} \\ G_a &= 800 \\ RCS &= 12 \text{ m}^2 \\ K &= 1.3 \end{aligned}$$

Now, we use the *Consequence* 1 for computing the optimal range theoretically. At first, a_1 , a_2 and a_3 are computed by (16) to (18).

$$\begin{aligned} a_1 &= 3483.16 \\ a_2 &= 7.11 \\ a_3 &= 14.08 \end{aligned} \tag{19}$$

Then with using (15), we calculate the optimal range as follow.

$$\begin{aligned} R_{opt} &= \sqrt[6]{3483.16 \times 7.11 \times 14.08} \\ &= 8.45 \text{ m} \in [5, 10] \end{aligned} \tag{20}$$

Note that in theoretical computation of the optimal range, some of the parameters like ω_{max} , k_v and so on are not generally used (against the simulation-based solution, The MATLAB code for solving the problem based on simulation is in Table 2.).

5. CONCLUSIONS

In this work, our aim is to introduce a computational method [5]-[10] in which we theoretically computed the optimal range of ATRs. Our approach's result was matched with the simulation result in which they are sufficiently similar to each other. In fact, main aim of the work is to create an extension for the approaches represented in [1]. The proposed approach is suitable for educational aspects too.

REFERENCES

- [1] M. Skolnik, "Introduction to Radar Systems," McGraw-Hill, 2001.
- [2] G. Brooker, "Sensors and Signals: Tracking Moving Targets," Chap. 15, University of Sydney, 2006.
- [3] G. Brooker, "Sensors and Signals: Range and Angle Tracking," Chap. 13, University of Sydney, 2006.
- [4] S. Samadi, "Lecture Notes on Advanced Radar Systems," *SUTech*, 2017.
- [5] M. Alhihi, M. R. Khosravi, H. Attar, M. Samour, "Determining the Optimum Number of Paths for Realization of Multi-path Routing in MPLS-TE Networks," *Telecommunication. Computing Electronics and Control (TELKOMNIKA)*, vol. 15(4), pp. 1701-1709, 2017.
- [6] M. Alhihi, M. R. Khosravi, "Operating Task Redistribution in Hyperconverged Networks," *International Journal of Electrical and Computer Engineering (IJECE)*, vol. 8(3), pp. 1629-1635, 2018.
- [7] P. K. Mane, K. N. Rao, "Granular Mobility-Factor Analysis Framework for enriching Occupancy Sensing with Doppler Radar," *International Journal of Electrical and Computer Engineering (IJECE)*, vol. 8(2), pp. 979-988, 2018.
- [8] M. Alhihi, M. R. Khosravi, "Formulizing the fuzzy rule for takagi-sugeno model in network traffic control," *The Open Electrical and Electronic Engineering Journal*, vol. 12(1), pp. 1-11, 2018.
- [9] M. Ahmed, M. Salleh, M. I. Channa, M. F. Rohani, "Review on Localization based Routing Protocols for Underwater Wireless Sensor Network," *International Journal of Electrical and Computer Engineering (IJECE)*, vol. 7(1), pp. 536-541, 2017.
- [10] M. Ahmed, M. Salleh, M. I. Channa, M. F. Rohani, "RMEER: Reliable Multi-path Energy Efficient Routing Protocol for Underwater Wireless Sensor Network," *International Journal of Electrical and Computer Engineering (IJECE)*, vol.8(6), pp. 4366-4373, 2018.

APPENDIX

Table 2. The MATLAB code for solving the problem based on simulation

```

sigma_t = zeros(1,1000);
for R=1:1:1000
    w_max = 0.01;
    k_v = 10;
    sigma_v2 = (w_max/k_v).^2;
    theta_b = 2; % azimuth/elevation beam width
    sigma_mec2 = (0.002*theta_b).^2;
    L = 4; % it is the largest dimension of the tracked target.
    sigma_g2 = (0.33*(L/R)).^2;
    Bs = 30;
    PRF = 1000;
    Pt = 1000;
    Lambda = 0.03;
    Ga = 800;
    RCS = 12;
    SNR = (Pt*(Lambda.^2)*(Ga.^2)*RCS)/((64*(pi^3))*(R.^4));
    % assume Pnoise = 1
    sigma_n2 = (theta_b/(1.3*sqrt(2*SNR*(PRF/Bs))))).^2;
    sigma_sc2 = (0.01*theta_b).^2;
    sigma_t(floor(R)) = sqrt(sigma_v2 + sigma_mec2 + sigma_g2
    + sigma_n2 + sigma_sc2);
end
figure;
RR=1:1:1000;
loglog(RR,sigma_t);grid;
axis([0 100 10^(-1) 100]);
title('Error Curve');
xlabel('R (meter)');
ylabel('General Standard Deviation of Angle Error');

```



RESEARCH ARTICLE

Vol. 7. Issue.1. 2020 (Jan-Mar)

ISSN

INTERNATIONAL
STANDARD
SERIAL
NUMBER
INDIA

2395-2628(Print):2349-9451(online)

A STUDY ON WOMEN EDUCATION: EDUCATE AND EMPOWER

DIVYA MS

Assistant Professor, English Department, SCMS School of Engineering and Technology, Ernakulum

Email: divya718@gmail.com



Article information

Received:27/02/2020

Accepted: 15/03/2020

Published online: 21/03/2020

doi: [10.33329/ijelr.7.1.179](https://doi.org/10.33329/ijelr.7.1.179)

ABSTRACT

Education is the key to women's empowerment. When education gets denied there isn't much to happen in her life. As usual she gets married and have children at a young age, work in unpaid or low-paying jobs, and rely on economic support from their husband or family. Without education, their future and their family's future gets limited. According to the Malala Fund, there are over 130 million girls worldwide who are not in school. Has anyone thought about them or their future? There might be an unpolished gem among them. Studies have found that if every girl completes 12 years of education, child marriage would drop by 64% and health complications from early pregnancy, like early births and child deaths, would drop by 59% and 49%, respectively. Educating women and girls also improve the economic status of a nation, which will reduce the risk of war and terrorism and can be a better harbinger of future. There are still many barriers preventing girls and women to pursue and complete their education like fees, distance or lack of transportation, being forced to work and provide for their families, being forced to marry and have children, or conflict in their hometown or country. The most difficult obstacle is the mentality of the family towards a girl child. They are denied education only because she is born as a girl. The United Nations found that as girls reach secondary school, their enrolment rates decline significantly. Only 39% of the countries have equal proportions of boys and girls enrolled in secondary education. In developing countries, 35% to 85% of girls are forced to stay at home from school to take care of their younger siblings and to manage the house while their brothers are provided with higher education. To reach the competition level and to expand their professional opportunities, women need the same experiences and skills, making post-secondary education an essential part of women's empowerment. Higher education instils them with the knowledge, competence and experience that are necessary to get involved in government, business, or even in a civil society. With higher education, women and girls have better access to health information and other beneficial services which in turn will only help the family or generation to grow and develop. We need more and more sheers to be the torch bearers of future.

Key words: Empowerment, Post-secondary education, Shero, Professional opportunities

“You educate a man; You educate a man.

You educate a woman; You educate a generation”-Brigham Young

We are living in a highly competitive world where survival is the only mantra to be focused. Such a fast growing world hardly differentiates between men and women. Education is the only key factor that brought towards such a change. Even when women have access to education, there can be many other factors that can make it difficult for her to take full advantage of those opportunities. It's women who still carries the cultural burden of being the primary homemakers and caregivers. This unpaid “second shift” means that they have less time and energy to dedicate to their studies. Family responsibilities doesn't become burden for them but that is the prime factor that is delimiting them from their higher education or carrier growth. When women become the sole providers for their families, they need to fulfil it with many other factors like being victims of domestic violence, threats like financial and from profession which becomes much more difficult for them to handle. The immense pressure that she is handling becomes worthless when it is labelled under the synonym ‘mother’ or ‘wife’. Today's era has witnessed a lot of change when it comes to single girl child nuclear family. Deciding voices are only that of their parents. Thus providing wings for them to fly high and capture their aim. Their dreams can't be in fetters and who knows there might be an unpolished gem that is being soiled. Women in India have been treated with utmost respect and dignity since time immemorial. For a nation to advance, empowering women is crucial. India was blessed with visionary women who broke the fetters of gender norms in every sector. Its long back we heard about the denial of education to women. A girl child was considered curse than a boon. Never to live in a world where mothers and sisters are dragged out of their homes and raped. Wherein she becomes both the victim and accused and its said by “them”, it's all because of her “out of the box” attitude that caused her this. Is this the caring that we need to give to our sisters, rather than rending a helping hand? We can't even skim through the news heads that is going on these days. What if such an accusation comes out, it needs to face a frequent trail from the social medias and channels who will make them even worse? Is the only solution, to remain silent and bear the tragic effects or to have a prolonged grudge and to end up in depression throughout the life? It's an open ended question towards the secularist nation. Here I would like to quote the famous wording of Michelle Obama,

“When girls are educated, their countries become stronger and more prosperous”

Let the nation realize her power of golden touch. She is to succeed where ever she goes, don't curtail her from her doing what is right. Listen to her inner voice that itself will keep the nation going. We do respect our mothers and all woman is an incarnation of her, our mother Earth. Its only she who can protect, provide, love, sacrifice selflessly. Split of the moment can we see her incarnations of a loving Sita, ready to sacrifice everything for her love and family, Durga the fearest of all who battle against evil for good. For us this is our mother, both deities in one, who loves and cares us with one hand and get furious with another. Still we love her and keep no grudges. Then how can we ever think of harming her. Where has our brains and minds gone, ready to stab the same womb from where we came? Is this what we call progression? Are we the real citizens bearing torches for a future developing nation? How can we sustain by spiting on our own veins? When will all these quires be dissolved? The only solution for all this is only education, it opens the eyes to a new world of realities and hopes for a better nation. It's clearly evident that the only means to attain empowerment is through education. Change should begin from her and its only she who can bring changes. Here I would like to cite the story of Rani Padmini a legendary 13th – 14th century Queen (Rani) of the Mewar kingdom of present day India. She was the wife of King Ratan Sen, captured and imprisoned by Delhi's sultan Alauddin Khalji. Alauddin Khalji became enamoured with Padmavati's beauty and decided to siege Chittor to obtain Padmavati. Before Chittor was captured they had to face defeat against Khalji, she and her companions committed Jauhar (self-immolation) thereby defeating Khalji's aim and protecting their honour. Coupled to the *Jauhar*, the Rajput men died fighting on the battlefield. Throughout the novel *Padmini: The Spirited Queen of Chittoor*, Mridula Behari tried to explain the immense beauty and knowledge that Padmavati possessed. It's only because of her education and knowledge, she had the courage to face such a situation where her husband the Rana itself was helpless. She was bold enough to convince everyone and to equip them for a war against the evils. There are many instances in the novel where we find her indulged in reading the ancient scriptures and getting mesmerised by that. It's the education that

brought her into a new world where she understands that action speaks more than words. There is always an urge for action than mere talks, that won't lead you anywhere. Education delimits the boundaries of caste, creed, gender, finance and what not. How true it is to quote Malala Yousafzai's wordings here,

"If one man can destroy everything, why can't one girl change it?"

As Prime Minister Narendra Modi said on the launch of the expanded 'Beti Bachao Beti Padhao' (March 8, 2018): "Daughters are not a burden but the pride of the whole family. We realise the power of our daughters when we see a woman fighter pilot. The country feels proud whenever our daughters bag gold medals, or for that matter any medal, in the Olympics." This is the time only when we think oh! are they capable of bagging a gold and that too for the nation? When they come to lime light we find applauds and cheering from all over the nation. But have ever we imagined the trials or pains that they have gone through to achieve that? Same is the case with the other gender, but they are always on safe side of the scrutiny eyes of the society. It's a boy, no matter if he is alone or late to home or traveling late or alone. The world is always open to him than to her. We need more Sheros to be an inspiration and to motivate others to come out from their shells that is encircling them towards darkness. Engaged in a combat to the march for equality with our sisters and mothers, let us understand the theme of Women's Day: "An Equal world is an enabled world: realizing women's power." After the adoption of the Beijing Agenda for Action, UN has set the year 2020 as a key year for assessing international progress towards achieving gender equality and human rights for all women and girls. The Ministry of Human Resource Development (MHRD) has much triggered up their progression under the leadership of PM Modi in providing equal opportunities. It is with immense happiness we can say that due to the Swachh Bharat Mission, 14,67,679 schools now have a functioning girl's toilet, an increase of 4.17 percentage points in comparison to 2013-14. The impact of the mission has resulted in an increase in enrolment of girls by 25 percentage points in 2018-19 from 2013-14. These figures get dimmed in a society which is indulging much more in a political game for their sustenance. We living in the safe shelters haven't ever thought about our sisters who is being victimized and marginalized. Minister of Finance Nirmala Sitharaman applauded the performance of Beti Bachao Beti Padhao in her speech on the budget: "Gross enrolment ratio of girls across all levels of education is now higher than boys. At the elementary level it is 94.32 per cent as against 89.28 per cent for boys, at the secondary level it is 81.32 per cent as compared to 78 per cent and at the higher secondary level girls have achieved a level of 59.7 per cent compared to only 57.54 per cent." The MHRD has approved 5,930 Kasturba Gandhi Balika Vidyalayas, which are girls' residential schools and have an enrolment of 6,18 lakh students, to increase equality of access and opportunity for girls. The National Incentive Scheme for Girls for Secondary Education has approved an incentive sum of Rs 8,56 crore for the 28,547 beneficiaries. According to the scheme Rs 3,000 is being deposited under the age of 16 in the name of deserving unmarried girls and entitles them to withdraw it along with interest in reaching 18 years of age and passing Class X. Besides an improvement in the girl's gross enrolment rate in schools, the educational outcomes and accomplishments have also improved.

Let's go ahead with this initiative for our sisters than to get involved in the cheap political drama that is being happening in our nation. There is considerable evidence that women's education and literacy tend to reduce the mortality rates of children. It's indeed true what Malala Yousafzai pointed out:

"We realize the importance of our voice only when we are silenced"

In accordance with the celebration of India's success in improving gender equality in the education system, much greater and collective efforts are needed to achieve the Sustainable Development Goal of eliminating gender disparities in education and ensure equal access to all levels of education and vocational training for the vulnerable, including persons with disabilities, indigenous peoples and children in vulnerable situations. History of Indian women is full of pioneers, who broke gender barriers and worked hard for their rights and made advances in politics, arts, science, law, etc. Let us cite few examples of our pioneers who made us think beyond Anandibai Gopalrao Joshi, who became the first Indian female physician in the year 1887. She was also the first Indian woman who get training in Western medicine and the first woman to travel to the United States of America. Arunima Sinha, is the first female amputee to climb Mount Everest. She is also the first Indian amputee to climb the Everest. She was a national level volleyball player who in 2011 was pushed by

robbers from a running train as she defied them. After meeting this accident, one of her legs was amputated below the knee. Arati Saha became the first Indian and Asian woman to swim across English Channel in the year 1959. She also became the first female sportsperson awarded with Padma Shri in 1960. Mother Teresa founded many Missionaries of Charity, a Roman Catholic religious congregation, giving her life to social work. Indira Gandhi became the first woman Prime Minister of India and served from 1966 to 1977. Indira Gandhi renowned as the "Woman of the Millennium" in a poll which was organised by BBC in 1999. In 1971, she became the first woman to receive the Bharat Ratna award. Justice M. Fathima Beevi became the first female judge to be appointed in the Supreme Court of India in the year 1989. In her autobiography she had said about the immense suffering that she had faced to reach such a highest peak. Her father was the only person who supported her thorough out her journey. Kalpana Chawla, the first Indian woman who reached in space. As a mission specialist and a primary robotic arm operator, she went into space in 1997.

We can move to our present Sheros starting with Mithali Raj, the first woman to score a double hundred in Test Cricket against New Zealand at Wellington, 2004. She was the first to achieve this landmark in the world. Pratibha Patil became the first woman President of India and held office from July 2007 to July 2012. Kiran Bedi, joining Indian Police Service (IPS) in 1972, she became the first woman officer in India. Moreover, later in 2003, Kiran Bedi also became the first woman to be appointed as the United Nations Civil Police adviser. Anjali Gupta is the first female flying officer in the Indian Air Force to be court martialled. She used to work for the Aircraft Systems and Testing Establishment unit in Bangalore. Anjali completed her Masters of Philosophy in Sociology from the Delhi University and was first posted at Belgaum in 2001. Sania Mirza, a professional tennis player, became the first ever Indian woman to win the Women's Tennis Association (WTA) title in 2005. Later in 2015, Sania Mirza became the first Indian woman titled as rank number one in WTA's double rankings. Saina Nehwal became the first Indian women to win a medal in Badminton at 2012 Olympic Games. Later in 2015, she became the first Indian woman to secure no. 1 position in world rankings. Mary Kom, is the only woman boxer who has won a medal in each of the six World Championships. She was the only Indian woman boxer who qualified for the 2012 Olympics and became the first Indian woman boxer to win a gold medal in Asian Games in 2014. Cited just a few but more hands of achievements are behind which are yet to be recognised and appreciated. They have set a model for us to think and act beyond.

Our government has also taken much initiative for protecting the rights of education for girls. India Post or Department of Posts, the postal system of the country, offers several savings schemes with different interest rates. The **Sukanya Samriddhi Yojana**, one such savings scheme offered by India Post, is a deposit scheme for the girl child that can be opened in any of the leading banks and post offices across the country. In such schemes the child is getting the benefit for future education and for her marriage or future life. There is a platform called WE, that is an empowerment program through which woman are trained to form self-organized and self-managed savings groups, each consisting of 15-25 members. Their aim is to develop individual empowerment and increase their access to financial resources which is the prime element for eradicating poverty. All the members meet weekly to make decisions and interact in life-skills training, discuss various issues of mutual interest. They not only give a platform for awareness but also make an effort to join together and take action to improve their lives and communities. We too need to make more and more efforts than *ME TOO* to raise our voice against the inhuman oppression and injustices that is happening worldwide. Amendments to laws are must as Judiciary is the ultimate power which we believe and rely on. For a common man judiciary is the only hope or last and final resort. We all need to respect our law than fearing it. If the administrators of law are more channelized and less corrupted, we don't have to wait for justice. It's absolutely true to say the famous phrase "Justice delayed is justice denied". Let us be the harbingers of a brighter future that initiates the slogan justice and tranquility. Let the coming era witness a world devoid of corruption, discrimination, poverty, illiteracy.

"Empower yourselves with a good education, then get out there and use that education to build a country worthy of your boundless promise"

-Michelle Obama

Bibliography

“Women empowerment”. Indian Express article. <https://indianexpress.com/article/opinion/columns/beti-bachao-beti-padhao/article/6297784>.

“First Indian Women”. India Today. <https://www.indiatoday.in/education-today/gk-current-affairs/story/the-first-indian-women-312243-2016-03-08>

“One Health and Disease: Tick-Borne.” *National Park Service*, U.S. Department of the interior, <https://www.nps.gov/articles/one-health-disease-ticks-borne.htm>.

Behari, Mridula . <https://www.amazon.in/Padmini-Spirited-Chittor-Mridula-Behari-ebook/dp/B0774NH95V>

Behari, Mridula. *Padmini: The Spirited Queen of Chittor*: Penguin publishers, 2017.

Skip to main content

Access and authentication: Please [visit our page](#).

Close X

Enter your search terms here



Advanced search

Access and purchase options

Preventing hijacked research papers in fake (rogue) journals through social media and databases

Varun G. Menon (Department of Computer Science and Engineering, SCMS School of Engineering and Technology, Kochi, India)

Mohammad R. Khosravi (Department of Electrical and Electronic Engineering, Shiraz University of Technology, Shiraz, Islamic Republic of Iran)

[Library Hi Tech News](#)

DOWNLOADS

ISSN: 0741-9058



Article publication date: 18 June 2019

International Standard

Serial [Permissions](#)

Number publication date: 6 August 2019

Citation

Menon, V.G. and Khosravi, M.R. (2019), "Preventing hijacked research papers in fake (rogue) journals through social media and databases", *Library Hi Tech News*, Vol. 36 No. 5, pp. 1-6.

<https://doi.org/10.1108/LHTN-11-2018-0070>

[Download as .RIS](#)

Publisher: Emerald Publishing Limited

Copyright © 2019, Emerald Publishing Limited

Related articles

Getting acquainted with social networks and apps: combating fake news on social media
Katie Elson Anderson, *Library Hi Tech News*, 2018

Types of hijacking in the academic world – our experiment in the scholarly publishing
Mehdi Dadkhah, *Library Hi Tech News*, 2016

Social media research in the context of emerging markets: An analysis of extant literature from information systems perspective
Kuttimani Tamilmami et al., *Journal of Advances in Management Research*, 2018

The people speak: social media on euthanasia/assisted dying
Chrystal Jaye et al., *Med Humanities*, 2021

Children's fitness and health: an epic scandal of poor methodology, inappropriate statistics, questionable editorial practices and a generation of misinformation
Jo Welsman et al., *Evid Based Med*, 2021

Promoting corporate image or preventing underage use?



Services

[Authors](#)

[Editors](#)

[Librarians](#)

[Researchers](#)

[Reviewers](#)

About

[About Emerald](#)

[Working for Emerald](#)

[Contact us](#)

[Publication sitemap](#)

Policies and information

[Privacy notice](#)

[Site policies](#)

[Modern Slavery Act](#)

[Chair of Trustees governance statement](#)

[COVID-19 policy](#)

[Accessibility](#)

Review of IS 1893-1(2002): Effect of Unreinforced Masonry Infill Walls on Seismic Response of Framed Structures



Gayathri Krishna Kumar and **M. G. Airin**

Abstract Earthquake, its occurrence and effects, its impact and structural response have been studied for many years in earthquake history and is well documented. The structural engineers have tried to examine the various method, with an aim to determine the complex dynamic effect of seismically induced forces in structures, for designing of earthquake resistant structures in a advanced and easy manner. From the study conducted it was found that more precise results are found from nonlinear static analysis method. An overview of the past researches conducted on the modelling of masonry infilled frame issues, it was found that macro model which consider the effect of masonry weak links is used for modelling the infill panels. Different factors governing the period of vibration was checked, and the result shows the effect of stiffness of the building is the most important factor influencing the period of vibration. Parametric study was conducted to determine the most influential factor that affects the period of vibration of a structure. From the observations it was clear that the effect of stiffness is the most important factor influencing the period of vibration. Therefore a curve with dimensionless height and lateral displacement were plotted using nonlinear static analysis obtained from SAP2000. From the above mentioned curve, the effective stiffness of the building under consideration is calculated, which route to find the period of vibration of the structure that is considered for the seismic analysis [1].

Keywords Dynamic · Infill · Vibration · Parametric

G. Krishna Kumar (✉)

Federal Institute of Science and Technology, Angamaly, India

e-mail: gaya3krishnakumar92@gmail.com

M. G. Airin

SCMS School of Engineering and Technology, Karukutty, India

e-mail: airinmg@scmsgroup.org

© Springer Nature Switzerland AG 2020

K. Dasgupta et al. (eds.), *Proceedings of SECON'19*,

Lecture Notes in Civil Engineering 46,

https://doi.org/10.1007/978-3-030-26365-2_60

See discussions, stats, and author profiles for this publication at: <https://www.researchgate.net/publication/337362793>

PERIÓDICO TCHÊ QUÍMICA ARTIGO ORIGINAL RUMO À REDUÇÃO DO ESFORÇO COMPUTACIONAL NAS PREDIÇÕES DE VIBRAÇÕES INDUZIDAS POR VÓRTICES DE UM RISCADOR CILÍNDRICO TOWARDS REDUCIN....

Article in *Periodico Tche Quimica* · November 2019

CITATIONS

0

READS

226

3 authors:



Vidya Chandran

SCMS School of Engineering and Technology, Karukutty

24 PUBLICATIONS 31 CITATIONS

SEE PROFILE



Sheeja Janardhanan

Indian Maritime University

66 PUBLICATIONS 77 CITATIONS

SEE PROFILE



M. Sekar

37 PUBLICATIONS 514 CITATIONS

SEE PROFILE

Some of the authors of this publication are also working on these related projects:



Design and Propulsion of an Autonomous Underwater Vehicle [View project](#)



Numerical Manoeuvring [View project](#)

RUMO À REDUÇÃO DO ESFORÇO COMPUTACIONAL NAS PREDIÇÕES DE VIBRAÇÕES INDUZIDAS POR VÓRTICES DE UM RISCADOR CILÍNDRICO

TOWARDS REDUCING COMPUTATIONAL EFFORT IN VORTEX INDUCED VIBRATION PREDICTIONS OF A CYLINDRICAL RISER.

VIDYA, Chandran¹; SHEEJA, Janardhanan²; SEKAR, M^{3*};¹Department of Mechanical Engineering, Karunya Institute of Technology and Sciences, Tamil Nadu, India²Department of Mechanical Engineering, SCMS School of Engineering and Technology, Kerala, India³Department of Mechanical Engineering, AAA College of Engineering and Technology, Tamil Nadu, India

* Correspondence author

e-mail: mailtosekar@gmail.com

Received 23 August 2019; received in revised form 30 October 2019; accepted 18 November 2019

RESUMO

As vibrações induzidas pelo fluxo geralmente denominadas vibrações induzidas por vórtices são de grande importância no projeto de *risers* marinhos. Esses *risers* cilíndricos flexíveis sofrem vibrações de amplitude muito alta quando a frequência de derramamento de vórtice corresponde à frequência natural do riser. Tais vibrações são capazes de colocar a segurança da tripulação trabalhando em plataformas *offshore* em questão. Portanto, a previsão de resposta de tais estruturas é considerada muito importante. Embora muito trabalho numérico tenha sido feito neste campo, tratando o problema como uma interação fluido-estrutura bidirecional, o fato de esses trabalhos exigirem esforços computacionais muito altos não o tornou pertinente quando os recursos computacionais de ponta não estão prontamente disponíveis. Uma rápida previsão da resposta estrutural de tais estruturas esbeltas precisa ser útil para os engenheiros em momentos de necessidade. Este artigo aborda uma técnica de solução para esse problema através de um método econômico para previsão rápida e confiável da resposta do riser sob vibração induzida por vórtice, utilizando o esforço computacional mínimo para o número moderado de Reynolds ($Re \leq 3 \times 10^5$). As simulações de fluxo bidimensionais são realizadas usando CFD baseado em RANSE, seguido pelo mapeamento uniforme das forças hidrodinâmicas no *riser* tridimensional. A grade usada para a simulação numérica foi validada com relação aos resultados experimentais do túnel de vento para $Re = 5,3 \times 10^4$. As forças hidrodinâmicas correspondentes aos três primeiros harmônicos da frequência natural do *riser* foram usadas como entrada no solucionador estrutural para analisar o resposta usando o método dos elementos finitos. Obtiveram-se trajetórias do cilindro nos três primeiros modos de vibração, um padrão típico de oito algarismos, característico da vibração de bloqueio. Verificou-se que o método é bastante eficaz no cálculo rápido de problemas de vibração induzidos por fluxo para números de Reynolds baixos e moderados.

Palavras-chave: CFD; cilindros de fluxo passado; lock-in; resposta estrutural; vibrações induzidas por vórtices

ABSTRACT

Vibrations induced by flow, generally referred to as vortex induced vibrations, are of great importance in the design of marine risers. These flexible cylindrical risers undergo vibrations of very high amplitude when the vortex shedding frequency matches the natural frequency of the riser. Such vibrations are capable of putting the safety of crew working on offshore platforms in question. Hence the prediction of response of such structures is considered very important. Although a lot of numerical work has been done in this field treating the problem as a two-way fluid structure interaction, the fact that these works demand very high computational efforts has not made it pertinent where high end computing resources are not readily available. A quick prediction of the structural response of such slender structures needs to be handy to the engineers at times of need. This paper addresses a solution technique for such a problem through an economical method for quick and reliable prediction of riser response under vortex induced vibration utilizing minimum computational effort for moderate Reynolds number ($Re \leq 3 \times 10^5$). Two dimensional flow simulations are carried out using RANSE based CFD followed by the uniform mapping of hydrodynamic forces on to the three dimensional riser. The grid used for the numerical simulation has been well validated against wind-tunnel experimental results for $Re = 5.3 \times 10^4$. Hydrodynamic forces corresponding to the first three harmonics of natural frequency of the riser have been used as input in the structural

solver to analyse the response using finite element method. Trajectories of the cylinder in the first three modes of vibration have been obtained, a typical eight figure pattern which is characteristic for lock-in vibration. It is found that the method is quite effective in the quick computation of flow induced vibration problems for low and moderate Reynolds numbers.

Keywords: CFD; flow past cylinders; lock-in; structural response; vortex-induced-vibrations.

1. INTRODUCTION

Vortex shedding around bluff bodies is natural yet a phenomenon that consumed years of comprehensive studies, for it is well known for the imminent catastrophes it brings with it. Tacoma Narrows Bridge disaster is the worst case one could recall while thinking about vortex shedding. With the ever-rising demand for petroleum products, the development of offshore oilfields has been growing fast over the past century. The drilling facilities are designed in such a way that it enables a prolonged offshore operation for a large period of time starting from a few months to several decades. Numerous studies are being carried out in this field for the proper design of the slender marine risers in ocean. The stability of structures especially those carrying pressurised fluid in them is a topic of research interest. (Ramírez *et al.* 2017, Pezzini, *et al.*, 2017) If the bluff structure is not mounted rigidly and the frequency of vortex shedding matches the natural frequency of the structure, the structure begins to resonate, vibrating with harmonic oscillations of large amplitude (Bourguet, 2011). This phenomenon is known as lock-in. During lock-in, vortex shedding frequency shifts to the natural frequency of the structure leading to large amplitude vibrations.

The vortex shedding occurs at a discrete frequency and is a function of the Reynolds number, defined by Equation 1.

$$Re = \frac{\rho V D}{\mu} \quad (\text{Eq. 1})$$

The dimensionless frequency of the vortex shedding, the shedding Strouhal number, $St = f_v D/V$, is approximately equal to 0.2 when the Reynolds number is greater than 1,000. When vortices are shed from the cylinder, uneven pressure distribution develops around the upper and lower surfaces of the cylinder, generating an oscillatory hydrodynamic loading (lift) on the cylinder. This unsteady force given by Equation 2

can induce significant cross flow vibrations on a structure, especially if the "resonance" condition is met.

$$F_L = \frac{1}{2} C_L \rho A V^2 \quad (\text{Eq. 2})$$

C_L is the coefficient of lift. The cylinder also experiences a net force along the flow direction and is called the drag force and is given by Equation 3.

$$F_D = \frac{1}{2} C_D \rho A V^2 \quad (\text{Eq. 3})$$

where C_D is the drag coefficient.

The phenomenon of lock-in was first observed by Feng during his classical experiment (Feng, 1968). He described the phenomenon observed as matching the frequency of cylinder vibration and fluid force to the natural frequency in a vacuum. Later it was observed that this matching of frequency holds good only for higher values of mass ratio, m^* (Blevins, 1990). Further research in the field explains the phenomenon as either large amplitude vibration of the cylinder (Sarpkaya, 1977) or matching of the frequency of cylinder vibration and fluid force (Khalak and Williamson, 1999). Synchronization and lock-in, are often used synonymously, but from the experiments it was shown that, for zero damping and sinusoidal motion, synchronization ($f = f_n$) occurs at only one condition, effective stiffness ratio, $k_{\text{eff}}^* = 0$ (Sheils *et al.*, 2001), where k_{eff}^* is defined as in Equation 4.

$$k_{\text{eff}}^* = \frac{m^*}{V_R^2} \quad (\text{Eq. 4})$$

Matching of vortex shedding frequency with one of the natural frequencies of the structure may not always be the only (sole) reason for lock-in. Contrary to classical lock-in, whereby the

oscillation frequency matches the structural natural frequency, in the experiments on stationary cylinder free to oscillate, it was found that the oscillation frequency increases markedly above the natural frequency, through the excitation regime while at the same time it is below the vortex shedding frequency (of the non-oscillating structures) (Khalak and Williamson, 1999). Even though vortex shedding and the vibration induced by it has been a topic of extensive research for several years, due to its intrinsic nature, the researchers are still not able to confidently define the phenomenon and describe the flow physics behind shifting of shedding frequency. Numerous analytical, experimental, and numerical investigations have been carried out in the field of vortex induced vibration (VIV) of long flexible cylinders. Most of these studies focused on the structural response of the cylinders rather than the phenomenon of lock-in (Trim *et al.*, 2005; Vandiver *et al.*, 2009). Freely oscillating cylinders were modelling as a spring mass system with single or two degrees of freedom (Sekar *et al.*, 2009). Experiments in wind tunnels using particle induced velocimetry (PIV) have proved to predict the flow characteristics and structural response with much accuracy (Wang *et al.*, 2015). Laboratory experiments and offshore large scale experiments have also been recognized as effective tools for analysis of VIV (Domal and Sharma, 2017; Gao *et al.*, 2017). However, for case specific analysis of the problem, experiments are not always possible, and hence most of the researchers rely on computational fluid dynamics (CFD) as a tool for predicting VIV (Daniels *et al.*, 2016). Unlike the experiments CFD facilitates detailed study of the flow physics which is otherwise impossible. Three dimensional (3D) numerical simulations are widely accepted in the research community as capable of predicting VIV characteristics accurately. Researchers were under the notion that two dimensional (2D) simulations are acceptable only for lower Reynolds numbers ($Re < 250$) because of the inherent 3D characteristics of vortices. Later on several researchers have proved that 2D simulations are capable of accurately predicting VIV phenomenon in rigid structure cases (Xie *et al.*, 2012). 3D numerical simulation demands high computational resources for flow analysis and also for generation of the 3D computational grid. The objective of the present work is to test the accuracy of 2D numerical simulations in predicting flow characteristics of VIV and to develop an easy and economical tool for comprehensive analysis of vortex shedding and the structural response during VIV. RANSE-based Commercial solver

ANSYS Fluent -15, as well as ANSYS Workbench -15, have been used as the tools for the study.

2. MATERIALS AND METHODS

The grid generated for the analysis has been validated using the experimental method. Experiments have been carried out on a subsonic wind tunnel, and the results have been compared with those of numerical studies for the same value of Reynold's number. Details of the material and dimensions of the test cylinder are shown in Table 1.

Table 1. Geometric specification of the riser and fluid domain

The diameter of the riser (D)	0.05 m
Distance from inlet to the riser	9 D
Distance from riser to outlet	27 D
Lateral distance from cylinder to both sides	7 D
Cylinder Material (Hollow)	PVC

2.1. CFD Prediction for Vortex Shedding

Geometric modeling and the generation of computational grids around the riser placed in a fluid domain, mimicking ocean environment (still water conditions) have been carried out using ANSYS ICEM CFD.

2.1.1. Creating a computational domain

The geometric specifications of the riser model and the fluid domain with respect to the diameter of the riser are given in Table 1. The length of the riser (L) has been chosen to be 0.4 m, so that the aspect ratio (L/D) is 20. At this value of aspect ratio, the model has been found to account for the three dimensional effects of vortex shedding (Vandiver *et al.*, 2009). Figure 1 shows the representation of fluid domain. Domain size has been fixed based on the published domain independency test results (Gutafsson, 2012).

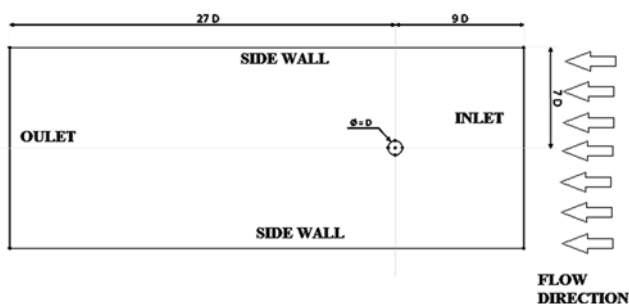


Figure 1. Dimensions of the fluid domain with the riser

Meshing or generating the computational grid in the fluid domain around the riser effectively is most important in capturing the vortex shedding phenomenon. The vorticity transport equation represented by Equation 5 gives an insight into the mechanism of generation and transport of vortices.

$$\frac{\partial \omega}{\partial t} + \mathbf{u} \cdot \nabla \omega + \omega(\nabla \cdot \mathbf{u}) = \omega \cdot \nabla \mathbf{u} + \frac{1}{\rho^2} \nabla p + \nu \nabla^2 \omega \quad (\text{Eq. 5})$$

The third term on the right hand side of the equation represents the diffusion of vorticity by viscosity. Due to this term, vorticity is generated along solid wall boundaries because of steep velocity gradients. These steep gradients make vortical motion susceptible to numerical dissipation. But in the near wall region, where the mesh is usually very fine, this is not an issue since the fine mesh can capture viscous effects. It is a bigger issue in the far field, where poor resolution can severely weaken and distort the vertical structures (Kamkar, 2011). Hence importance must be given even to the far field wake, where the major concern is the mesh resolution.

2.1.2. Mesh Generation

Mesh element size near the surface of the cylinder is of great importance in case of turbulent flow compared to laminar flow. The interaction between the mean flow and the boundary layer flow is more in turbulent flow, and turbulence plays the most important role in the transport of momentum and hence must be properly resolved, especially at the boundary for better results. To accurately capture the features of flow near the boundary, the spacing of the first grid point should be such that it is well within the laminar sub layer of the boundary layer for turbulent flow and within the boundary layer for laminar flow. In the outset a mesh has been generated, and the drag force computed has been compared with the value

obtained through experiments. The experimental set up is described in the previous section. The flow over the cylinder corresponds to a $Re = 5.3 \times 10^4$ which is in the laminar flow regime. The boundary layer at $Re = 5.3 \times 10^4$ is laminar before separation, but during vortex shedding the wake of the cylinder turns turbulent in nature at any $Re > 300$. Hence while meshing the geometry due consideration must given to the possible influence of turbulence on the boundary layer.

From Blasius's solution of the equation for the boundary layer in laminar flow, represented by Equation 6, the boundary layer thickness, considering the boundary layer to be completely laminar, is 1×10^{-3} m.

$$\delta = \frac{4.91 D}{\sqrt{Re_D}} \quad (\text{Eq. 6})$$

If, for an additional factor of safety, we consider the influence of turbulence on the boundary layer, then the minimum element size near the cylinder wall must be chosen so that it is well with the laminar sub-layer of the boundary layer. The thickness of the laminar sub-layer is obtained from Equation 7.

$$\delta' = \frac{11.6 \nu}{V^*} \quad (\text{Eq. 7})$$

Where V^* is the frictional velocity given by Equation 8.

$$V^* = \sqrt{\frac{\tau_0}{\rho}} \quad (\text{Eq. 8})$$

And τ_0 the wall shear stress is obtained as in Equation 9.

$$\tau_0 = \frac{0.664 \rho V^2}{2\sqrt{Re_D}} \quad (\text{Eq. 9})$$

For $Re = 5.3 \times 10^4$, the thickness of the laminar sub-layer has been obtained from the Von-Karman momentum integral equation as 2.8×10^{-4} m. While generating mesh for computation, 3×10^{-4} m has been fixed as the global minimum seed element size with a scale factor of 1. An unstructured mesh has been generated with view that the same mesh may be used for analyzing the

variation in flow characteristics with oscillating cylinder. Quad dominant mesh type has been preferred in shell meshing parameters as it suits accurate meshing of curved cylindrical surface. Patch dependent mesh method has been selected since it gives the best quad dominant quality while capturing surface details. Tetra/Mixed mesh type and Robust (Octree) mesh method have been selected for surface meshing. Moreover it is to be observed that the first grid point should exhibit a Y^+ (wall normal dimensionless distance) value of less than 1 in case of RANS simulations. Near wall spacing or element size has been calculated as 2×10^{-5} from Equation 10.

$$\Delta S = \frac{\mu Y^+}{\rho V^*} \quad (\text{Eq. 10})$$

This value of near wall spacing is ensured by fixing maximum element size and height 3×10^{-5} m and height ratio 1.05 with 20 numbers of prism layers to cover the entire boundary layer in the part mesh set up of cylinder surface. After a thorough grid independency study, the final mesh for analysis has been chosen with 41,932 elements. Unstructured mesh used for the flow analysis using ANSYS 15 is shown in Figure 2.

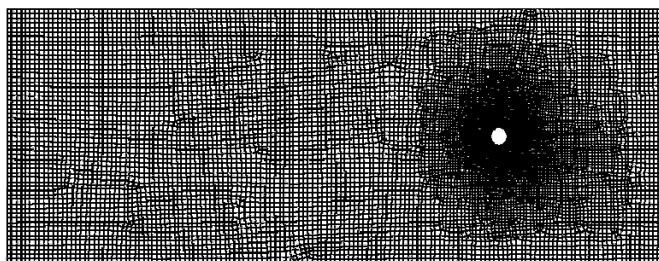


Figure 2. Unstructured 2D mesh generated in ANSYS ICEM CFD

2.1.3. Flow Analysis

Flow past the cylinder at $Re = 5.3 \times 10^4$ has been simulated using the generated unstructured mesh in ANSYS Fluent -15. Pressure based transient analysis has been carried out. Fluid flowing has been chosen to be water at density 998.2 kg/m^3 , and the inlet velocity 1.06 m/s in order to match the Re value. $k-\omega$ SST turbulence model has been selected, which has been tested against other models and proven to be the most adaptable model to predict the near cylinder and wake flow characteristics (Chandran *et al.*, 2018). Velocity inlet boundary condition has been given at the inlet, pressure outlet at the outlet boundary, and

for both sides of the domain, symmetry boundary condition (Chandran *et al.*, 2019). Pressure velocity coupling has been done using PISO scheme. Second order upwind spatial discretization has been selected for momentum and turbulent kinetic energy. Second order implicit transient formulation has been used. The spatial discretization gradient is least squares cell based. Since the simulation has been compared with the results obtained from wind tunnel experiments turbulent intensity has been calculated from the empirical correlation for a duct flow given by Equation 11.

$$I = \frac{V'}{V_{\text{avg}}} = 0.16 (Re_D)^{\frac{1}{8}} \quad (\text{Eq. 11})$$

Where V the root mean square of velocity fluctuations and V_{avg} is the mean flow velocity. For $Re = 5.3 \times 10^4$, the turbulence intensity will be 4 % according to Equation 11 and hence so chosen for analysis. The time step size for the transient simulation has been calculated based on vortex shedding frequency corresponding to $Re = 5.3 \times 10^4$. The time period of vortex shedding has been calculated from the definition of Strouhal number (St) given by Equation 12.

$$St = \frac{fD}{V} \quad (\text{Eq. 12})$$

where f is the vortex shedding frequency.

The time period has been obtained as 0.25 seconds from the value of frequency. For accurately capturing the shedding phenomenon one-time period should contain at least 20 time steps. Accommodating 25 time steps per time period, the time step size obtained is 0.01 seconds. Further for ensuring stability of the solution, Courant Friedrichs Lewy (CFL) condition must be satisfied as given by Equation 13.

$$\Delta t = \frac{C_m \Delta x}{V} \quad (\text{Eq. 13})$$

where C_m is the maximum allowable CFL number.

For explicit solver $C_m = 1$. Δx is the minimum element size. The time step size obtained from Equation 13 is 3×10^{-4} seconds. A time step size of 1×10^{-4} seconds has been selected for the transient analysis of the flow with a safety factor. Simulations have been performed for various time step sizes ranging from 1×10^{-3} to

5×10^{-5} . Above a value of 1×10^{-4} the results have been found to be independent of time step size. Simulations have been run for 5 seconds, and it took nearly 1.5 hours of physical time to complete the runs on an 8 GB RAM machine. Analysis of flow took 1.36 seconds computational time for reaching convergence. RMS value of coefficient of drag (C_D) obtained from the analysis is 0.63, and that of coefficient of lift (C_L) is 0.61. Shedding frequency has been calculated from the period of oscillation of the lift force. Lift force oscillates about zero mean value at the same frequency as that of vortex shedding. The frequency of oscillation of C_L , and hence that of shedding, has been found to be equal to be 35.7 Hz, which corresponds to a $St = 0.28$. A relationship between St and Re (Techet, 2005) it is observed that at $Re = 5.3 \times 10^4$ for a smooth cylinder, Strouhal number value is just above 0.3. Hence the obtained shedding frequency value from the numerical simulation has been proved to be in acceptable range. C_D and C_L time histories after convergence for a number of time periods are presented in Figure 3 and Figure 4.

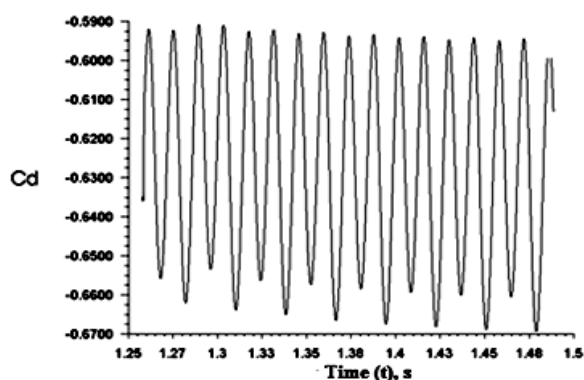


Figure 3. Time history of the coefficient of drag (C_D) at $Re = 5.3 \times 10^4$

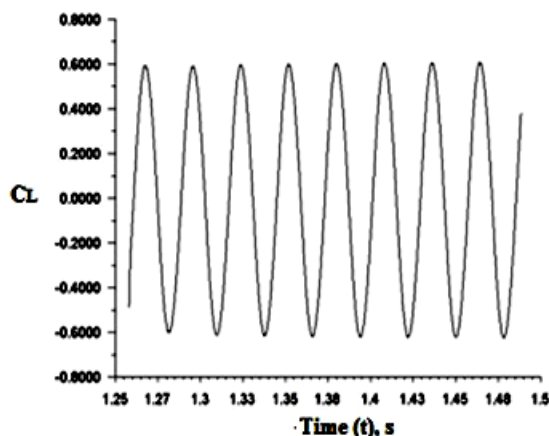


Figure 4. Time history of the coefficient of lift (C_L) at $Re = 5.3 \times 10^4$

2.2. Experiment - Flow Past Horizontal Cylinder

Experiments have been conducted with two folded objectives. The first one does a quantitative comparison, and the other one for a qualitative comparison. Quantitative comparisons with the numerical study have been established through a test at moderate $Re = 5.3 \times 10^4$ while the qualitative ones employed lower Re tests for flow visualizations, thus proving the efficacy of the mesh at moderate and low Re .

2.2.1. Quantitative Comparisons

A smoke test was carried out in the subsonic wind tunnel of Aerospace Laboratory of Karunya Institute of Technology and Sciences, Coimbatore, India. A horizontal cylinder of diameter 50 mm and length 600 mm fitted with pressure tapings has been used as the model for testing. The compressor of the wind tunnel unit was operated at 600 rpm, which corresponds to 16.4 m/s ($Re = 5.3 \times 10^4$) velocity at the test section. Smoke was inducted into the test section by burning liquid paraffin. Flow patterns and vortex shedding around the cylinder were captured using a high resolution camera. C_D and C_L values have been calculated from the measured pressure distribution. Details of the wind tunnel are as follows.

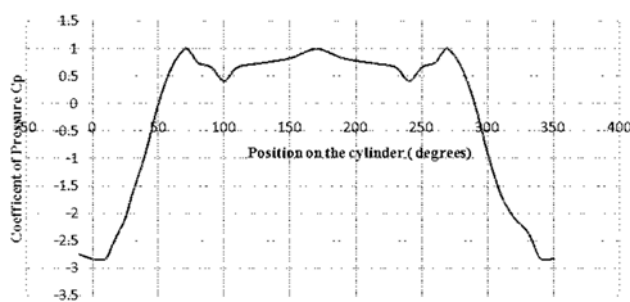
2.2.1.1. Wind tunnel specification

Test Section Size	:	Cross section = 600 x 600 mm
Length	:	4000 mm
Maximum Speed	:	45 m/s
Contraction Ratio	:	6:1
Contraction Length	:	1.8 m
Entry Section	:	Bell mouthed.
Smoke	:	Provided in the contraction cone
Power	:	22 kW/30 HP AC motor.

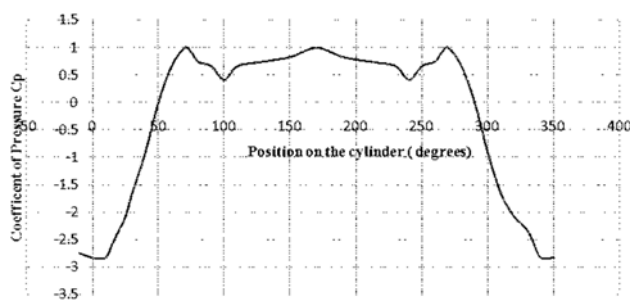
An inclined manometer with ethanol as the manometric fluid is fixed on the tunnel. The two limbs of the manometer are connected to the static pressure holes one in the settling chamber just before the contraction and the other to that at the entrance of the test section. The reading on the manometer is very near to the dynamic head of the fluid in the test section, and it serves as a reference for keeping the tunnel speed constant. The tunnel is also provided with a pitot static tube

which can be traversed across the tunnel cross section.

Pressure readings have been observed from the pressure ports provided on the circumference of the cylinder. Static and stagnation pressure have also been observed. Plots of pressure distributions around the cylinder and coefficient of pressure are represented in graphs Figure 5(a) and 5(b). C_D has been calculated by integrating $C_p \cos\theta$ over 360° using Simpson's method of integration. The value of C_D obtained from the wind tunnel experiment is 0.62. A comparison of the results obtained from the simulations and experiment are given in Table 2.



a)



b)

Figure 5. (a) Pressure distribution around the cylinder at $Re = 5.3 \times 10^4$ (b) Coefficient of pressure around the cylinder at $Re = 5.3 \times 10^4$

2.2.2. Qualitative Comparisons

An experiment to visualize, study, and analyze the characteristics of wake behind the horizontal cylindrical model has been conducted through smoke injection tests in the wind tunnel. A 50 mm diameter cylinder with 600 mm length has been used for flow visualization. The model is exactly similar to the one used for pressure measurement but without pressure ports. The model which had been used for pressure measurement cannot be used in this scenario because of the risk of the pressure ports getting

clogged with smoke particles. The recommended maximum tunnel speed for smoke visualization experiments is 4 m/s. Smoke tests have been performed at 0.6 m/s which corresponds to $Re = 2000$. Numerical simulations also have been performed using ANSYS Fluent 15 for the same Reynolds number using the previously generated mesh. Results obtained from the experiment and simulations are compared in Table 2. St has been calculated from the frequency of vortex shedding using Equation 12. In numerical simulations the shedding frequency is taken to be equal to the oscillation frequency of lift coefficient. Shedding frequency is obtained as 0.99 Hz and Strouhal number as 0.1995 for $Re = 2000$. Vortex shedding frequency from the wind tunnel experiment has been calculated by repeatedly noting from the recorded video of shedding phenomenon, the time is taken for shedding 20 vortices from the upper boundary of the cylinder, and then taking the average time observed for the calculation. Results obtained are presented in Table 2 for comparison with those obtained from numerical simulations.

Figures 6(a) and 6(b) represent the flow pattern obtained from the numerical study after convergence at 1.6 seconds of flow and wind tunnel test respectively for flow past cylinder at $Re = 2000$. Distances to the lower pressure zones (vortices) shed from the cylinder are indicated on a scale of the diameter of the cylinder. The length of the line segment in both figures corresponds to the diameter of the cylinder. The angle of separation of the boundary layer is shown in the wake patterns given in Figures 7(a) and 7(b). The numerical value of the separation angle is given in Table 2. For verification of the results from the present grid, flow analysis has been carried out at $Re = 1000$, in order to validate the grid using other published numerical works. The RMS value of C_D is found to be 1.24, which is very much comparable with the published results at $Re=1000$ ($C_D= 1.15$) (Braza. *et al.*, 1986).

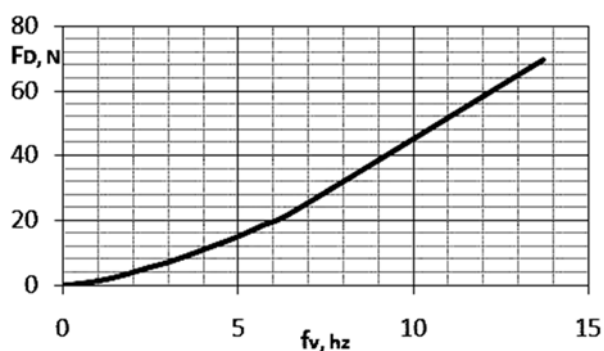
2.3. Force - Frequency Plot and Structural Analysis

Characteristics of flow past cylinder is a topic extensively investigated by researchers. Many have proposed plots from experimental, analytical, and numerical simulation results, which show the relationship between various flow parameters such as. with Re . The present work focuses on a marine riser model of specified dimension. A methodology has been developed to predict the structural response especially the trajectory of any section of the riser under vortex induced vibration. As the first phase, a data sheet has been created using the unstructured 2D mesh

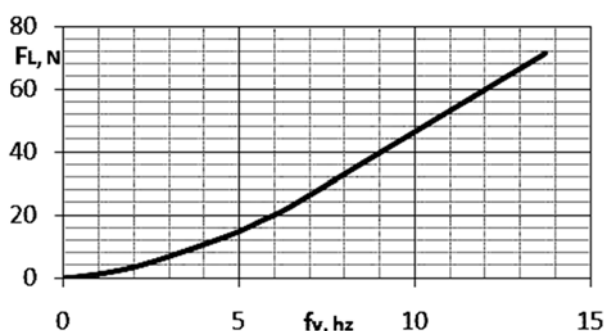
given in Figure 2. The sheet gives the numerical results of C_D , C_L , and vortex shedding frequency (f_v) from the 2D simulations performed in ANSYS Fluent-15 for a range of Reynolds number up to the sub critical value and the values have been mapped over the entire length of a 3D cylinder

Simulations have been performed for $Re = 100$ to $20,000$. The velocity of flow has been assumed to be uniform along the span of the cylinder. Using the values of C_D and C_L obtained from the flow analysis lift and drag force acting on a cylindrical riser of 8 m length, and 0.05 m diameter has been estimated. Figures 8(a) and 8(b) show the plot for drag and lift forces on a cylindrical riser model of 0.05 diameter and 8 m length against its vortex shedding frequency.

From the plot, the hydrodynamic forces acting on the cylinder at various frequencies can be obtained. The value of hydrodynamic loads obtained from the plot at a specific frequency has been used as the input for predicting the structural response of the cylinder and the trajectory of any point on the surface of the cylinder.



a)



b)

Figure 8. (a) Drag Force – Frequency plot
(b) Lift Force – Frequency plot

Structural analysis of the cylinder model has been performed in ANSYS Workbench-15. Drag and lift forces acting on the cylinder as a

result of vortex shedding have been given as input in the solver. It has been treated as an oscillating force having an amplitude equal to maximum lift in the direction perpendicular to the flow (cross flow) and equal to maximum drag in the direction of flow (in line). The frequency of oscillation of lift and drag forces has also been obtained from flow analysis. It has been observed that the drag coefficient is oscillating about a non-zero value at double the frequency of the lift coefficient. Vortices are shed behind the cylinder at the same frequency as that of the oscillating lift force. When the vortex shedding frequency matches the natural frequency of oscillation of the cylindrical structure, a resonance condition, well known as lock – in vibration occurs, which gives rise to oscillations of very high amplitude. This may bring in extensive damage to the structure and to the working crew. Hence the analysis of the response of structures vibrating at their natural frequencies due to vortex shedding is considered to be most desirable in design of offshore structures.

The cylinder has been modeled in ANSYS Workbench-15 as a hollow vertical, having a thickness of 2.5×10^{-3} mm. The material of the riser model has been chosen to be Poly Vinyl Chloride (PVC) of density 1400 kg/m^3 . The simulation has been performed as a transient case since it involves time varying forces and deformation. The top end has been modeled fixed in the x and y directions, and the bottom end with motion in x, y, and z direction arrested. Since the riser is a flexible structure, Mechanical ANSYS Parametric Design Language (APDL) has been used as the solver. Stiffness and mass coefficients were provided as input in the damping control of analysis settings of the solver. After performing a grid independency analysis, a mesh having 66,158 elements have been chosen for the response analysis. The meshing of the geometry has been done using tetrahedral elements. The time step size has been chosen to be 5×10^{-2} based on the oscillating frequency of hydrodynamic loads. Transient simulation has been performed for 10 seconds. Local displacements at estimated locations of maximum vibration amplitude at the first three modes of vibration were obtained by inserting a displacement probe at the respective locations on the cylinder. Time histories of displacement in the X and Y directions and the trajectory of the cylinder during vibration have been plotted from the probe data.

The first three modes of vibration and the corresponding natural frequencies of the riser in the air have been obtained as 2.99, 9.7, and 20.23

Hz, respectively, from the modal analysis. Natural frequencies of the riser in water have been obtained solving Equation 14, considering added mass to be 70% of the total system mass, $m_a = 1.12$ kg, and stiffness of the riser $k = 17.73$ N/m. The first three natural frequencies of the riser in water have been obtained as 2.88 Hz, 7.16 Hz, and 9.41 Hz, respectively.

$$\frac{1}{\omega_{n \text{ water}}^2} = \frac{1}{\omega_{n \text{ air}}^2} + \frac{m_a}{k} \quad (\text{Eq. 14})$$

Drag and lift forces, corresponding to the identified natural frequencies of the riser, have been obtained from the plotted frequency – force graph. The amplitude of variation of drag force has been observed to be much less compared to the lift force. Lift force has been considered as periodically varying force, which oscillates about zero and acting in the cross flow direction as given in Equation.15 in the structural solver.

$$F(t) = F_0 \cos(\omega_v t) \quad (\text{Eq. 15})$$

Drag force oscillates with double the frequency of lift force, and it oscillates about a non-zero value. Drag force has two components, viz. average drag and the fluctuating component of drag force. From the numerical simulation, both RMS value and fluctuation about RMS value of drag forces have been obtained. Drag force is applied to the cylinder in the structural solver, as given by Equation 16.

$$F_D(t) = F_{D \text{ avg}} + F'_D \cos(2\omega_v t) \quad (\text{Eq. 16})$$

Where $F_{D \text{ avg}}$ is the RMS value of drag force, and F'_D is its fluctuating component. The lift and drag forces obtained from the flow analysis corresponding to the flow regimes at which vortex shedding frequency (ω_v) matches the first three harmonics of the natural frequency of the cylinder (ω_n) have been used for structural analysis. This condition is generally referred to as lock-in condition. The drag force oscillates at double the frequency of lift coefficient. This phenomenon is well established in published literature (Durbin, 2007).

For the identified natural frequencies, structural analysis has been carried out to study various response parameters. A deformation probe has been inserted at $z = 4$ m for first and third modes of vibrations and at $z = 2$ m for the second mode to observe the response of the

cylinder under oscillating load.

3. RESULTS AND DISCUSSION

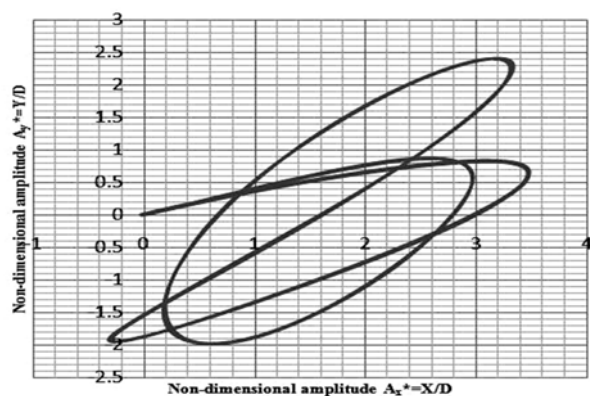
It can be observed that the numerical simulation with the grid generated, as shown in Figure 2 in the present work, is capable of replicating the wake pattern behind the cylinder exactly in the way the experiments do. Wake dimensions are comparable in both cases in terms of the span and angle of separation. Quantitative comparisons between the experimental and numerical values presented in Table 2 indicate the reliability in the present numerical predictions. Here the important observation is that at lower $Re = 2000$, a better prediction of St is achieved (9% deviation from the experimental ones) while at higher $Re = 4000$, a deviation of 22% is observed from the corresponding experimental value.

From the history of cylinder displacement during the lock-in, it can be observed that, as the frequency of shedding increases, the amplitude of displacement in cross flow direction goes on decreasing and that in the inline direction increases. This is because, at higher Re corresponding to higher shedding frequencies, the value of C_D is also high. A huge number of researchers are focusing on the cross flow response of cylinder. The observation made here emphasizes the need for investigating the inline response during lock-in at higher harmonics of natural frequency.

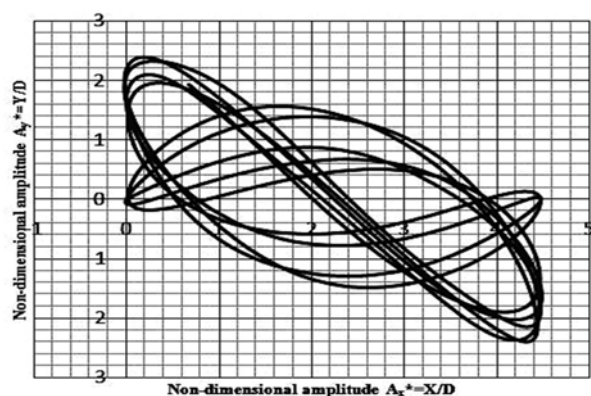
By plotting the non-dimensional amplitude of the cylinder in IL and CF directions, the trajectory of the probe location has been traced, as shown in Figures 9 (a) – (c) for all three frequency regimes. It can be observed that the cylinder point follows an eight figure trajectory during lock - in. The cylinder is expected to follow an eight figure trajectory due to oscillating lift and drag forces induced by vortex shedding at its wake. In lock-in condition the frequency of the inline vibration is twice that of cross flow vibration, and the trajectory of the cylinder corresponds to “Lissajou figure 8” (Vandiver *et al.*, 2009). Trajectory obtained from the numerical study is very much comparable with the response of an 8 m riser model obtained from the experimental study (Liangjie *et al.*, 2004). The trajectory from the experiment is given in Figure 10.

The trajectories traced show the increasing importance of accounting for IL response at higher harmonics of natural frequency. The maximum amplitude in the CF direction is obtained to be equal to 2.5D, where D is the diameter of the cylinder when the cylinder locks on to the first

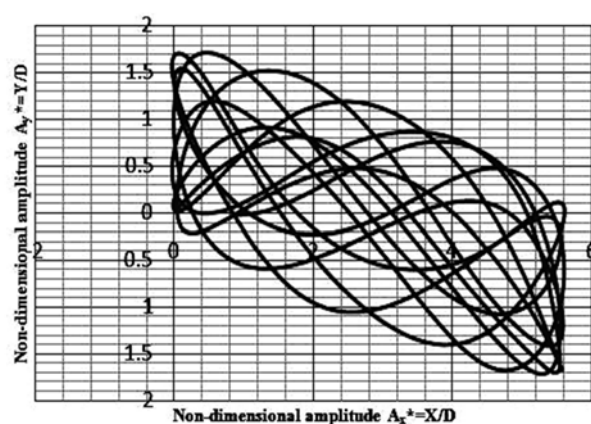
natural frequency. During the first natural frequency lock-in vibration, the cylinder traces the same path repeatedly for several cycles of oscillation. But moving to higher harmonics, there is considerable uncertainty in the case of exact path traced. The magnitude of the non-dimensional amplitude of oscillation and the pattern of trajectory matches reasonably well with the published experimental and numerical results.



a)



b)



c)

Figure 9. Trajectory of the cylinder (a) shedding frequency equal to the first harmonic of natural frequency (b) shedding frequency equal to second harmonic of natural

frequency (c) shedding frequency equal to third harmonic of natural frequency

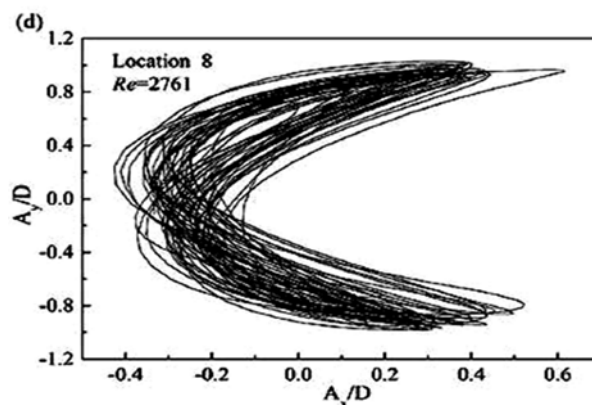


Figure 10. Trajectory obtained from an experimental study of the response of cylindrical riser

4. CONCLUSIONS

This paper presents a method that is computationally economic at the same time efficient in predicting VIV of cylindrical risers. Two dimensional flow analysis is capable of predicting the numerical values of hydrodynamics loads, pressure patterns during vortex shedding, the amplitude of oscillation and the trajectory as well for VIV problems. Vortex induced vibration of slender structures especially petroleum risers and mooring cables are one of the important aspects that should never be neglected in their design. Hence a thorough understanding of the loads and responses of such slender structures is essential before its design and deployment. Numerical analysis using two way fluid structure interaction (FSI), which can predict the parameters with considerable accuracy is always not handy for everyone dealing with this type of problem because of the heavy computational requirement needed for such solvers. This method has been proposed in a view to supporting young researchers in the field of the intrinsic flow phenomenon of vortex shedding, who lack high computational facility but may also understand the phenomenon without compromising much accuracy.

The method has been well validated in two stages, initially the grid, which yields the same flow physics as that of conventional experiments and then the structural behaviour which also is in good agreement with similarly published works (Liangjieet *al.*,2004 ,Vandiveret *al.*,2009). On the whole, it is found that the method is quite effective in the quick computation of VIV problems for low and moderate Re. At high Re, 3D studies find their

use as 2D predictions do not suffice in providing the minute details of flow physics.

5. ACKNOWLEDGEMENT

The authors of this paper wholeheartedly express their gratitude and acknowledgement to Mr. K. Alfred Sunny and Mr. Kumar of Karunya Institute of Science and Technology, Coimbatore, India, for the technical support rendered by them while conducting experiments on the sub-sonic wind tunnel. We also extend our deepest sense of gratefulness to Prof. M. Madhavan, former Principal, SCMS School of Engineering and Technology, Eranakulam, India, for his timely advice and support.

6. REFERENCES

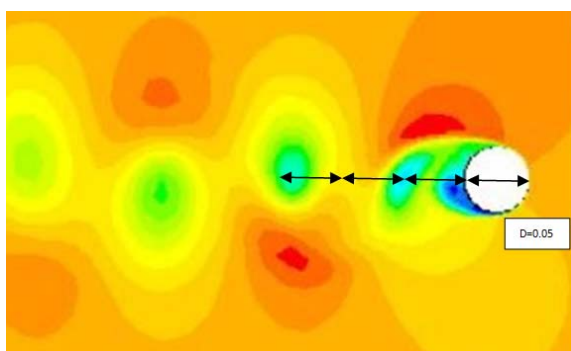
1. Gustafsson, A. Analysis of Vortex-Induced Vibration of Risers, Master's thesis in Applied Mechanics, Chalmers University of Technology, Sweden, **2012**.
2. Blevins, R.D. Flow-Induced Vibration, second ed., Van Nostrand Reinhold, New York, **1990**.
3. Bourguet, R., Karniadakis, G.E., Michael, S., and Triantafyllou, M.S. Lock-in of the vortex-induced vibrations of a long tensioned beam in shear flow, *Journal of Fluids and Structures*, **2011**, 27, 838–847.
4. Braza, M., Chassaing, P., and Minh, H.H. The Numerical Study and Physical Analysis of the Pressure and Velocity Fields in the Near Wake of a Circular Cylinder, *Journal of Fluid Mechanics*, **1986**, 165, 79–130.
5. Chandran, V., Sekar, M., Janardhanan, S., and Menon, V.A. numerical study on the influence of mass and stiffness ratios on the vortex induced motion of an elastically mounted cylinder for harnessing the power. *Energies*, **2018**, 11, 2580.
6. Chandran, V., Sekar, M., Janardhanan, S., Influence of Frequency Ratio on Hydroelastic Response of a Cylinder with Degrees of Freedom under Vortex Induced Vibration., *International Journal of Innovative Technology and Exploring Engineering*, **2019**, 8, 9S3, 307 -312.
7. Daniels, S.J., Castro, I.P., and Xie, Z. Numerical analysis of free stream turbulence effects on the vortex-induced vibrations of a rectangular cylinder, *Journal of Wind Engineering and Industrial Aerodynamics*, **2016**, 153, 13–25.
8. Domala, V., and Sharma, R. An experimental study on vortex-induced vibration response of marine riser with and without semi-submersible, *Journal of Engineering for the Maritime Environment*, **2017**.
9. Durbin, P.A., and Medic, G. Fluid dynamics with a computational perspective, **2007**, Cambridge University Press, Newyork.
10. Feng, C.C., The measurement of vortex-induced effects in flow past stationary and oscillating circular and D-section cylinders, Master's thesis, **1968**, University of British Columbia.
11. Gao, Y., Fu, S., Xiong, Y., Zhao, Y., and Liu, L. Experimental study on response performance of vortex-induced vibration on a flexible cylinder, *Ships, and Offshore Structures*, **2017**, 12, 116–134.
12. Kamkar S.J. Mesh Adaptation Strategies for vortex dominated flows, Ph. D Thesis, **2011**, Stanford University.
13. Keshavarzian, B., and Khosravi, M. Numerical Investigation of the Structural Frequencies Effects on Flow Induced Vibration and Heat Transfer, *Journal of Material and Environmental Science*, **2015**, 6 (7), 1949–1956.
14. Khalak, A., and Williamson, C.H.K. Motions, forces, and mode transitions in vortex-induced vibrations at low mass-damping, *Journal of Fluids and Structures*, **1999**, 13, 813–851.
15. Liangjie, M., Qingyou, L., and Shouwei, Z. Experimental Study of the Vortex-Induced Vibration of Drilling Risers under the Shear Flow with the Same Shear Parameter at the Different Reynolds Numbers, *PLoS ONE*, **2004**, 9, e104806.
16. Pezzini, A., Brião, V.B., and DE BONI, L.A. B. Preliminary study for a cleaning and water reuse system, *PERIÓDICO TCHÊ QUÍMICA*, **2017**, 28, 127–132.
17. Ramírez, Ann-Katrin, P., Wolff, and Carl, F. Building quality infrastructure services for water and sanitation providers in latinamerica – examples from german development cooperation, *PERIÓDICO TCHÊ QUÍMICA*, **2017**, 28, 18–28.
18. Sarpkaya, T., Transverse Oscillations of

Circular Cylinder in Uniform Flow, Part I Report No. NPS-69L 77071-R, **1997**, Naval Postgraduate School, Monterey, Calif.

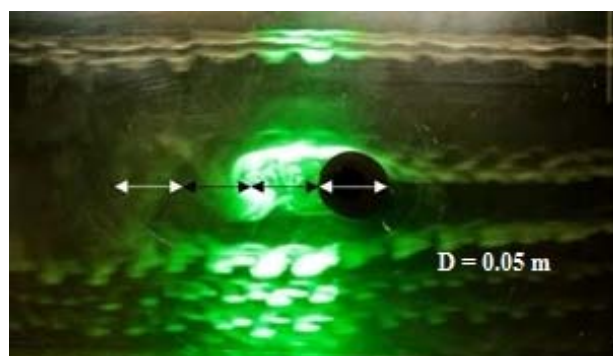
19. Sekar, M., Srinivas, J., Kotaiah, K.R., and Yang, S.H. Stability analysis of turning process with the tailstock-supported workpiece, *Int J Adv. Manuf. Technol*, **2009**, 43, 9–10, 862–871.
20. Shiels, D., Leonard, A., and Roshko, A. Flow-Induced Vibration of a Circular Cylinder at Limiting Structural Parameters, *Journal Of Fluids And Structures*, **2001**, 15, 3–21.
21. Techet, A., 13.42 Lecture: Vortex induced vibration – MIT open courseware, **2005**, Massachusetts Institute of Technology, USA.
22. Trim, A.D., Braaten, H., Lie, H., and Tognarelli, M.A. Experimental investigation of vortex-Induced vibration of long marine risers. *Journal of Fluids and Structures*, **2005**, 21, 335–361.
23. Vandiver, J.K., Jaiswal, V., and Jhingran, V. Insights on vortex-induced, traveling waves on long risers. *Journal of Fluids and Structures*, **2009**, 25: 641–653
24. Wang, Q., Li, M., and Xu, S., Experimental study on vortex induced vibration (VIV) of a wide-D-section cylinder in a cross flow, *Theoretical and Applied Mechanics Letters*, **2015**, 5: 39–44.
25. Xie, F., Deng, J., Xiao, Q., and Zheng, Y.A. Numerical simulation of VIV on a flexible circular cylinder, *Fluid Dynamics Research*, **2012**, 44, 21.

Table 2. Comparison between wind tunnel experiments and numerical simulations.

Reynolds Number (Re)	Coefficient of Drag (C_D)		Strouhal Number (St) (Non-dimensional Frequency)		Wake Dimension	
	Experiment	Numerical	Experiment	Numerical	Experiment	Numerical
53000	0.62	0.63	NA		NA	
4000	-	-	0.178	0.22	$\theta = 126^\circ$	$\theta = 120^\circ$
2000	-	-	0.183	0.1995	D = 0.05m	D = 0.02m

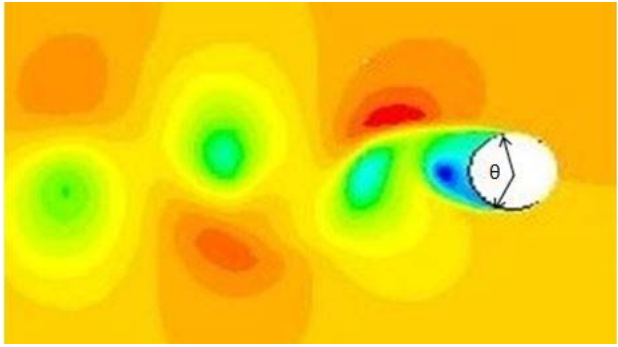


a)

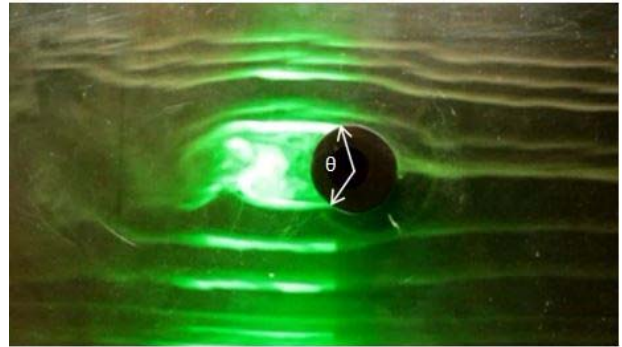


b)

Figure 6. Pressure pattern at the wake of the cylinder at $Re = 2000$ (a) obtained from numerical simulations (b) obtained from the smoke test conducted in the subsonic wind tunnel



a)



b)

Figure 7. Boundary layer separation at the wake of the cylinder at $Re = 4000$. (a) obtained from numerical simulations (b) obtained from the smoke test conducted in the subsonic wind tunnel

Received May 21, 2019, accepted June 3, 2019, date of publication June 6, 2019, date of current version September 26, 2019.

Digital Object Identifier 10.1109/ACCESS.2019.2911375

Brain-Controlled Adaptive Lower Limb Exoskeleton for Rehabilitation of Post-Stroke Paralyzed

P. G. VINOJ^{1,2}, SUNIL JACOB^{1,3}, VARUN G. MENON⁴, SREEJA RAJESH⁴,
AND MOHAMMAD REZA KHOSRAVI⁵

¹Department of Electronics and Communication Engineering, SCMS School of Engineering and Technology, Ernakulam 683576, India

²Department of Electronics and Communication Engineering, APJ Abdul Kalam Technological University, Thiruvananthapuram 695016, India

³Center for Robotics, SCMS School of Engineering and Technology, Ernakulam 683576, India

⁴Department of Computer Science and Engineering, SCMS School of Engineering and Technology, Ernakulam 683576, India

⁵Department of Electrical and Electronic Engineering, Shiraz University of Technology, Shiraz 71355-313, Iran

Corresponding author: Varun G. Menon (varunmenon@scmsgroup.org)

This work was supported by the EPICS, Institute of Electrical and Electronics Engineers (IEEE), USA, under Grant 2016-12.

ABSTRACT Stroke is a standout amongst the most imperative reasons of incapacity on the planet. Due to partial or full paralysis, the majority of patients are compelled to rely upon parental figures and caregivers in residual life. With post-stroke rehabilitation, different types of assistive technologies have been proposed to offer developments to the influenced body parts of the incapacitated. In a large portion of these devices, the clients neither have control over the tasks nor can get feedback concerning the status of the exoskeleton. Additionally, there is no arrangement to detect user movements or accidental fall. The proposed framework tackles these issues utilizing a brain-controlled lower limb exoskeleton (BCLLE) in which the exoskeleton movements are controlled based on user intentions. An adaptive mechanism based on sensory feedback is integrated to reduce the system false rate. The BCLLE uses a flexible design which can be customized according to the degree of disability. The exoskeleton is modeled according to the human body anatomy, which makes it a perfect fit for the affected body part. The BCLLE system also automatically identifies the status of the paralyzed person and transmits information securely using Novel-T Symmetric Encryption Algorithm (NTSA) to caregivers in case of emergencies. The exoskeleton is fitted with motors which are controlled by the brain waves of the user with an electroencephalogram (EEG) headset. The EEG headset captures the human intentions based on the signals acquired from the brain. The brain-computer interface converts these signals into digital data and is interfaced with the motors via a microcontroller. The microcontroller controls the high torque motors connected to the exoskeleton's joints based on user intentions. Classification accuracy of more than 80% is obtained with our proposed method which is much higher compared with all existing solutions.

INDEX TERMS Artificial skin, assistive technologies, brain-computer interface (BCI), electroencephalogram (EEG), brain-controlled exoskeleton, paralyzed, stroke.

I. INTRODUCTION

Stroke is an important reason of physical disability in developed countries, and in fact the third most common reason [1]. Almost 80% of survivors of stroke have experienced movement impairment on one side of the body [2-3]. Hand or arm impairment is particularly disabling and persistent, and lead to reduced quality of life [3-4]. Many of the stroke survivors

have a less physical disability by the end of the first three months (almost in all cases). Nearly, 35% of survivors having an initial paralysis of the leg do not regain the basic and essential function, and 20 to 25% of all the survivors are not able to walk without complete physical assistance [5]. Within six months, nearly 65% of patients are unable to use the affected hands for doing common life activities. Most of the patients are thus forced to be dependent on others in the remaining part of life.

The associate editor coordinating the review of this manuscript and approving it for publication was Mohammad Zia Ur Rahman.



All



ADVANCED SEARCH

Journals & Magazines > IEEE Access > Volume: 7

Artificial Muscle Intelligence System With Deep Learning for Post-Stroke Assistance and Rehabilitation

Publisher: IEEE

Cite This



Sunil Jacob ; Varun G. Menon ; Fadi Al-Turjman ; Vinoj P. G. ; Leonardo Mostarda

All Authors

33 Paper Citations

4062 Full Text Views



Alerts

Manage Content Alerts Add to Citation Alerts

Open Access Comment(s)

Under a Creative Commons License

Abstract



Document Sections

- I. Introduction
- II. Related Works
- III. Mathematical Model
- IV. System Architecture
- V. Results and Discussion

Show Full Outline

Authors

Figures

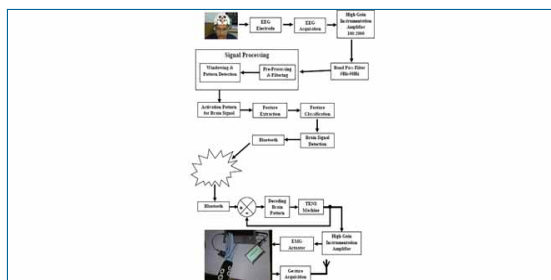
References

Citations

Keywords

Metrics

More Like This



Architecture of Artificial Muscle Intelligence with Deep Learning (AMIDL) System.

Abstract:Stroke is one of the prime reasons for paralysis throughout the world caused due to impaired nervous system and resulting in disability to move the affected body parts. R... [View more](#)

Topic: Machine Learning Designs, Implementations and Techniques

Metadata

Abstract:

Stroke is one of the prime reasons for paralysis throughout the world caused due to impaired nervous system and resulting in disability to move the affected body parts. Rehabilitation is the natural remedy for recovering from paralysis and enhancing the quality of life. Brain Computer Interface (BCI) controlled assistive technology is the new paradigm, providing assistance and rehabilitation for the paralysed. But, most of these devices are error prone and also hard to get continuous control because of the dynamic nature of the brain signals. Moreover, existing devices like exoskeletons

PDF Help

brings additional burden on the patient and the caregivers and also results in mental fatigue and frustration. To solve these issues Artificial Muscle Intelligence with Deep Learning (AMIDL) system is proposed in this paper. AMIDL integrates user intentions with artificial muscle movements in an efficient way to improve the performance. Human thoughts captured using Electroencephalogram (EEG) sensors are transformed into body movements, by utilising microcontroller and Transcutaneous Electrical Nerve Stimulation (TENS) device. EEG signals are subjected to pre-processing, feature extraction and classification, before being passed on to the affected body part. The received EEG signal is correlated with the recorded artificial muscle movements. If the captured EEG signal falls below the desired level, the affected body part will be stimulated by the recorded artificial muscle movements. The system also provides a feature for communicating human intentions as alert message to caregivers, in case of emergency situations. This is achieved by offline training of specific gesture and online gesture recognition algorithm. The recognised gesture is transformed into speech, thus enabling the paralysed to express their feelings to the relatives or friends. Experiments were carried out with the aid of healthy and paralysed subjects. The AMIDL system helped to reduce mental fatigue, miss-operation...

(Show More)

Topic: Machine Learning Designs, Implementations and Techniques

Published in: IEEE Access (Volume: 7)

Page(s): 133463 - 133473

INSPEC Accession Number: 19002006

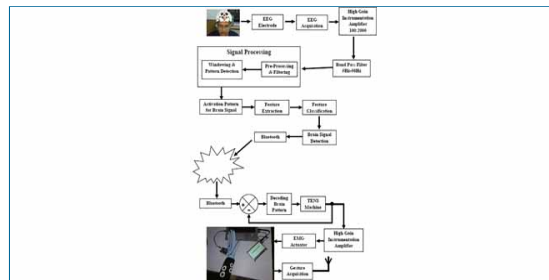
Date of Publication: 16 September 2019

DOI: 10.1109/ACCESS.2019.2941491

Electronic ISSN: 2169-3536

Publisher: IEEE

Funding Agency:



Architecture of Artificial Muscle Intelligence with Deep Learning (AMIDL) System.

Hide Full Abstract ^

Contents

CCBY - IEEE is not the copyright holder of this material. Please follow the instructions via https://creativecommons.org/licenses/by/4.0/ to obtain full-text articles and stipulations in the API documentation.

SECTION I. Introduction

The recent survey by reeve foundation revealed the impact of paralysis on world population, affecting approximately 5.4 million people [1], [2]. The survey also identified stroke (33.7%) as the major cause for paralysis. Paralysis is the deficiency of brain to activate muscle function of any body part. Paralyzed persons find it difficult to perform their routine activities without assistance. Rehabilitation is one of the natural ways of healing paralysis. Because of this there is increasing interest and involvement in the field of post stroke rehabilitation. Exoskeleton-assisted technologies have emerged as a reliable means for rehabilitation of the affected upper and lower limbs [3]. Exoskeleton movements were controlled using sensors like gyroscopes, accelerometers, and potentiometers. Recently the focus is on controlling exoskeleton using Brain Computer Interface (BCI) [4]. Antelis et al. demonstrated upper limb movement of the paralyzed using EEG signals [5]. A closed loop is established between human thought and movement of paralyzed limb using non-invasive BCI [6]. Android feedback based BCI training is employed to enhance brain rhythms



PDF Help

during motor imagery task. The realistic feedback is realized in training session using humanoid robot [7]. Humanoid robot is navigated in real-time indoor environment based on human intentions. The asynchronous BCI system was designed using two level classifiers [8]. Co-operation and co-ordination of dual robotic arm is demonstrated using EEG based system. SSVEP (Steady-State Visual Evoked Potentials) are utilized to improve the user concentration level [9]. Electromyography (EMG) sensors are also used to control exoskeleton movements, EMG returns the information regarding human muscular activity [10]. The motor adaptability of upper limb is predicted using resting state functional connectivity. The system could identify effectiveness of robotic upper limb rehabilitation in different patients [11]. However, the system does not investigate real time human behaviors and thoughts. The clinical trials to investigate the effectiveness of BCI training sessions on stroke patients with upper limb paralysis are carried out. The results of the trial indicate that BCI based assistive devices are effective for post stroke rehabilitation [12]. Human intentions measured through cortical potentials were used to control upper-limb exoskeleton movements. The BMI system eliminated the need for recalibration but resulted in large false positive rates [13]. Grasping feature is incorporated into the assistive device for amputees using non-invasive EEG control. The participants were able to grasp the objects, but resulted in low success rate without sufficient training [14]. Brain activity is modulated to control robotic arm with multiple degrees of freedom. The system demonstrated the effective control of robotic arm with few training sessions, but increased the latency periods during certain operations [15]. Hybrid BMI system based on sensorimotor cortical desynchronization (ERD) and electromyography (EMG) activity was designed to control upper limb movements. The integration of BMI, NMES and exoskeleton improved the system accuracy, but increased the system complexity [16]. The linear control of upper limb is demonstrated using motor imagery based BCI and Functional Electrical Stimulation (FES), support is provided to the arm using passive exoskeleton. The generated limb movement is evaluated to identify the precise positioning [17]. The self-induced EEG variations based on ERD/ERS is utilized for controlling upper limb movements. Distinguishable patterns are obtained for left and right-hand movements in both motor imagery and motor execution experiments [18]. Online robot control using motor imagery based BCI is designed with high classification accuracy. The mental imagination of hand movement is detected for controlling the robot movements [19]. An integrated platform consisting of BCI controlled exoskeleton, functional electric stimulation (FES) with proprioceptive feedback is developed. Goal directed motor task is used for training and subjects could complete the task with minimum latency period [20].

In our previous works [21]– [23], we have demonstrated an alternative technology to exoskeletons using non-invasive brain signals. Also, exoskeletons with feedback mechanism has also been implemented by us [22]. The paralyzed body part is stimulated using Transcutaneous Electrical Nerve Stimulation (TENS) device and Microcontroller [24]. Because of the dynamic and uncertain nature of brain signals, most of the BCI systems result in miss-operation, mental fatigue and it is hard to produce continuous control. The proposed system is designed to address the above gaps in research.

AMIDL is designed to reduce miss-operation, user fatigue and to enhance user capabilities. In the proposed work, human intentions are monitored in real-time employing 16 channel EEG sensors. TENS machine is integrated with Muscle Inspired Algorithm (MIA) to produce movements on the upper limb. Subjects are relieved from the task of carrying exoskeleton structure. The system is designed to perform six different movements on the affected upper limb. The different hand postures used to trigger the rehabilitation process are Release, Grasp, Rollup, Roll down, Rollup Release and Rollup grab. In the offline phase, Artificial Muscle movements corresponding to each posture are recorded to create the database. The decoded EEG signals are transformed into muscle activation signals in real-time environment. The captured EEG signal is converted into frequency domain using Walsh Hadamard Transform (WHT) for feature extraction. The extracted features along with WHT coefficients are utilized for the classification of different limb movements. The activation signal is then correlated with the recorded muscle movements. The signal with superior characteristics is passed on to the upper limb electrodes for inducing motion. In case of ambiguity or inadequate EEG signal, the periodic activation of the affected body part will be taken care by the artificial muscle movements. If the activation is executed by brain signal, the produced gesture is recognized and passed on to the care giver as voice command. Thus, AMIDL transforms human thoughts into different movements on the unique upper limb structure. The EEG activated movements are utilized for communicating paralyzed person's emergency need to the caregivers.

The contributions of our research are,

- An Artificial Muscle Intelligence with Deep Learning (AMIDL) system without exoskeleton structure, in which movements of paralyzed body part is controlled based on user intentions.

- An adaptive mechanism based on recorded muscle movements is integrated with the system to enhance continuous control and facilitate rehabilitation.
- Designed flexible assembly, which can be customized according to the degree of disability.
- Communication aid is incorporated in the system using gesture recognition
- The subject concentration is improved by using multimedia feed back

The rest of the paper is organized into four sections in which section 2 describes different existing methods used in BCI controlled upper limb movements.

SECTION II. Related Works

In this section, we discuss few existing devices controlled by Brain-Computer Interface designed specifically for paralyzed people. But the problem with most of them is that the users are unable to get continuous control over the device. The users are required to have high level of concentration to get sufficient control on the device, which results in mental fatigue and frustration. Additionally, there is no arrangement to take care of the miss-operations. The subjects are also burdened with the task of carrying the load of exoskeleton on the affected body parts. Our research focus on overcoming these major problems and provides an efficient and flexible solution, which can enhance the post stroke recovery process. Our system also provides a communication aid for the paralyzed to express their feelings.

The assistive rehabilitation devices and its EEG control techniques are systematically reviewed and the major gaps are identified [25]. Three-dimensional robotic assistance using motor imagery task for upper limb rehabilitation is demonstrated with multi-joint exoskeleton. Desynchronization of sensorimotor oscillations in the β -band is measured to control the different robotic hand movements [26]. Different upper limb exoskeletons like Track hold [27] and Armeospring [28] are employed to track upper limb movements. Both these devices have integrated passive robots with virtual reality environment to help patients carry out their daily routine activities. Control of assistive robots are improved by integrating electroencephalography (EEG) and electrooculography (EOG). This hybrid approach called as brain/neural-computer interaction (BNCI) is adopted to control grasping movements of a hand exoskeleton [29]. Multimodal signal approach is further used to enhance control system for external device connected to the upper limb. EEG and EMG signals are integrated to improve the classification accuracy and to reduce the false positive rate [30]. Upper limb robotic orthosis, FES, and wireless BCI are combined in an efficient way on account of EEG signals. EMOTIV EEG device is employed to measure EEG signal, which is used to control grasp/release of an object [31]. An integrated passive robotic system is developed for assisting the paralyzed. The system employs a robotic device which compensates gravitational effects to allow exercise, virtual engines to facilitate interaction and EEG to monitor brain activities. The three components are coordinated in real-time to enhance the rehabilitation process [32]. The effects of BCI therapy on post stroke rehabilitation is analyzed based on motor imagery tasks. The analysis is performed by measuring coherence of EEG in different regions of the brain and the best result for motor recovery is obtained for the activation of lesion hemisphere [33]. The online BCI coupled with hand exoskeleton is employed to address the issues related to proprioceptive feedback on the regulation of cortical oscillations. The results show an enhancement in SMR desynchronization with proprioceptive feedback during flexing and extending fingers of the exoskeleton [34]. Multimodal architecture based on BCI, exoskeleton and an active vision system is proposed to enhance BCI control and rehabilitation process. The VR environment coupled with bio feedback help to reduce mental fatigue and improve user interactions [35]. Few studies have also been conducted in related areas recently [36]– [42] Al-Turjman *et al.* proposed another interesting system using optimal haptic communications [43]. Xu *et al.* [44] proposed a three-dimensional animation to guide upper limb movements using EEG signals. Feature extraction is carried out by Harmonic Wavelet Transform (HWT) and linear discriminant analysis (LDA) classifier was utilized to classify the patterns for controlling the upper limb movements. MR-compatible robotic glove operates pneumatically and doesn't cause any disturbance to functional Magnetic Resonance imaging (fMRI) images during rehabilitation process [45]. The resistance to mechanically actuated movements in exoskeleton robot is measured based on spasticity. The relevant guidelines for practical neuro-rehabilitation robot design based on degree of spasticity and resistance is established [46]. In most of the design it is hard to get continuous control on the exoskeleton due to the non-stationary nature of the EEG

signal. Moreover, the subjects experience mental fatigue and frustration due to lack of superior control. None of the device in the literature focused on providing communication aid for the paralyzed. Our research focus on solving these issues in an efficient manner using AMIDL system proposed in this paper. Table 1 shows the comparisons between AMIDL and existing systems in the literature.

TABLE 1 AMIDL Comparisons With Existing System (Sorted by Success Rate)



TABLE 2 Data Statistics for Brain Actuated Rollup Signal

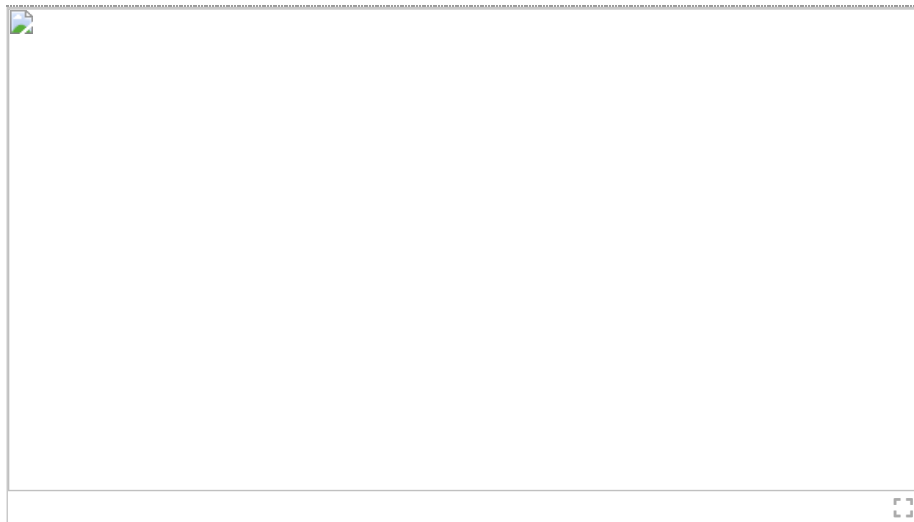


TABLE 3 Data Statistics for Posture Actuated Rollup Signal

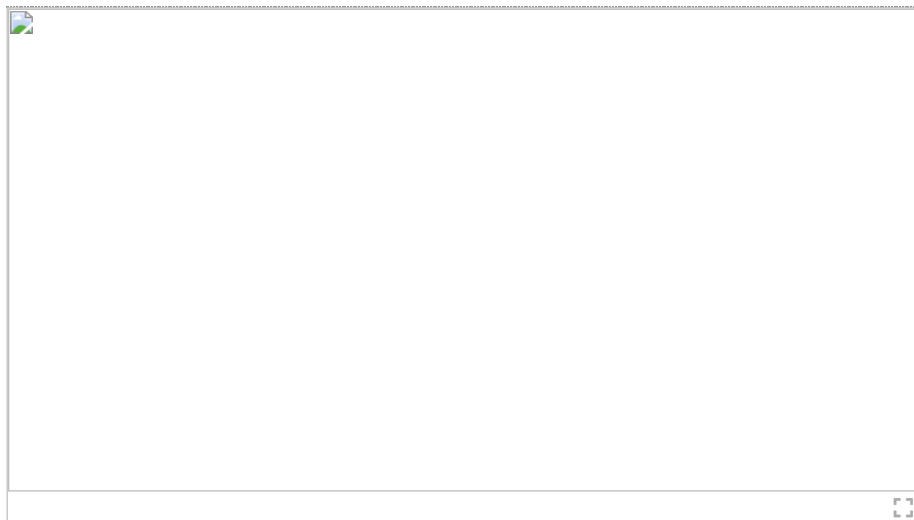
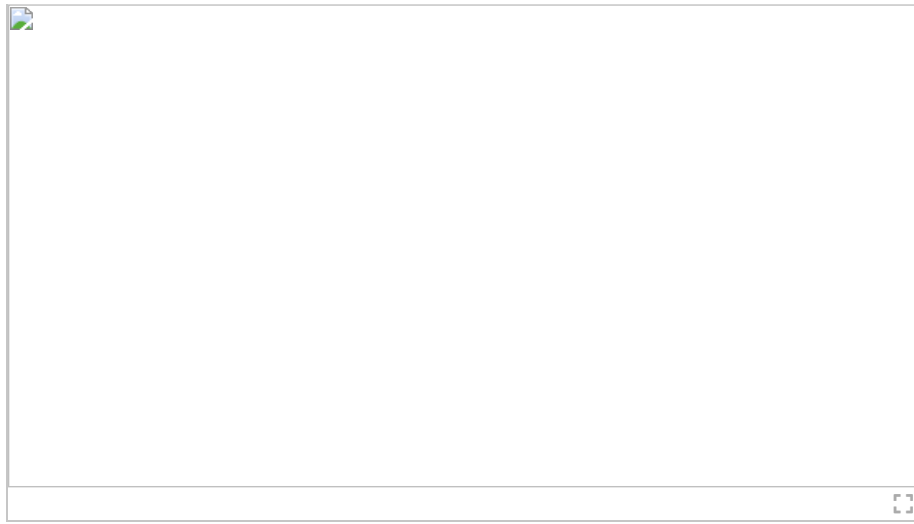


TABLE 4 Data Statistics for Brain Actuated Rolldown Signal



**TABLE 5** Data Statistics for Posture Actuated Rollup Signal

SECTION III.

Mathematical Model

This section presents and discusses the mathematical modelling of the proposed system. The system is designed to perform six different movements on the affected upper limb. The different hand postures used to trigger the rehabilitation process are Release, Grasp, Rollup, Roll down, Rollup Release and Rollup grab. In the offline phase, Artificial Muscle movements corresponding to each posture are recorded to create the database. The decoded EEG signals are transformed into muscle activation signals in real-time environment.

In Hand Posture Release operation, the voltage and current applied to electrodes are assumed as V_{H-P-R} & I_{H-P-R} . Similarly, the voltage and current applied to electrodes in the other postures are defined as,

Hand Posture Release $\rightarrow V_{H-P-R} I_{H-P-R}$

Hand Posture Grasp $\rightarrow V_{H-P-G} I_{H-P-G}$

Hand Posture Roll up $\rightarrow V_{H-P-Ru} I_{H-P-Ru}$

Hand Posture Roll down $\rightarrow V_{H-P-Rd} I_{H-P-Rd}$

Hand Posture Role up Release $\rightarrow V_{H-P-R-R} I_{H-P-R-R}$

Hand Posture Roll up Grasp $\rightarrow V_{H-P-R-G} I_{H-P-R-G}$

The voltage for Hand Posture Release, $V_{H-P-R} \neq$ Hand Posture Grasp, V_{H-P-G} . If they are same the hand posture will be stable. If $V_{H-P-R} > V_{H-P-G}$, then Hand Posture Release will be activated compared to Hand Posture Grasp.

The other parameters in the system is defined as follows. The diameter of EEG electrode is D_E . The scalp resistance is S_R . The conductivity of the EEG electrodes depends upon the multiplying factor is assumed as "T".

When the multiplying factor "T" is more, the conductivity will be more & vice versa. The multiplying factor depends on the positioning of EEG electrodes, the diameter of EEG electrodes and scalp resistance.

The V_{H-P-T} denotes the Hand Posture Threshold. The threshold varies depending on the different types of postures.

A. The Poster Activation Region

The Hand Posture Current in the system is given by,

$$I_{H-P} = \frac{D_E}{S_R} \int_{V_{H-P-initial}}^{V_{H-P-final}} T(E_Q) dV_{initial-final} \quad (1)$$

[View Source](#)

For the condition from Hand Posture Grasp to Hand Posture Release with the Hand Posture Threshold acting as an intermediate, the Hand Posture Release current is given by,

$$I_{H-P-R} = \frac{D_E}{S_R} \int_{V_{H-P-G}}^{V_{H-P-R}} T(E_Q) dV_{R-G} \quad (2)$$

[View Source](#)

where E_Q is the net potential to EEG electrodes. Also, we have,

$$E_Q = V_{H-P-R} - V_{H-P-T} - V_{H-P-G} \quad (3)$$

[View Source](#)

If E_Q is positive then, V_{H-P-R} is dominating V_{H-P-T} & V_{H-P-G} . The required potential to EEG electrodes will be analyzed and the Hand Posture Release operations will be performed.

For $V_{H-P-G} < V_{H-P-T} \leq V_{H-P-R}$, neglecting the surrounding areas of EEG electrodes and conductive loss. The hand posture for release will be activated as,

$$I_{H-P-R} = V_{H-P}(V_{H-P-G}, V_{H-P-R}) \quad (4)$$

[View Source](#)

Similar relation can be developed for the remaining postures.

If the movement is a combination of different postures, say Roll up and Release, then,

PDF

Help

Let say the initial posture is in grasp stage,

$$I_{H-P-R-R} = \frac{DET}{S_R} \left\{ \int_{V_{H-P-G}}^{V_{H-P-Ru}} (V_{H-P-Ru} - V_{H-P-T} - V_{H-P-G}) dV_{G-Ru} + \int_{V_{H-P-Ru}}^{V_{H-P-R}} (V_{H-P-R} - V_{H-P-T} - V_{H-P-Ru}) dV_{Ru-R} \right\} \quad (5)$$

[View Source](#)

Using the current value in the first integral and in the second integral we will have,

$$I_{H-P-R-R} = I_{H-P-G-Ru} (V_{H-P-G}, V_{H-P-G-Ru}) + I_{H-P-Ru-R} (V_{H-P-Ru}, V_{H-P-R}) \quad (6)$$

[View Source](#)

The mathematical model of the system can be summarized as I_{H-P} , as shown at bottom of the next page.

SECTION IV. System Architecture

The architecture of the proposed system is presented in figure 1.

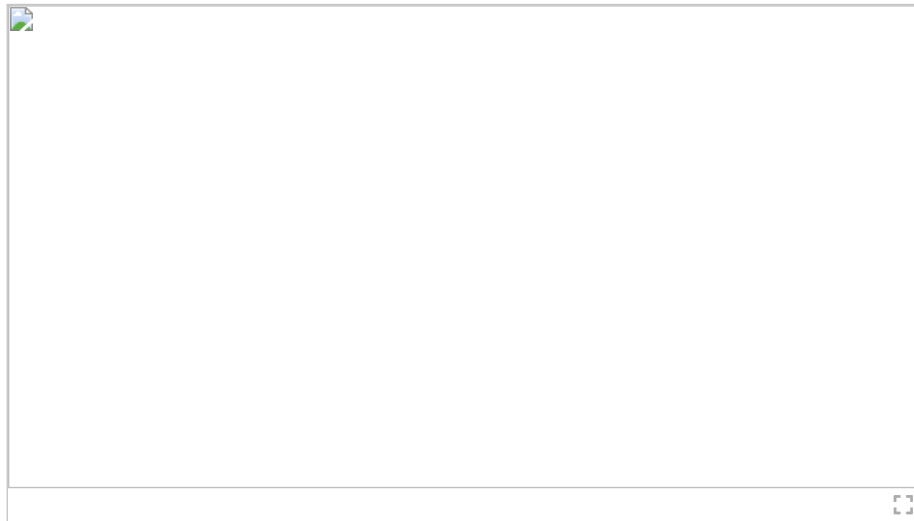


FIGURE 1. System architecture: AMIDL EEG acquisition and muscle stimulation modules.

A. AMIDL EEG Acquisition Module

The system architecture is designed using modular approach, it consists of three main modules. They are 1) EEG Acquisition Module, 2) Muscle Stimulation Module and 3) Gesture to Voice Conversion Module. Figure 1 indicates the two main modules of the system. The system captures brain signal using EEG sensor module, which has 14 electrodes to make measurement and two acts as reference. The acquired signal undergoes pre-processing, feature extraction and classification. The low amplitude EEG signal is amplified using high gain instrumentation amplifier with a gain of approximately 1000–2000 db. The signal is band limited by employing band pass filter having a pass band frequency of 5–50Hz. Windowing and pattern selection is utilized for getting finite response. Feature coefficients of the signal are extracted using Walsh Hadamard Transform (WHT). These extracted features are used to classify the thoughts into six different movements. The actual brain pattern is reconstructed using the transmitter Hadamard coefficients. The decoded brain

pattern is given to the TENS device, which transforms the thought into muscular actions. The muscle inspired algorithm stored in the controller facilitates the process of conversion. In the offline phase, muscle movements correspond to the six different pre-defined hand postures are recorded to create the database. The hand postures are recorded using 7 Electromyography (EMG) sensors on the different hand muscles. Five EMG electrodes are placed on the finger muscles to record finger activity. Two electrodes are placed on either side of the elbow to identify roll movements. In the online phase, brain signal based on the human thought is acquired and transformed into muscle movement. This transformed muscle movement is then correlated with the recorded muscle movements. The signal with superior characteristics is selected by the controller for producing movements on the affected body part. If the brain signal fails to provide sufficient activation, periodic movements in the upper limb will be triggered by artificial muscle.

B. AMIDL Gesture to Voice Conversion Module

If the brain signal with superior features activate the upper limb, the created gesture will be captured. Flex sensors placed on each finger is used for acquiring the gesture. The captured gesture will be recognized by the algorithm and transforms it into voice commands for the care givers. Figure 2 depicts the AMIDL gesture to voice conversion module. This module is used to give emergency alert messages to the caregivers or relatives.

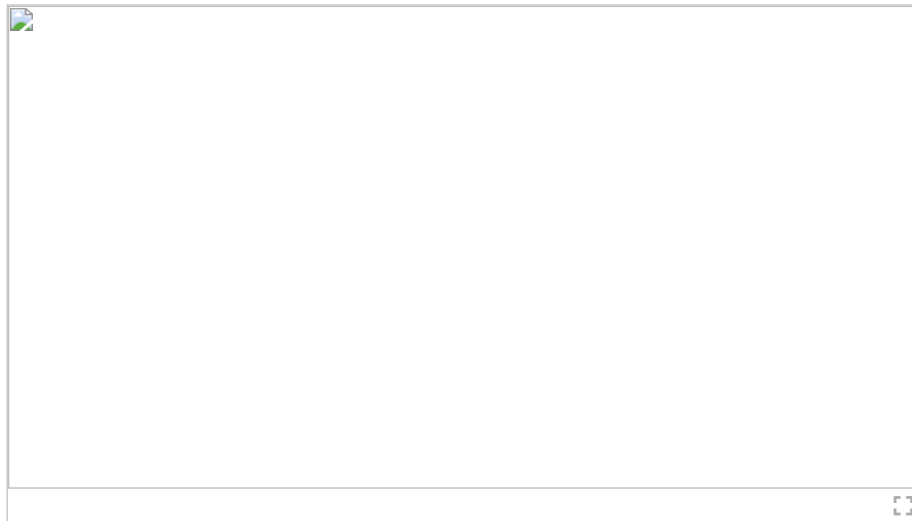


FIGURE 2.
AMIDL gesture to voice conversion.

The main hardware designed for the system has two parts 1) Acquisition module and 2) Muscle stimulation module. The brain signals of the user are acquired by using the EEG sensor. The non-invasive EEG sensor employed captures human intentions using 16 electrodes placed in the structure. 14 electrodes are used for capturing the signal and two electrodes act as reference. Figure 3 depicts the capturing of EEG signal using sensor from a human subject. The acquired signal is amplified using high gain instrumentation amplifier. The signal is band limited by employing band pass filter with pass band frequency in range of 5–50Hz

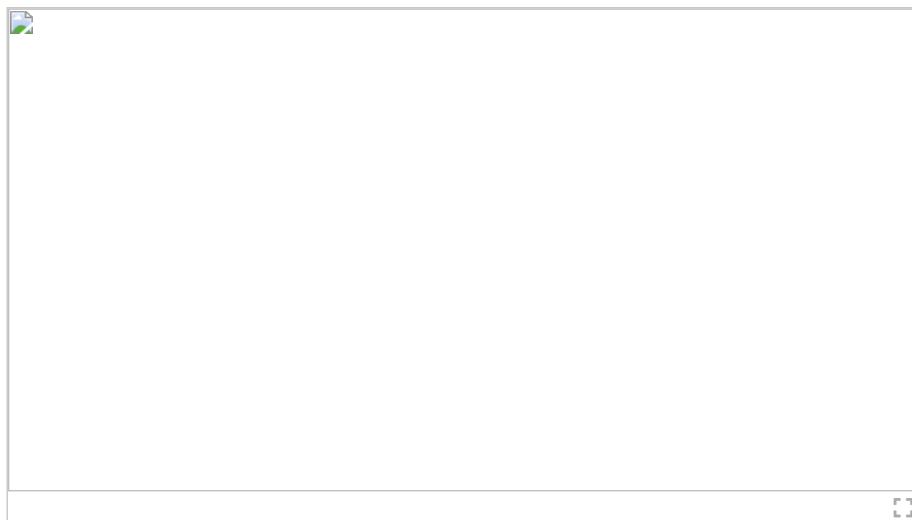


FIGURE 3.
Signal acquisition using EEG sensor [21].

Signal undergoes further pre-processing and filtering to reduce the high frequency noise. Frequency domain conversion of the signal is done by using WHT transform and finite sample is selected using window technique. The design uses microcontroller in the acquisition and muscle stimulation module. The microcontrollers communicate with each other using Bluetooth technology. Bluetooth is selected because of short distance between modules and data rate required is less than 1mbps. EEG sensor and other electronic circuits are interfaced to the microcontroller to design the PCB. Figure 4 shows the electronic assembly used in our experimentation.

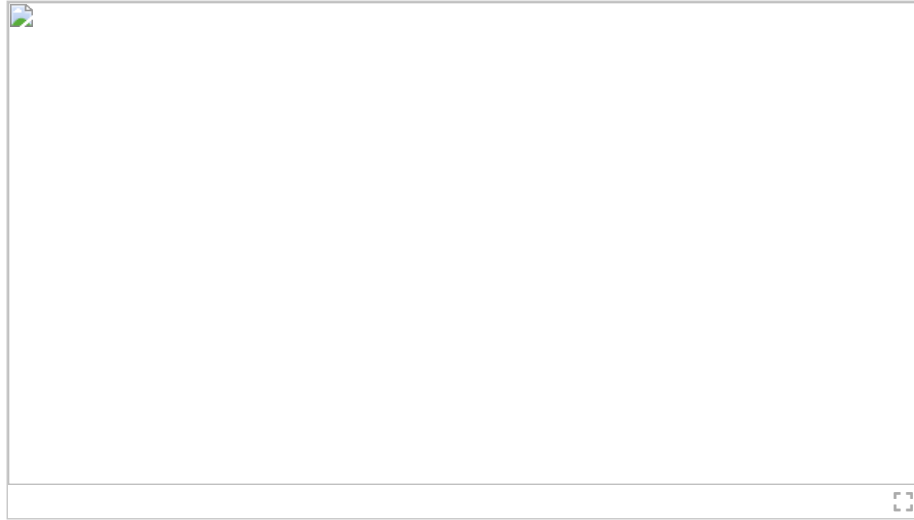


FIGURE 4.
PCB designed for the experimentation.

The muscle stimulation module receives the data using wireless module. The received data is converted into muscle movements or stimulation using muscle inspired algorithm stored in Arduino along with the TENS device interfaced to it. The output of the TENS is connected to the EMG electrode through EMG shield to activate the affected upper limb movements. The EMG shield helps to customize the stimuli produced by the TENS device. The entire assembly used for acquisition and stimulation is depicted in figure 5.

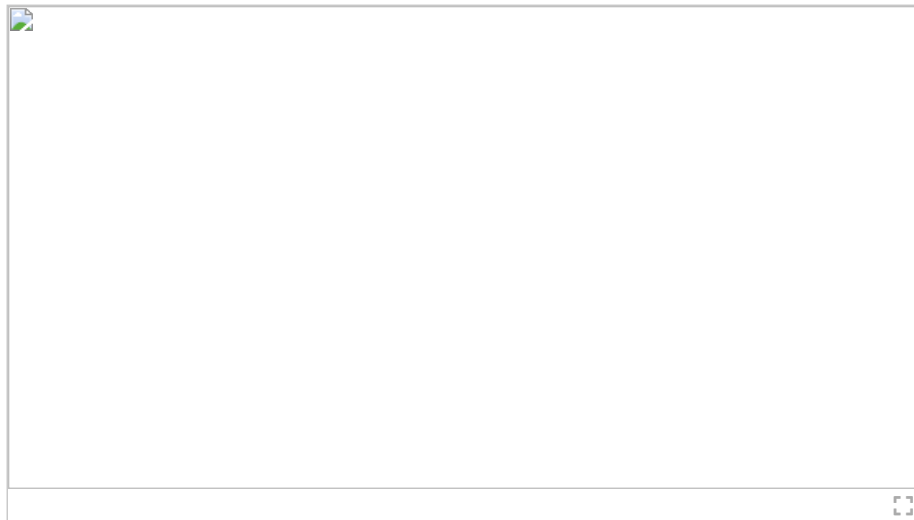


FIGURE 5.
Acquisition and stimulation process.

SECTION V. Results and Discussion

Experimentation is carried out in two phases, offline training phase and online recognition phase. Experimentation and validation are done on 10 healthy and 10 paralyzed subjects. In offline phase

EEG activity of the paralyzed and EMG activity of the healthy subjects were recorded. In the training phase, subjects were given the familiarization of six different intended actions like, Grasp, Release, Rollup, Rolldown, Rollup Release etc. Multimedia feedback is given to the subjects to enhance the brain patterns. The subjects are enlightened by using encourages messages and appreciation speeches in the feedback, rather than simple live streaming the actions. Rollup-grasp, Rolldown-Release movements of the upper limb are used for communicating the need to the caregivers. In the online phase, user thoughts are recognized and converted into muscular action. The generated muscular action is correlated with the EMG activity of the healthy subjects. Based on the correlation result microcontroller selects the superior signal, which is used for stimulating the affected body part.

A. Results Comparison of EEG Activated and Posture Actuated Movements

Figure 6 shows the correlation of brain actuated real time EMG and posture actuated EMG for the subject intention to grasp the object. The EMG activity is recorded using EMG electrodes and measurement is done using Digital Storage Oscilloscope (DSO). The graph shows the amplitude variations of EMG signal with respect to frequency. The amplitude is normalized between $+/-0.5mv$ and frequency range used is 0–500Hz.

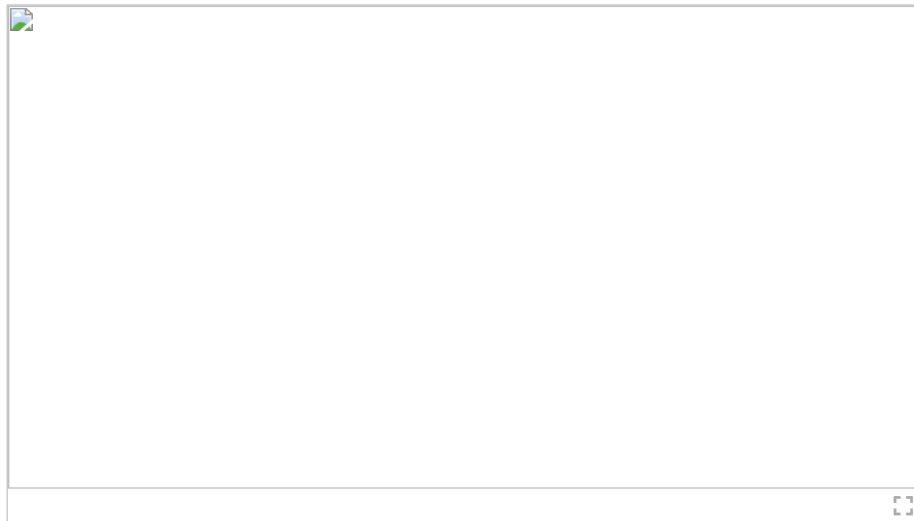
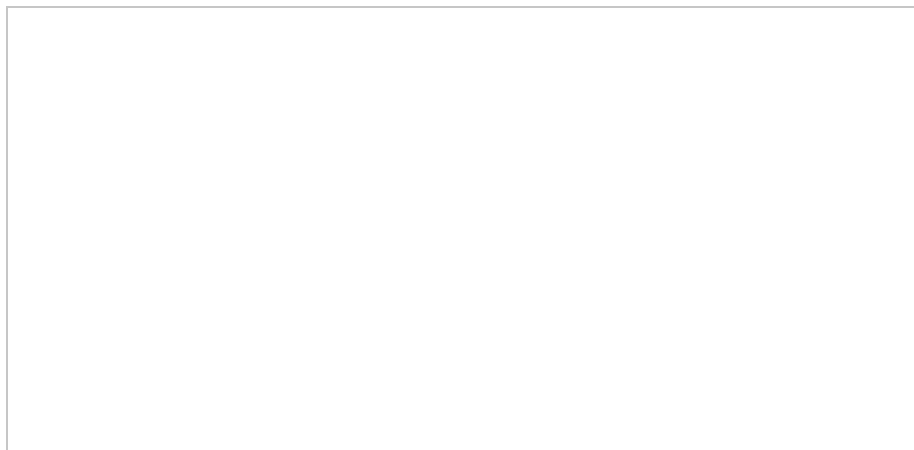


FIGURE 6.
EMG activity for attempting grasp movements.

Figure 7 indicates the EMG variations observed in brain actuated and posture activated movements corresponding to human intention of “Release”. Based on the correlation result brain actuated signal is selected for the stimulation of upper limb. Figure 8 shows the real time and recorded EMG activity for “Roll up” movement. Roll up movement is recorded using two electrodes placed on the either side of the Elbow. The rollup movement requires high intensity stimulation. In most of the time brain actuated EMG fallen below the desired level, so the stimulation of affected part is initiated in this case by artificial muscle movements. Figure 9 shows the EMG actuated by real time human Intention and the EMG activity produced using the training of “roll down” hand Posture. Roll down ideally requires low intensity signals, so in this movement selection priority is given to signal with low signal strength in the correlation. Figure 10 shows the EMG data acquired for the gesture “Roll down-grasp”. This EMG activity is used for communicating the paralyzed subject’s need to the caregivers.



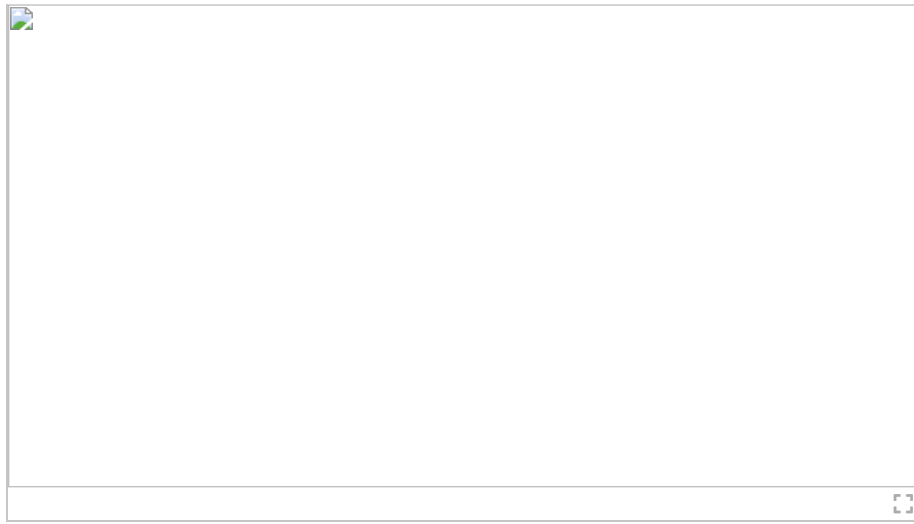


FIGURE 7.
EMG variations corresponding to release movement.

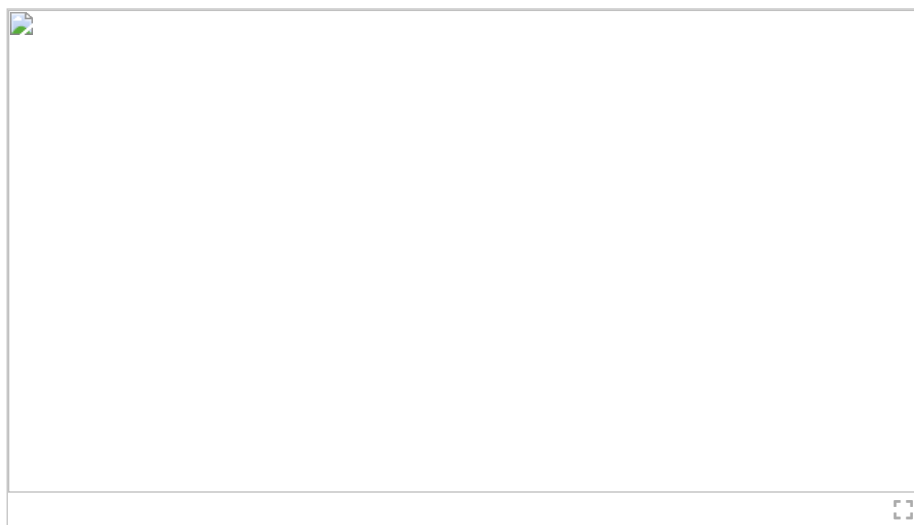


FIGURE 8.
EMG activity based on ROLL up upper limb movement.

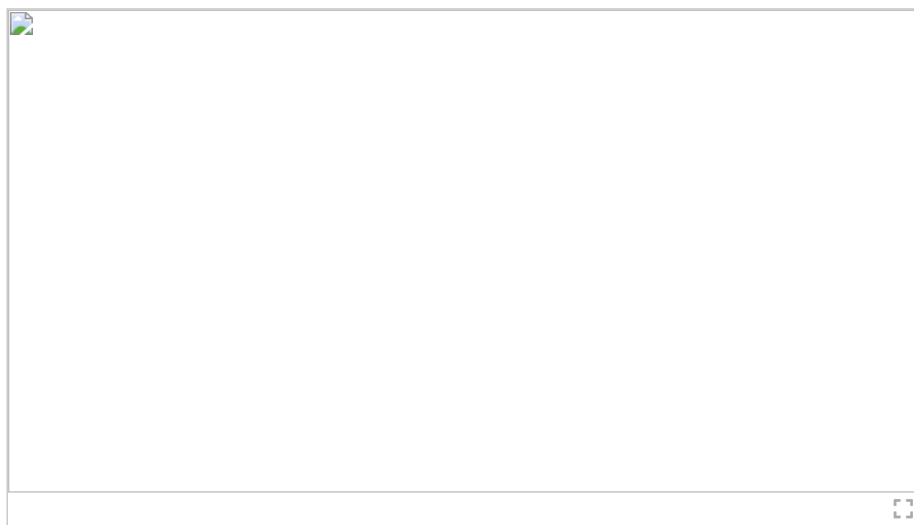


FIGURE 9.
EMG activity based on ROLL down upper limb movement.

PDF
Help

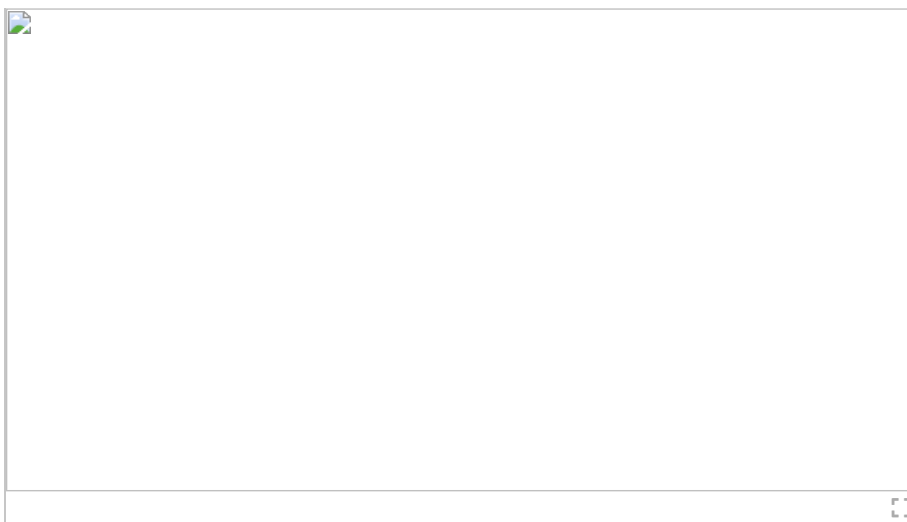


FIGURE 10.
EMG activity for the gesture roll down-grasp.

B. Result of EEG Patterns on the Realistic Head Models

Realistic head models are used for the analysis of EEG signals. EEG sensors with 16 electrodes are used for the capturing the brain signals. The unique electrode placement scheme used in this experimentation is shown in figure 11. The placement scheme mainly concentrated on the frontal and parietal regions of the brain.

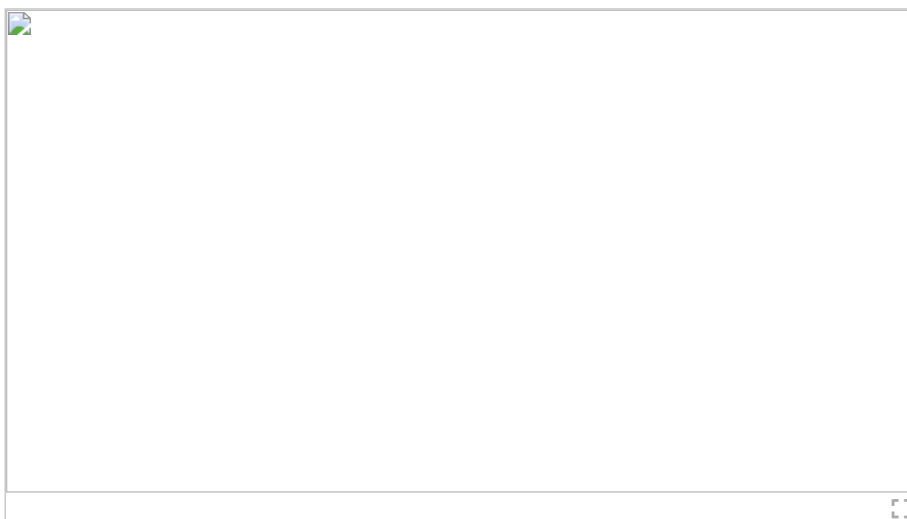
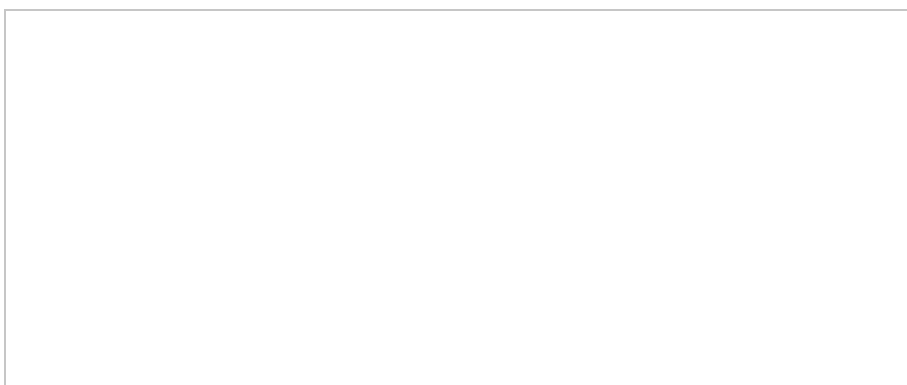


FIGURE 11.
Electrode placement on the brain [21].

The variations of brain patterns with different frequencies are analyzed to facilitate the feature extraction and classification process.

In figure 12 red indicated the maximum interaction of neuron and blue indicates minimum interaction of neurons. The neuron connectivity in the head model on the left is improved when multimedia feedback is used, compared to the figure on right which does not use feedback.



PDF
Help

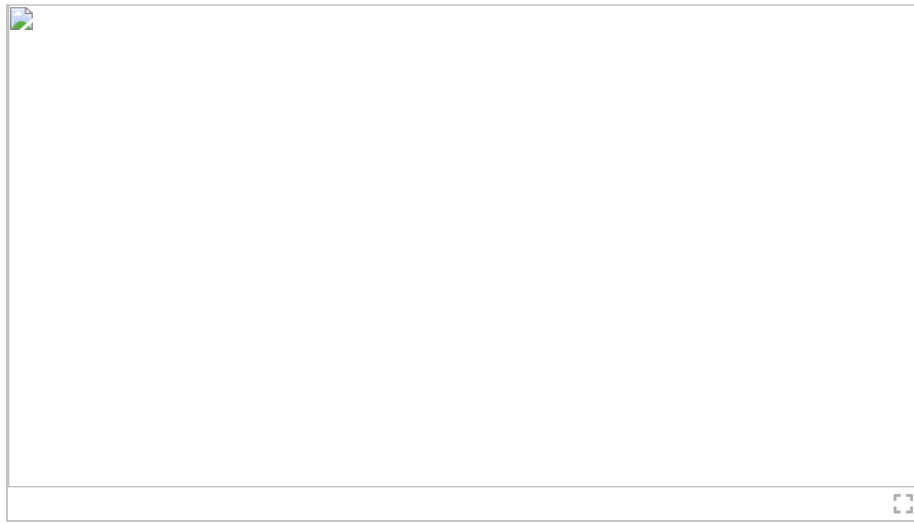


FIGURE 12. Brain pattern comparisons with and without multimedia feedback [21].

C. Statistical Analysis of Generated EMG Signal

Statistical analysis is carried out to determine the correlation between Brain actuated EMG signal and posture actuated EMG signal. The data obtained during Rollup and Rolldown movement of the upper limb are utilized for the analysis.

Correlation matrix help to identify whether the human intentions match the recorded muscle movements. This matrix acts as a second level of classifier before the final actuation of the body part is made.

Correlation Matrix obtained

[1.0000 0.0867 0.0867 1.0000]

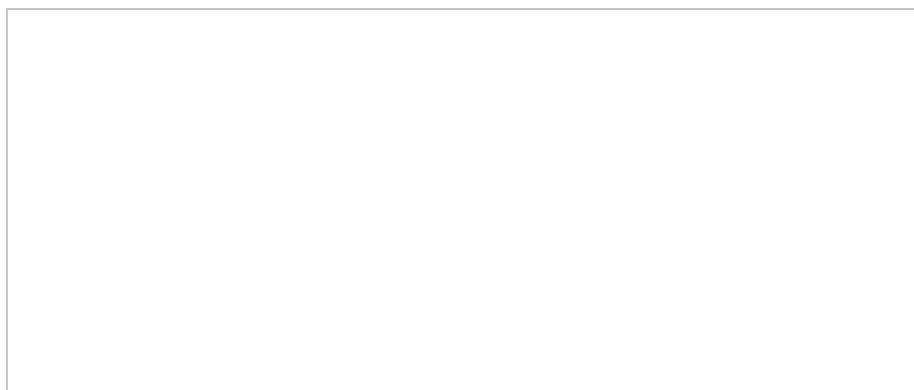
Correlation matrix obtained

[1.0000 -0.0640 -0.0640 1.0000]

Correlation matrix help to identify whether the human intentions match the recorded muscle movements. This matrix acts as a second level of classifier before the final actuation of the body part is made.

D. Results of Classification Accuracy of Different Subjects

The classification accuracy of the system is verified by performing the test on 10 healthy subjects and 10 paralyzed persons. Maximum obtained 88% efficiency and on an average 80.45% classification accuracy based on the six different human intentions for upper limb movements. The experimentation result shown in figure 13 is the summary of results on 20 participants. U1-U10 are represent healthy subjects, U11-U20 represents paralyzed persons. The reason for improved accuracy for classification among subjects is due to systematic training undertaken and usage of feedback. The healthy subject U2 is an experienced user and is more familiar with similar interfaces, obtained high accuracy. However, the unhealthy subjects U11 and U12 also obtained high accuracy through their dedication and passion. Visual feedback and voice encouragement are also given to paralyzed during training. The participants U9 and U13 has shown similar low classification accuracy due to their age and unfamiliarity with the system



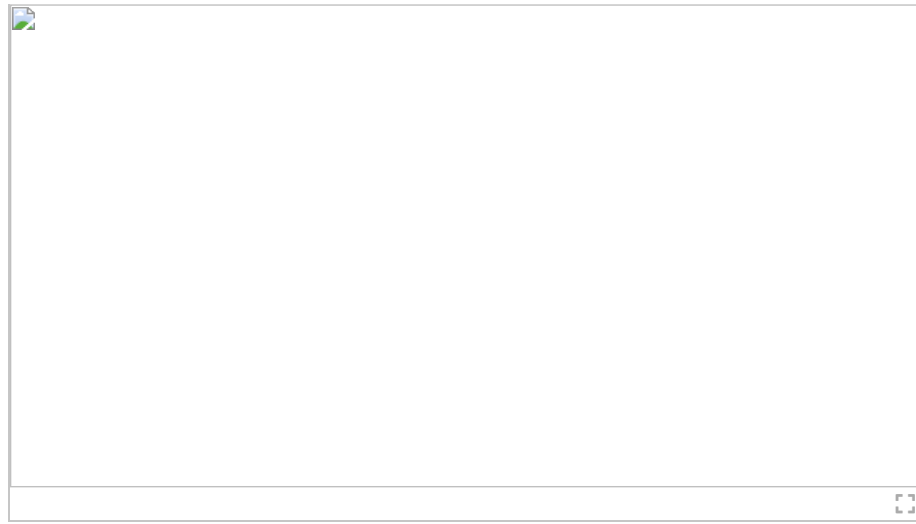


FIGURE 13.
Classification accuracy of six different movements on 20 subjects.

The authors used EEG signal to identify the human Intentions and to control upper limb movements of the paralyzed person. Artificial muscle movements are integrated into the system to get continuous movement of the affected body part. Recorded muscle movements help to enhance the rehabilitation process. The burden of carrying exoskeleton is avoided by incorporating by using innovative assembly. The communication aid for the paralyzed is provided by implementing gesture recognition module. AMIDL obtained better classification accuracy compared to many existing methods mentioned in the literature. The two-level classification employed in the system help to reduce false operations. The future research should focus on reducing human workload by incorporating efficient controllers. Accuracy of mapping human intentions with muscle movements has to be increased. Machine leaning algorithms that can effectively map human intentions to the desired muscle movements are the way forward.

SECTION VI. Conclusion

AMIDL system with 3 different modular units is designed and implemented. The system validation is carried out by performing online and offline testing on 10 healthy and 10 paralyzed subjects. AMIDL is designed to perform six different movements like Grasp, Release, Rollup, Rolldown, Rollup Release, Rolldown Grasp on the paralyzed upper limb. WHT transform is utilized for feature extraction and classification of EEG signals. The EMG activity of the healthy subjects are correlated with the real-time EMG signals generated by the paralyzed. Selection criteria for the ideal signal is finalized based on the EMG analysis carried out on all six hand postures. The two-level classification method improved the accuracy of the system. The system produced continuous response even in the presence of uncertain real-time inputs. Results indicate that mental fatigue and miss-operations are reduced. The burden of carrying exoskeleton is minimized by an innovative assembly having array of sensors and control units. Periodic stimulation in the absence of ideal brain signal enhance the rehabilitation process. Gesture Recognition method is utilized for providing communication aid for the paralyzed. In our future work, we are trying to incorporate closed loop controller with haptic feedback. Deep learning algorithms will be used to effectively map EEG signals with recorded EMG signals. The user experience can be enhanced by measuring the user emotions while performing the different activities.

ACKNOWLEDGMENT

Authors would like to thank Ms. Asha Jacob, SCMS Center for Robotics for providing assistance and guidance in testing and conducting the experiments.

Authors



Figures



References



PDF

Help

Citations



Keywords



Metrics



ALSO ON IEEE XPLORE

FLY-SMOTE: Re-balancing the ...

a year ago · 1 comment

In recent years, the data available from IoT devices have increased rapidly. ...

High-precision External Parameter ...

5 months ago · 1 comment

The fusion of camera and lidar plays an important role in the field of robotic ...

An Efficient Approach for the Detection ...

3 months ago · 1 comment

Vehicular Ad-Hoc Networks (VANETs) deliver a wide range of commercial as ...

Modeling and Analysis of Cascading ...

10 months ago · 1 comment

The cyber-physical power systems(CPPS) may experience cascading ...

Hybrid Metaheuristic Using Rough ...

10 months ago · 1

Quality of Service aware service cc plays an increas

0 Comments

Login



Start the discussion...

LOG IN WITH



OR SIGN UP WITH DISQUS ?

Name

Email

Password

Please access our [Privacy Policy](#) to learn what personal data Disqus collects and your choices about how it is used. All users of our service are also subject to our [Terms of Service](#).



Share

Best Newest Oldest

Be the first to comment.

Subscribe

Privacy

Do Not Sell My Data

PDF

Help

More Like This

Feature Extraction of Brain-Computer Interface Electroencephalogram Based on Motor Imagery

IEEE Sensors Journal

Published: 2020

A Convolutional Spiking Network for Gesture Recognition in Brain-Computer Interfaces

2023 IEEE 5th International Conference on Artificial Intelligence Circuits and Systems (AICAS)

Published: 2023

Show More

IEEE Personal Account

CHANGE
USERNAME/PASSWORD

Purchase Details

PAYMENT OPTIONS
VIEW PURCHASED
DOCUMENTS

Profile Information

COMMUNICATIONS
PREFERENCES
PROFESSION AND
EDUCATION
TECHNICAL INTERESTS

Need Help?

US & CANADA: +1 800
678 4333
WORLDWIDE: +1 732
981 0060
CONTACT & SUPPORT

Follow



[About IEEE Xplore](#) | [Contact Us](#) | [Help](#) | [Accessibility](#) | [Terms of Use](#) | [Nondiscrimination Policy](#) | [IEEE Ethics Reporting](#) | [Sitemap](#) | [IEEE Privacy Policy](#)

A not-for-profit organization, IEEE is the world's largest technical professional organization dedicated to advancing technology for the benefit of humanity.

© Copyright 2023 IEEE - All rights reserved.

PDF

Help

IEEE Account

- » Change Username/Password
- » Update Address

Purchase Details

- » Payment Options
- » Order History
- » View Purchased Documents

Profile Information

- » Communications Preferences

» Profession and Education

» Technical Interests

Need Help?

» **US & Canada:** +1 800 678 4333

» **Worldwide:** +1 732 981 0060

» Contact & Support

[About IEEE Xplore](#) | [Contact Us](#) | [Help](#) | [Accessibility](#) | [Terms of Use](#) | [Nondiscrimination Policy](#) | [Sitemap](#) | [Privacy & Opting Out of Cookies](#)

A not-for-profit organization, IEEE is the world's largest technical professional organization dedicated to advancing technology for the benefit of humanity.

© Copyright 2023 IEEE - All rights reserved. Use of this web site signifies your agreement to the terms and conditions.

PDF

Help



IETE Technical Review >
Volume 38, 2021 - Issue 4

Enter keywords, authors, DOI, etc

This Journal >
Advanced search

Submit an article | Journal homepage

987 Views
29 CrossRef citations to date
0 Altmetric

Articles

Blockchain For Intelligent Transport System

Anandkumar Balasubramaniam, Malik Junaid Jami Gul

Varun G. Menon

2 Department of Computer Science and Engineering, SCMS school of Engineering and Technology, Kochi 683576, India
View further author information

Pages 438-449 | Published online: 31 May 2020

Cite this article | <https://doi.org/10.1080/02564602.2020.1808449>

Full Article | Figures & data | References | Citations | Metrics | Reprints & Permissions | Read this article

ABSTRACT

Sample our Engineering & Technology

Intelligent Transportation System (ITS) is gaining attention but at the same time, road connection delays etc have also increased. Relative information about such

Related Research

People also read | Recommended articles | Cited by 29

Full Article | Figures & data | References | Citations | Metrics | Reprints & Permissions | Read this article

Dataset. Likewise, error rate for LDA and NMF are 36% and 35%, respectively. While keeping in mind that such reduced data is helpful in many legal processes, we introduce Blockchain in the framework. Blockchain can make data immutable thus can be considered as digital proof. Blockchain also requires a smart contract in this situation between insurance companies to collect data in case of any uncertain situation. Such analysis can offer a different point of views and trends in data. Information can be more explainable to define the situation and helps to develop a friendly environment for day-to-day customers. The proposed framework provides dimensionality reduction of data that eventually reduce the data dimension to store in Blockchain.

KEYWORDS: Accident analysis | Blockchain | ITS | Principal component analysis | Smart transportation system | Traffic surveillance

Acknowledgements

This study was supported by the National Research Foundation of Korea (NRF) grant funded by the Korean government (NRF2017R1C1B5017464).

Related Research

People also read | Recommended articles | Cited by 29

- Blockchain in transport and logistics – paradigms and transitions >
- Lenny Koh et al. International Journal of Production Research Published online: 6 Apr 2020
- Blockchain applications in supply chains, transport and logistics: a systematic review of the literature >
- Mehrdokht Pournader et al. International Journal of Production Research Published online: 11 Aug 2019
- Blockchain technology and its relationships to sustainable supply chain management >
- Sara Saberi et al.